Experimental Investigation of Subcooled Flow Boiling and CHF at Prototypical Pressures of Light Water Reactors

by
Artyom Kossolapov

B.Eng. Nuclear Engineering, Peter the Great St.Petersburg Polytechnic University, 2015
M.S. Nuclear Science and Engineering, Massachusetts Institute of Technology, 2018

Submitted to the Department of Nuclear Science and Engineering in partial fulfillment of the requirements for the degree of

Doctor of Philosophy in Nuclear Science and Engineering
at the
MASSACHUSETTS INSTITUTE OF TECHNOLOGY

SEPTEMBER 2021

Author:_____
Artyom Kossolapov
Department of Nuclear Science and Engineering
August 4, 2021

Certified by:_____
Matteo Bucci
Norman C. Rasmussen Assistant Professor of Nuclear Science and Engineering
Thesis Supervisor

Certified by:_____
Jacopo Buongiorno
TEPCO Professor of Nuclear Science and Engineering
Director, Center for Advanced Nuclear Energy Systems (CANES)
Director, Science and Technology, Nuclear Reactor Laboratory
Thesis Reader

Accepted by:_____
Ju Li, Ph. D.
Battelle Energy Alliance Professor of Nuclear Science and Engineering
Professor of Materials Science and Engineering
Chair, Department Committee on Graduate Students

Experimental Investigation of Subcooled Flow Boiling and CHF at Prototypical Pressures of Light Water Reactors

by
Artyom Kossolapov

Submitted to the Department of Nuclear Science and Engineering on August 4, 2021
In partial Fulfillment of the Requirements for the Degree of
Doctor of Philosophy in Nuclear Science and Engineering

ABSTRACT

Boiling crisis is an important phenomenon that affects the performance and safety of pressurized water reactors (PWRs). Accurate predictions of the boiling crisis are difficult to make because they require a clear understanding of the physical mechanisms leading to the boiling crisis combined with accurate models of nucleate flow boiling heat transfer. High-resolution, in situ experiments performed at prototypical pressures of light water reactors (LWRs) are needed in order to elucidate the phenomenon of the boiling crisis and to inform the development of boiling models suitable for LWRs. In the present Thesis, we developed a high-pressure flow boiling experiment together with a new phase detection technique, allowing us to investigate high pressure flow boiling with high spatial and temporal resolutions. We explored aspects of bubble departure, microlayer and triple contact line evaporation, boiling parameters (i.e. nucleation site density, bubble departure frequency, wait and growth times), heat flux partitioning and departure from nucleate boiling. The results reveal that in high pressure flow boiling bubbles depart by sliding immediately after nucleation, with no adhesion force holding a bubble in place. Drag, buoyancy and inertia were identified as the only forces governing bubble departure process. We demonstrated that bubble microlayer disappears entirely for pressures above 3 bar, with its disappearance explained by the decrease in bubble growth rate at higher pressures. The depletion of the microlayer was also analyzed, revealing that both thermal and hydrodynamic effects could be responsible for microlayer depletion process. The analysis of the triple contact line evaporation showed that it cannot account for more than 20% of the total heat flux removed by the boiling surface. Temporal boiling parameters (i.e. bubble departure frequency, wait and growth times) vary considerably between nucleation sites and nucleation events. The distribution of bubble departure frequency is particularly intriguing, since it not only exhibits a power-law, but also reveals an abundance of nucleation sites with extremely low departure frequencies (i.e. in the order of a few hertz). The analysis of the three major heat flux partitioning mechanisms (i.e. evaporation, forced convection and transient conduction) reveal that these mechanisms can only account for 40% to 60% of the total heat flux at the boiling surface, suggesting that either the modeling of these mechanisms does not accurately describe the realistic boiling scenario, or another heat transfer mechanism should be introduced to account for the missing heat flux.

Thesis Supervisor: Matteo Bucci
Title: Norman C. Rasmussen Assistant Professor of Nuclear Science and Engineering

ACNOWLEDGEMENTS

First, I would like to thank my advisor, Prof. Matteo Bucci. You have been a guide to me through all my years at MIT, from the times when it took me a month to tap a hole all the way to the era of high-pressure boiling experiments. It was a great pleasure working with you because I was always able to rely on your help and advice, would it be related to the research, my professional development or personal matters. I am extremely grateful for everything I learned from you.

Next, I would like to acknowledge Prof. Jacopo Buongiorno, who was my advisor for the first year here at MIT and continued to help me during all of the years I spent here. You have been a great help for me at the start of my time at MIT, letting me slowly adjust to the research life by not only giving me a flexibility in choosing the research project, but also guiding me in my investigations. You are one of the greatest teachers that I know, I learned a great deal from you.

Next, I would like to thank Dr. Bren Phillips. The amount of technical knowledge I received from you is extremely large. Your experience and advice were the determining factors in my success here at MIT. Countless hours that we spent going over the designs of experiments were some of the most enjoyable aspects of my work. It was also great to chat with you on many topics, from all of the Star Trek shows to economics and politics.

I would also like to acknowledge the rest of my thesis committee, Prof. Emilio Baglietto and Prof. Peter Stephan as well as my defense chair, Prof. Michael Short. Thank you for the insightful comments during my defense and for your guidance throughout my PhD research. Special thanks to Prof. Emilio Baglietto for teaching me the aspects of CFD, I had a great time taking your class.

Next, I would like to acknowledge Dr. Tom McKrell. Sadly, I only worked with Dr. McKrell for my first year at MIT. Nevertheless, I learned a great deal from him over that time. Many skills that Dr. McKrell taught me were a tremendous help in my research, and I am taking them with me into my future endeavors. I will never forget the vigor and enthusiasm with which Dr. McKrell approached every problem. We miss him dearly.

I would like to thank many amazing professors from whom I had a chance to learn both at NSE and other Departments. Your teaching styles and dedication to your students are truly inspiring. Thanks to you, I am leaving MIT with a truckload of knowledge to apply in my future career. I also want to thank the administrative staff here at NSE. You truly embody the problem-solving spirit of MIT, because there is no problem you cannot resolve, making the great machine that is the graduate education at NSE run smoothly.

I want to extend many thanks to the amazing friends that I made during my time here. Stephen, Malik, and Sam, you have been a great support to me during all six years that I spent here. You were there for me through all too short nights of study before exams, fourteen-hour work days when preparing for quals, and all the way to my defense. Despite many challenges that I faced here at MIT, I made a plethora of happy memories sharing

these challenges with you. Special thanks also go to Gustavo and Ana. You are the most positive people that I know, and I am lucky to call you my friends. In addition to making some of the greatest parties in the world, you were always supportive and made me feel better any time I face an obstacle. I know that I can always rely on you. Gustavo, you are also a great colleague, your help with my research cannot be overstated. I would also like to acknowledge many other friends that I made here. Anna, Mattia, Kelly, Reed, Ben, Evan, Ethan, and many others, you made my days here at MIT so much brighter. I also want to thank my undergraduate friends and former band mates, Alexander and Violetta. Thank you for being supportive of me, despite that fact that I leaved the band and moved half way around the globe.

Next, I would like to thank all of the amazing colleagues with whom I had a chance to work here at MIT. Andrew, thank you for all the help in the beginning of my studies. We truly made a great team. I still remember the moment we saw the DNB on the IR camera the first time, it felt like a true achievement made possible through teamwork. Florian, thank you for all the insightful conversations, math insights, and honest opinions. I also want to thank all of the people with whom I had a chance to work over the years. Md, Madhumitha, Limiao, Jee, Haeseong, Chi, Guanyu, Bert, Reza, Mathias, Raksmy, Anupam, Jerry, Honghyun, Ran, Megan, Warner, Makita, Carolyn, Ravi, Etienne, Alex, Giacomo, and Matevz, it was a blast working with you on experiments or discussing the mysteries of boiling heat transfer.

Lastly, I would like to extend my biggest gratitude to my mother, Larisa, my father, Sergey, my sister, Alexandra, and my late grandfather, Igor. Without your help and love I could not have made it through this challenging period of my life. I am very lucky to have a family like you. I was deeply saddened that my grandfather did not live to see me finish my PhD. He was an extremely positive person, always giving me advice and supporting my every endeavor. We miss him dearly.

CONTENTS

LIST OF FIGURES

LIST OF TABLES

Thesis Supervisor: Matteo Bucci
Title: Norman C. Rasmussen Assistant Professor of Nuclear Science and Engineering

1. INTRODUCTION

1.1. BACKGROUND

The research presented in this thesis revolves around the phenomenon of boiling. Boiling is an extremely useful phenomenon due to its high heat transfer efficiency compared to single-phase heat transfer mechanisms. The efficiency of boiling can be quantified by a heat transfer coefficient (HTC). HTC defines the amount by which the boiling surface heat flux will increase when its temperature is raised by one degree. In contrast to single-phase convective cooling where HTC remains almost independent of the driving temperature difference (i.e. wall temperature minus the bulk temperature), boiling HTC increases significantly with the increase of wall temperature. This leads to some of the highest HTCs achievable across all heat transfer modes [1]. The high heat transfer efficiency of boiling allows for the creation of very compact heat transfer systems, while also keeping the components of such a system at relatively low temperature. It is no surprise that such advantages led to the use of boiling in a variety of application where high heat fluxes and HTCs are required. In this thesis a specific focus is given to the application of boiling to the heat removal from fuel rods inside nuclear reactors.

Despite multiple advantages, there exist a significant limitation to boiling efficiency that comes in a form of a heat flux instability, called departure from nucleate boiling (DNB). When a sufficiently high heat flux (called critical heat flux, or CHF) is applied to the boiling surface, it could create too many bubbles that will merge and form a stable vapor layer covering the boiling surface. This layer will insulate the boiling surface from the bulk liquid, leading to the extreme degradation of HTC and a rapid escalation of the wall temperature. A visualization of this effect is shown in Figure 1-1, where the distributions of heat flux and wall temperature at the boiling surface at DNB are shown. As the vapor layer forms at a particular point on the boiling surface, it creates a local dry spot where the boiling surface is directly in contact with vapor. Since the HTC inside of such a dry spot is extremely low, this will lower the instantaneous heat flux within the dry spot region almost to zero (see a dark blue region in Figure 1-1 right). It should be noted that in the experiment shown in Figure 1-1 the average heat flux on the boiling surface is set to a constant value of 2.45 MW/m^2 and is controlled independently by the means of joule heating. Therefore, a natural response of the system to a sudden drop in HTC is to increase its temperature until it is high enough to transfer the applied heat flux (2.45 MW/m^2 in this case). Naturally, this leads to the creation of a local hot spot, whose temperature can rise by as much as 1000 ^oC in less than a second! Such hot spot can be seen clearly in Figure 1-1 (left).

If DNB conditions are met at any place inside a nuclear reactor, this will result in a local failure of the fuel cladding and a release of radioactive materials into the reactor coolant. If such failures happen on a small scale, they can lead to the plant shutdown and multi-million financial losses. In contrast, large scale DNB dry spots can lead to a serious damage to the reactor core. Special care is taken by nuclear engineers to ensure that DNB conditions

are never met during the operation of nuclear reactors. DNB is avoided by limiting the reactor power to keep heat fluxes everywhere in the core below the CHF limit. Such limitations prevent nuclear reactors from utilizing all benefits of boiling. However, there are evidences suggesting that the limitations to the reactor power can be removed by enhancing the CHF limit through design modifications, which will in turn reduce the risk of large- and small-scale DNB dry spots. Multiple studies found a considerable improvement in pool boiling CHF with micro- and nano-scale surface modifications [2]. Additionally, several researchers were successful at achieving extremely high heat fluxes in highly subcooled flow boiling cases. A comprehensive review of the most extreme heat fluxes achieved experimentally is presented by Gambill and Lienhard [3]. They present evidences that the heat fluxes as high as 224.5 MW/m^2 were achieved in high velocity flow boiling of water. Another study reported that the CHF of 211.9 MW/m^2 was reached when a boiling surface was cooled by a highly subcooled impinging jet [4]. Despite the abundance of DNB studies, the mechanisms responsible for the DNB in general and CHF enhancement in particular are not fully understood. Such limited understanding not only hinders the application of CHF enhancement techniques to large scale power reactors, but also results in considerable uncertainties when it comes to CHF predictions, making power limits the only practical way to avoid DNB in a commercial nuclear reactors. While the overall limit to the reactor power is driven by various design considerations, approximately 20% of the penalty to the reactor power is associated with the CHF prediction uncertainties, meaning that existing reactor fleet can produce more power if CHF prediction uncertainties are reduced. Furthermore, if a large-scale application of CHF enhancement methods became possible, DNB might not be an issue at all. Given the above arguments, it is no surprise then that DNB prediction was recognized as one of six challenging problems facing nuclear industry by the Consortium for Advanced Simulation of Light Water Reactors (CASL) [5]. This challenge was addressed by developing and improving modeling and simulation tools. Interestingly, accurate DNB predictions cannot be achieved without accurate predictions of boiling heat transfer because two phenomena are tightly connected. Such link was emphasized by recent studies, one of which argued that DNB can be considered as a stability limit of the heat flux partitioning triggered by the formation of the dry area on the heated surface [6]. Another work suggests that the boiling crisis is triggered by an instability of the bubble interaction process, linked to the distribution of the bubble footprint area on the heated surface [7]. These findings suggest that the development of robust modeling and simulation tools for boiling heat transfer is key in creating an accurate tool for DNB characterization. The development of such tools relies heavily on our understanding of boiling physics, specifically for the high-pressure conditions relevant to nuclear reactor operation. Unfortunately, very little is known about high pressure boiling, making it challenging to design modeling and simulation tools for high pressure conditions. The limited knowledge is mainly related to the scarcity of experimental studies caused by experimental challenges associated with the high-pressure conditions.

The main purpose of this thesis is to improve the understanding of high-pressure boiling heat transfer by conducting special experiments that allow a close look at the phenomena underlying boiling at the conditions that replicate as close as possible the environment inside PWR cores. The research presented in this thesis provides valuable information

about the flow boiling of water at high pressure and temperature conditions, typical to nuclear reactors. Nevertheless, many insights gained throughout this research can be used in other applications with similar boiling behavior.

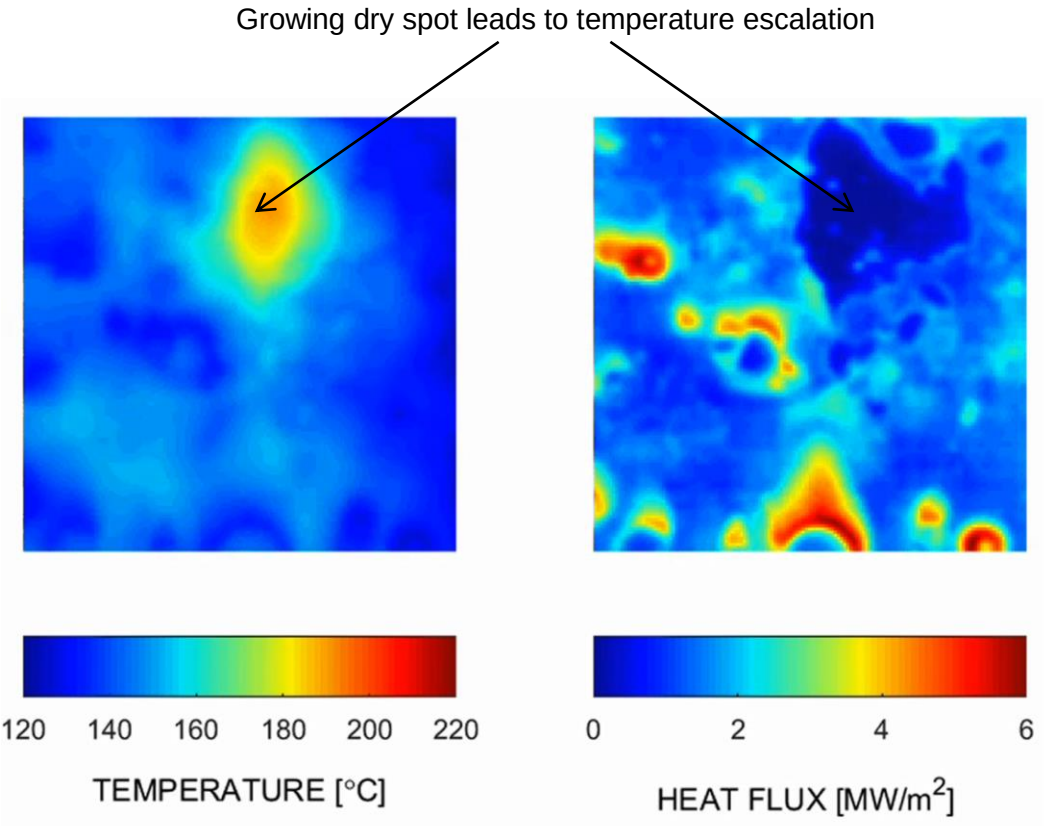

Figure 1-1. Departure from nucleate boiling visualized with infrared thermometry. Temperature distribution is shown on the left, while heat flux distribution is shown on the right. A large dry spot is forming at the top of the image, resulting in extreme degradation of the heat transfer coefficient and a significant increase of the wall temperature. Images are adapted from [8]

1.2. STRUCTURE OF THE THESIS

The thesis is divided into seven main chapters. This first chapter is the introduction, where we give an overview of the motivation behind the current work, while also providing a comprehensive literature review that highlights the current state of understanding of boiling heat transfer. This chapter also emphasizes three main topics addressed by the thesis. The first topic is the process of bubble departure and its mechanism at high pressure. The second topic is evaporative heat transfer, including both the microlayer and triple contact line evaporation. The final and third topic is the heat flux partitioning. It touches a broad range of parameters that are used to characterize boiling heat transfer within modeling and simulation tools. Each of these topics is addressed in details in Chapters 3, 4 and 5. Chapter 2 gives a detailed description of experimental methods used in the present study, together with the post-processing techniques and associated uncertainties. Chapter 6 provides a brief

analysis of the DNB dry spot formation and the distributions of dry area sizes on the boiling surface. Finally, Chapter 7 provides a conclusion to the thesis and proposes directions for the future work.

1.3. CURRENT UNDERSTANDING AND MODELING FRAMEWORKS

This section contains a literature review that addresses several current modeling frameworks used to characterize boiling heat transfer. It also provides information about the current understanding of several physical mechanisms that govern boiling heat transfer. Finally, a number of research gaps that are being addressed by the thesis are identified.

1.3.1. Mechanistic heat flux partitioning frameworks

Mechanistic heat flux partitioning (HFP) models lie at the intersection of basic physical understanding and practical application. An ideal mechanistic HFP model will combine the breadth of knowledge about boiling phenomena into a set of mathematical relations that can be used to quantify the boiling heat transfer coefficient based only on *a priori* known parameters (i.e. operating conditions such as the system pressure or mass flow rate). In this section, we analyze several HFP models that were proposed since the work of Bowring in 1962 [9]. This analysis provides a historical overview of how the knowledge of boiling has been evolving over the past 60 years, highlighting the discoveries of several important phenomena that govern boiling heat transfer and providing an overview of how these phenomena were quantified within HFP frameworks. Finally, this analysis allows us to identify many limitations and unknowns that are still present even in the newest HFP frameworks. These unknowns are of particular interest for the present work, since they highlight the most important and the least explored aspects of the boiling physics, motivating the current research.

The majority of current HFP models are being developed to be integrated within computational fluid dynamics (CFD) modeling tools, where they are used to prescribe the heat transfer rates at the boiling wall. The typical structure of an HFP model is shown in Figure 1-2. The calculation of the heat flux at the boiling wall starts by identifying system parameters (e.g. pressure, subcooling, mass flux, etc.) and local fluid properties (density, heat capacity, surface tension, etc.). These quantities combined with a guess of the wall temperature are used to calculate a set of boiling parameters. Each boiling parameter characterizes one aspect of boiling physics. Active nucleation site density (N'') quantifies the number of sites per unit area of the boiling surface at which bubbles can nucleate. Bubble departure diameter (D_d) quantifies the average size that a bubble has when it leaves the nucleation site. Bubble departure frequency (f) quantifies the rate at which new bubbles are produced at the nucleation site. Many more parameters are typically found within full formulations of modern HFP models. Models for calculation of each of the boiling parameters are generally complex and continue to evolve year after year as better experimental and analytical results are generated by the scientific community. When a complete set of boiling parameters is calculated, another set of mathematical models is used to calculate partitioned heat fluxes. Each partitioned heat flux characterizes a

particular mode of heat transfer. These modes are generally divided in three major categories:

- Evaporation captures the heat transfer due to the phase change. It accounts for the energy spent on creating vapor phase. Evaporation at the liquid microlayer or at the triple contact line (TCL) are normally the only modes of a direct heat transfer from the wall to the bubble by means of evaporation. However, additional phase change happens close to the boiling surface, where the superheated liquid layer is being evaporated at the bubble interface. Strictly speaking, the heat transfer through the evaporation of the superheated liquid layer surrounding the liquid-vapor interface should not be considered when constructing an HFP evaporation term because the energy required to increase the temperature of the superheated liquid layer above saturation was supplied by other single-phase wall heat transfer mechanisms. Therefore, including the evaporation of the superheated liquid layer in the evaporation term results in the double-counting of energy and overestimation of the evaporative term. Despite this problem, several HFP models base their evaporative term on the entire volume of a bubble, hence counting TCL and microlayer evaporation, as well as the evaporation of the superheated liquid layer. In the present study we will refer to such models as near-wall HFP models, since they consider both the wall and near-wall evaporation. In contrast, mechanistically accurate HFP models that only consider the evaporation of the microlayer and TCL will be referred to as true wall HFP models.
- Convection captures single-phase heat transfer due to either forced or natural convection in the areas that are not occupied by bubbles (i.e. areas where no active nucleation sites are present). These mechanisms are either treated through the normal convection analysis or by introducing additional heat transfer enhancement that bubbles induce by disturbing the boundary layer.
- Non-evaporation enhancement can be broadly quantified as anything related to bubble agitation. Growth and movement of bubbles can induce complex flow patterns in the vicinity of the wall that will disrupt the thermal boundary layer. Therefore, non-evaporation enhancement is usually associated with the high heat flux that is present during the re-establishment of the thermal boundary layer. Because of this underlying logic, most non-evaporation components like quenching and sliding conduction are calculated using the laws of transient conduction.

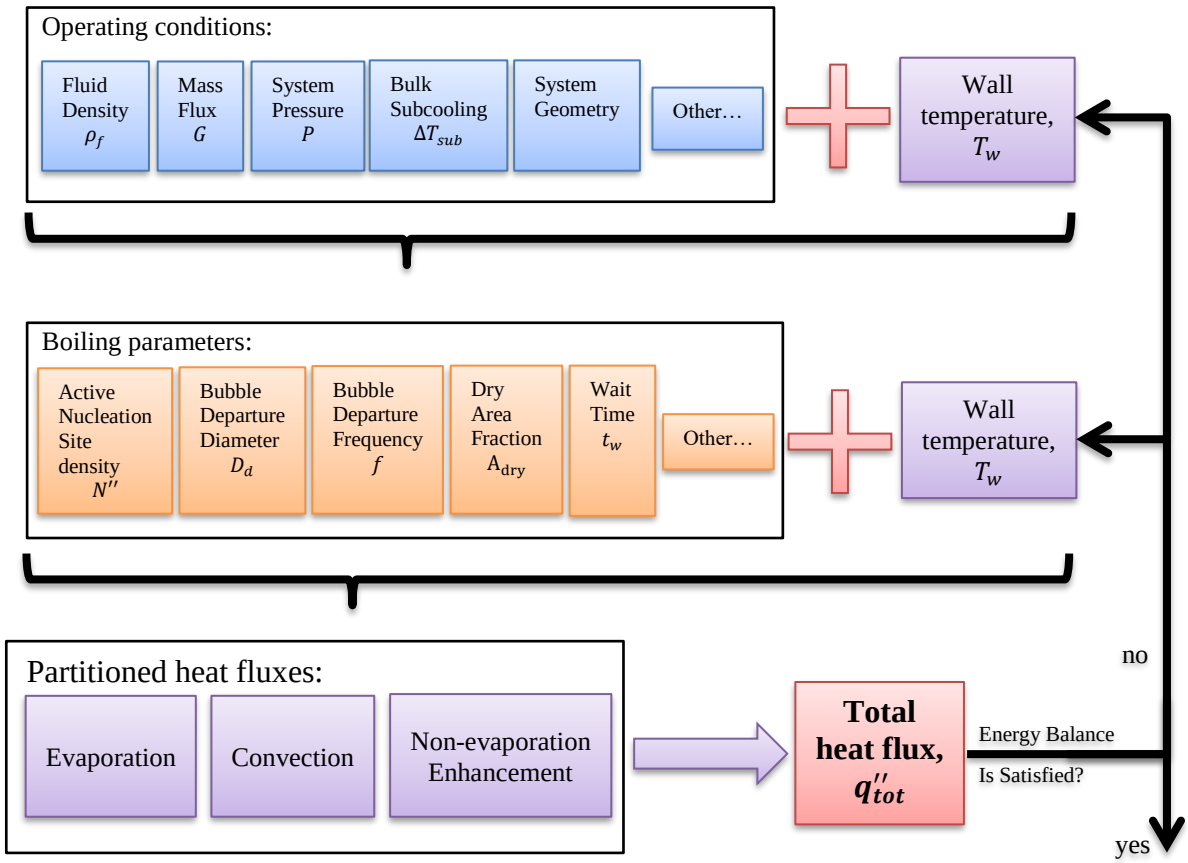

Figure 1-2. Basic structure of HFP models

Practically, given a target heat flux, the heat flux partitioning algorithm can be implemented as follows. All the partitioned heat fluxes are calculated based on a tentative wall temperature and are added together to calculate the total heat flux on the boiling surface. If the energy balance is not satisfied (i.e., if the calculated heat flux is different from the target heat flux), the wall temperature is adjusted and the entire process is repeated until the energy balance is satisfied. In this Sub-Section we will provide a literature review of the third row in Figure 1-2, focusing on the current understanding of different heat transfer mechanisms that govern boiling heat transfer.

To the best of the author's knowledge, the idea to partition heat fluxes on the boiling surface into several components based on the associated heat transfer mechanisms was first formalized by Bowring in 1962 [9], who investigated subcooled flow boiling in a vertically oriented heated surface. Bowring recognized the existence of areas on the boiling surface that are unaffected by either bubbles or bubble columns. The bubble columns are typically created when multiple bubbles are departing from the same nucleation site and slide near the boiling surface. Bowring also noted that larger portion of the boiling surface is affected by boiling when the heat flux is increased or when bulk subcooling is decreased. Based on these observations and an array of experimental data, an empirical relation was proposed that quantified the heat transfer associated with forced convection (see Table 1-1, where

q_c'' is the forced convection partitioned heat flux, h_c is the convective HTC, ΔT_{sub} is the bulk subcooling, q'' is the total heat flux at the boiling surface, p is the system pressure). For the evaporative heat flux Bowring postulated that if a bubble departs from the nucleation site at a certain volume V_{bd}, then the energy required to create this bubble can be calculated by multiplying the departure volume V_{bd} by vapor density ρ_g and the latent heat of evaporation h_{fg} (see Table 1-2). In order to account for all the bubbles that are being produced on the boiling surface and to convert the energy into the heat flux, nucleation site density (N'') and bubble departure frequency (f) were included into the equation (see Table 1-2). The final component, called bubble agitation was attributed to the fact that when a bubble grows and departs, it pushes the superheated liquid layer away from the wall into the bulk, causing colder liquid to rush into the place of the departed bubble, inducing the enhancement of the heat transfer. This enhancement was related to the nucleation sites density (N'') departure frequency (f) and bubble volume at the departure (V_{bd}) with the addition of liquid density ρ_l, heat capacity c_p and the effective temperature difference between the cold water that is rushing in after the departing bubble and the boiling surface $\Delta T_{ba,eff}$. This last parameter was quantified empirically together with a few other constituents of the model. Despite the abundance of empiricism in the formulation of Bowring's model, the mathematical description of the partitioned heat fluxes is very similar to more recent and perhaps popular HFP approaches, such as the RPI model of Kurul and Podowski [10]. The formulations of Bowring provided a clear direction for the future improvements of HFP frameworks, while also highlighting some of the most important boiling parameters in the form of nucleation site density, bubble departure frequency and departure volume.

The next major improvement in quantifying boiling heat transfer mechanisms came in the work of Mikic and Rohsenow in 1969 [11]. Since their work was concerned with pool boiling, the correlations for natural convection were used to quantify convective heat flux (see Table 1-1, where h_c is the convective HTC, T_w is the wall temperature, T_b is the bulk temperature, Nu_c is the Nusselt number and Ra is the Rayleigh number). Mikic and Rohsenow also recognized that only a fraction of the surface area will be affected by the pure natural convection. Hence, the ratio of the area affected by convection, A_c to the total surface area A_{tot} was also introduced into the equation (see Table 1-1). Note that the model of Mikic and Rohsenow does not have an evaporation component (see Table 1-2). In their work only the evaporation of the microlayer was considered among evaporative heat transfer mechanisms. Mikic and Rohsenow stated that several models that were successful at predicting bubble growth for various experiments did not account for the microlayer evaporation. Therefore, they concluded that microlayer evaporation does not provide a significant contribution to the bubble growth and can be ignored. Nowadays we have evidences clearly demonstrating that in certain cases microlayer evaporation can account for more than a half of bubble volume [12], making the argument of Mikic and Rohsenow only valid for certain operating conditions when bubbles do not form microlayers. Nevertheless, the mere fact that Mikic and Rohsenow considered microlayer evaporation and not the evaporation of the total bubble volume, like in the case of Bowring, marks a significant advancement in HFP modelling. The model of Mikic and Rohsenow is a true wall HFP model, rather than being a near-wall HFP model, like in the case of Bowring. The problem with near-wall HFP models is that they are prone to double counting of the

heat flux. In near-wall HFP models it is assumed that the energy required to create the entire volume of the bubble is supplied directly by the boiling surface. However, the volume of the bubble is created not only through the evaporation of microlayer and TCL, but also through the evaporation of the superheated liquid layer surrounding the bubble. However, the energy transferred to the superheated liquid layer is already calculated through the other two heat transfer mechanisms, namely, convection and non-evaporation-based enhancement. Therefore, by using the total volume of the bubble for evaporative component it is likely that the total heat flux on the boiling surface will be overestimated. Near-wall HFP models also have limitations when applied to highly subcooled flows. In such flows the apex of a bubble can be exposed to the subcooled liquid, leading to condensation. This will further increase the error associated with the calculation of the heat flux. Therefore, a true wall HFP model is always preferable as it is clearer how to establish its energy balance compared to near-wall HFP approaches. The final major advancement in the work of Mikic and Rohsenow was made by modeling the non-boiling enhancement with the use of transient conduction (see Table 1-3). Mikic and Rohsenow assumed that disruption and replenishment of the thermal boundary layer happens after each bubble cycle, leading to the integration of the solution for the transient conduction in a semi-infinite body performed over the entire bubble departure period (i.e. the inverse of bubble departure frequency f). Such approach is only valid when the growth time of a bubble is negligible compared to the wait time. In contrast, when the growth time is comparable to the wait time, the integration of the solution for the transient conduction should only be performed over the period of time when the bubble is not attached to the boiling surface (i.e. the wait time). Mikic and Rohsenow also introduced for the first time the concept of the area of influence of a bubble. Modeled as a multiplication factor K_i, the concept of the area of influence accounts for the fact that a departing bubble carries with it a portion of the superheated layer that is larger than the projected area of the bubble, hence affecting an area of the boiling surface that is K_i times larger than the projected area of the bubble. Both the transient conduction laws and area of influence factor are being utilized even in the most recent HFP models. In their work Mikic and Rohsenow used the value of $K_i = 4$, warning that their expression is only valid when the overlapping of influence areas is insignificant.

The next advancement appeared in the work of Judd and Hwang [13], who recognized the importance of the microlayer evaporation to the total heat flux. They used a formulation that accounts for the energy removed by the evaporation of the microlayer volume $V_{\mu L}$, which was converted into the average heat flux on the boiling surface by adding nucleation site density N'' and bubble departure frequency f to the equation (see Table 1-2). In order to prescribe the volume of the microlayer that was evaporated, Judd and Hwang used experimental data from several interferometric studies where the thickness of the microlayer can be measured. Their approach to the modeling of the other two components was very similar to Mikic and Rohsenow [11], with the exception of the area of influence factor K_i that was reduced to 1.8 (see Table 1-1 and Table 1-3).

The model of Kurul and Podowski [10], also known as the RPI model, gained great popularity since its introduction in 1990. In fact, HFP framework is only a small portion of the 1990 publication. The majority of the paper presents a complete set of closures that can

be applied directly to a CFD solver. This fact can probably explain the popularity of the RPI model. In addition to the improvements that the RPI model made to the calculation of boiling parameters (second row in Figure 1-2), several modifications to the way partitioned heat fluxes are calculated were made compared to the formulation of Judd and Hwang. First, the RPI model was designed to be applied to flow boiling, leading to the use of Reynolds analogy with the local Stanton number St_y to calculate convective heat flux (see Table 1-1, where y refers to a certain position inside the buffer layer of the turbulent boundary layer). They also recognized that only a fraction of the boiling surface is being affected by pure convection. The evaporation was treated in the same way as in the work of Bowring [9], where the total volume of the bubble at the point of departure was considered (see Table 1-2). Such total volume was calculated through the use of bubble departure radius R_d. This modification to the evaporation term makes RPI model a near-wall HFP model. The improvement to the quenching term was made by recognizing that the period of transient conduction only appears during the waiting period t_w between consecutive bubble nucleations, rather than throughout the entire bubble period, different from the works of Judd and Hwang [13] and Mikic and Rohsenow [11] (Table 1-3). The value of the influence factor $K_i = 4$ was used within the RPI model.

As the boiling research continued, scientists began to realize that a new effect can be responsible for significant heat transfer from the boiling surface when subcooled flow boiling at the vertical surface is studied. Specifically, it was observed that multiple bubbles slide near the wall following their departure from the nucleation site. A sliding bubble will not only continue to disrupt the thermal boundary layer following its departure, it will also induce additional evaporation, as a thin lubrication layer will be inevitably trapped in between the wall and the sliding bubble. Yeoh et al. [14] proposed a HFP model that takes into account the effect of sliding bubbles. They used transient conduction to quantify the enhanced heat transfer due to bubble departure and sliding separately (see Table 1-3). In their formulation, transient conduction appeared during both the wait and growth periods of a bubble, however, different magnitudes were assigned to these periods. The distinction was made between departure radius R_d (i.e., the radius at which a bubble leaves its nucleation site) and lift-off radius R_l (i.e., the radius at which a bubble moves away from the heated wall towards the bulk liquid). In addition, Yeoh et al. recognized that as the bubble slides on the surface, it can pass over the neighboring nucleation sites, deactivating them. Therefore, a reduction factor R_f that is based on the active nucleation site density and bubble sliding length was introduced to reduce the active nucleation site density available for sliding. Yeoh et al. used the area of influence factor $K_i = 1.8$, similar to Judd and Hwang [13]. The evaporation term was calculated in a similar manner as in the RPI formulation, while also accounting for the additional evaporation that happens during the sliding period. This was achieved by using bubble lift-off radius in order to calculate the evaporation heat flux (see Table 1-2). This makes the model of Yeoh et al. a near wall HFP model. Finally, convective heat flux was calculated in the same manner as in the RPI formulation.

More recently, Gilman and Baglietto [15] proposed a HFP framework that encompasses many relevant physical phenomena affecting boiling heat transfer. All three of the heat transfer modes were modified. The forced convection component was modified to not only

account for the convection in the areas unaffected by bubbles, but also to include areas that are weakly affected by bubbles where the thermal boundary layer has time to fully recover between two consecutive nucleation or sliding events (see Table 1-1). The time t^* that defines the point when transient conduction and convection HTC are equal was used to prescribe a switchover point for convection to be applied to the areas affected by bubbles. Similar to the work of Yeoh et al. [14], a reduction factor R_f was used to quantify the interaction between sliding bubbles and neighboring nucleation sites. This reduction factor was used in addition to a separate model that accounts for bubble interaction. Additionally, a convective HTC was modified (h_c^* in Table 1-1) in order to account for the way in which bubbles attached to the boiling surface can change the turbulent boundary layer and further enhance the HTC. The evaporation heat flux was split into three parts. The first part accounts for the evaporation of the bubble during the rapid, inertia-controlled growth phase. In modelling this component, Gilman and Baglietto refer to the work of Gerardi et al. [16], suggesting that the bubble volume at the end of the inertia controlled phase can be approximated as a hemisphere with a radius equal to the eventual bubble departure radius R_d. The other two evaporation components model the evaporation of the microlayer during the bubble growth at the nucleation site as well as the evaporation of the lubrication layer during the bubble sliding (see Table 1-2, where $\delta_{\mu L,max}$ is the maximum thickness of the microlayer and δ_{sl} is the thickness of a lubrication layer that is evaporated during the sliding process). Since the framework of Gilman and Baglietto contains both the direct evaporation that happens at the wall (microlayer and lubrication layer) as well as the inertia-controlled bubble growth, which is primarily fueled by the evaporation of the superheated liquid layer surrounding the bubble, it makes this framework to occupy a middle ground between near-wall and true wall HFP models, approaching the true wall model when the bubble size at the end of the inertia controlled growth is negligible. The transient conduction heat flux due to sliding bubbles was formulated in such a form as to consider the characteristic time t^* required for the re-establishment of thermal boundary layer (see Table 1-3). In addition, a concept of solid quenching was introduced, accounting for the excess energy accumulated inside the substrate during the periods of low HTC when the bubble microlayer dries out and the boiling surface is contacted directly by vapor. This term accounts for the fact that the boiling wall temperature is not spatially uniform and constant. Notably, the concept of the area of influence was completely removed from this formulation, improving the robustness of the model by excluding the empiricism associated with the selection of K_i.

The final model considered here is of a particular interest for the present research because it was optimized for high pressure application. This model was developed by Kommajosyula [17] based on the works of Gilman [18], Gilman and Baglietto [15], Baglietto et al. [6] and Demarly [19]. Recent direct numerical simulation (DNS) results of Guion [20] suggested that the extent of the area under the bubble occupied by the microlayer compared to the dry area will decrease as the capillary number associated with the bubble growth rate gets smaller. Based on these DNS results, Demarly [19] formulated an expression that scales the ratio between the dry area radius R_{dry} and the microlayer radius $R_{\mu L}$ with both the capillary number Ca and the contact angle θ. This formulation was adopted in the work of Kommajosyula (see Table 1-2). Kommajosyula recognized that the growth rate of the bubble may decrease at high pressure, leading to the complete

absence of the microlayer. In the model of Kommajosyula the contribution of the microlayer evaporation gradually decreases with increasing pressure, becoming zero at high pressure. If a true wall HFP model does not consider TCL evaporation, then the absence of the microlayer will lead to the absence of the evaporative heat flux term. In the model of Kommajosyula, the evaporative heat flux component is preserved at high pressures through the evaporative term that accounts for the evaporation at the bubble inception. The radius of the bubble at the inception has the same capillary number Ca and contact angle θ scaling as the extend of the dry area relative to the microlayer, making the inception radius equal to the departure radius when the microlayer disappears. Therefore, the model of Kommajosyula can be characterized as a near-wall model at high pressures when the microlayer is absent.

Table 1-1. Approaches to the calculation of convective heat flux component

	Convection type	Equation
Bowring (1962) [9]	Forced	$q_c'' = h_c \cdot \Delta T_{sub}; \quad for\ \Delta T_{sub} > \Delta T_{sub,sp}$ $q_c'' = 0; \quad for\ \Delta T_{sub} \le \Delta T_{sub,sp}$ $\Delta T_{sub,c} = 0.7 \cdot \frac{q''}{h_c} - \beta_B \cdot (0.7q'')^{0.25}$ $\beta_B = 7.8 \cdot \exp[-0.0163 \cdot (p-1)]$
Mikic and Rohsenow (1969) [11]	Natural Laminar $(10^5 < Ra < 2 \cdot 10^7)$	$q_c'' = \frac{A_c}{A_{tot}} \cdot h_c \cdot (T_w - T_b)$ $Nu_c = 0.54 \cdot Ra^{\frac{1}{4}}$
	Natural Turbulent $(2 \cdot 10^7 < Ra < 3 \cdot 10^{10})$	$q_c'' = \frac{A_c}{A_{tot}} \cdot h_c \cdot (T_w - T_b)$ $Nu_c = 0.14 \cdot Ra^{\frac{1}{3}}$
Judd and Hwang (1976) [13]	Natural	$q_c'' = h_c \cdot (T_w - T_b) \cdot (1 - K_i \cdot \pi \cdot R_d^2 \cdot N'')$ $Nu_c = 0.18 \cdot Ra^{\frac{1}{3}}$ $K_i = 1.8$
Kurul and Podowski (1990) [10]	Forced	$q_c'' = \frac{A_c}{A_{tot}} \cdot \rho_l \cdot c_{pl} \cdot u_{l,y} \cdot St_y \cdot (T_w - T_y)$
Yeoh et al. (2008) [14]	Forced	$q_c'' = \frac{A_c}{A_{tot}} \cdot \rho_l \cdot c_{pl} \cdot u_l \cdot St \cdot (T_w - T_b)$
Gilman and Baglietto (2017) [15]	Forced convection over the areas unaffected by bubbles	$q_{c1}'' = h_c^* \cdot (1 - A_{sl} \cdot N''^*) \cdot (T_w - T_b)$
	Forced convection over the areas affected by sliding during the time when forced convection HTC is higher than sliding conduction HTC	$q_{c2}'' = h_c^* \cdot A_{sl} \cdot N''^* \cdot (1 - f \cdot t^*) \cdot (T_w - T_b)$ $t^* = \frac{\varepsilon_l^2}{\pi \cdot h_c^2}$ $N''^* = R_f \cdot N''$
Kommajosyula (2020) [17]	Forced	$q_c'' = \frac{A_c}{A_{tot}} \cdot h_c \cdot (T_w - T_b)$

Table 1-2. Approaches to the calculation of evaporative heat flux component

	Evaporation modes considered	Equation
Bowring (1962) [9]	Evaporation of the total bubble volume	$q_e'' = N'' \cdot f \cdot V_{bd} \cdot \rho_g \cdot h_{fg}$
Mikic and Rohsenow (1969) [11]	-	-
Judd and Hwang (1976) [13]	Microlayer evaporation	$q_e'' = q_{\mu L}''$ $q_{\mu L}'' = \rho_l \cdot h_{fg} \cdot N'' \cdot f \cdot V_{\mu L}$
Kurul and Podowski (1990) [10]	Evaporation of the total bubble volume	$q_e'' = \frac{4}{3} \cdot \pi \cdot R_d^3 \cdot \rho_g \cdot h_{fg} \cdot f \cdot N''$
Yeoh et al. (2008) [14]	Evaporation of the total bubble volume	$q_e'' = R_f \cdot \frac{4}{3} \cdot \pi \cdot R_l^3 \cdot \rho_g \cdot h_{fg} \cdot f \cdot N''$
Gilman and Baglietto (2017) [15]	Bubble inception	$q_{e,init}'' = \frac{2}{3} \cdot \pi \cdot R_d^3 \cdot \rho_g \cdot h_{fg} \cdot f \cdot N''$
	Microlayer evaporation	$q_{e,\mu L}'' = V_{\mu L} \cdot \rho_l \cdot h_{fg} \cdot f \cdot N''$ $V_{\mu L} = \frac{2}{3} \cdot \pi \cdot \left(\frac{R_d}{2}\right)^2 \cdot \delta_{\mu L,max}$
	Evaporation of a lubrication layer under a sliding bubble	$q_{e,sl}'' = V_{sl} \cdot \rho_l \cdot h_{fg} \cdot f \cdot N''$ $V_{\mu L} = A_{sl} \cdot \delta_{sl}$
Kommajosyula (2020) [17]	Bubble inception	$q_{e,init}'' = \frac{4}{3} \cdot \pi \cdot R_i^3 \cdot \rho_g \cdot h_{fg} \cdot f \cdot N''$ $R_i = R_d \cdot \max[0.1237 \cdot Ca^{-0.373} \cdot sin(\theta)\,; 1]$ [1]
	Microlayer evaporation	$q_{e,\mu L}'' = V_{\mu L} \cdot \rho_l \cdot h_{fg} \cdot f \cdot N''$ $V_{\mu L} = \delta_{\mu L,max} \cdot R_{\mu L}^2 \cdot \frac{\pi}{3} \cdot \left\{2 - \left[\left(\frac{R_{dry}}{R_{\mu L}}\right)^2 + \frac{R_{dry}}{R_{\mu L}}\right]\right\}$ $R_{\mu L} = \frac{R_i}{2}$ $\frac{R_{dry}}{R_{\mu L}} = \max[0.1237 \cdot Ca^{-0.373} \cdot sin(\theta)\,; 1]$

Table 1-3. Approaches to the calculation of non-evaporation heat flux enhancement by bubbles

[1] While this expression was replicated from the original document (Ref. [17]), we suspect that instead of the "maximum" operator the "minimum" operator should be used to prevent the inception radius from becoming larger than the departure radius at low Capillary numbers

Author	Original name of the heat transfer mode	Equation
Bowring (1962) [9]	Bubble agitation	$q''_{ba} = N'' \cdot f \cdot V_{bd} \cdot \rho_l \cdot c_p \cdot \Delta T_{ba,eff}$
Mikic and Rohsenow (1969) [11]	Transient conduction	$q''_{tc} = 2 \cdot \sqrt{\pi} \cdot \varepsilon_l \cdot K_i \cdot R_d^2 \cdot \sqrt{f} \cdot N'' \cdot (T_w - T_b)$ $K_i = 4$
Judd and Hwang (1976) [13]	Nucleate boiling	$q''_{nb} = 2 \cdot \sqrt{\pi} \cdot \varepsilon_l \cdot K_i \cdot R_d^2 \cdot \sqrt{f} \cdot N'' \cdot (T_w - T_b)$ $K_i = 1.8$
Kurul and Podowski (1990) [10]	Quenching	$q''_q = t_w \cdot f \cdot (K_i \cdot \pi \cdot R_d^2 \cdot N'') \cdot \frac{2}{\sqrt{\pi \cdot t_w}} \cdot \varepsilon_l \cdot (T_w - T_y)$ $K_i = 4$
Yeoh et al. (2008) [14]	Transient conduction in the region of nucleation	$q''_{tc} = t_w \cdot f \cdot (K_i \cdot \pi \cdot R_d^2 \cdot N'') \cdot R_f \frac{2}{\sqrt{\pi \cdot t_w}} \cdot \varepsilon_l \cdot (T_w - T_b) +$ $(1 - t_w \cdot f) \cdot (\pi \cdot R_d^2 \cdot N'') \cdot R_f \frac{2}{\sqrt{\pi \cdot t_w}} \cdot \varepsilon_l \cdot (T_w - T_b)$ $K_i = 1.8$
	Transient conduction due to sliding bubbles	$q''_{tcsl} = t_w \cdot f \cdot (K_i \cdot L_{sl} \cdot 2\bar{R} \cdot N'') \cdot R_f \frac{2}{\sqrt{\pi \cdot t_w}} \cdot \varepsilon_l \cdot (T_w - T_b) +$ $(1 - t_w \cdot f) \cdot (\pi \cdot \bar{R}^2 \cdot N'') \cdot f \cdot t_{sl} \cdot R_f \frac{2}{\sqrt{\pi \cdot t_w}} \cdot \varepsilon_l \cdot (T_w - T_b)$ $K_i = 1.8$ $\bar{R} = \frac{R_d + R_l}{2}$
Gilman and Baglietto (2017) [15]	Sliding conduction	$q''_{sc} = t^* \cdot f \cdot A_{sl} \cdot N''^* \cdot \frac{2}{\sqrt{\pi \cdot t^*}} \cdot \varepsilon_l \cdot (T_w - T_b)$ $t^* = \frac{\varepsilon_l^2}{\pi \cdot h_c^2}$ $N''^* = R_f \cdot N''$
	Solid quenching	$q''_{sq} = \rho_s \cdot c_{ps} \cdot V_{sq} \cdot \Delta T_s \cdot f \cdot N''$ $V_{sq} = \frac{2}{3} \cdot \pi \cdot R_{dry}^3$
Kommajosyula (2020) [17]	Sliding conduction	$q''_{sc} = t^* \cdot f \cdot A_{sl} \cdot N'' \cdot \frac{2}{\sqrt{\pi \cdot t^*}} \cdot \varepsilon_l \cdot (T_w - T_b)$ $t^* = \frac{\varepsilon_l^2}{\pi \cdot h_c^2}$

It should be noted that it is impossible to judge which of the HFP models presented above provides the best description of the boiling process. All of these models were successful at predicting specific sets of experimental results, while using drastically different formulation of the partitioned heat fluxes. The difference between each model becomes

even larger when the values of boiling parameters (row two in Figure 1-2) that they predict are considered. This undermines the generality of each of the HFP frameworks, making it impossible to tell whether these HFP models can be applied to a wide range of operating conditions. However, the purpose of this literature review is not to attack the limitations of each HFP framework, but rather to identify the overall logic that permeates the entire history of HFP modeling, allowing us to pinpoint the areas where the understanding of the boiling process can be improved.

One of the biggest mysteries of boiling lies in our understanding (or misunderstanding) of the non-evaporation heat transfer. The signature of this mystery is the abundant use of the area of influence factor K_i. While Table 1-3 shows area of influence factors of 1.8 and 4, other researchers found K_i to cover a much wider range, from as low as 0.25 to as high as 8. A review of different studies concerning the area of influence factor can be found in [21]. Such variability between studies suggests that the concept of the area of influence is not a good model for describing the real physics of non-evaporative enhancement. In fact, the concept of the area of influence goes back to the work of Mikic and Rohsenow [11], who advised against the application of the area of influence concept to regimes where such areas begin to overlap. Therefore, it should not be possible to apply the same value of K_i to processes where bubbles interact with each other. However, the overlap between areas of influence cannot be the only shortcoming of the concept, as was demonstrated by Del Valle and Kenning [22] who performed flow boiling investigation at high subcooling and used high speed photography to quantify nucleation sites positions, bubble departure sizes and frequencies. They took special care to quantify the interaction between areas of influence and delineated clusters of bubbles under which transient conduction heat transfer was calculated. Despite their effort, they needed the values of K_i to be as high as 7.5 in order to match their experimentally measured heat flux values. It should also be noted, that the physical explanation behind the concept of the area of influence states that an isolated bubble moving away from the boiling surface in a pool of water will carry away some portion of the superheated liquid layer that is larger than the projected area of the bubble. Therefore, it should not be expected that the same approach will be applicable to cases with fundamentally different hydrodynamics (e.g. turbulent flow boiling). This, however, leads us to the following question:

> *does the concept of the area of influence simply accounts for some new and unexplored heat transfer mechanism that acts together with the classical transient conduction approach, or is it simply a remedy to poor models used for the calculation of boiling parameters (row 2 in Figure 1-2)?*

Recent studies suggest that it could be both. In the recent work of Gilman and Baglietto [15] new heat transfer mechanisms were added (e.i. sliding conduction and solid quenching) together with the modifications to the models used for the calculation of boiling parameters. This allowed for the removal of the area of influence factor from the modeling framework. In addition, the work of Baglietto et al. [6] used experimentally measured values of boiling parameters to successfully predict the boiling curves and CHF values. Nevertheless, given the number of degrees of freedom each HFP model has, we should continue examining experimental evidences and try to fully grasp the extent to which newly

introduced heat transfer mechanisms could account for the non-evaporative enhancement. Such investigation is especially important for high pressure cases, in which experimental data is sparse. A detailed analysis of the single-phase heat transfer is presented in Chapter 5 of the thesis.

Another important aspect of the current HFP frameworks is the modeling of evaporation term. The approach used to model the evaporation will define whether the HFP model can be considered as a true wall HFP model or a near-wall HFP model, with the limitations of the near-wall approach discussed above. A true wall boiling model should only contain microlayer and TCL evaporation terms within its formulation. However, recent HFP models also added evaporation at the bubble inception, defining bubble inception diameter as the diameter at the end of the inertia-controlled growth phase. Note that even such definition makes these models partially near-wall, because the classical solution of the inertia-controlled bubble growth is utilizing the energy of the superheated liquid that surrounds the bubble [23]. However, if this approach to the evaporation is used, a more important question to ask is:

> *would the growth of a bubble in high pressure boiling be dominated by thermally controlled or inertia-controlled phase?*

In the case of Gilman and Baglietto [15], half of the bubble departure volume was used, while in the work of Kommajosyula [17] the inception diameter scaled from half of the departure diameter at low pressure to being equal to the departure diameter at high pressure. These approaches to calculating the inception diameter involve severe approximations. However, we need to investigate how close are these approximations to the reality and whether they lead to overestimation of the evaporative term and potential double-counting of the heat flux. The simplest way to determine if a bubble is in inertia-controlled or thermally controlled growth phase, is to look at the radius of a bubble as a function of time. During the inertia-controlled growth the radius of a bubble is proportional to time t, while during the thermally controlled growth it is proportional to the square root of time $\sqrt{t}$. Therefore, in order to provide estimates for the inception diameter, a brief look at bubble growth histories is taken in Chapter 3. Another important question is concerned with the evaporation of the triple contact line (TCL). Since the size of the bubbles will decrease at high pressure, it will result in a certain scaling for each partitioned heat flux. Since most of the partitioned heat fluxes are proportional either to the bubble radius to the power 2 or 3, they will scale down relatively fast. In contrast, the heat flux at the triple contact line will be proportional to the contact line density, which is probably scaling as the bubble radius to the power 1. Therefore, a question arises:

> *is it possible that TCL evaporation will become a relevant heat removal mechanism at higher pressure?*

The relative magnitude of the TCL heat flux is investigated in Chapter 4. The final component of the evaporative heat flux is the microlayer evaporation, which is discussed in the next sub-section.

1.3.2. Microlayer formation

When it comes to microlayer evaporation, the most important parameter to quantify is the volume of the microlayer that is evaporated before the departure of the bubble. Defining this parameter is not an easy task, since it depends on the extent of the microlayer, microlayer thickness, microlayer slope and evaporation rate. In addition, a microlayer will only form under the right conditions. In fact, several studies suggest that no microlayer is created under high pressure conditions [17], [24]. One of the main questions that we pose in the Thesis is:

- *at what pressure will the microlayer disappear entirely?*

For perfectly wetting and non-volatile liquids the process of microlayer formation is well known. In the case of a plate being vertically drawn from the liquid pool with the velocity v, a microlayer will form with a median thickness δ. This median thickness can be expressed using the Landau-Levich law (Equations (1-1) through (1-3) reproduced from [24]), where C is a coefficient equal to 0.94 for a flat plate, L_c is the capillary length, Ca is the capillary number, μ_l is the dynamic viscosity of the liquid, σ is the surface tension, ρ_l is the liquid density and g is the gravitational acceleration. In these idealized conditions the microlayer will always form, regardless of the magnitude of the dewetting velocity v.

$$\delta = C \cdot L_c \cdot Ca^{2/3} \tag{1-1}$$

$$Ca = \frac{\mu_l \cdot v}{\sigma} \tag{1-2}$$

$$L_c = \sqrt{\frac{\sigma}{\rho_l \cdot g}} \tag{1-3}$$

However, water is neither perfectly wetting nor a non-volatile liquid. Both the partial wetting and volatility could be responsible for the disappearance of the microlayer, either through the retraction of the contact line or microlayer evaporation. First, let us consider the question of wettability. Whenever the liquid contact angle θ is non-zero, there will be a critical velocity v_c that is required to form the microlayer. The value of the critical velocity is proportional to the cube of the contact angle θ^3 as was shown both analytically and experimentally [25]. Recent DNS analyses about the hydrodynamic formation of the microlayer by Guion et al. [26] suggest that the fraction of bubble footprint area occupied by the microlayer decreases with higher contact angles.

However, the microlayer could disappear simply as a result of evaporation. In other words, no microlayer will be observed if it evaporates faster than it forms. A detailed investigation of thermal effects was performed in the recent study of Schweikert et al. [24], who developed an experiment that allowed them to replicate the plate drawing conditions and create a stable microlayer. In their experiment wall superheat, heating power and dewetting velocity were varied. The effect of the contact angle was removed from the experiments

by using FC-72, which had a contact angle close to zero. Schweikert et al. demonstrated that a regime map can be developed, defining a criterion for microlayer formation based on the wall superheat and dewetting velocity. Interestingly, the effect of the wall superheat on the microlayer formation was not unlike that of the wettability, clearly defining a critical dewetting velocity below which the microlayer is not formed. The value of the critical dewetting velocity was higher for higher wall superheat, approaching zero as the wall superheat was brought to zero.

The discussion presented here suggests that two mechanisms could be responsible for the disappearance of the microlayer at high pressure. What complicates the issue is that both effects lead to a similar observable quantity – the critical dewetting velocity. Identifying which mechanism is responsible for the disappearance of the microlayer at higher pressure is crucially important because it will define the correct approach to use when modeling microlayer heat flux. If microlayer disappearance is driven by surface wettability, then we can expect a significant depletion rate of the microlayer which is independent of its evaporation rate. Therefore, for a certain initial microlayer thickness, only a portion of the microlayer volume will be consumed by evaporation with the rest being removed hydrodynamically. In contrast, if the disappearance is purely thermal, then the entirety of the initial microlayer thickness will be consumed by evaporation, potentially leading to higher energy removed by microlayer evaporation. Therefore, another important question that is addressed by Chapter 4 of the thesis is:

> *whether thermal or hydrodynamic depletion of the microlayer defines its disappearance in the high-pressure flow boiling of water?*

In addition to dealing with the question of the microlayer disappearance, Chapter 4 also provides data that elucidates the deformation of the microlayer under the effect of flow. We analyzed experimental data for several pressures and mass fluxes and connected the asymmetry of the microlayer with the apparent contact line velocity in Chapter 4. Finally, more evidences are presented, supporting a recent discovery of the reversal in microlayer slope close to the edge of the bubble, first observed by Chen et al. [27], [28].

1.3.3. Bubble departure diameter

Until now the discussion presented in this section was limited to heat transfer mechanisms that govern boiling process (row 3 in Figure 1-2). However, understanding the behavior of bubbles on the boiling surface is equally important. Typically, boiling parameters (row 2 in Figure 1-2) are used to quantify nucleation, growth and departure of bubbles. Bubble departure diameter is one of the most important boiling parameters because of the high sensitivity of partitioned heat fluxes to this parameter (see Table 1-1 through Table 1-3). Therefore, understanding bubble departure mechanism in high pressure conditions is extremely important for being able to predict bubble departure diameter with high accuracy. Before proceeding further with the discussion, it is emphasized that the application of the same bubble departure models to low and high heat fluxes should be done with extreme caution because of the bubble interaction and the phenomenon called “vapor clotting”. Vapor clotting appears at high heat flux conditions when multiple

departing bubbles coalesce to form a large vapor clot that positions itself between the boiling surface and bulk liquid. Interestingly, a vapor clot will remain at a certain distance from the boiling surface creating a liquid film that is trapped between the boiling surface and the vapor clot. This phenomenon was observed by many researchers. Bowring [9] was already referencing other studies that observed this phenomenon, suggesting that it was first observed even before 1960. A more recent review of experimental evidences highlighting this phenomenon was presented by Le Corre et al. [29]. Of higher importance for the present discussion is the liquid film trapped in between of the boiling surface and a vapor clot. This film is typically referred to as the liquid macrolayer. It served as the basis for several macrolayer-based CHF models [30]–[33]. At the moment, the typical thickness of the macrolayer is unknown, with estimates ranging from ~ 5 μm [31] to 300 μm [28], even though these estimates are not supported by comprehensive measurements. Despite this uncertainty, it is likely that the presence of the vapor clot and liquid macrolayer will affect the departure and growth of bubbles. If the macrolayer is too thin, the bubbles can coalesce with the vapor clot before departure, while thicker macrolayers may allow for bubble departure but limit the sliding length. While a few extra evidences of vapor clotting at high pressure conditions are presented in Chapter 3, the question of bubble departure at high heat flux is beyond the scope of this thesis. The above discussion is presented only to delineate the distinction between high and low heat flux boiling. Therefore, this study will only focus on the low heat flux bubble departure, during which bubble interaction is limited.

There are two main limitations that prevent an accurate prediction of bubble departure diameters in high pressure flow boiling. The first limitation is related to the scarcity of high pressure data. Figure 1-3 summarizes available experimental data on bubble departure diameter. The majority of early studies focused on pool boiling conditions at pressures up to 10 bar (Tolubinski and Ostrovski, [34]) and 137 bar (Semeria, [35]). More recently, Sakashita and Ono [36] reported bubble departure diameter measurements in pool boiling up to the pressure of 50 bar. Several studies [37]–[39] focused on flow boiling conditions. Nevertheless, each of these studies used a different approach to evaluate the bubble size, and none of them gives the exact measurement of bubble diameter at departure. Treschev [37] captured the maximum diameter reached by bubbles in flow boiling at pressures as high as 50 bar. Ünal [38] reported measurements of bubble diameters made in an adiabatic sapphire tube that followed a 10 m long heated section. The measurements were done at pressures as high as 177 bar. In the work of Griffith et al. [39], the bubble diameters were measured based on the photographs of the boiling surface that were taken at time intervals too long to track the growth and coalescence of individual bubbles. Simply put, to the best of the authors' knowledge, high-quality data for bubble departure diameters in flow boiling conditions at high pressure are not available in the literature. Therefore, one of the goals of this thesis is

> *to provide a detailed analysis of the bubble departure process in high pressure flow boiling.*

Experimental results and analytical investigation of this problem are presented in Chapter 3. Despite the possible differences in the experimental approaches, both pool boiling [34]–

[36] and flow boiling [37]–[39] studies have revealed that the diameter of a bubble decreases from a few millimeters (e.g., ~1 mm) at 1 bar down to approximately 10 to 100 μm at 100 bar. This information is relevant for the discussion of experimental challenges caused by small bubble sizes that is presented in Section 1.4.

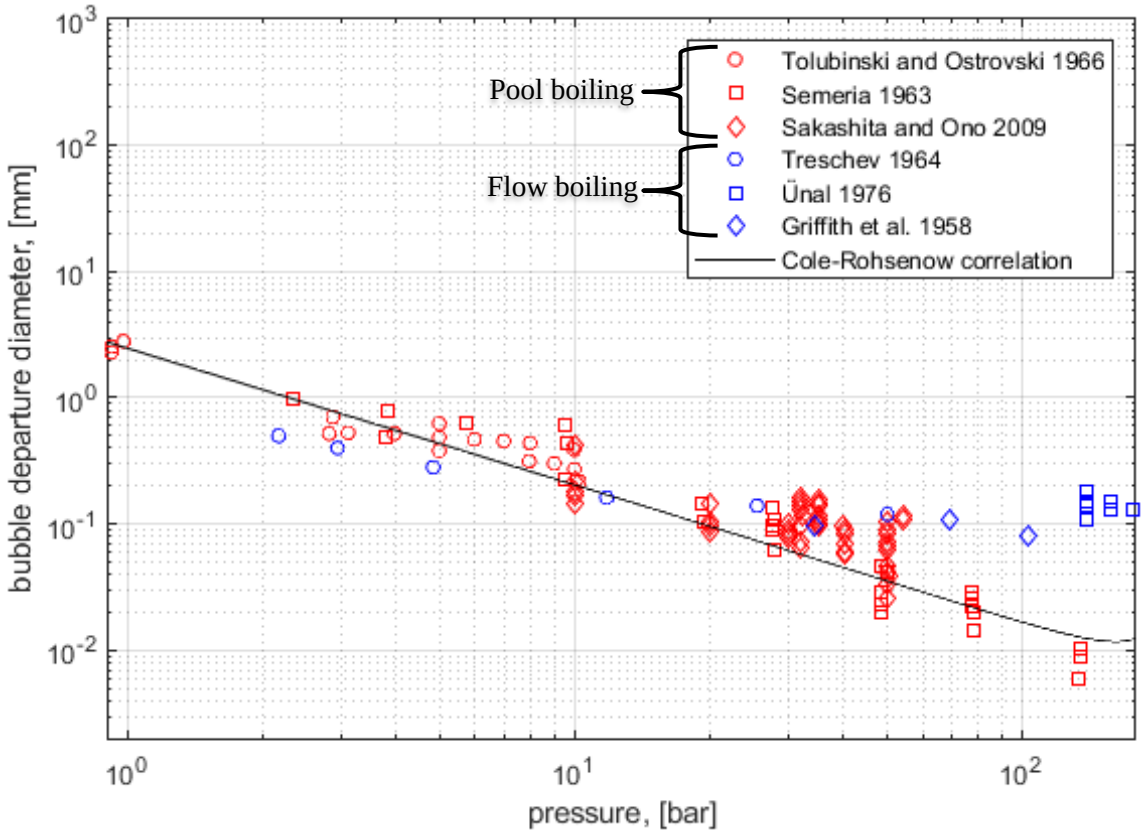

Figure 1-3. Summary of the available data on bubble departure diameter at high pressure conditions. Cole-Rohsenow correlation was reproduced from Ref. [40].

The second limitation is related to the mechanistic force balance models that are commonly used to predict bubble departure diameter. Multiple models with varying degrees of complexity and empiricism were developed in the past (see refs. [41]–[43] as examples). The logic of force balance models revolves around the conservation of momentum for an individual bubble. Before departure the momentum of the bubble remains close to zero since the bubble is barely moving while being attached to the wall. As soon as the bubble starts to depart, its momentum will increase rapidly. Based on this logic, force balance models attempt to quantify all external forces acting on a bubble. The point of departure is defined as the time when the sum of external forces exceeds zero, signifying the imbalance of forces that will push the bubble away from its nucleation site. One large issue with all available force balance models is that before the point of departure all of them predict a large negative force acting on a bubble. However, the change of bubble momentum before departure remains extremely low, meaning that force balance models do not conserve momentum. The major issue preventing the force balance models from conserving momentum lies in the lack of robustness of the force balance approach. Even if the forces

are calculated correctly, the force balance approach is based on predicting a small imbalance in the bubble inertia, which is calculated by subtracting forces that are two to three orders of magnitude larger than the inertial force. The problem is further exacerbated by inaccurate models that are used to calculate individual forces acting on bubbles. These limitations of the force balance models were recently demonstrated in the work of Bucci et al. [44], who performed experimental and analytical investigation of forces acting on an individual bubble in pool boiling, demonstrating that by carefully quantifying the shape of a bubble during its growth, one can calculate realistic values of forces acting on such a bubble. Bucci et al. have demonstrated that with such careful analysis the momentum is fully conserved and all external forces acting on a bubble prior to departure add up to zero. Additionally, several studies involving quasi-static bubbles injected through orifices [45]–[47] also found that in a carefully controlled environment the sum of forces acting on a bubble prior to departure is zero. Nevertheless, achieving momentum conservation required the careful quantification of forces acting on a bubble throughout the entire bubble growth cycle, making it extremely sensitive even to the low values of uncertainties. This shows the limitations that current force balance models have when it comes to describing the real physics of bubble departure process. However, the force balance approach can still provide meaningful insights into the forces and phenomena governing bubble departure process, especially in high-pressure conditions. In contrast to low pressures, the change in bubble inertia at high pressure could be significant due to the increase in vapor density. Additionally, due to the small size of bubbles, they will potentially remain spherical in shape because of the surface tension force, reducing the uncertainty caused by applying idealized analytic force balance models to the realistic boiling scenario. These facts may potentially allow the successful application of the force balance models to high pressure conditions. In the present work the force balance modeling is applied to our experimental data. Such analysis highlights relevant forces and phenomena that govern bubble departure process in high pressure flow boiling. The derivation of the force balance for high pressure flow boiling conditions together with the application of the force balance analysis to experimental data is presented in Chapter 3.

1.3.4. Nucleation site density, departure frequency, wait and growth times

Similar to bubble departure diameter, the boiling parameters that prescribe the number of nucleation sites at which bubbles are formed (i.e., nucleation site density, N'') as well as the temporal characteristics of bubbles (i.e., bubble departure frequency, f; growth time t_g and wait time t_w) suffer from extremely limited amount of high-pressure data as well as modeling limitations. First, the limited data is discussed. Tolubinsky and Ostrovsky [34] found that the bubble departure frequency did not change between 1 and 10 bar in pool boiling of water, suggesting that the decrease in bubble growth rate compensates the decrease in bubble departure diameter. Sakashita and Ono [36] found similar results, but for coalesced bubbles. They reported that the departure frequency of coalesced bubbles is almost constant between the pressures of 1 and 50 bar, observing only a slight increase. Sakashita [48] also measured nucleation site density in pool boiling on a vertically oriented surface for pressures up to 50 bar and heat fluxes up to 0.34 MW/m^2. Sakashita found that the nucleation site density can be predicted well with the Hibiki-Ishii model [49] for a value of the contact angle $\theta = 90°$. Despite such good agreement with the data of Sakashita, the

model of Hibiki and Ishii requires further testing in different high pressure situations. One should remember that the validation of the high-pressure performance of the Hibiki-Ishii model was made with derived values of nucleation sites density, which were calculated based on a boiling correlation. Therefore, further experimental measurements are needed to fully validate the model of Hibiki and Ishii at high pressures. Treschev [37] measured the nucleation site density in flow boiling of water at pressures as high as 50 bar, subcoolings between 13 and 85 °C and heat fluxes up to 2.9 MW/m^2, and proposed an empirical correlation to fit the measured data.

To the best of author's knowledge, these are the only studies that provide empirical information on nucleation site density and temporal characteristics of high pressure boiling of water. This fact makes it very challenging to ensure that the models for these parameters that are based on low pressure results can be extended to high pressure conditions. While providing raw data for these parameters is one of the goals of the present study, there is a much more important question that needs to be addressed concerning the connection between the nucleation site density and temporal characteristics of boiling. One of the most influential models for nucleation site density is the mechanistic model of Hibiki and Ishii [49]. This model uses nucleation theory together with the detailed information about the distribution, size and shape of cavities on a typical commercial metallics surface. The output of the model is the number of sites that can support nucleation. Since the development of this model, evidences show that it significantly overpredicts the nucleation site density at high heat fluxes, leading to unphysically high values. A reason for such overprediction was suggested by Gilman and Baglietto [15], who recognized that the model of Hibiki and Ishii predicts the total number of available nucleation sites on the boiling surface. However, it is not guaranteed that all the available sites will be active. Certainly, if a nucleation site is located under a bubble it will not be active. Additionally, local cooling that is induced by bubbles can prevent certain sites from being active, even if on average the wall superheat on the boiling surface is high enough to allow for nucleation of such sites. To account for these effects, Gilman and Baglietto introduced an additional model that accounts for bubble interaction. This model used not only the information about bubble footprint size, but also the temporal characteristics of boiling. In the end, the model of Gilman and Baglietto allowed for the conversion between the available nucleation site density predicted by Hibiki and Ishii and the active nucleation site density that is more relevant for HFP calculations.

However, this observation invites the following question:

> *how active should a nucleation site be to be considered active? If a site produces one bubble in an hour, will this site be important, or can it be ignored?*

The answer to this question depends on the way the temporal characteristics (i.e. f, t_g and t_w) are distributed between the sites. In order to demonstrate this point, here we perform a derivation of the partitioned heat flux responsible for the microlayer evaporation, while assuming that all boiling parameters are varied between nucleation sites and individual nucleation events. Such variability is expected because boiling is a stochastic process. Assume that a site s had a nucleation event e during which a certain microlayer volume

$V_{\mu L}(s;e)$ was evaporated. The energy removed by such nucleation event $Q_{\mu L}(s;e)$ is given by Equation (1-4).

$$Q_{\mu L}(s;e) = \rho_l \cdot h_{fg} \cdot V_{\mu L}(s;e) \tag{1-4}$$

If a nucleation site s has certain number of nucleation events $N_e(s)$ during the period of time t, then the total energy removed by microlayer evaporation at site s is given by Equation (1-5).

$$Q_{\mu L}(s) = \rho_l \cdot h_{fg} \cdot \sum_{e=1}^{N_e(s)} V_{\mu L}(s;e) \tag{1-5}$$

Finally, the microlayer evaporation energy removed by all nucleation sites on the boiling surface with the area A is given by Equation (1-6)

$$Q_{\mu L} = \rho_l \cdot h_{fg} \cdot \sum_{s=1}^{N_s} \sum_{e=1}^{N_e(s)} V_{\mu L}(s;e) \tag{1-6}$$

where N_s is the total number of active nucleation sites on the boiling surface. Finally, the heat flux removed by the microlayer evaporation is given by Equation (1-7).

$$q''_{\mu L} = \rho_l \cdot h_{fg} \cdot \frac{1}{A \cdot t} \cdot \sum_{s=1}^{N_s} \sum_{e=1}^{N_e(s)} V_{\mu L}(s;e) \tag{1-7}$$

However, if instead of tracking bubbles appearing at individual nucleation sites we simply count every bubble b that nucleates on the boiling surface then Equation (1-7) can be rewritten to give us Equation (1-8).

$$q''_{\mu L} = \rho_l \cdot h_{fg} \cdot \frac{1}{A \cdot t} \cdot \sum_{b=1}^{N_b} V_{\mu L}(b) \tag{1-8}$$

where N_b is the total number of bubbles nucleated at the boiling surface. Equations (1-7) and (1-8) are equivalent to each other and represent a way of calculating microlayer evaporation heat flux by which the energy fully conserved. The key to having an energy conserving form of a particular partitioned heat flux is in accounting for the total flux of a parameter that defines energy removal by a particular mechanism. In the case of microlayer evaporation, the total flux of microlayer volume evaporated at the boiling surface $\Phi_{\mu LV}$ is the defining quantity (see Equation (1-9)).

$$\Phi_{\mu LV} = \frac{1}{A \cdot t} \cdot \sum_{b=1}^{N_b} V_{\mu L}(b) = \frac{1}{A \cdot t} \cdot \sum_{s=1}^{N_s} \sum_{e=1}^{N_e(s)} V_{\mu L}(s;e) \tag{1-9}$$

However, Equations (1-7) and (1-8) have no practical use since it is impossible to know *a priori* how many bubbles will nucleate at the boiling surface and how much of their microlayer will be evaporated. Instead, we can rederive the energy conserving form of the microlayer evaporation heat flux in terms of boiling parameters like the nucleation site density N'' and bubble departure frequency f. Let's start with the total energy removed by individual nucleation site (Equation (1-5)). If the period of time between each bubble nucleation is $t_b(s;e)$, then the time-averaged "power" removed by evaporation of the microlayer at a nucleation site s can be expressed by Equation (1-10)

$$\dot{Q}_{\mu L}(s) = \rho_l \cdot h_{fg} \cdot \frac{\sum_{e=1}^{N_e(s)} V_{\mu L}(s;e)}{\sum_{e=1}^{N_e(s)} t_b(s;e)} \tag{1-10}$$

By replacing sums in Equation (1-10) with arithmetic means, one gets Equation (1-11)

$$\dot{Q}_{\mu L}(s) = \rho_l \cdot h_{fg} \cdot \frac{\langle V_{\mu L}(s;e)\rangle_e \cdot N_e(s)}{\langle t_b(s;e)\rangle_e \cdot N_e(s)} = \rho_l \cdot h_{fg} \cdot \frac{\langle V_{\mu L}(s;e)\rangle_e}{\langle t_b(s;e)\rangle_e} \tag{1-11}$$

where the operator $\langle\,\rangle_e$ represents averaging performed for all events of a particular nucleation site s. We can redefine parameters in Equation (1-11) as the average bubble departure frequency for site s ($\bar{f}(s)$, Equation (1-12)) and the average microlayer volume for site s ($\overline{V_{\mu L}(s)}$, Equation (1-13)).

$$\bar{f}(s) = \frac{N_e(s)}{t} = \frac{N_e(s)}{\sum_{e=1}^{N_e(s)} t_b(s;e)} = \frac{\cancel{N_e(s)}}{\langle t_b(s;e)\rangle_e \cdot \cancel{N_e(s)}} = \frac{1}{\langle t_b(s;e)\rangle_e} \tag{1-12}$$

$$\overline{V_{\mu L}}(s) = \langle V_{\mu L}(s;e)\rangle_e \tag{1-13}$$

The power attributed to microlayer evaporation on the entire boiling surface is given by Equation (1-14).

$$\dot{Q}_{\mu L}(s) = \rho_l \cdot h_{fg} \cdot \sum_{s=1}^{N_s} \bar{f}(s) \cdot \overline{V_{\mu L}}(s) = \rho_l \cdot h_{fg} \cdot N_s \cdot \langle \bar{f}(s) \cdot \overline{V_{\mu L}}(s)\rangle_s \tag{1-14}$$

Finally, the energy conserving form of the microlayer evaporation heat flux is given by Equation (1-15).

$$q''_{\mu L} = \rho_l \cdot h_{fg} \cdot N''_a \cdot \langle \bar{f}(s) \cdot \overline{V_{\mu L}}(s)\rangle_s \tag{1-15}$$

where N_a'' is the active nucleation site density. According to Equation (1-15) the evaporation heat flux is dependent on the number of active sites per unit area (N_a'') and the departure frequency times microlayer volume averaged over all sites. This average is implicitly connected to the active nucleation site density (see Equation (1-16))

$$\langle \bar{f}(s) \cdot \overline{V_{\mu L}(s)} \rangle_s = \frac{\sum_{s=1}^{N_s} \bar{f}(s) \cdot \overline{V_{\mu L}}(s)}{N_s} = \frac{\sum_{s=1}^{N_s} \bar{f}(s) \cdot \overline{V_{\mu L}}(s)}{N_a'' \cdot A} \tag{1-16}$$

The activity of a particular nucleation site is determined by its bubble departure frequency, $\bar{f}(s)$. It could be tempting to assume that sites with low activity (i.e. low departure frequency) can be ignored because such sites will produce very few bubbles and hence will have only a minor contribution to the microlayer volume flux (Equation (1-9)). They will also have an insignificant effect on the average given by Equation (1-16). However, if there are many more sites with low activity compared to sites with high activity, then such assumption will be invalid and sites with low activity can still contribute significantly to the amount of energy removed by boiling. In order to assess the importance of sites with low activity, it is important to know how the departure frequency $\bar{f}(s)$ is distributed among the nucleation sites. Such distributions are extremely difficult to measure because they require a large amount of high-resolution data to achieve convergence. Not only that the data itself needs to be of high fidelity, the sheer amount of bubbles that have to be analyzed requires automated post-processing to be used in data analysis. Because of these complications the true definition of active nucleation site density, a parameter so relevant to HFP modeling, remains unclear. What is needed to resolve this issue is the measurement of spectral nucleation site density. In other words, it is important to know how many active nucleation sites on the boiling surface have a particular bubble departure frequency. Only with such a knowledge we could ensure that the models for partitioned heat fluxes conserve energy. To the best of author's knowledge, experimental measurements of the spectral nucleation site density are not available in the literature. For high pressure boiling, even the average values of nucleation site density are very scarce. To the best of the author's knowledge, the only studies in which the average NSD was measured at pressures higher than 10 bar are the works of Treschev [37] and Sakashita [48], with the former being limited to highly subcooled flow boiling, while the latter concentrating on low heat fluxes in saturated pool boiling. Therefore, one of the main goals of this thesis is

> *to provide the measurements of spectral nucleation site density for high pressure conditions to guide further development of energy conserving HFP models.*

The results of this investigation are presented in Chapter 5.

1.3.5. Departure from nucleate boiling

The mechanism for DNB is one of the most challenging problems in boiling research. Countless models and correlations were introduced in the past trying to predict CHF and identify the DNB mechanism. A comprehensive review of such models and correlations is given in [50]. Generally, a trend can be observed where older models, such as the hydrodynamic instability model of Kutateladze-Zuber, attributed DNB to the global far-

filed behavior of liquid and vapor surrounding the boiling surface. In contrast, more recent models, such as those focused on dry spot formation, emphasize the importance of near-wall phenomena. Such trend is fostered by new experimental observations of the DNB phenomenon, with levels of resolutions much higher than it was possible in the past. Specifically, the works of Theofanous et al. [51], Kim et al. [52] and Richenderfer et al. [8] clearly show that DNB is associated with the formation of irreversible dry spot. A recent study by Zhang et al. [7] analyzed distributions of bubble footprints together with boiling parameters such as the nucleation site density, bubble departure frequency and growth time. They found that DNB is not only associated with the formation of irreversible dry spot, but also with the growth of a large connected bubble cluster. Further analysis of bubble footprint distribution revealed that at the point of DNB, the distribution of bubble footprints becomes scale-free. This observation suggests that bubble footprints of any size exist on the boiling surface and are all equally important in triggering the boiling crisis. Thus, describing the DNB phenomenon with a single length scale (e.g. Taylor instability wavelength in the model of Zuber) may be a drastic simiplification. The scale-free nature of the boiling crisis was also captured by Zhang et al. by performing a Monte Carlo simulation of the bubble interaction process using experimentally measured values of boiling parameters. The importance of boiling heat transfer prior to CHF and the interaction between bubbles was further corroborated by the study of Baglietto et al. [6], who created a fully mechanistic HFP model that not only matches experimentally measured boiling curves and partitioned heat fluxes, but also captures the CHF in a form of the degradation of heat flux due to the formation of dry areas and limited heat removal capabilities of evaporative and single-phase heat transfer mechanisms. In summary, the majority of recent DNB studies highlight the importance of understanding the behavior of bubble interactions both before and at the moment of the boiling crisis. Therefore,

> *a detailed visualization of bubble footprints at high pressure and up to CHF is one of the main goals of this thesis.*

The results of such visualization together with the quantitative analysis of bubble footprint size distributions are presented in Chapter 6.

1.4. EXPERIMENTAL CHALLENGES

Previous section described current understanding of boiling heat transfer, highlighted research gaps and outlined the main goals of the present research. These goals serve as design criterions for the development of experimental apparatus, methods and procedures. The main reason for the limited understanding of high pressure boiling of water is the difficulty in conducting experimental research at such conditions. The full pressure of pressurized water reactors (PWRs) is 155 bar, leading to the saturation temperature of 344.8 ^{o}C. Experiments operating at such conditions are expensive, difficult to design and built, and most importantly create serios hazards for laboratory personnel. Designs of such experiments are further complicated by the need to have optical access to the boiling surface in order to quantify the behavior of bubbles. In this section we discuss measurement requirements posed by the research goals of this thesis, complexities associated with high

pressures, and review available measurement techniques with the focus on the requirement for the advanced phase detection technique that was developed as a part of the current research.

1.4.1. What measurements are needed to answer scientific questions?

Three key measurements are needed in order to quantify boiling behavior: bubble size, wall temperature distribution and wall phase distribution. Bubble size provides the information about the bubble growth rate and departure process. Wall temperature is a key parameter allowing us to understand the heat transfer associated with different mechanisms. When measured with sufficiently high spatial and temporal resolution, temperature distributions at the boiling surface allow calculating the heat flux distributions as well quantifying the heat transfer enhancement made by each bubble and the partitioned heat fluxes. The detection of phase (liquid or vapor) that is in contact with the boiling surface allows at the very least to identify the points of bubble nucleation. If spatial and temporal resolution of a phase detection technique is high enough, then size and distribution of bubble footprints can be measured while also quantifying bubble footprint interaction. The time evolution of bubble footprints provides the information needed for the measurement of bubble departure frequency, wait and growth times. Some phase detection techniques also distinguish between areas contacted by the bulk liquid and areas occupied by microlayers, allowing not only to track the extent and evolution of the microlayer, and also its thickness. Figure 1-4 shows a schematic representation of the ideal dataset that could be collected using all three measurement types. Such dataset will have synchronized measurements of bubble diameter (a), temperature (b) and heat flux (c) distributions together with the distribution of phases (d) and microlayer thicknesses (e).

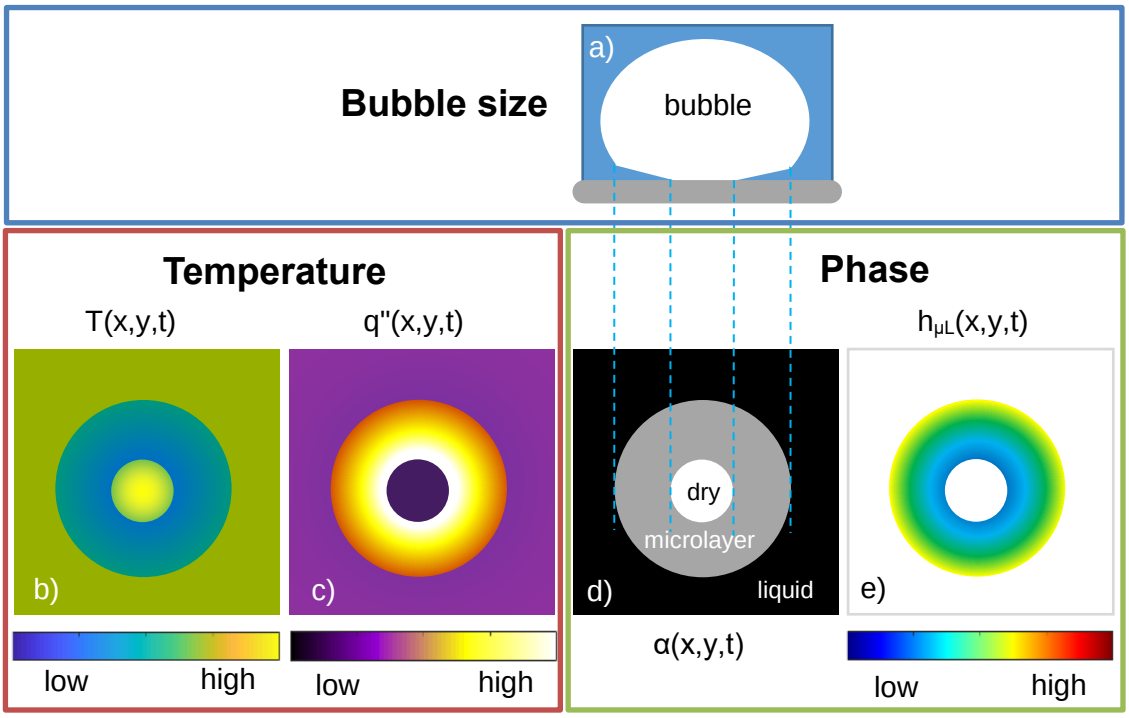

Figure 1-4. Schematic representation of the ideal dataset that can provide the majority of the information required to quantify boiling heat transfer

While experiments providing such detailed view of the boiling process are possible at low pressure, they are not easy to achieve in high pressure conditions due to the decrease in bubble size. Therefore, the majority of studies that were done in the past were limited to visualizing the overall behavior of bubbles at the boiling surface, which could only provide an idea of the bubble size and, in rare occasions, nucleation site density. Figure 1-5 through Figure 1-8 demonstrate the level of detail that previous studies were able to achieve by high-speed videography and simple photography. In the experiments of Semeria (Ref. [35] and Figure 1-5) high speed video recordings of bubbles in saturated pool boiling were taken, allowing for the measurements of bubble departure diameters at pressures up to 137 bar. Griffith et al. (Ref. [39] and Figure 1-6) captured short exposure photographs of the boiling surface in subcooled flow boiling conditions at pressures up to 103 bar. The pictures captured by Griffith et al. represent snapshots of void distribution at the boiling surface. In contrast to Griffith et al., Treschev captured long exposure photographs, which highlighted areas of extensive bubble nucleation, hence allowing for the identification of nucleation sites positions (Ref. [37] and Figure 1-7). In a more recent study, Sakashita captured high-speed videos of saturated pool boiling on a vertical surface, making measurements of the bubble size, growth rate, and nucleation site density at low heat fluxes. Note that the data shown in Figure 1-5 through Figure 1-8 were captured under the conditions of either low heat flux or high subcooling mainly to limit bubble interaction, allowing for the identification of the bubble size and position. Therefore, experiments that are focused on identifying the size of a bubble, while ignoring phase and temperature distributions on the boiling surface can only provide a very limited characterization of the boiling process. Therefore, it is crucially important to supplement measurements of the bubble size with as many distributions shown in Figure 1-4 as possible. To the best of the author's knowledge,

the present study is the first which successfully acquired phase detection measurements in high pressure flow boiling of water. The major challenge in making phase detection measurements possible is connected to the reduction in bubble size at high pressure and will be discussed further in the next Sub-Section.

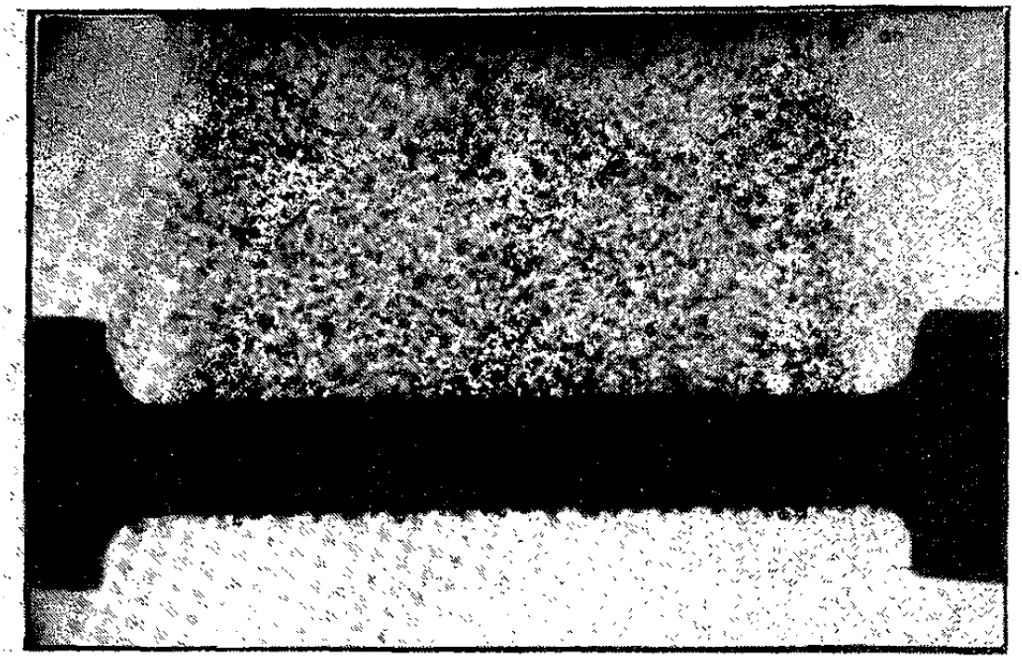

Figure 1-5. Saturated pool boiling of water at the pressure of 137 bar and the heat flux of 0.085 MW/m^2. Adapted from [35]

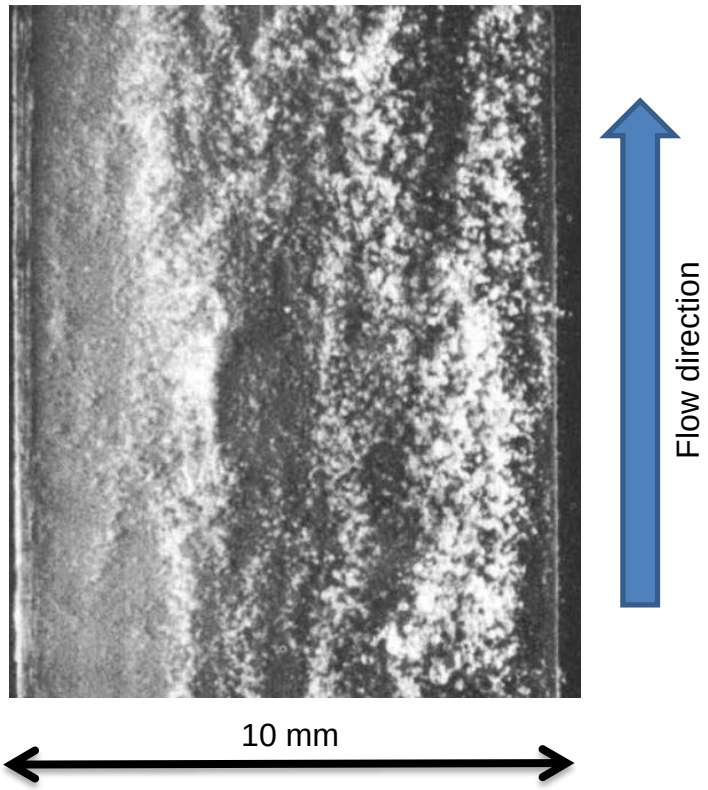

Figure 1-6. Subcooled flow boiling of water at the pressure of 69 bar and the subcooling of 25 ºC. Adapted from [39]

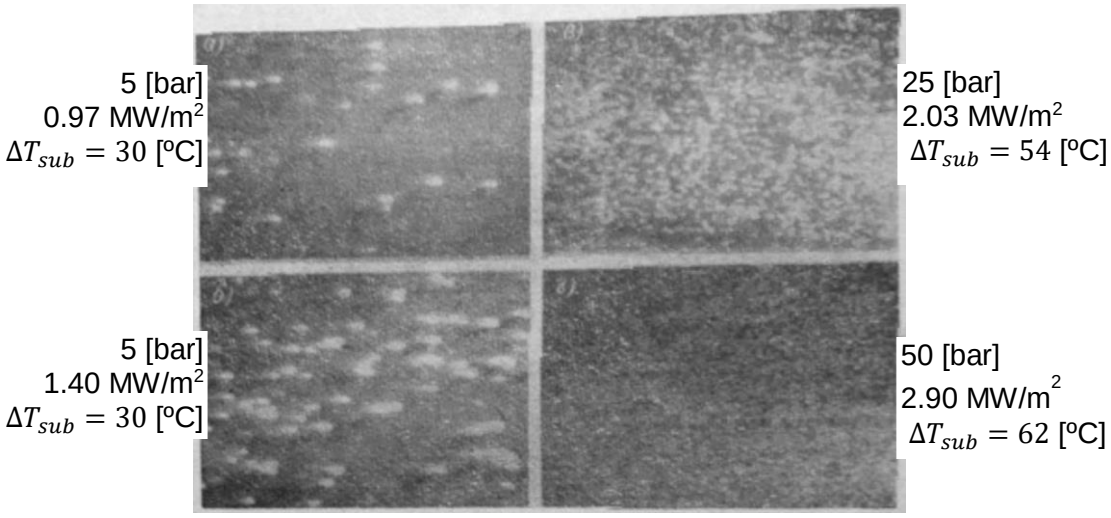

Figure 1-7. Long exposure photographs of the subcooled flow boiling adapted from [37]

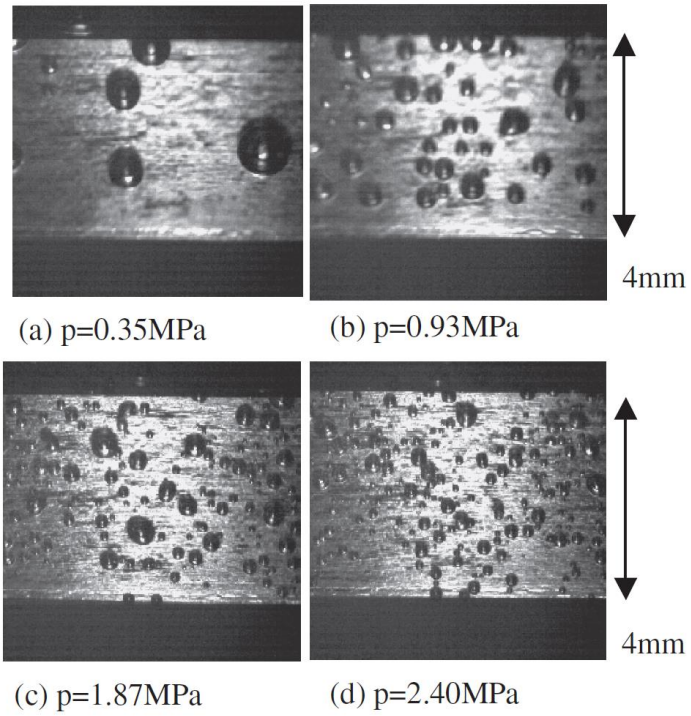

Figure 1-8. Saturated pool boiling of water at different pressures and the heat flux of 0.05 MW/m^2. Adapted from [48]

1.4.2. Requirement for high-resolution phase detection technique

One of the major advancements in experimental boiling research in the last 20 years was the application of high-speed and high-resolution infrared thermometry to the measurement of boiling wall temperature. This technique is often combined with specially designed boiling surfaces consisting of IR-transparent substrates covered by a very thin IR-opaque film. Most of the time a thin IR-opaque film also serves as a joule heater. The unique feature of such setup is in allowing IR thermometry to measure temperature and heat flux exactly at the boundary between the substrate and fluid. Since each phase has a different effect on the temperature and the heat flux, it is possible to determine which phase is in contact with boiling surface based on IR camera recording alone. A clear distinction can be made between dry areas that exhibit almost zero heat flux and microlayers that exhibit extremely high heat flux due to the rapid evaporation of the microlayer film. A demonstration of such capabilities can be found in the work of Richenderfer et al. [8].

However, extending an IR-based technique to high pressure conditions is challenging. The main difficulty in making high resolution measurements at high pressure stems from the relationship between pressure and the bubble size (see Figure 1-3). At PWR operating pressure (155 bar) the diameter of a bubble could be as small as 10 microns according to Figure 1-3, while the footprint left by such a bubble could be even smaller. Any measurement technique that relies on photons will have an absolute theoretical limit to its spatial resolution, called the diffraction limit. While measurement techniques capable of

sub-diffraction limit resolution had been proposed, they typically result in a significant increase in complexity of the measurement system [53]. For a more standard optical setup, the absolute theoretical diffraction limit can be roughly approximated as half of the wavelength of light that is being used for the measurement [53]. However, no real optical system could achieve such limit because it will either require for an object to be incredibly close to the lens, or for the lens to have infinitely large effective aperture (i.e. infinitely large lens diameter). Since the diameter of bubbles approaches the wavelength of infrared light, it is difficult to imagine an infrared-based technique that will be able to resolve individual bubbles at high pressure conditions. Therefore, in order to uncover the details of high pressure boiling, a phase detection technique that utilizes light in the visible, ultraviolet or x-ray range is needed. In the present work, we focused on the visible light. In the next subsection we explore available phase detection techniques while also discussing their limitations and advantages.

1.4.3. Review of available phase detection techniques

Several techniques allow detecting the phase in contact with the boiling surface. A summary is given in Table 1-4. While approaches like MEMS micro-thermometers [54]–[56], laser extinction [57], time-domain thermo-reflectance (TDTR) [58], and chromatic confocal sensors [24] have provided valuable information about the microlayer thickness and the heat transfer rate under the bubble, they have significant limitations. These methods can have a very high temporal resolution. However, they enable point-wise measurements only. Thus, they cannot be used to capture the dynamics of the dry spots formation and interaction over a large boiling surface. Infrared radiation has also been used to detect microlayers and dry areas using a technique called DEPIcT [59]. DEPIcT utilizes IR radiation emitted by water and transmitted through the heated IR-transparent substrate. Where the substrate is wet, the IR camera measures the radiation from the high temperature water that is in contact with the heated wall. In contrast, in dry areas the IR camera measures radiation from the cooler temperature water beyond the vapor (e.g., at the bubble apex). The contrast between these radiation signals reveals the distribution of phases. DEPIcT was also successful at visualizing interference fringes created by microlayers, hence allowing the measurement of microlayer thickness. Nevertheless, DEPIcT relies on IR radiation, which is not applicable to high pressure measurements (see previous sub-section for detailed discussion). Additionally, DEPIcT requires IR transparent boiling surfaces and, while attempts have been made [60], there is no simple way to combine it with infrared thermometry measurements. Schlieren flow visualization was successfully used to detect liquid films and droplets on the channel wall in adiabatic two-component flows inside a microchannel [61], [62]. Still, the application of this technique to boiling has not been demonstrated yet.

Techniques that utilize visible light rely on the difference in refractive index between liquid and vapor to detect dry areas, as well as on the phenomenon of thin-film interference to detect microlayers. Practically, the microlayer area coincides with the region covered by an interference pattern, e.g., light fringes. Such fringes can only be observed with coherent light sources. Therefore, lasers have been used extensively for this purpose [21], [28], [63]–[70]. However, while the large coherence length of the laser light makes microlayer fringes

visible, it also degrades the image due to the creation of undesirable, parasite interference patterns. As discussed by Koffman and Plesset [64], the interference pattern observed with laser lights comes not only from the microlayer, but also from the interface between the vapor and the bulk liquid, and the slightest variation in the parallelism of the substrate. In addition to that, reflected laser light typically creates a grainy image due to the occurrence of the laser speckle pattern [71]. All these effects prevent laser-based techniques from resolving small features prevalent in high pressure boiling, while also making it challenging to apply automated post-processing algorithms to the acquired images. Finally, lasers are very expensive, and their use creates a safety hazard in the lab.

Table 1-4. Summary of phase-detection techniques

Technique	References	Advantages	Limitations
MEMS temperature sensors	[54]–[56]	• High temporal resolution	• Point-wise measurement • Indirect measurement (requires assumptions about the heat transfer)
Time-domain Thermo-Reflectance (TDTR)	[58]	• High temporal resolution	• Point-wise measurement • Indirect measurement (requires assumptions about the heat transfer)
Chromatic confocal sensor	[24]	• High temporal resolution • Measurement of the absolute microlayer thickness	• Point-wise measurement • It cannot measure thicknesses smaller than a few microns.
DEPIcT	[59]	• Microlayer fringes are resolved • Simple optical setup	• Requires IR opaque liquid and IR transparent boiling surface • Contrast depends on the temperature distribution within the liquid • Difficult to combine with IR thermometry
Laser extinction	[57]	• Measurement of the absolute microlayer thickness • High temporal resolution	• Point-wise measurement
Schlieren in a microchannel	[61], [62]	• Can detect both bulk and near wall phases • Avoids problems with laser speckle • Avoids parasite interference patterns • Good signal-to-noise ratio	• Complicated optical setup • Unable to resolve microlayer fringes • Temperature non-uniformity within the fluid can affect results (i.e. applicability to diabatic flows is not yet investigated)
Optical laser transmission	[63], [64]	• Microlayer fringes are resolved • Simple optical setup	• Limited applicability to high heat flux measurement due to the light scattering by bubble interface • Problems with parasite interference patterns

Broadband light transmission	[16], [72], [73]	• Avoids problems with laser speckle • Avoids parasite interference patterns • Good signal-to-noise ratio • Simple optical setup	• Limited applicability to high heat flux measurement due to the light scattering by bubble interface • Unable to resolve microlayer fringes
Optical laser reflection (small angles)	[28], [65]–[67]	• Microlayer fringes are resolved • Simple optical setup	• Creates parasite interference patterns • Laser speckle
Optical laser reflection (TIR angle)	[21], [68]–[70]	• Microlayer fringes are resolved • Good signal-to-noise ratio	• Creates parasite interference patterns • Laser speckle • Complicated optical setup (prism)
Broadband light reflection (small angles)	[74], [75]	• Simple optical setup • Avoids parasite interference patterns • Good signal-to-noise ratio	• Unable to resolve microlayer fringes
Broadband light reflection (TIR angle)	[76]–[78]	• Avoids parasite interference patterns • Good signal-to-noise ratio	• Unable to resolve microlayer fringes • Complicated optical setup (prism)

The mitigation of these problems was partially achieved by studies that either used an incoherent broadband light with a small coherence length [16], [72], [73], [76]–[78] or operated at the angle of total internal reflection (TIR) to improve the signal to noise ratio [21], [68]–[70], [76]–[78]. Interference patterns were also removed using a system of polarizers [70]. However, the use of incoherent broadband light makes it impossible to measure the thickness of the microlayer, and the operation at the TIR angle requires the addition of a prism attached to the substrate. The latter may complicate the design of the experimental apparatus significantly and is particularly limiting in applications that require high spatial resolution because it increases the distance between the boiling surface and the lens of the camera. As such, it may lower the maximum spatial resolution that can be achieved with an optical setup. Additionally, a typical way to attach a prism to the substrate is with the help of oil that matches the refractive index of the substrate and the prism. The use of oil removes additional reflections at the air gap between the substrate and the prism. This approach is not applicable to high temperature cases, since most oils will not be stable at such extreme conditions. Furthermore, the operation at the TIR angle does not entirely remove parasitic interference patterns.

The discussion presented in this subsection highlights the need for the new phase detection technique, one that will be directly applicable to high pressure and temperature conditions, while also providing extremely high spatial resolution. Additionally, the new technique would need to resolve the structure of the microlayer, since its effect on high pressure boiling is one of the main questions studied in this thesis. The details of the new phase detection technique are presented in Chapter 2.

1.5. SCIENTIFIC QUESTIONS

This section concludes Chapter 1 with a summary of scientific questions, methods that will be used to answer them, and the major findings. The questions are divided into two categories based on the amount of attention that each question will receive over the course of the thesis. Primary focus questions are explored in greater details, resulting in valuable conclusions about the physics of high pressure boiling. Secondary focus questions provide a glimpse into certain aspects of boiling and serve more as the basis for future research. The questions are summarized hereafter.

1.5.1. Primary focus

- **Microlayer disappearance at high pressures – is it governed by evaporation or wettability?** We will explore several pressures and flow rates to quantify the conditions at which the microlayer disappears. We will show that the disappearance of the microlayer can be tied to the critical velocity of the triple contact line, below which the microlayer does not form. Furthermore, we will demonstrate that the specific value of the critical contact line velocity is governed by the combination of thermal and hydrodynamic dewetting.
- **Which forces and phenomena govern bubble departure at high pressure?** We will track multiple bubbles and record their growth histories and pathlines for different pressures and mass fluxes. We will demonstrate that sliding is the main departure mechanism in high pressure flow boiling on a vertical boiling surface. We will also identify forces that dominate bubble departure process at high pressure and create a simplified force balance model to predict experimentally measured bubble pathlines. We will demonstrate that in high pressure flow boiling bubbles begin to depart immediately after nucleation. Based on this fact, we will proposed a criterion for the bubble departure and combine it with the simplified force balance approach to create a bubble departure model for high pressure flow boiling.
- **Could spectral nucleation site density redefine active nucleation site density?** We will create a special algorithm allowing us to track dry areas for virtually all nucleation events on the boiling surface. By applying this algorithm to high resolution phase detection data, we will measure statistical distributions of several boiling parameters. Such distributions quantify the variation in boiling parameters between nucleation sites and individual nucleation events. We will demonstrate that most of the boiling parameters vary by several orders of magnitude, while also being distributed in a complex way, with the distributions of some parameters exhibiting a power-law. The implications of boiling parameter distributions for HFP modeling is also explored.

1.5.2. Secondary focus

- **How good are current HFP models in quantifying boiling heat flux at high pressure conditions?** We will utilize statistical distributions of the boiling parameters to quantify forced convection and transient conduction heat transfer modes for several mass fluxes and the pressure of 10.5 bar. We will demonstrate

that given the standard formulations of these two partitioning components, we can only account for 40% of the applied heat flux at the boiling surface. We will also demonstrate that microlayer evaporation is absent in high pressure boiling and triple contact line evaporation cannot account for more than 20% of the applied heat flux. Therefore, as much as 40% of the heat flux at the boiling surface is removed by yet unknown mechanism, which is likely to enhance either the forced convection or transient conduction heat transfer modes.

- **What is the diameter of a bubble at the end of the inertia-controlled phase?** We will analyze multiple bubble growth histories captured at different pressures and mass fluxes to demonstrate that the growth of bubbles in high pressure conditions is dominated by the thermally controlled phase.
- **What makes the microlayer to deform in flow boiling conditions compared to pool boiling?** We will measure the velocities of the contact lines for upstream and downstream portions of the microlayer, demonstrating that the flow-induced movement of a bubble results in a slower upstream and faster downstream contact line velocity, leading to non-uniform growth of the microlayer.
- **Will vapor clotting be present in high pressure flow boiling?** We will analyze images captured by phase detection and shadowgraphy to confirm the formation of vapor clots in high pressure flow boiling.
- **How does dry area size distribution evolves in high pressure DNB conditions?** We will analyze the distributions of dry area sizes, identifying its evolution as the boiling surface approaches DNB condition. In all cases a power-law shape emerges when the heat flux is brought close to CHF. In the majority of cases the distribution retains an exponentially damped portion for the low dry area sizes. We will speculate that this effect is caused by limited dry spot interaction at small dry spot sizes.

2. EXPERIMENTAL SETUP AND METHODS

In this chapter the details of the experimental apparatus, measurement techniques and post-processing algorithms are presented. First, we present the design of the test section – the key component of the experiment where all important measurements are performed. The design of the high-pressure flow loop necessary to achieve relevant operating conditions is presented next. Later, a brief description of the low-pressure flow boiling setup is presented. The low-pressure setup was used for experiments at pressures lower than 10 bar. A detailed description of the low pressure flow boiling setup is found in [8]. Next, a design of the compact pool boiling setup is presented. This setup was built specifically to have a high-resolution baseline measurement of microlayer formation under saturated pool boiling conditions. In the following section, a description of LED-based phase detection technique is given. This technique was developed specifically to address the need for high spatial resolution at high pressures. Later, details of different infrared camera calibration techniques are presented. The final section provides details of all post-processing algorithms as well as the uncertainties associated with each measured quantity.

2.1. HIGH PRESSURE TEST SECTION

The design goals for the test section were as follows:

- Working fluid – deionized water
- Maximum operating pressure – 155 bar
- Maximum operating temperature – 340 ºC
- Maximum operating mass flux – 3600 kg/(m^2-s)
- Channel hydraulic diameter – 11.78 mm (matching the hydraulic diameter of an inner subchannel of AP1000 [79])
- Fully-developed momentum boundary layer needs to be established at the point where water enters the active area of the test section.
- Optical access from all 4 sides of the channel.
- The window looking at the back side of the heater must allow infrared thermometry measurements of the heater temperature.
- The distance between the window looking at the back side of the heater and the active area of the heater must be as short as reasonably achievable in order to maximize the spatial resolution of phase detection technique.

In this section, we will first give details of each component that constitutes the test section, following by the results of stress analysis and finishing with a description of measurement techniques and instrumentation used in each experiment.

2.1.1. Components and their functions

A Specially designed infrared heater was used for bubble generation. The design of the infrared heater is shown in Figure 2-1. The body of the heater consists of a 20×20×1 mm^3 slab of sapphire. Sapphire serves as a substrate for the deposition of a 0.7 μm thick film of indium tin oxide (ITO). ITO is electrically conductive and therefore serves as a joule heater. While sapphire is mostly transparent to the IR radiation, ITO is perfectly opaque, allowing

the measurement of the ITO temperature with IR camera. Due to the negligible thermal resistance of the ITO film, temperature measurements performed by the IR camera correspond to the exact temperature of the boiling surface. Chromium pads are deposited on top of ITO. They provide an electrical connection and limit the active area of the heater to 10×10 mm^2. The thickness of chromium pads was sufficiently large to have negligible voltage drop through the pads, allowing all of the electrical power to be deposited in the active area of the ITO film. The boiling surface is nano-smooth except small imperfections caused by the machining and polishing of the sapphire substrate and possibly by the process of film deposition. These imperfections have diameters from under a micron to several microns and serve as sites for bubbles nucleation. These imperfections are visualized in Figure 2-1 with the use of dark field microscope, which makes them appear as bright dots on the image.

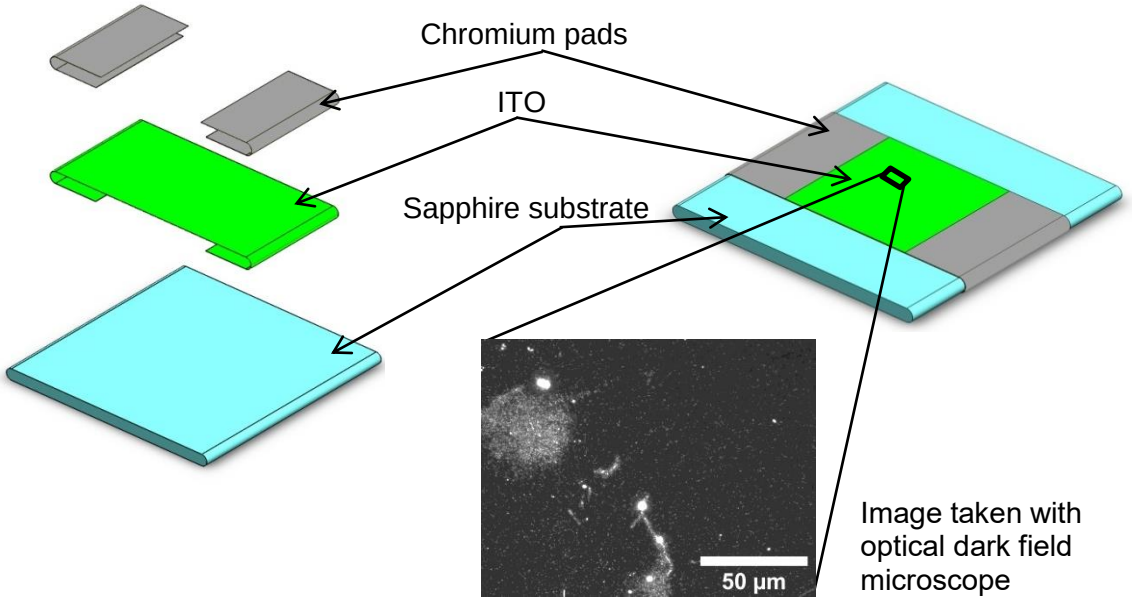

Figure 2-1. Design of the infrared heater. The surface of the heater is nanosmooth, with the exception of micron and sub-micron scale imperfections

In order to provide mechanical support and means of electrical connection, the heater is installed inside a specially designed boiling cartridge. Two distinct cartridge designs were successfully used throughout the experimental campaign. The cartridge of an earlier design was made of a ceramic material called Shapal (see Figure 2-2). Shapal is less brittle than other ceramics and electrically non-conductive. An IR heater was clamped at the front side of the cartridge, while the electrical power was supplied from the back by using a conductive copper tape. The later design was made of 316 stainless steel (see Figure 2-3). Functionally it had the same features with the exception of an added taper to the back side of cartridge. Such taper enhances signal-to-noise ratio of the phase detection technique by allowing the images of the boiling surface to be taken at a larger angle of incidence. More details about the phase detection technique are given in the later sections. While Shapal cartridge makes electrical connection straightforward due to its insulating property, it showed significant degradation over repeated tests, resulting in cracks appearing

throughout the body of the cartridge. In contrast, metallic cartridge is more robust. However, the copper tape cannot be applied directly to the metallic cartridge because it would create a short circuit. In order to avoid this issue, a layer of insulating gasket was positioned in between of the copper tape and the cartridge body.

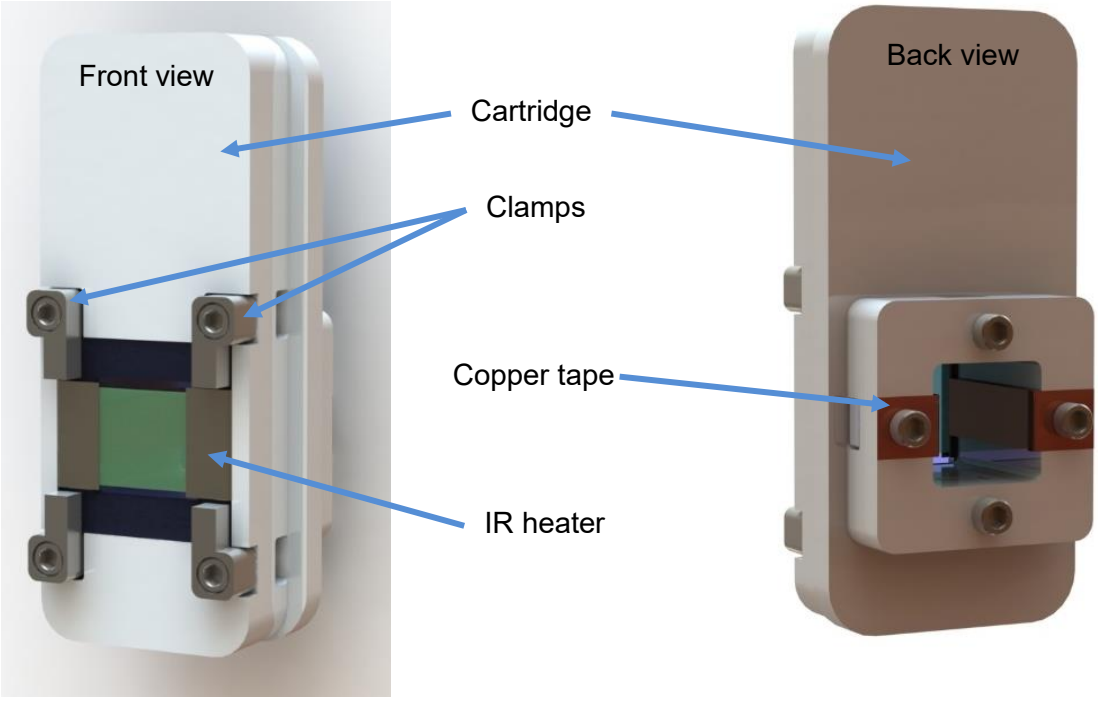

Figure 2-2. Diagram of the Shapal boiling cartridge

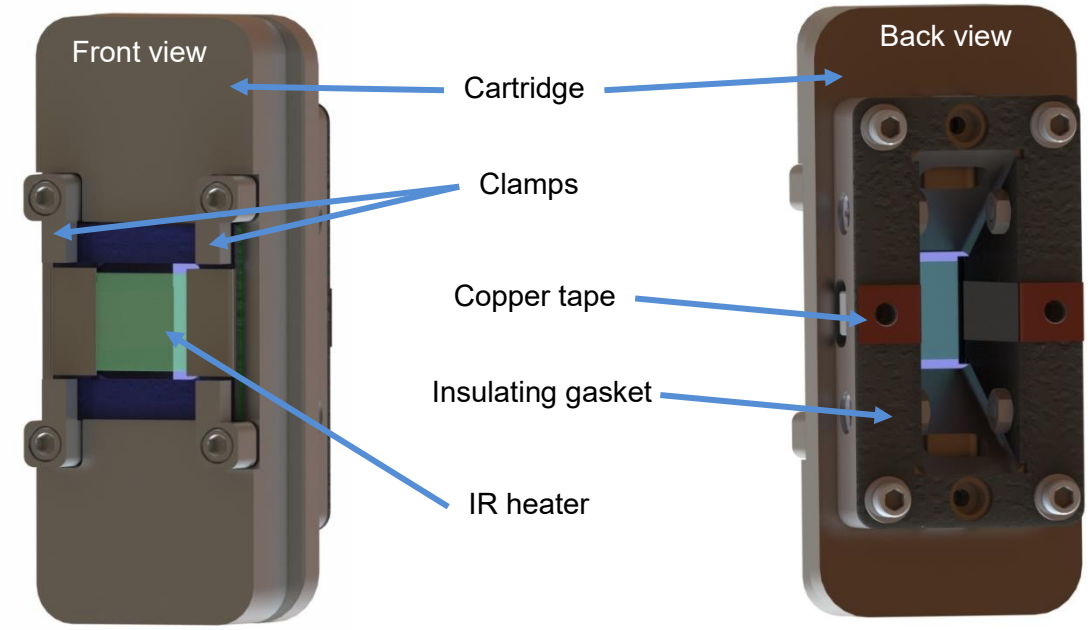

Figure 2-3. Diagram of the metallic boiling cartridge

The complete design of the test section is shown in Figure 2-4. Pressurized water is flowing through a square channel with a hydraulic diameter of 11.78 mm. The same channel dimensions are maintained throughout the entrance region. The total length of the entrance region is larger than 65 hydraulic diameters which ensures a fully-developed momentum boundary layer at the measurement area of the test section. The measurement area itself is equipped with 4 thick sapphire windows, two of which can be seen on a closed-up view in Figure 2-4. These windows serve as pressure boundaries and allow non-intrusive visualization measurement techniques to be applied to the experiment. Internally, the measurement area consists of two compartments. On one side, a water compartment is filled with stagnant water and is connected to the main flow channel, i.e., it is at the same pressure as the flow channel. On the other side, a gas compartment is filled with nitrogen gas, whose pressure is controlled to match the flow channel pressure. The boiling cartridge that contains the infrared heater serves as the physical boundary between the water and gas compartments. A special insert made of sapphire and stainless steel is used to preserve the same cross-section geometry throughout the length of the channel. The large flange at the front of the test section is used to install the insert and the cartridge before each experiment. Having such installation process allows for the area of the gas compartment pressure boundary (i.e. sapphire window) to be much smaller. This in turn shortens the distance between the surface of the heater and the back side of the test section, allowing the visualization from the back side to be made at very high spatial resolution.

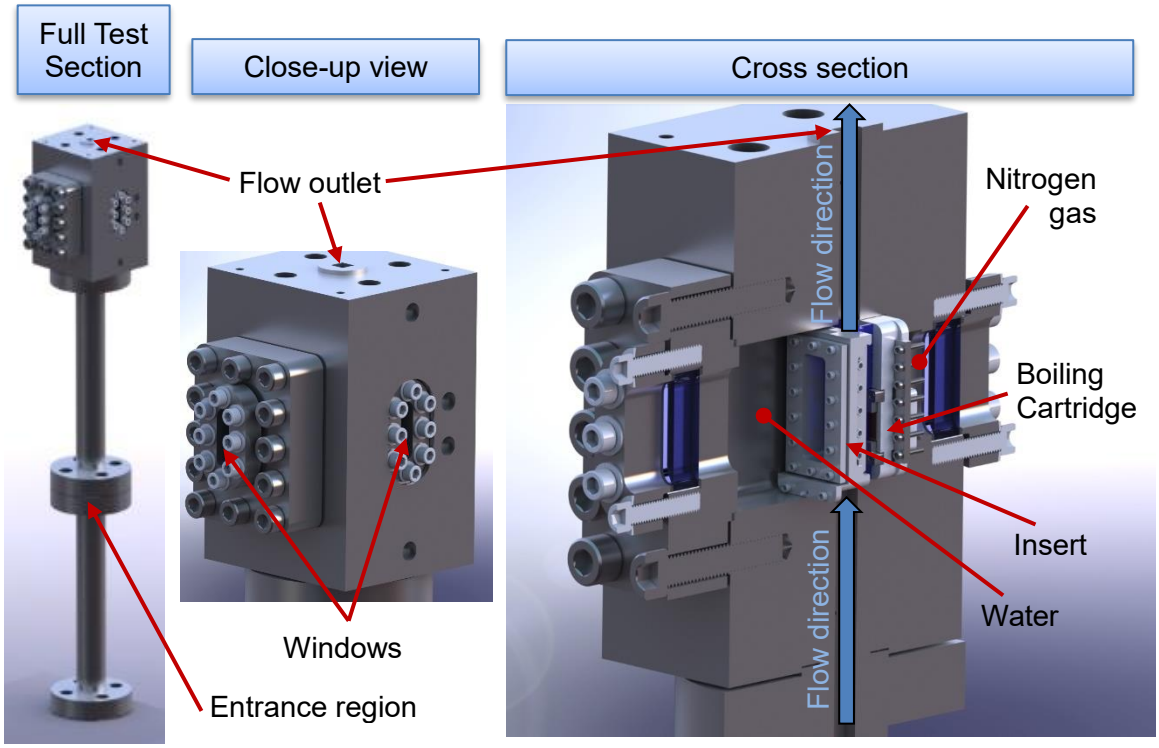

Figure 2-4. Diagram of the test section

2.1.2. Mechanical design

The analysis of stresses in each component of the test section was performed in order to ensure safe operation. For metallic components the guidelines for the allowable stresses at the maximum operating temperature (340 ºC) were taken from the ASME Boiler and Pressure Vessel Code Section II [80]. For sapphire, the peak stress was kept below 1/3 of its tensile strength. The number of bolts was selected such that the stresses from pressure on each bolt constitute approximately half of the allowable stress level. This approach allows for an additional margin required to accommodate the clamping force that is added to the force from the pressure. The entire analysis is presented in more details below.

Designation names for each test section component area shown in Figure 2-5. Finite element analysis (FEA) was performed for each component. The peak stress given by the FEA was then identified, and the component's size was changed until the peak stress was below the allowable stress value for each material. Details of FEA analysis are presented in Appendix A. A summary of resulting stresses is given in Table 2-1. Note that the flow loop to which the test section is attached has several pressure relief valves (PRVs) installed. It is important to ensure that the components of the test section are rated for the maximum pressure possible in the system, i.e. the highest PRV relief pressure. Properties of inconel and stainless steel were taken from material certificates provided by the supplier. Properties of sapphire were taken from the website of sapphire manufacturer.

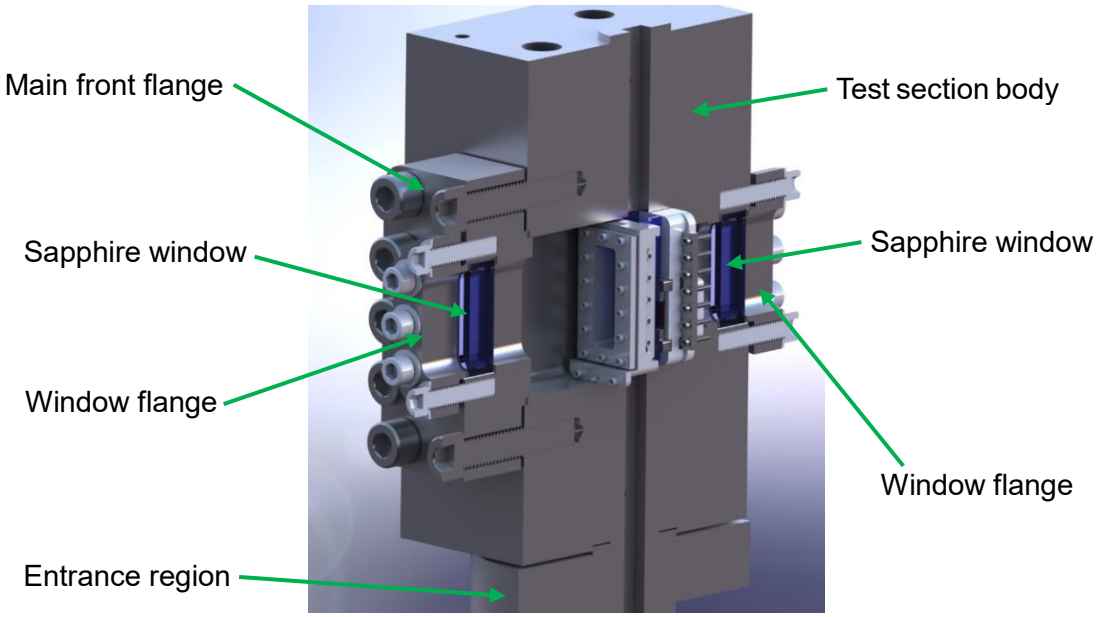

Figure 2-5. Designation names for each test section component

Table 2-1. Summary of the stress analysis

Component	Yield strength @ room temperature MPa	UTS @ room temperature MPa (psi)	Allowable stress, MPa (psi)	Maximum stress at normal operating conditions (2248 psi)	Maximum stress at the PRV setpoint of the pressurizing	Maximum stress at the PRV setpoint of the whole

	(psi)			MPa (psi)	pump (2473 psi) MPa (psi)	system (2600 psi) MPa (psi)
Sapphire window	250 (36,259) [81]	250 (36,259) [81]	N/A	72.2 (10,470)	79.4 (11,520)	83.5 (12,110)
Test section body	269.9 (39,140)	654.9 (94,990)	160.6 (23,300) [80]	124.2 (18,020)	136.6 (19,810)	143.6 (20,830)
Main front flange	269.9 (39,140)	654.9 (94,990)	160.6 (23,300) [80]	57.9 (8,397)	63.7 (9,238)	67.0 (9,717)
Sapphire flange	269.9 (39,140)	654.9 (94,990)	160.6 (23,300) [80]	78.9 (11,440)	86.7 (12,580)	91.2 (13,230)
Upper entrance region	253.7 (36,800)	572.3 (83,000)	94.4 (13,700) [80]	31.5 (4,576)	34.7 (5,029)	36.4 (5,287)
Lower entrance region	253.7 (36,800)	572.3 (83,000)	94.4 (13,700) [80]	29.6 (4,297)	32.6 (4,727)	34.3 (4,970)

The required number of bolts for each flange was calculated based on the force exerted on the bolt by the flange as a result of internal pressure of the system. The calculations are shown in Table 2-2. In case of the entrance region, the number of bolts and their sizes were selected based on the 2500 class ANSI flange [82] specification. All bolts are made of 316 Stainless Steel.

Table 2-2. Calculation of the required size and number of bolts

Flange	Main front flange	Window flange
Pressure, psi	2248	2248
Flange area, in^2	4.78	1.14
Force, Lbf	10736	2568
thread	1/2-13	5/16-18
Minor diameter of the thread, in	0.404	0.243
Minor area of the bolt, in^2 [83]	0.1283	0.0464
Max. Allowable stress, psi	13700	13700
Max. Allowable Force per bolt, Lbf	1757	636
Minimum number of bolt	6.11	4.04
Actual number of bolt used	12	8
Actual stress on each bolt, psi	6,973	6,918

2.1.3. Instrumentation and measurement techniques

Optical arrangement and instrumentation are shown in Figure 2-6. Two cameras were used for boiling visualization. High speed video (HSV) camera was positioned behind the heater. Two LED lights were used for two different measurements. An LED light that was located at the front of the test section had its light beam passing through the heater and directed into the camera. When bubbles are formed on the surface, they block a portion of the light, creating dark shadows in the image. This technique is called visible light shadowgraphy and it was used to measure sizes and velocities of individual bubbles. Another LED light is positioned at the back of the test section. Its light beam is reflected at an angle of approximately 20 degrees from the ITO layer. The reflected beam is then directed to the high speed video camera. This arrangement of the light allows for the detection of phase at the boiling surface. More details about the phase detection technique are given in the following chapters. Phantom v2512 was used for all recordings with RESOLV4K long working distance microscope lens from Navitar. The spatial resolution (i.e. the pixel size) in all high pressure experiments was between 5 and 6 microns per pixel. Temporal resolution was between 15,000 and 30,000 frames per second (fps).

IR camera is also positioned behind the heater, but at a 90 degree angle with respect to the HSV camera. The IR radiation from the heater is redirected with the use of IR/VIS beam splitter. Such beam splitter reflects all of the IR radiation, while passing the visible light through. Telops M3k high speed infrared camera was used for all recordings with 100 mm lens from Janos. Since bubble size at high pressure is extremely small, it is impossible to resolve individual bubble footprints with the IR camera. Therefore, a coarse spatial resolution of 115 microns per pixel was used for IR recordings. The temporal resolution was between 500 and 3000 frames per second. IR camera allows the measurement of wall temperature during the steady-state boiling phase. It also provides visualization and temperature measurement of the dry spot during the boiling crisis.

Inlet and outlet temperatures were measured with two K-type thermocouples. Their positions are shown as “TCin” and “TCout” in Figure 2-6. The pressure was measured at the outlet (“Pout” in Figure 2-6). For the current investigation one pressure measurement at the test section was sufficient to provide required information about the system pressure. However, the test section is equipped with an additional pressure tap at the inlet which, in the future, can be used both to measure the inlet pressure and the pressure drop over the measurement area of the test section.

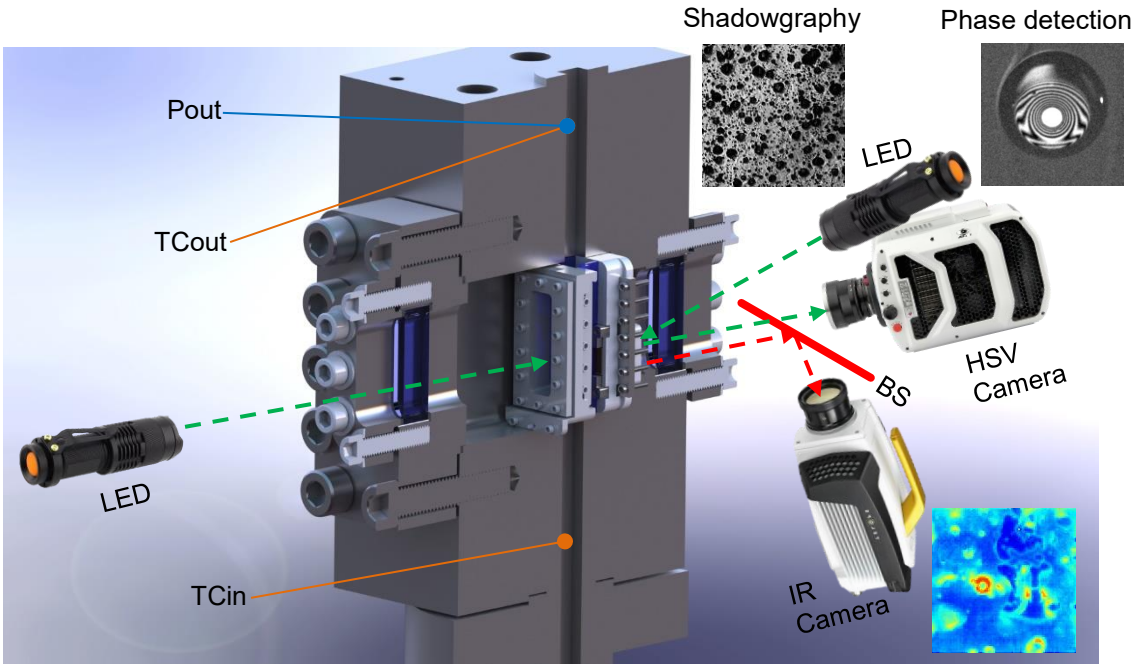

Figure 2-6. Optical arrangement and instrumentation diagram

2.1.4. Sealing solutions

All seals of the test section were made with the use of different gasket materials. Where possible, the sealing faces were designed in a way that fully constrains the gasket, preventing it from being squeezed out by either the tightening process or the internal pressure. Most seals used flexible graphite (also known as grafoil) either plain or stainless steel reinforced. Stainless steel reinforced version was used for seals in which the gasket is not well constrained. For sapphire windows and the heater, Carbon/Buna-N gasket was used. Note that flexible graphite is much softer than any other gaskets rated for high temperature and therefore could be a better option for the seal between the IR heater and the boiling cartridge. However, flexible graphite is electrically conductive, preventing its use with electrically powered components.

2.2. HIGH PRESSURE FLOW LOOP

The design goals for the flow loop were as follows:

- Working fluid – deionized water
- Maximum operating pressure – 155 bar
- Maximum operating temperature – 340 ºC
- Maximum operating mass fluxes – 3600 kg/(m^2-s)

These design parameters dictated the selection of the components. In order to ensure that a sufficient flow rate and temperature can be reached, both the hydraulic and thermal design was performed. While selection of the components, hydraulic and thermals analyses were done iteratively, for the clarity of the presentation the arrangements and a list of all components in the final version of the loop are given first, followed by the results of hydraulic and thermal design

The schematic of the flow loop is shown in Figure 2-7. A circulation pump (1) is used to establish the required flow rate through the test section, which is measured by a venturi-type flow meter (2). The temperature of the flow loop is raised by means of a series of tape heaters that are wrapped around the primary piping. A pressurizing pump (8) takes water from the tank (7) and injects it into the system. At the same time, a controlled leak is established by a backpressure regulator (5). These two mechanisms create a feed-and-bleed dynamics, which is used to maintain the required pressure in the flow loop. Additionally, feed and bleed streams pass through the regenerative heat exchanger (4), which is used to cool the bleed stream and preheat the feed stream. An accumulator (3) is used to equilibrate pressures between water and gas compartments of the test section. Deionized (DI) water was used in all experiments. Before each test, argon gas was sparged through the tank (7) in order to remove oxygen from the water. A vacuum pump (6) was used to remove any additional air present in the flow loop before filling the loop with water.

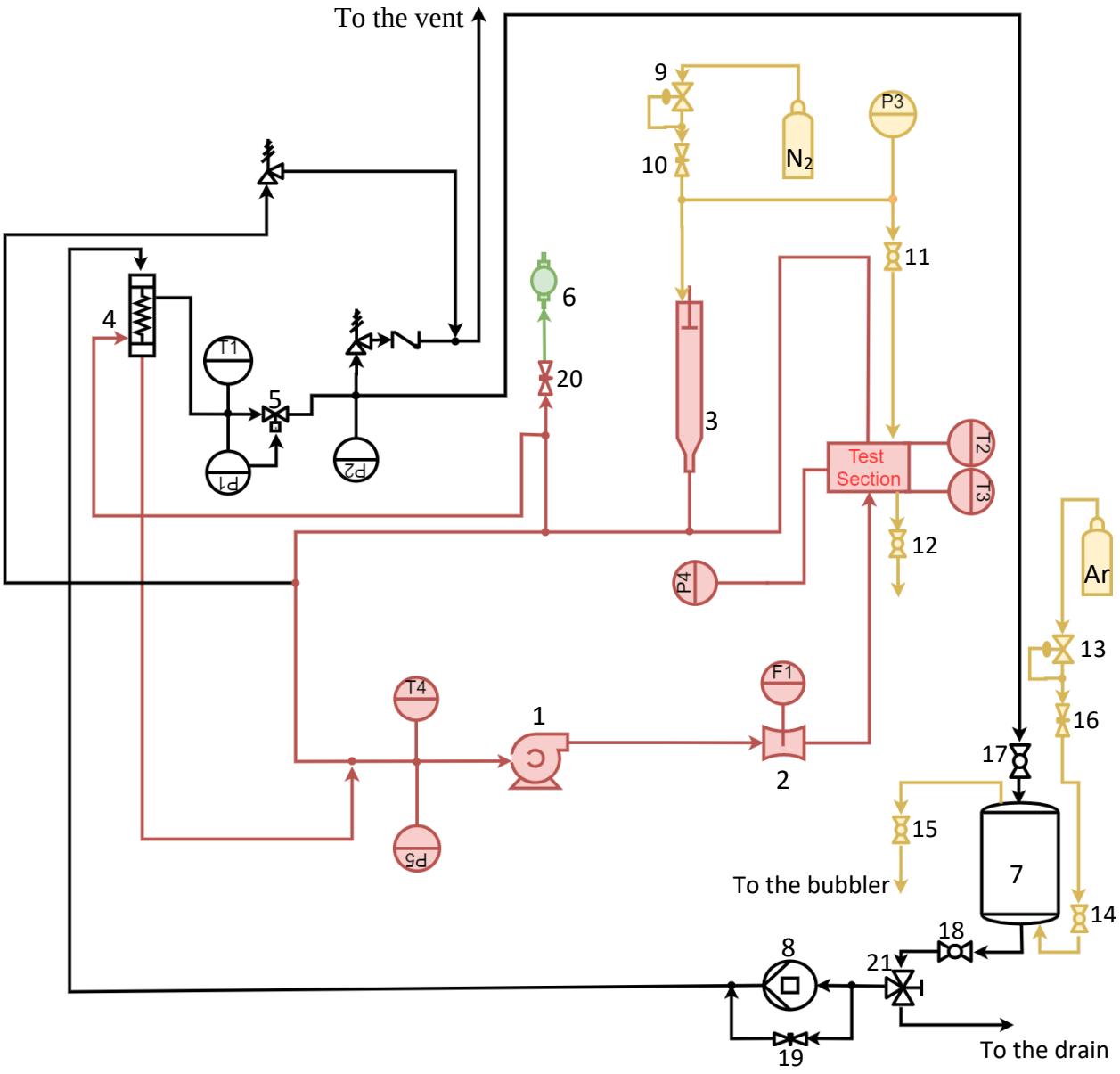

Figure 2-7. Process and instrumentation diagram. 1 – circulation pump; 2 – flow meter; 3 – piston accumulator; 4 – heat exchanger; 5 – pressure reducing valve; 6 – vacuum pump; 7 – water tank; 8 – pressurizing pump; 9 – N2 bottle pressure regulator; 10 – N2 supply isolation valve; 11 – Test section gas chamber isolation valve; 12 – Test section gas chamber vent valve; 13 – Argon bottle pressure regulator; 14 – Sparger intake valve; 15 – sparger exhaust valve; 16 – Argon flow rate regulation valve; 17 – Bleed line valve; 18 – Charging pump inlet isolation valve; 19 – Charging pump bypass valve; 20 – vacuum line valve; 21 – drain valve.

2.3. LOW PRESSURE FLOW BOILING TEST SECTION

Figure 2-8 shows the design of the low pressure test section. This test section was used for experiments performed at pressures below 10 bar. Only a brief overview of the test section is presented here, since the details about this experimental setup are already published elsewhere [8]. The main body of the test section is made of 316 stainless steel. It has three openings to accommodate quartz windows and one opening for the installation of the heater cartridge. Both windows and the heater cartridge are held in place by stainless steel flanges. The test section is designed to operate at pressures up to 10 bar and temperatures up to 180 ºC. The flow channel has a rectangular shape (3×1 cm2) with a hydraulic diameter of 1.5 cm. The entrance channel has the same cross section as the test section. The length of the entrance channel is 965 mm, i.e. roughly 65 hydraulic diameters, which ensures a fully developed momentum boundary layer before the test section. The heater cartridge is used to provide a structural support for the IR heater, insulate it from the test section body and provide means for electrical connections. The body of the cartridge is made of Shapal®. Copper leads are connected from behind and are used to supply electrical power to the heater. However, aluminum (or copper) tape is used to connect electrically the power supply with the silver pads of the heater.

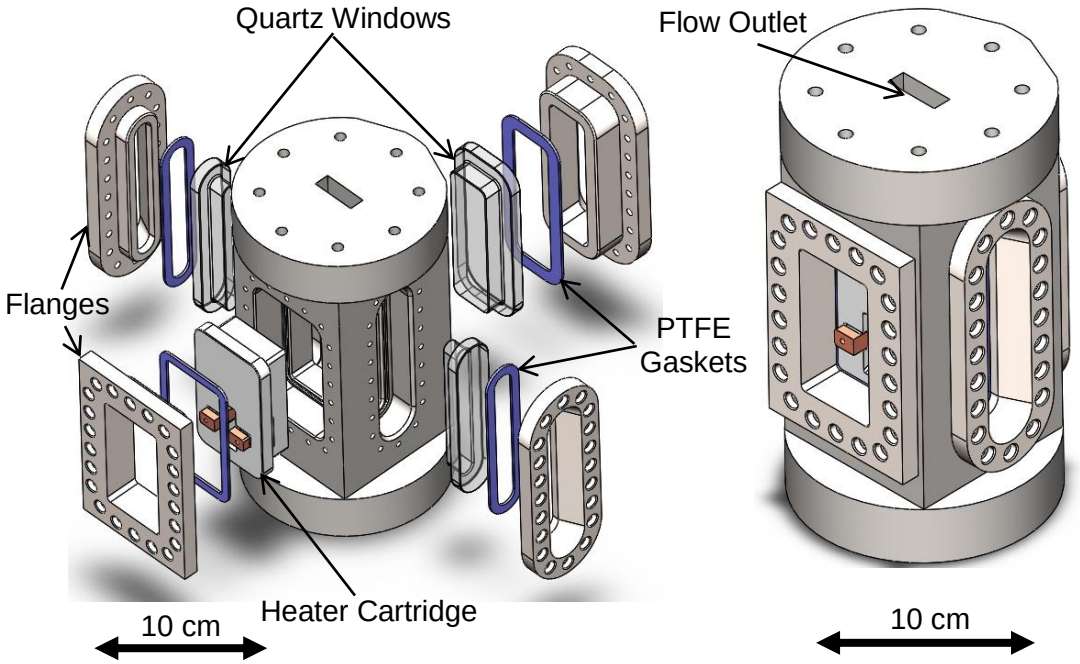

Figure 2-8. Exploded (left) and assembled (right) views of the low pressure flow boiling test section.

2.4. ATMOSPHERIC PRESSURE POOL BOILNG SETUP

The new pool boiling apparatus was built as a part of the present thesis. The new setup presents a simplified version of another pool boiling apparatus that is detailed in [84]. The details of the new design are shown in Figure 2-9. The main objective of the new design

was the decrease in overall volume, making the setup more compact. The compact design makes it possible to position IR and HSV cameras closer to the boiling surface which in turn leads to the better spatial resolution. The same heater design as shown in Figure 2-1 was used for pool boiling tests. Two T-type thermocouples are positioned at different elevation with respect to the boiling surface. Readings from these thermocouples ensure temperature uniformity inside the boiling vessel. An additional thermocouple (not shown in Figure 2-9) is attached to the sapphire and positioned a few millimeters away from the active area of the heater. This thermocouple is used for the calibration of the IR camera. Before each test, water is heated by 2 cartridge heaters until the saturation temperature is reached. Due to the small volume of the vessel, the water level may drop during the test due to evaporation. This could uncover the cartridge heaters, leading to their burnout. In order to avoid this issue, a water supply line was added to the design. During the test, the water supply line is connected to the large water reservoir. The water reservoir is elevated to a certain height, such that the water level in the reservoir is above the cartridge heaters in the pool boiling vessel. Whenever the water level inside the pool boiling vessel is decreased, it will be replenished passively by siphoning fresh water from the reservoir. The volume of the water reservoir was large enough to ensure that the drop in the water level of the reservoir is negligible throughout the test. During the shakedown of the apparatus it was confirmed that the flow rate of water from the reservoir into the pool boiling vessel is small enough to prevent any temperature non-uniformities caused by the influx of cold water from the reservoir. Furthermore, the cold water entering the test section through the water supply line is being preheated by the hot water surrounding the water supply tube inside the pool boiling vessel. The pool boiling vessel is also equipped with 4 glass windows that provide a side view of the boiling surface. The bulk of the pool boiling vessel was 3D-printed using High Temp resin [85] from FormLabs. The internal structure of the pool boiling vessel was made hollow in order to reduce heat losses.

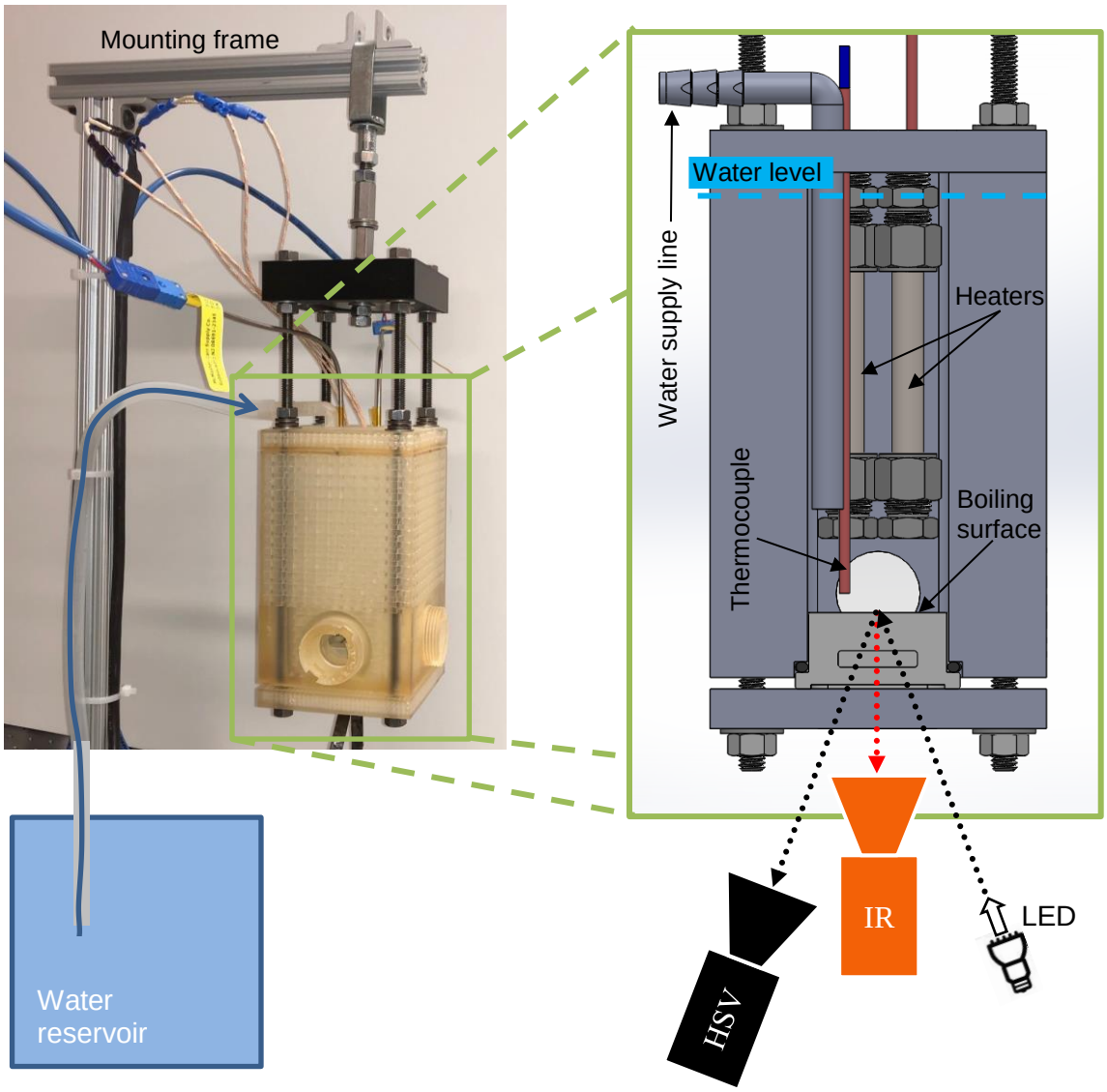

Figure 2-9. Schematic of the pool boiling apparatus

2.5. PHASE DETECTION TECHNIQUE

In this section, the details about the phase detection technique are presented. The main motivation for the development of this technique was the inability of IR thermometry to resolve scales on the order of 10 μm that dominate high pressure boiling. By switching to the technique that utilizes visible light it is possible to significantly improve the spatial resolution. The major features of the technique that were pursued during its development are:

- Ability to visualize dry areas created by individual bubbles
- Ability to visualize the structure of the microlayer
- Simple optical setup to lower the minimum working distance of the lens thus maximizing spatial resolution.

Currently available phase detection methods are unable to realize all three features listed above. Therefore, a new technique was developed as a part of this thesis research in order to allow the study of high pressure flow boiling. This technique utilizes high intensity, narrow bandwidth light emitting diodes (LEDs) as a light source. In the next subsection I will detail the theoretical basis of the new phase detection technique and highlight how the use of LED light is more advantageous compared to a more commonly used laser light. Next, details of the optical arrangement used with the proposed technique are presented. For more details about the broad range of the new technique's capabilities, the reader is referred to [86].

2.5.1. Theoretical basis

The theoretical basis for understanding the behavior of colored, monochromatic LED lights and their advantages compared to highly coherent light sources, i.e., lasers, are discussed hereafter. All derivations follow the thin-film interference theory detailed in Ref. [87].

Consider the optical system shown in Figure 2-10. When an incident light wave, whose electric field at a wavelength λ is $E_{is}(\lambda)$, enters the microlayer from the substrate, it experiences multiple reflections at each interface where the index of refraction has a discontinuity. Adding all the reflected waves, one gets a reflected electric field equal to

$$E_{r,\mu L}(\lambda, h_{\mu L}) = E_{is}(\lambda) \cdot \frac{r_{sl} + r_{lv}\, e^{i\delta_{\mu l,p}}}{1 + r_{lv}\, r_{sl}\, e^{i\delta_{\mu l,p}}} \tag{2-1}$$

where r_{sl} and r_{lv} are the reflection coefficients at the substrate-liquid and liquid-vapor interfaces. $\delta_{\mu l,p}$ is the phase difference accumulated over a single pass through the microlayer, given by Equation (2-2).

$$\delta_{\mu l,p} = \frac{4\pi\delta_{\mu L}}{\lambda} \cdot \sqrt{n_l^2 - n_s^2 \cdot sin^2\,\theta_{is}} \tag{2-2}$$

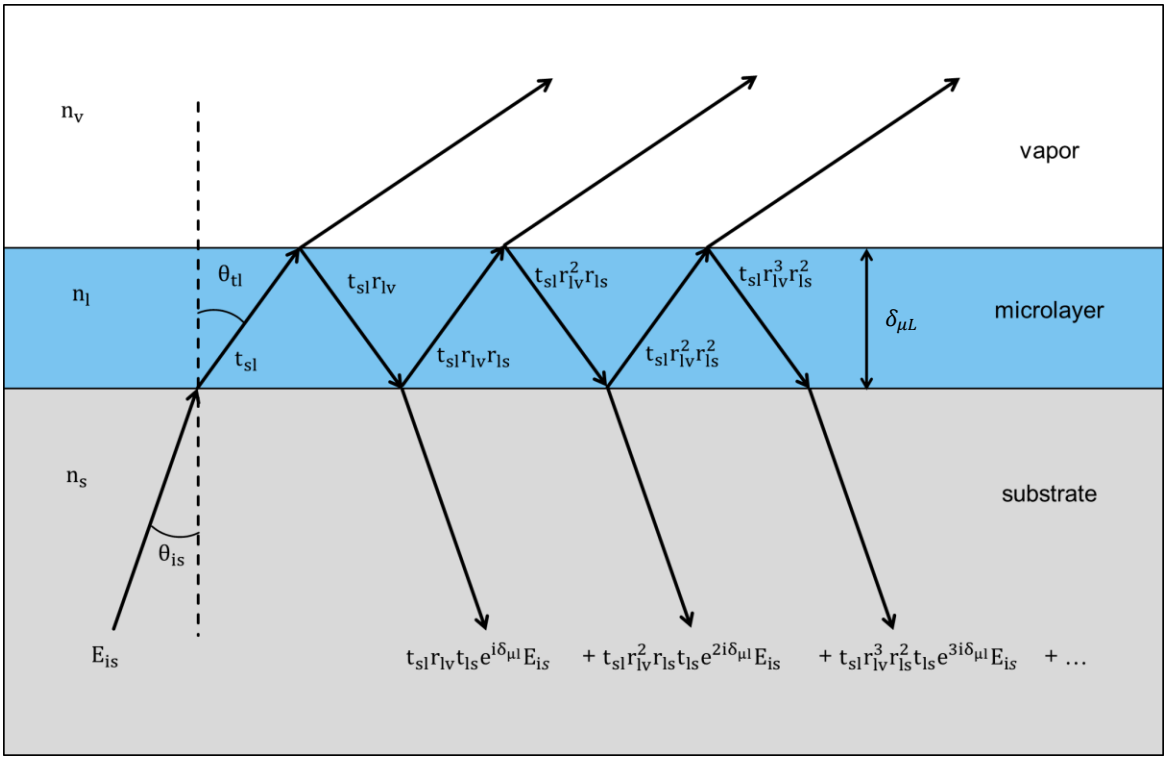

Figure 2-10. Multiple reflections within the microlayer. Here, tsl is the transmission coefficient at the substrate-liquid interface. All other symbols are defined in the text.

Here, $\delta_{\mu L}$ is the microlayer thickness, n_l and n_s are the real refractive indices of the liquid and the substrate, respectively, and θ_{is} is the angle of incidence. The intensity of the reflected light is expressed by Equation (2-3)

$$I_r(\lambda, \delta_{\mu L}) \propto \left[E_r(\lambda, \delta_{\mu L}) \cdot E_r^*(\lambda, \delta_{\mu L})\right] = I_{is}(\lambda) \cdot \frac{r_{sl}^2 + r_{sl}r_{lv} \cdot 2\,cos(\delta_{\mu l,p}) + r_{lv}^2}{1 + r_{lv}r_{sl} \cdot 2\,cos(\delta_{\mu l,p}) + r_{lv}^2 r_{sl}^2} \quad (2\text{-}3)$$

where $E_r^*(\lambda, \delta_{\mu L})$ is the complex conjugate of $E_r(\lambda, \delta_{\mu L})$ and $I_{is}(\lambda)$ is the spectral intensity of the incident light beam. Finally, the effective reflectivity of the microlayer is found by dividing Equation (2-3) by the intensity of the incident light beam, $I_{is,tot}$, and integrating over the spectral range of the incident light.

$$R_{eff,\mu L}(\delta_{\mu L}) = \int_{\lambda_1}^{\lambda_2} \frac{I_{is}(\lambda)}{I_{is,tot}} \cdot \frac{r_{sl}^2 + r_{sl}\,r_{lv} \cdot 2\,cos(\delta_{\mu l,p}) + r_{lv}^2}{1 + r_{lv}\,r_{sl} \cdot 2\,cos(\delta_{\mu l,p}) + r_{lv}^2 r_{sl}^2} \cdot d\lambda \quad (2\text{-}4)$$

Figure 2-11 (left) shows how the reflectivity, i.e., Equation (2-4), changes (for θ_{is}= 0) as a function of the microlayer thickness for the spectral properties of the LED lights used in the current study as well as a typical He-Ne laser light used for this kind of investigation. In this study I used a red color LED light from Wayllshine with a central wavelength of 630 nm and full width at half maximum (FWHM) of 14 nm, and a blue color LED light from the same supplier with a central wavelength of 452 nm and an FWHM of 16 nm [88].

Note that the curves in Figure 2-11 (left) represent the intensity of the light that would be reflected back by a microlayer of uniform thickness. This situation would not create an interference pattern. Instead, if the microlayer thickness is not uniform, e.g., it increases with the distance from the nucleation site, the intensity of the reflected light would oscillate radially, creating interference fringes. Figure 2-11 (right) shows examples of how these fringes would look like for a microlayer thickness growing linearly with a typical 5 μm/mm slope. The top grayscale image shows the theoretical behavior, whereas the figures underneath demonstrate how the measured signal would degrade as the spatial resolution of the optical setup coarsens. Here, the image degradation was evaluated by making box-averages of the theoretical image, with the size of each box corresponding to the pixel size for a given spatial resolution.

Note that the coherence length of a light source is inversely proportional to its spectral bandwidth (i.e., the FWHM). Thus, the laser light has coherence length in the order of meters, which allows for static interference patterns to be created for any practical microlayer thickness (i.e., << 1mm). Instead, the coherence length of the LED lights is in the order of a few tens of microns only. This property prevents the formation of a static interference pattern for relatively large microlayer thicknesses. However, while the amplitude of the fringes gradually decreases as the microlayer thickness grows, the signal is sufficiently high for practical microlayer thickness measurements, e.g., up to 2.5 and 5 μm for the blue and the red LED lights, respectively.

Note that, usually, the thickness is not measured directly based on the intensity of the reflected light. Instead, as the distance between these fringes indicates the slope of the microlayer, the microlayer profile, i.e., its thickness, can be reconstructed by integrating the measured microlayer slope. This integration requires a reference point where the microlayer thickness is known a priori, e.g., the dry spot where the microlayer thickness is just zero. Note also that the maximum gradient that can be measured depends on both the spatial resolution of the optical setup and distance between the interference fringes, as shown in Figure 2-11. This limitation introduces errors in the reconstruction of the microlayer profile near the triple-point contact line, where the slope of the microlayer can be very high. If that's the case, the thickness of the microlayer obtained with this integration is potentially underestimated compared to the actual microlayer thickness.

The capability to visualize the fringes and reconstruct the microlayer profile is also affected by the spatial resolution of the optical setup, as can be seen in Figure 2-11 (right). Fringes are well defined for high-spatial resolutions, i.e., ≤ 10 μm/pixel, while for coarser spatial resolution, the contrast deteriorates, and the fringes are barely visible. In particular, for the blue LED light, at a resolution of ~20 μm/pixel the microlayer appears as a uniform area, slightly darker than the dry spot, but practically without interference patterns.

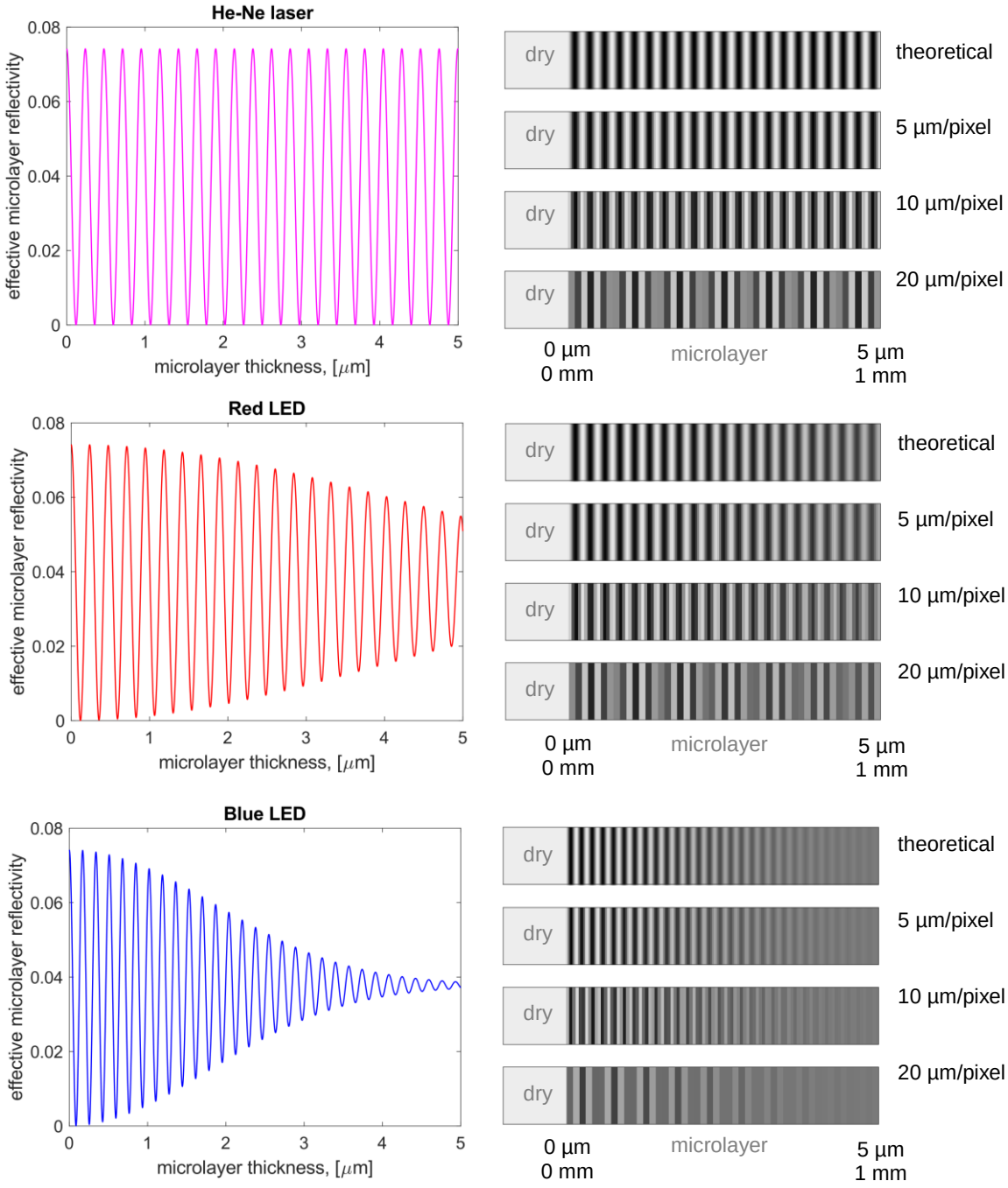

Figure 2-11. Effective reflectivity of a uniformly thick microlayer as a function of the microlayer thickness calculated using Equation (2-4) (left) and theoretical spatial fringes for a microlayer thickness growing linearly with a 5 µm/mm slope as a function of the distance from the contact line (right). Here, the top figure is the ideal signal, whereas the figures underneath demonstrate how the coarsening of the imaging resolution (from 5 to 20 µm/pixel) would degrade the signal. All results are obtained for a zero-degree angle of incidence.

Finally, it is interesting to note that the ratio between the peak reflectivity of red and blue LED lights is a unique function of the local microlayer thickness and can potentially be used as an additional reference for the direct measurement of the absolute microlayer thickness. Such an approach may be used to reduce the uncertainty associated with the limited resolution of fringes near the triple point contact line.

The advantages of LED lights compared to coherent light sources are particularly clear when analyzing the reflection caused by the substrate, which can create parasite interference patterns contaminating the final image. Similar to Equation (2-4) the effective reflectivity of the substrate (for a completely wet case) is given by Equation (2-5) and plotted in Figure 2-12 for sapphire (with a refractive index $n_s \approx 1.75$).

$$R_{eff,s}(\delta_s) = \int_{\lambda_1}^{\lambda_2} \frac{I_i(\lambda)}{I_{i,tot}} \cdot \frac{r_{as}^2 + r_{as}r_{sl} \cdot 2\,cos(\delta_{s,p}) + r_{sl}^2}{1 + r_{sl}r_{as} \cdot 2\,cos(\delta_{s,p}) + r_{sl}^2 r_{as}^2} \cdot d\lambda \tag{2-5}$$

where r_{as} is the reflection coefficient of the air with the substrate, and $\delta_{s,p}$ is the phase difference accumulated over a single pass through the substrate, given by Equation (2-6).

$$\delta_{s,p} = \frac{4\pi\delta_s}{\lambda} \cdot \sqrt{n_s^2 - n_a^2 \cdot sin^2\,\theta_i} \tag{2-6}$$

Here, δ_s is the substrate thickness, n_a is the real refractive index of air, and θ_i is the angle of incidence of the light with the substrate.

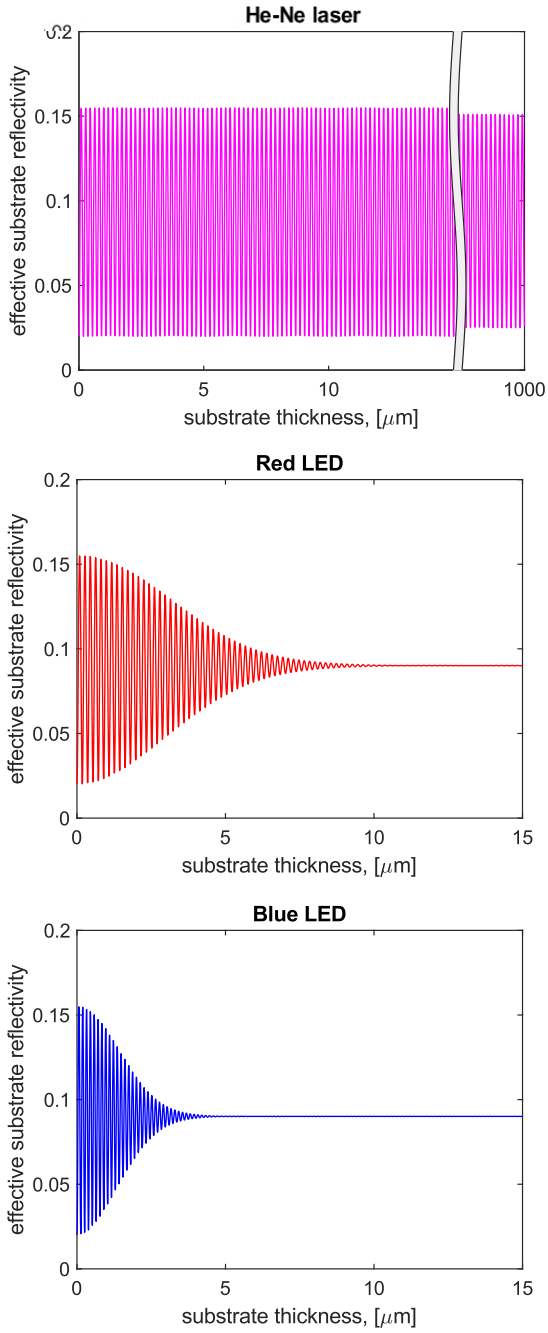

Figure 2-12. Effective reflectivity of the sapphire substrate for a He-Ne laser (top), the red (middle), and blue LED (bottom) lights. All results are obtained for a zero-degree angle of incidence.

Figure 2-12 demonstrates that for the substrate thickness as low as 15 μm the interference that creates the parasite light pattern has completely vanished for both LED colors. Therefore, with the use of LED light, a uniform background is achieved. Such background can be easily subtracted from the raw image to expose important features (i.e., dry areas and microlayers). In contrast, with the popular He-Ne laser approach, the interference pattern persists up to a thickness of 1 mm and beyond. This behavior significantly affects

the quality of the images if the surfaces of the substrate are not perfectly parallel, i.e., even a few microns difference in the local thickness would create parasite interference patterns.

2.5.2. Optical arrangement

The typical optical arrangement used for phase detection is shown in Figure 2-13 (left). The phase detection LED is pointed at the sapphire substrate with an incident angle θ_i. The reflected beam (called the main beam in Figure 2-13) is directed towards the high speed video camera. By recording the main beam, dry area and microlayer are revealed (Figure 2-13 (bottom right)). The dry areas appear as uniform bright spots on the image, while the microlayer appears as a series of interference fringes. The areas of the boiling surface that are in contact with liquid appear dark. A portion of the light emitted by the phase detection LED is reflected and scattered by the boiling vessel. This light can find its way back towards the HSV camera, creating an additional light source called backscattered (BS) beam in Figure 2-13. If the BS beam is recorded by the HSV camera together with the main beam, it can reveal the outline of a bubble in addition to visualizing the dry area and the microlayer (see Figure 2-13 (middle right)). Whether the BS beam is recorded by the camera is determined by the angle of incidence of the phase detection LED light θ_i, with larger angles resulting in smaller amounts of the BS light recorded by the camera. While it might be useful to visualize the outline of the bubble in addition to the dry area and the microlayer, the presence of BS light makes image post-processing more challenging, since it can make areas occupied by liquid almost as bright as the dry areas in the resulting image. Therefore, the incident angle θ_i can be adjusted based on the measurement objective. In other words, if the objective of the measurement is to capture the evolution of dry areas and microlayers, then large values of θ_i are preferable, since they will prevent the BS light from reaching the camera. In contrast, when the behavior of the entire bubble is of interest, it can be revealed by utilizing small values of θ_i. Additionally, large values of θ_i make it easy to combine the phase detection technique with IR thermometry (see Figure 2-13 (left)). However, even for small values of θ_i the application of IR thermometry is possible, but require the addition of a spectral beam splitter (see Ref. [86] for more details). Another way of revealing the outlines of the bubble is by using an additional light source opposite to the HSV camera (Shadowgraphy (SG) LED in Figure 2-13). The use of the SG beam is preferable to the BS beam because the intensity of the SG beam can be adjusted independently of the phase detection LED light. This allows for the accurate tuning of the contrast between the dry area, wet area and the bubble outline, hence simplifying the post-processing (see Figure 2-13 (top right)). All three visualization approaches shown in Figure 2-13 (right) were utilized in the present study. Note that in Figure 2-13 (middle right) the microlayer fringes cannot be resolved. This is caused by the combination of coarse spatial resolution and blue LED light, both of which made it more challenging to resolve microlayer fringes (see previous Sub-Section for more details). The inability to resolve microlayer fringes in Figure 2-13 (middle right) has nothing to do with the presence of the BS beam.

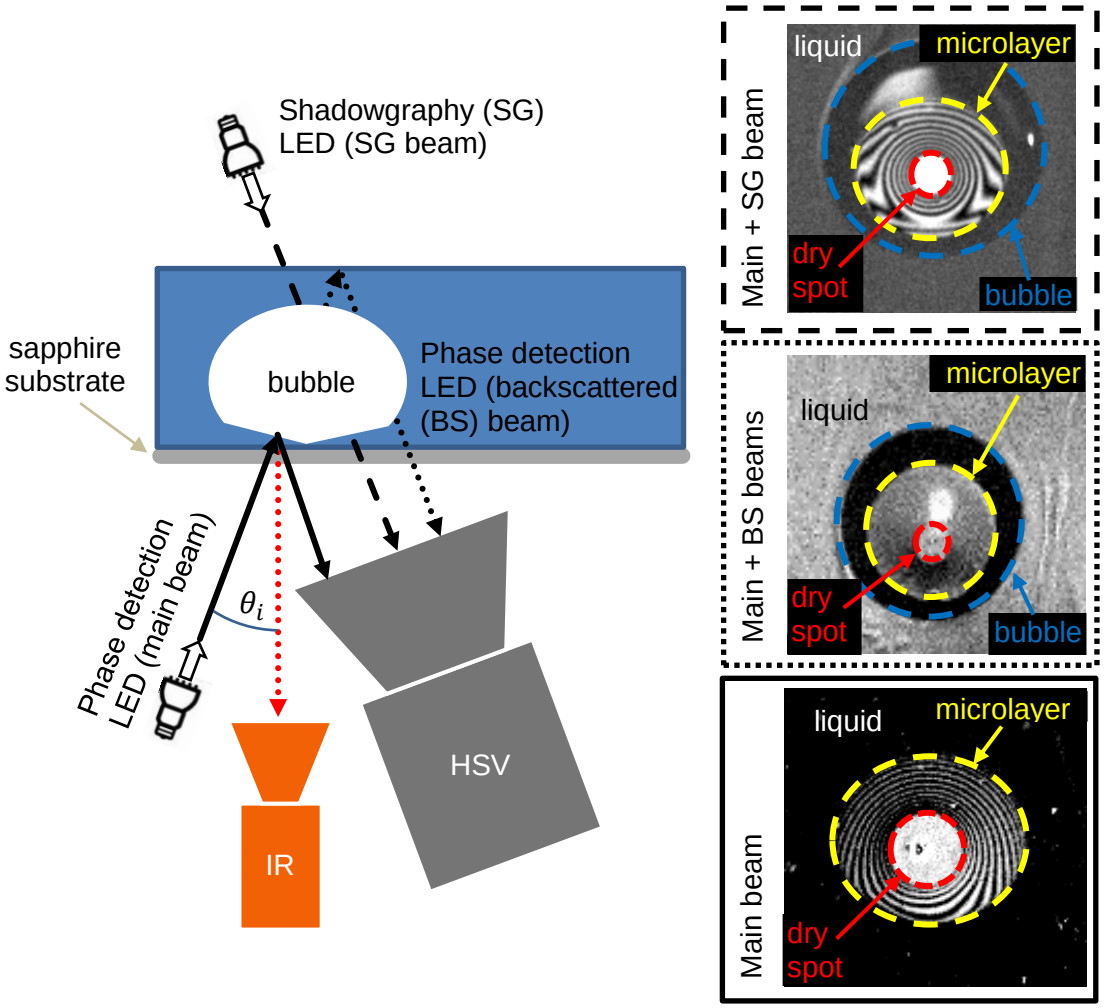

Figure 2-13. Schematic of the optical setup used for phase detection (left) and sample HSV image acquired with a different combination of beams.

As discussed in the previous Sub-Section and shown in Figure 2-13, the proposed technique avoids problems associated with parasitic interference patterns, while also allowing the visualization of microlayer structure. The proposed technique has become possible only in the recent years due to the availability of powerful colored LEDs with superior beam coherence compared to the mercury lamps that were unsuccessfully applied to the same problem in the past [74], [75]. Such LED lights are simple in operation, affordable, and much safer than lasers, making it easier for more research groups to enter the field and improve the knowledge of boiling phenomena. While the new technique can be used as a standalone measurement, its value increases substantially when combined with infrared thermometry. More examples of the application of the present technique are found throughout the thesis and in Ref. [86].

2.6. INFRARED CAMERA CALIBRATION APPROACH

This section details the procedures used for the calibration of the IR camera. For low pressure tests (using the low pressure flow boiling setup as well as the atmospheric pressure pool boiling setup) the mechanistic IR calibration technique was used. Only a brief overview of the mechanistic calibration technique is presented here. The details of this approach can be found in [89].

2.6.1. Mechanistic calibration

A brief description of the IR calibration technique is presented below. For more details the reader can refer to Ref. [89]. The temperature of the ITO is proportional to the IR radiation it emits. However, in addition to the IR radiation from ITO, the IR camera also receives the radiation from the sapphire substrate (which is not completely transparent in the 3-5 μm wavelength range and whose optical properties are strongly wavelength dependent) and the radiation reflected from the background, as sketched in Figure 2-14. Therefore, it is important to exclude contributions from the sapphire and background radiations from the total signal in order to measure the actual ITO temperature. This is achieved by solving an inverse problem coupling radiation and conduction. The problem is inverse because the boundary condition of the problem, i.e. the actual ITO temperature, is not known but is part of the solution, which is obtained iteratively. A guess ITO temperature is used as tentative boundary condition for the 3D conduction equation, which is solved in the sapphire substrate. The updated temperature distribution in the substrate is used to calculate the radiation emitted and reflected by the whole heater and received by the camera. This radiation is compared to the actual radiation detected by the IR camera. If these two radiations are not exactly the same, the guess ITO temperature is updated and the process is repeated until satisfactory convergence is achieved. Such procedure is applied to each IR frame throughout the recording.

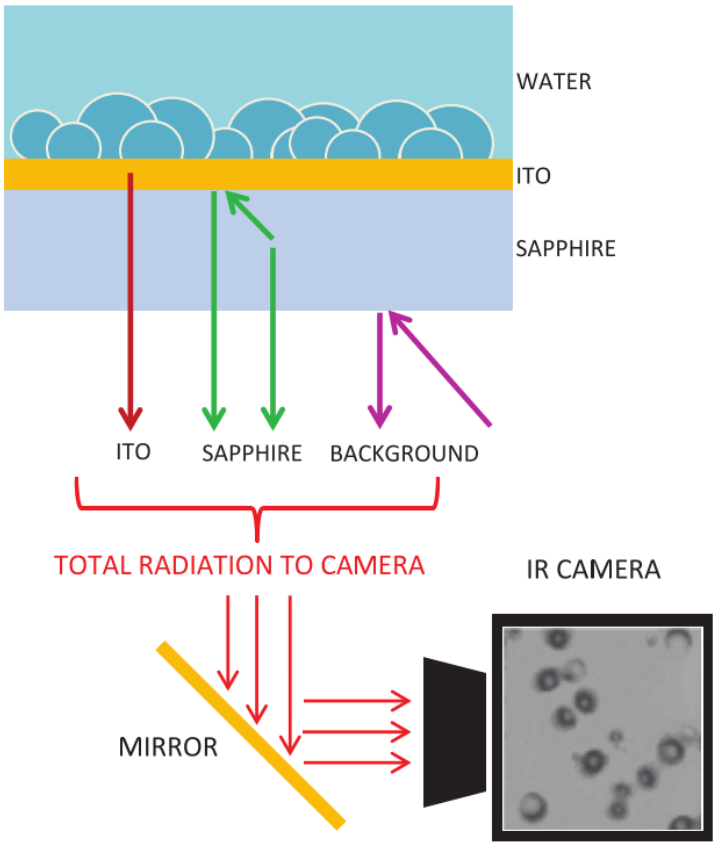

Figure 2-14. Different sources of the IR radiation received by infrared camera in a typical boiling experiment. The image is adapted from [89]

2.6.2. Calibration using analytical solutions for the transient conduction

The mechanistic IR calibration technique was only applied to the tests made using the low-pressure flow boiling and pool boiling setups. The mechanistic calibration technique was not applicable to the tests made using the high-pressure test section due to additional signal contamination stemming from the gas compartment of the test section. Figure 2-15 highlights several additional radiation sources that are not present in low-pressure test section. First, the thick sapphire window that serves as a pressure boundary for the gas compartment will emit a considerable amount of IR radiation due to its partial transparency in the 3 – 5 μm range. Additionally, the enclosed shape of the gas compartment will result in emissions from hot internal structures to be redirected towards the IR camera by the ITO. The magnitude of these emissions will depend on the temperature of the test section. Due to the large thermal inertia of the test section, its temperature will lag behind the temperature of the ITO layer, leading to a large variability of the radiative signal emitted by the structure during heatup, cooldown and when approaching a steady state. The contamination of the signal coming from the sapphire was avoided by introducing a wide band-pass filter in between the lens and the sensor of the IR camera. The full width at half maximum (FWHM) of the band-pass filter spanned a range of wavelengths between 3.372 and 3.946 μm. The range of the band pass filter covers the spectral region in which sapphire

emissivity is negligible, hence preventing most of the radiation emitted by sapphire from reaching the sensor of the IR camera.

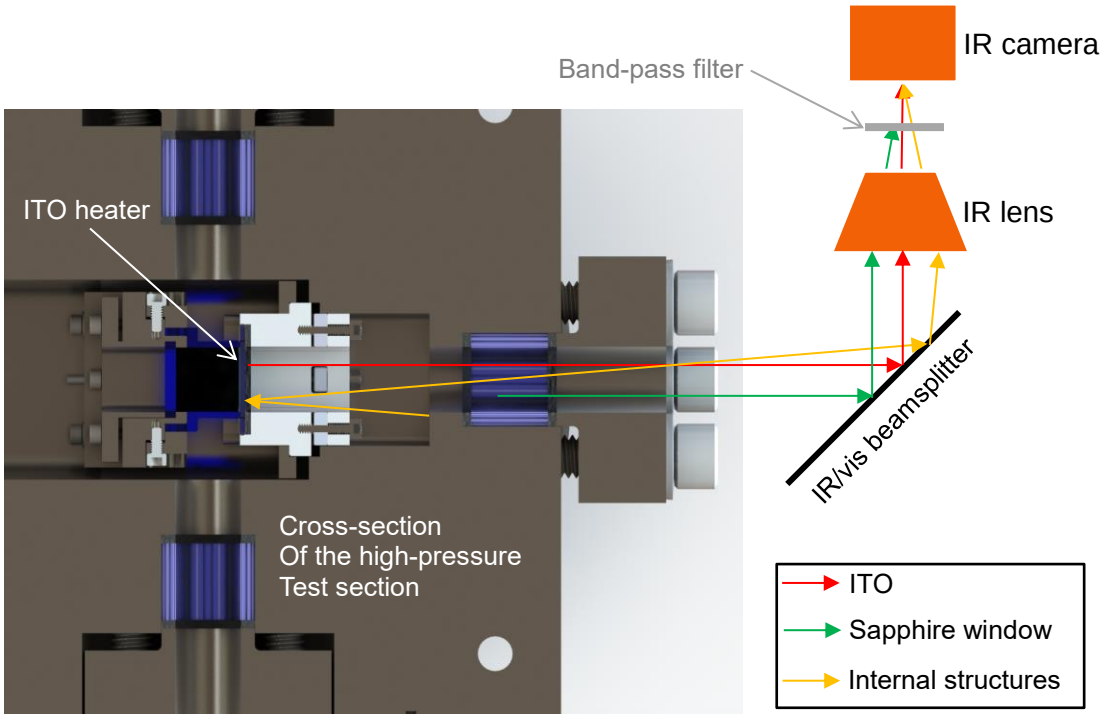

Figure 2-15. Multiple IR radiation sources that contaminate main signal emitted by ITO

The contamination of the signal stemming from the emissions of the internal structures was avoided by a separate calibration procedure. First, the test section was brought to the equilibrium at the desired operation temperature. In each experiment one and a half hour was given to the test section in order to reach thermal equilibrium with the bulk temperature of the water channel. Reaching the equilibrium ensures that the emissions from the internal structures will remain constant throughout the experiment. Next, the IR heater is energized with a series of fast exponential transients, in which the power $\dot{Q}$ varies according to Equation (2-10)

$$\dot{Q} = \dot{Q}_0 \cdot e^{\frac{t}{\tau}} \tag{2-7}$$

where $\dot{Q}_0$ is the starting power, t is time and τ is the period of the exponential power rise. The mass flux was set to 500 kg/m^{2}s and the exponential period τ was set to 5 ms. For the selected value of the mass flux, the period of 5 ms is sufficiently short to make convective heat transfer negligible compared to conduction [90]. Therefore, a temperature rise of the ITO ΔT_{ITO} can be calculated using the analytical solution presented in [84] and given by Equation (2-11)

$$\Delta T_{ITO} = \frac{\frac{\dot{Q}_0}{A_H} \cdot e^{\frac{t}{\tau}}}{\frac{\varepsilon_s}{\sqrt{\tau}} \cdot \tanh\left(\frac{1}{\sqrt{Fo_s}}\right) + \frac{\varepsilon_w}{\sqrt{\tau}}} \tag{2-8}$$

where A_H is the area of the heater, ε_s is the thermal effusivity of the sapphire, ε_w is the thermal effusivity of water, and Fo_s is the Fourier number of the sapphire, calculated with Equation (2-12)

$$Fo_s = \frac{\alpha_s \cdot \tau}{\delta_s} \tag{2-9}$$

where α_s is the thermal diffusivity of the sapphire and δ_s is the thickness of the sapphire. During the transient, both the power of the heater and the signal of the IR camera are recorded and synchronized. Since the IR heater is too small to change the temperature of the gas compartment internal structures, the increase in IR signal during the transient can be attributed solely to the increase in ITO emissions. Such increase is combined with the analytically calculated temperature rise (i.e. Equation (2-8)) to give us the calibration curve for the IR camera.

2.7. DATA POST-PROCESSING AND UNCERTAINTIES

2.7.1. Bubble tracking algorithm

In this section I describe the algorithm used to track bubbles and detect the distance they have traveled from the nucleation site as well as their diameter. Steppes involved in this algorithm are illustrated in Figure 2-16. This algorithm requires shadowgraphic images taken at relatively low heat fluxes. Low heat flux ensures that the interaction between bubbles is minimal. First, isolated nucleation sites that produce bubbles consistently are identified manually. The raw HSV image is then cropped in the vicinity of such nucleation site. HSV images then undergo several preparatory steppes. First, they are resized by a factor of 5 in order to improve the detection of bubble perimeter. Later, the image is inverted and binarized. There are many built-in Matlab functions that allow for easy processing of binary images. Using these functions, the centroids and areas of each white region in the binary image are found. The radius of each bubble is estimated with Equation (2-10). Since bubbles remain almost circular at high pressures, the use of Equation (2-10) for the estimation of bubble radius is fully justified.

$$R = \sqrt{\frac{A}{\pi}} \tag{2-10}$$

From now on, the distinction is made between the current HSV frame (i^{th} frame in Figure 2-16) and the preceding HSV frame ($(i-1)^{th}$ frame in Figure 2-16). The procedure used to

correlate the positions of bubbles between these two frames is illustrated schematically in Figure 2-17. Assume that several bubbles are already being tracked and their positions and diameters in $(i-1)^{th}$ frame are known. In order to find the new positions of bubbles in i^{th} frame, first the distances between each bubble in i^{th} frame and each tracked bubble in $(i-1)^{th}$ frame are calculated. For each tracked bubble, there will be a bubble in i^{th} frame which position is closest to the tracked bubble in $(i-1)^{th}$ frame. As long as the recording frame rate is sufficiently high, such proximity criterion will allow the new position of each tracked bubble to be identified. In order to improve the versatility of the algorithm, in addition to checking the distance between each bubble in two frames, the sign of y-displacement was also identified. Since negative y-displacement will imply that the bubble is moving against the flow, shortest distances between bubbles in two frames with negative y-displacement were ignored and instead second shortest distance was used to identify the new position of each bubble. This procedure prevents false detections when in the time between two camera frames bubbles in a bubble column travel distances that are close to the distance between each bubble in the column. Adding this step to the algorithm allows its application to higher flow velocity with fixed camera frame rate, or to lower frame rates for the same flow velocity. When the identification of new positions in i^{th} frame is done, it is possible that there will be bubbles left in i^{th} frame that did not find a pair in $(i-1)^{th}$ frame. For such bubbles, their distance to the nucleation site is checked. If among the unpaired bubbles a bubble is found which is close enough to the nucleation site, this bubble is considered newly nucleated and its diameter and position are added to the pool of tracked bubbles. Bubbles that neither found a pair or were too far away from the nucleation site to be considered as newly nucleated were ignored. An example of bubble tracking algorithm applied to the measurements performed at the pressure of 20 bar, mass flux of 1000 $kg/(m^2-s)$ and 10 ^oC of subcooling is shown in Figure 2-18.

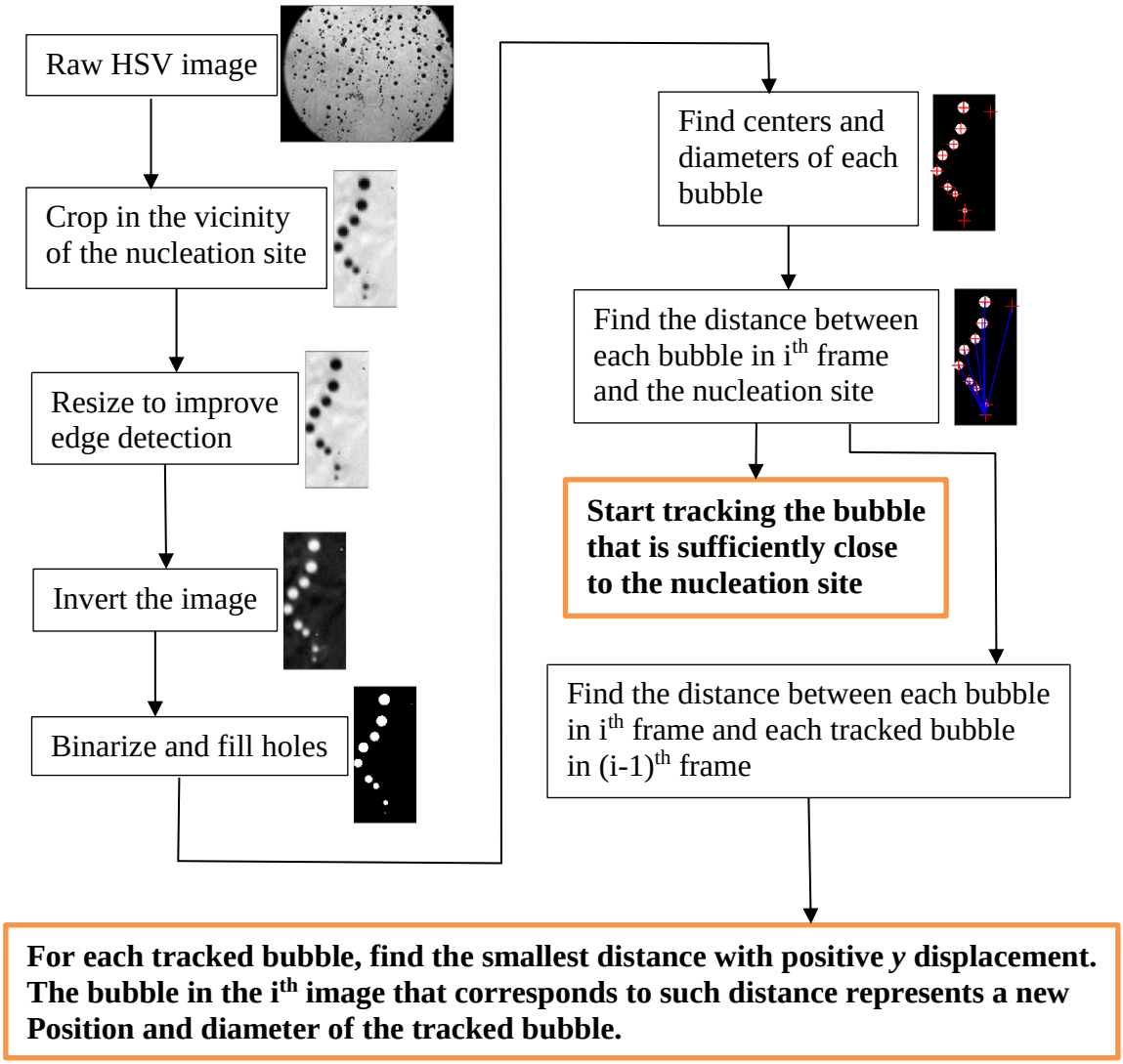

Figure 2-16. Steppes of the bubble tracking algorithm

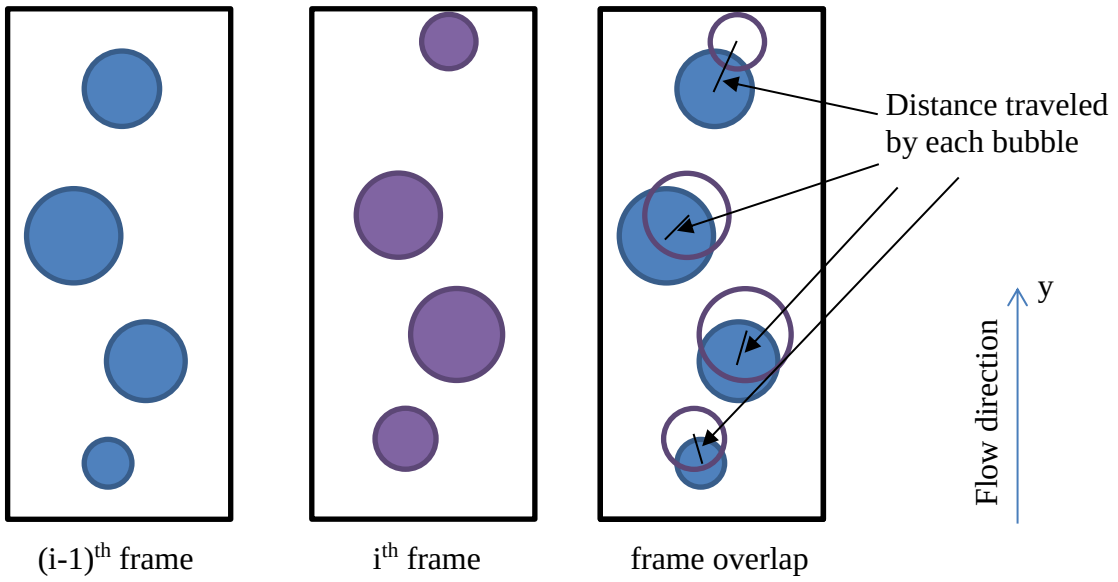

Figure 2-17. Illustration of the procedure that was used to correlate bubble positions between two consecutive frames. Flow direction is upwards, which also coincides with the direction of the y-axis

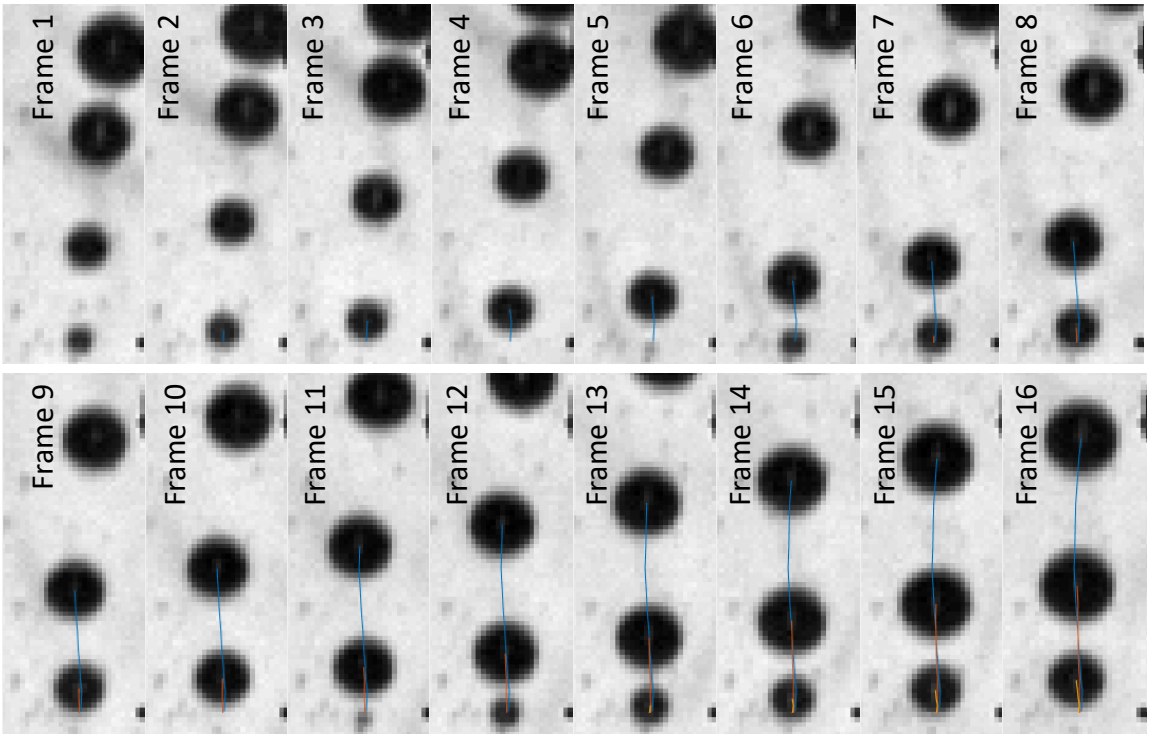

Figure 2-18. Demonstration of the bubble tracking algorithm performance for 16 consecutive frames. Blue, red and yellow lines represent bubble pathlines

Important parameters that are measured by the bubble tracking algorithm are bubble radius, diameter, position and distance traveled from the nucleation site. The uncertainties

associated with these parameters are discussed next. The uncertainty of the bubble radius measurement is associated with the limited spatial resolution of the optical setup. The spatial resolution will be limited by 4 factors:

1) Actual physical size of the pixel in the camera sensor.
2) Magnification of the lens.
3) Diffraction limit. If an image is taken with a diffraction-limited optical setup, then it is possible to observe blurry edges of objects even if the pixel size of the camera and the magnification of the lens are sufficient to provide a well resolved image of an object.
4) Focus. The position of an object can change due to the thermal expansion, or the initial setting of the focal plane can be incorrect due to a human error involved in identifying the right position of the focus ring on the lens.

In order to quantify these sources of uncertainties within our measurements we perform an analysis of the pixel intensity profile from the real measurements. Such analysis can be seen in Figure 2-19. Here a bubble is selected in the middle of an image and a profile of image intensity is extracted from the central cross section of this bubble (Figure 2-19 right). Such intensity profile indicates that the full transition from the dark interior of the bubble (low intensity) to the bright background (high intensity) happens within a span of 3 pixels. Therefore, in identifying the edge of the bubble we will have an uncertainty band of 3 pixels, or ± 1.5 pixels. This will also be the uncertainty associated with the measurement of the bubble radius. In contrast, the diameter will have twice this uncertainty, i.e. ± 3 pixels. The position of each bubble is measured by calculating the position of its centroid. Note that Figure 2-19 (right) shows a very symmetric transition from the area occupied by the bubble to the background on both sides of the bubble. Additionally, Figure 2-19 (left) demonstrates that blurry edges around all bubbles are fairly symmetric. This indicates that the position of centroids will be the same, no matter what threshold value is used to binarize the images. Therefore, the uncertainty of the bubble position is extremely small and is likely smaller than the pixel size. Finally, the uncertainty of the distance to the nucleation site will depend on the exact measurement of the nucleation site position. While at first the position of the nucleation site is measured manually, this initial value is only used within the algorithm to allow for the correct initiation of bubble tracking. Later, when hundreds of bubble growth histories are recorded, the correct position of the nucleation site is calculated as an average between points of origin of all bubbles. Therefore, the uncertainty of the nucleation site position measurement is also expected to be small. However, the value of standard deviation for nucleation site position will be reported in the later sections for each family of bubble growth histories.

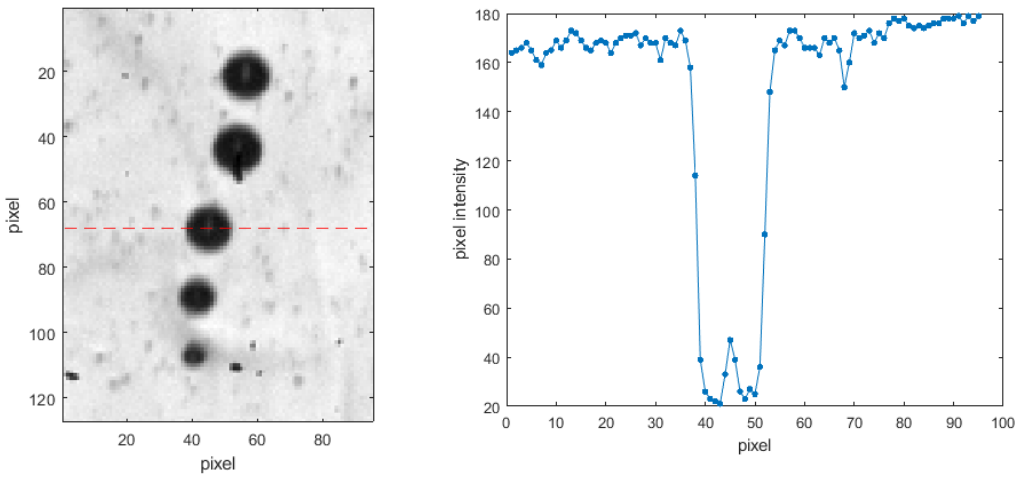

Figure 2-19. Shadowgraphic image of bubble on the surface (left) and the intensity profile of the image at the cross-section drawn through the middle of one bubble (right). Dashed red line in the left image indicates the position of the cross-section

2.7.2. Microlayer shape and thickness

The thickness of the microlayer $\delta_{\mu L}$ is measured by identifying the order of dark interference fringe k. The fringe order is then substituted into Equation (2-11)

$$\delta_{\mu L} = \frac{\lambda \cdot (2k+1)}{4 \cdot \sqrt{n_l^2 - n_s^2 \cdot sin^2\,\theta_{is}}}; \qquad k = 0,1,2,\ldots \tag{2-11}$$

The locations of the dark fringes were identified manually based on the phase detection images. This process is illustrated in Figure 2-20. We assumed that the first dark fringe adjacent to the dry area corresponds to the zeroth order (i.e. $k = 0$).

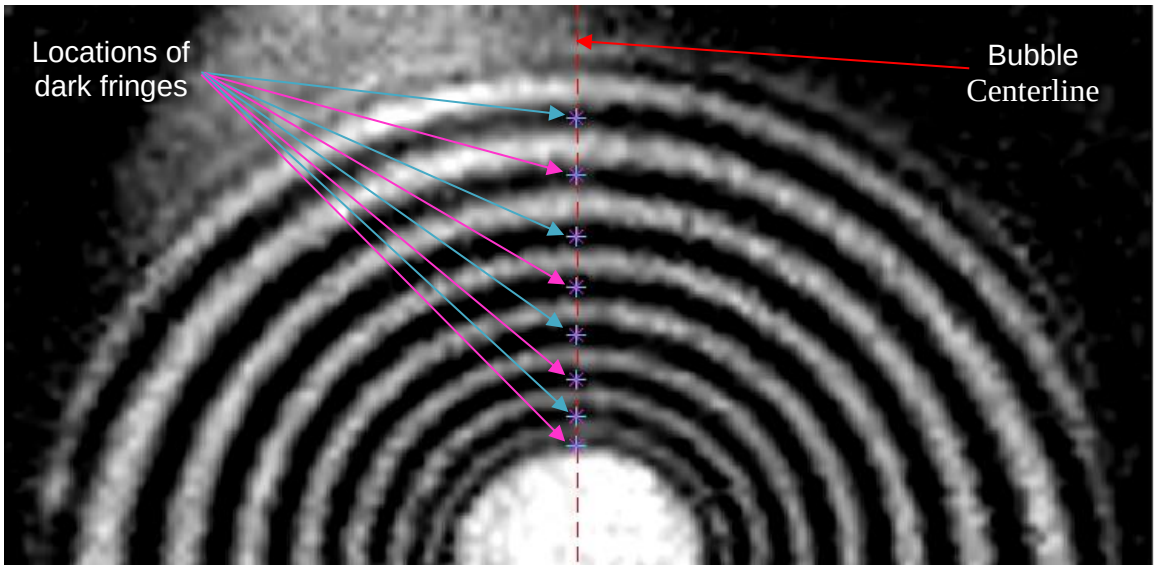

Figure 2-20. Dark microlayer fringes identified by manual picking

Note, that as long as the spatial resolution is sufficient to resolve individual fringes, the uncertainty of the microlayer thickness $\Delta h_{\mu L}$ can be defined as the difference in thicknesses of the two adjacent fringes given by Equation (2-12). Such difference will depend on the wavelength and the angle of incidence of the light. For the case presented here, we used the red LED with an angle of incidence in air $\theta_i = 20$ degree, which leads to the angle of incidence in sapphire $\theta_{is} = 11.3$ degree. This leads to the uncertainty of $\pm$ 122 nm. Additional uncertainty may come from the identification of the first fringe adjacent to the dry area. If the slope of the microlayer near the dry area is steep, this could result in light fringes being too close to each other for the optical system to resolve them. This may lead to the underestimation of the microlayer thickness.

$$\Delta h_{\mu L} = \frac{\lambda}{2 \cdot \sqrt{n_l^2 - n_s^2 \cdot sin^2\,\theta_{is}}} \qquad (2\text{-}12)$$

2.7.3. Apparent and real contact lines positions and movement velocity

If a bubble on a boiling surface contains liquid microlayer, then a distinction is made between the apparent and real contact lines (CLs). This difference is illustrated in Figure 2-21. The real CL (RCL) is defined as the line where liquid, vapor and solid wall coexist. In other words, RCL is the line that traces the perimeter of the dry area under the bubble. Liquid microlayer generally forms and annular region centered at the nucleation site. The inner perimeter of the microlayer annulus coincides with the RCL, while the outer perimeter forms an apparent CL (ACL). Since the maximum thickness of the microlayer does not exceed several microns, for any practical imaging system it would appear that the bubble is touching the surface at ACL, hence the use of the word “apparent” in the name.

in the current study the measurements of both RCL and ACL positions are made through the use of the phase detection technique detailed in the previous section.

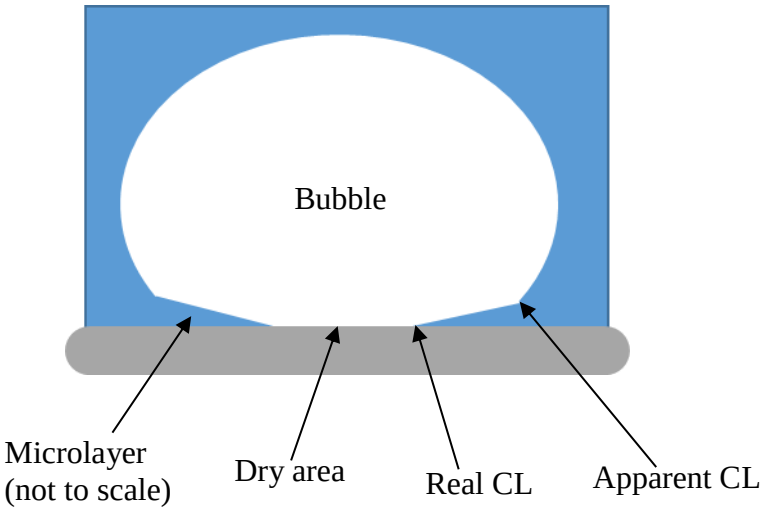

Figure 2-21. Illustration of the difference between the real and apparent contact lines

One of the goals of the present study is to quantify the effects of flow and pressure on microlayer formation. One way in which flow influences the microlayer is by making its annulus non-symmetric compared to pool boiling cases. In order to study this effect, positions and velocities of ACL and RCL at upstream and downstream portions of the bubble were measured. The measurement approach is illustrated in Figure 2-22. First, a line was drawn through the nucleation site, aligned with the flow direction. The points where this line crosses ACL and RCL at upstream and downstream directions were picked manually. This procedure was repeated for each HSV frame until the point where dry area fully receded, signifying bubble departure. Measured values of ACL and RCL positions were then converted to their velocities by taking a time derivative of their positions.

Here we adopt the same general treatment of the uncertainty as was described in section 2.7.1. Since the same optical setup was used for the measurement of the contact line velocity, we will use ±1.5 pixels as a general uncertainty value. There is, however, an additional source of uncertainties involved in our measurements that cannot be fully quantified. This uncertainty comes from the fact that the outer edge of the microlayer can end with the dark fringe. This will make the outer edge almost indistinguishable from the background, resulting in a slight underestimation of the microlayer extent. The error will depend on the flatness of the microlayer at its edge. This effect is illustrated in Figure 2-22, where the red arrow that highlights the upstream ACL is pointing in a general area where the dark fringe should end. While in Figure 2-22 it is fairly easy to determine the extent of the upstream ACL by fitting an oval into the entire microlayer profile, this is not always the case, and in some situations such approach is not possible. The effect of this issue will be seen in the following sections where the data illustrating microlayer position is examined. Having a small error in determining the positions of the microlayer will result in a much larger error when it comes to calculating contact line velocities. In order to

mitigate this problem, a moving average filter was used to dampen the oscillations of the contact line position associated with the dark fringe detection.

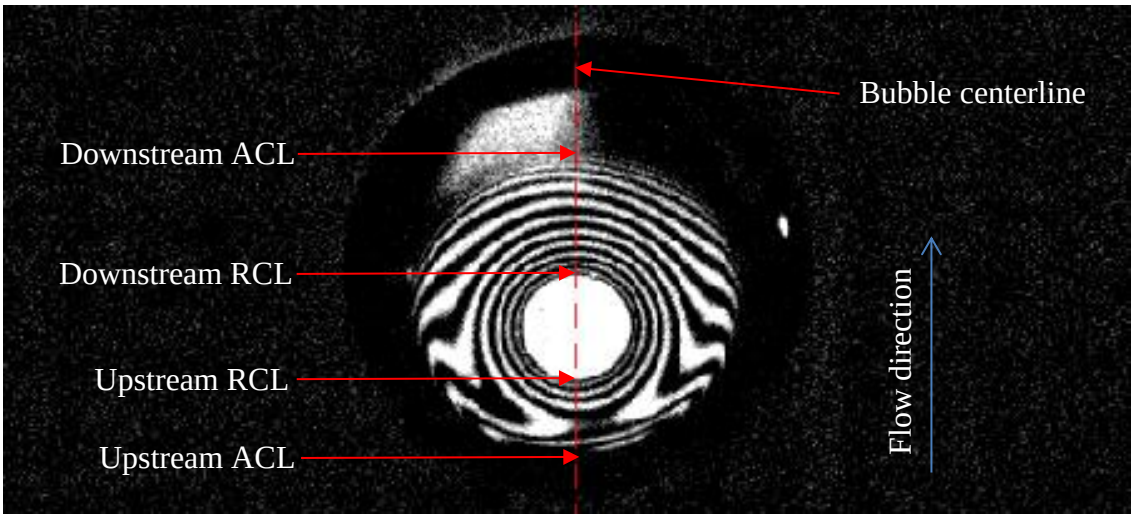

Figure 2-22. Illustration of the measurement approach that was used to determine the positions of ACL and RCL for both the upstream and downstream directions

2.7.4. Dry area tracking and spectral nucleation sites distribution

Dry area tracking algorithm was developed as a part of the present research. This algorithm was used to post-process raw phase detection images and to extract valuable boiling parameters. The flow chart of the algorithm is shown in Figure 2-23. First, raw phase detection images are thresholded in order to create binary images in which the pixels covered by vapor are assigned values of "1" and pixels covered by liquid are assigned values of "0". This process is repeated for all frames in the video. Figure 2-23 shows an example of the thresholding process for a single frame. Then image segmentation is performed on the binary images. Segmenting the image makes it easy to distinguish between each individual dry spot by assigning a unique ID number to each dry spot. The segmentation process is repeated for each frame. Later the consecutive frames are compared to each other. Consider two consecutive frames with frame numbers i and $(i + 1)$. For frame $(i + 1)$ consider the position of a dry spot with the ID number j, while for frame number i consider another dry spot with the ID number k. When two frames are compared to each other, three outcomes are possible:

- 1st outcome. The position occupied by the dry spot j in the $(i + 1)^{th}$ frame was covered by liquid in the i^{th} frame. In this case, the dry spot j in the $(i + 1)^{th}$ frame corresponds to a newly nucleated bubble. This bubble is tallied and its growth is monitored by finding a match in the next frame (i.e. $(i + 2)^{th}$ frame). Also, a centroid of the dry spot j in the $(i + 1)^{th}$ frame is taken as the nucleation site for the newly nucleated bubble.
- 2nd outcome. The positions of the dry spot j in $(i + 1)^{th}$ frame overlaps with the dry spot k in i^{th} frame. In this case, dry spots k in i^{th} frame and j in $(i + 1)^{th}$ frame

correspond to the same bubble. Therefore, the dry spot j in $(i+1)^{th}$ frame is considered to be the next step in the growth of the dry spot k in i^{th} frame.

- 3rd outcome. The position occupied by the dry spot k in i^{th} frame is covered by liquid in $(i+1)^{th}$ frame. This means that the bubble associated with the dry spot k in i^{th} frame has departed in the $(i+1)^{th}$ frame.

Figure 2-23 demonstrates all three outcomes on the example of a single bubble. The bubble is first nucleated within the Frame #1, representing the 1st outcome with the value of $i = 0$. The bubble continues to grow for Frames # 2, 3, 4, 5 and 6 which all provide an example of the 2nd outcome. Finally, the bubble departs in the Frame #7, representing the third outcome with the value of $i = 6$. After the tracking of dry areas is completed, several important parameters about the bubble associated with this dry spot are known. Namely, the position of its nucleation site, the total area of the boiling surface visited by the dry spot (A_{bub}) and the growth time (t_g) for this bubble. The total area visited by the dry spot A_{bub} is accumulated as the bubble is being tracked. The procedure for measuring A_{bub} is shown schematically in Figure 2-24, where all dry spots captured while the bubble is attached to the boiling surface are overlapped with each other, giving together the measure of all regions on the boiling surface that were visited by a bubble. The process of dry area tracking is repeated for all footprints and every frame of the video. Eventually it provides an identification of nucleation site positions for all nucleation events on the boiling surface. Such positions are shown as a series of red dots in Figure 2-23. Figure 2-23 illustrates that nucleation sites appear to cluster around certain areas. However, whenever the sites are clustered together within a radius of a few pixels of each other, it is impossible to tell whether all nucleation events within one such cluster were produced by a single nucleation site, or if there are multiple nucleation sites positioned near each other. This uncertainty is caused by the fact that the exact position of the nucleation site is difficult to determine, since the finite temporal and spatial resolution of the imaging technique will result in slightly different positions of the bubble footprint centroids that are used to determine the nucleation site position for each new nucleation event. Therefore, as a final post-processing step the map of nucleation sites is refined based on their proximity to each other. Any two nucleation sites that are within 3 pixels of each other (i.e. 15 to 18 μm, depending on the test) are considered as a single nucleation site. The position of the resulting site is calculated as the average between the two, and the number of nucleation events for each site is tallied during the proximity filtering process. The final outcome results in more realistic distribution of nucleation sites, while also provides the information about the number of nucleation events occurring in each site. The number of nucleation events for each site determines the bubble departure frequency for each site. The bubble departure frequency is calculated by dividing the total number of nucleation events by the duration of the phase detection recording. The final positions of the nucleation sites after the proximity filtering are shown in Figure 2-23 as a series of red circles. The size of each circle is proportional to the logarithm of the nucleation frequency for each nucleation site. In the present work we refer to this representation of nucleation sites as the spectral nucleation sites map, since it not only provides the information about the positions of nucleation sites, but also describes the spectrum of bubble departure frequencies.

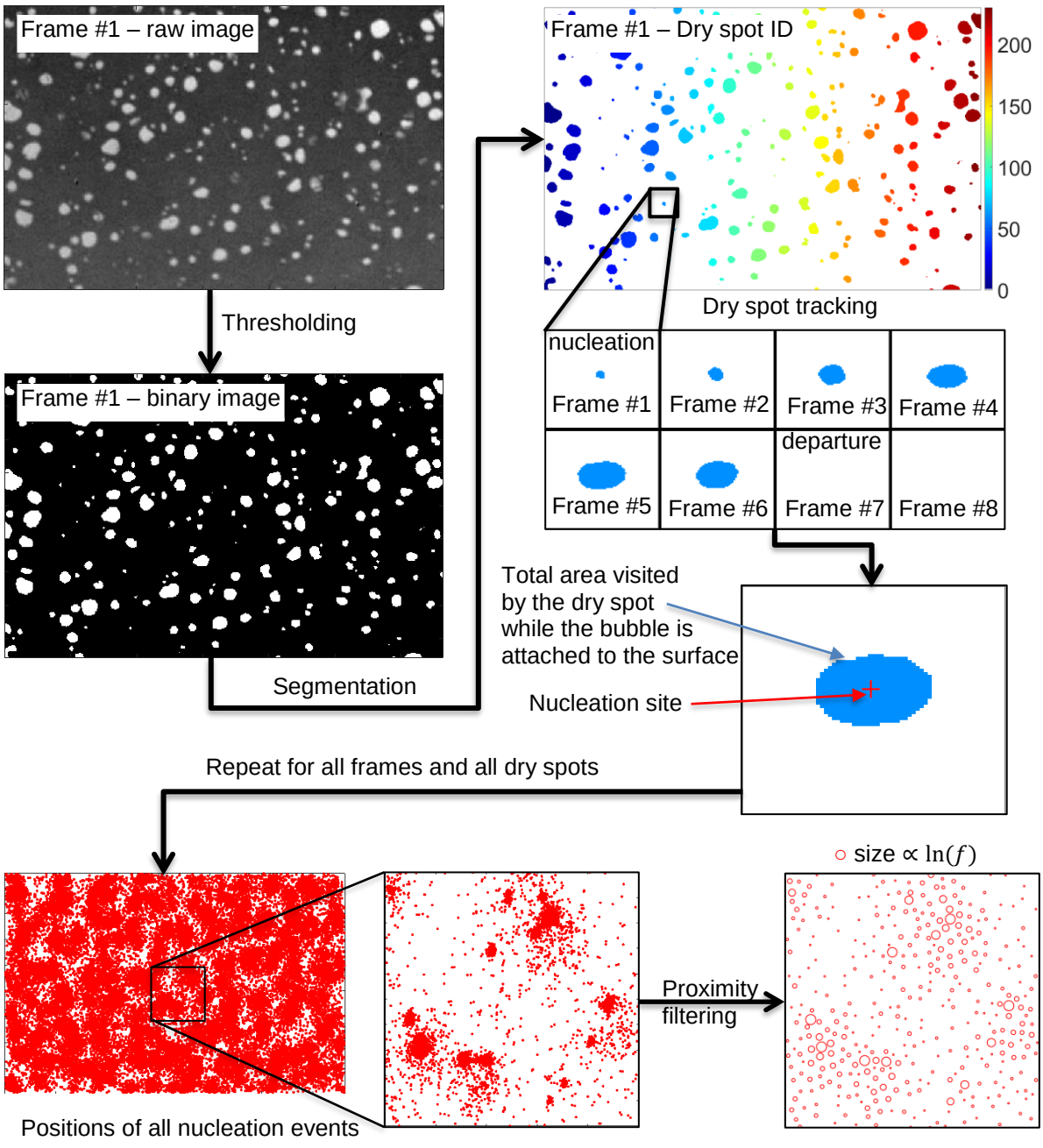

Figure 2-23. Flow chart of the dry area tracking algorithm

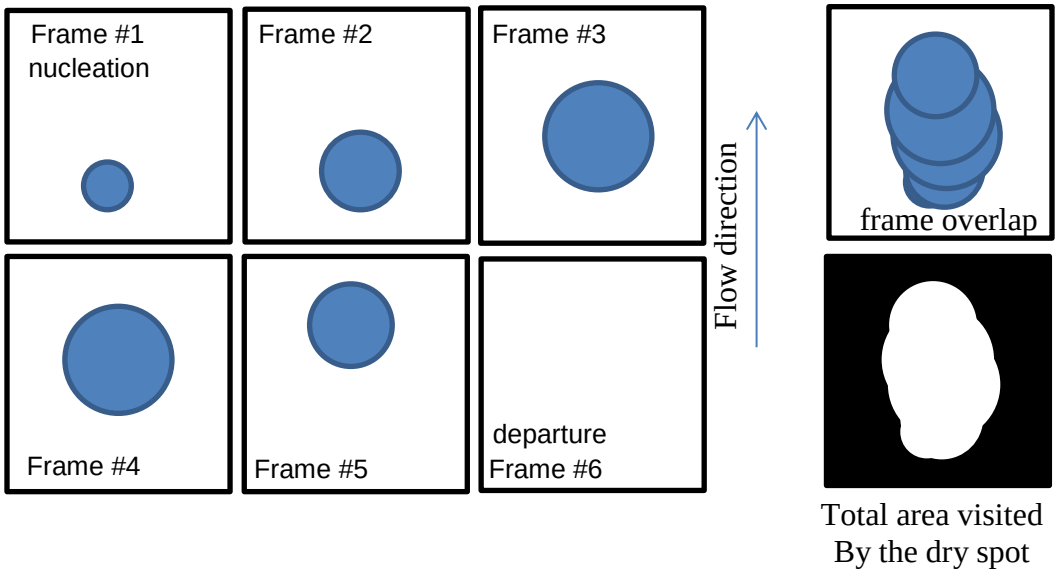

Figure 2-24. Schematic representation of the procedure used to measure the total area visited by the dry spot A_{bub}

2.7.5. System parameters (bulk temperature, system pressure, mass flux, and heat flux)

The uncertainties of the main system parameters are given in Table 2-3. Since the high-pressure test section was used only for pressures higher than 10 bar, the uncertainties differ based on the pressure range.

Table 2-3. Measurement uncertainties		
Parameter	For pressures $\leq$ 10 bar	For pressures $>$ 10 bar
System pressure	$\pm$0.025 bar	$\pm$0.16 bar
Subcooling	$\pm$0.5 °C	$\pm$1.1 °C
Mass Flux	$\pm$10 kg/(m^2-s)	$\pm$20 kg/(m^2-s)
Heat Flux	$\pm$0.1 MW/m^2	

3. BUBBLE DEPARTURE IN PRESSURIZED FLOW BOILING

In this chapter the question of bubble departure is investigated in greater details. First, evidences of vapor clotting in high pressure subcooled flow boiling are presented in Section 3.1. The potential effects of vapor clotting on bubble departure and lift-off are qualitatively demonstrated. With the exception of Section 3.1, this chapter is focused on low heat flux boiling, where isolated bubbles can be observed and their growth and departure quantified. Section 3.2 analyzes bubble growth histories at low and high pressures with the aim to establish the functional relationship between the bubble radius and time elapsed since the bubble nucleation. Such functional relationship allows identification of phenomena that govern bubble growth (i.e. inertia or thermally controlled growth). Next, Section 3.3 uses classical force balance models to examine the importance of different forces acting on a bubble when applied to high pressure boiling. Section 3.3 also examines the direction of forces with respect to the boiling surface specifically for the case of flow boiling on a vertical surface. The competition between sliding and lift-off departure modes is discussed based on both the analytical analysis and experimental evidences. Section 3.4 provides a derivation of a simplified force balance model that can be applied to high pressure flow boiling. The predictions of the force balance model are compared with experimental results. Based on the proposed force balance approach, Section 3.5 develops a criterion for bubble departure diameter in high pressure conditions. Finally, Section 3.6 concludes this chapter by summarizing the results and discussing their implications.

3.1. VAPOR CLOTTING IN HIGH PRESSURE FLOW BOILING

The transition between the isolated bubbles regime to the regime of vapor clotting is best demonstrated by examining shadowgraphic visualizations of the boiling process presented in Figure 3-1. Images shown in Figure 3-1 were captured at 76 bar. At this pressure bubbles depart with diameters in the order of 10 μm (see data of Semeria in Figure 1-3). These small bubbles can be barely seen at the bottom of the heater for low heat fluxes (upper part of Figure 3-1). However, the majority of departed bubbles appear to slide in the vicinity of the boiling surface, as evidenced by the fact that they are growing to larger sizes as they move upwards. These bubbles also coalesce with each other, forming large vapor masses at the upper part of the heater. As the heat flux is increased, such vapor masses become larger, until their projected area covers almost the entire boiling surface (heat flux of 3.07 MW/m^2 in Figure 3-1). In the reminder of this Section we will demonstrate that when the heat flux approaches CHF, all vapor masses can merge together, leading to an almost continuous vapor blanket covering the boiling surface. In the present work we refer to a vapor blanket that is detached from the boiling surface and flowing parallel to it as a "vapor clot". Similar definition was used in the previous studies, although the naming of the phenomenon was different (e.g. "vapor slugs" in the work of Celata et al. [91] and "vapor blanket" in the work of Katto [92]). To the best of the authors' knowledge, the name "vapor clot" was first introduced in the work of Le Corre et al. [29]. The adapted definition does not specify how large should a vapor mass become to be considered as a "vapor clot". Furthermore, Figure 1-3 shows that vapor masses become larger and more connected with higher heat flux. In order to better define the process of vapor clot formation from isolated

bubbles, we will refer to the continuous vapor mass that appears close to CHF as a "vapor clot", while any vapor mass formed by the coalescence of two or more bubbles will be referred to as a "vapor clot precursor".

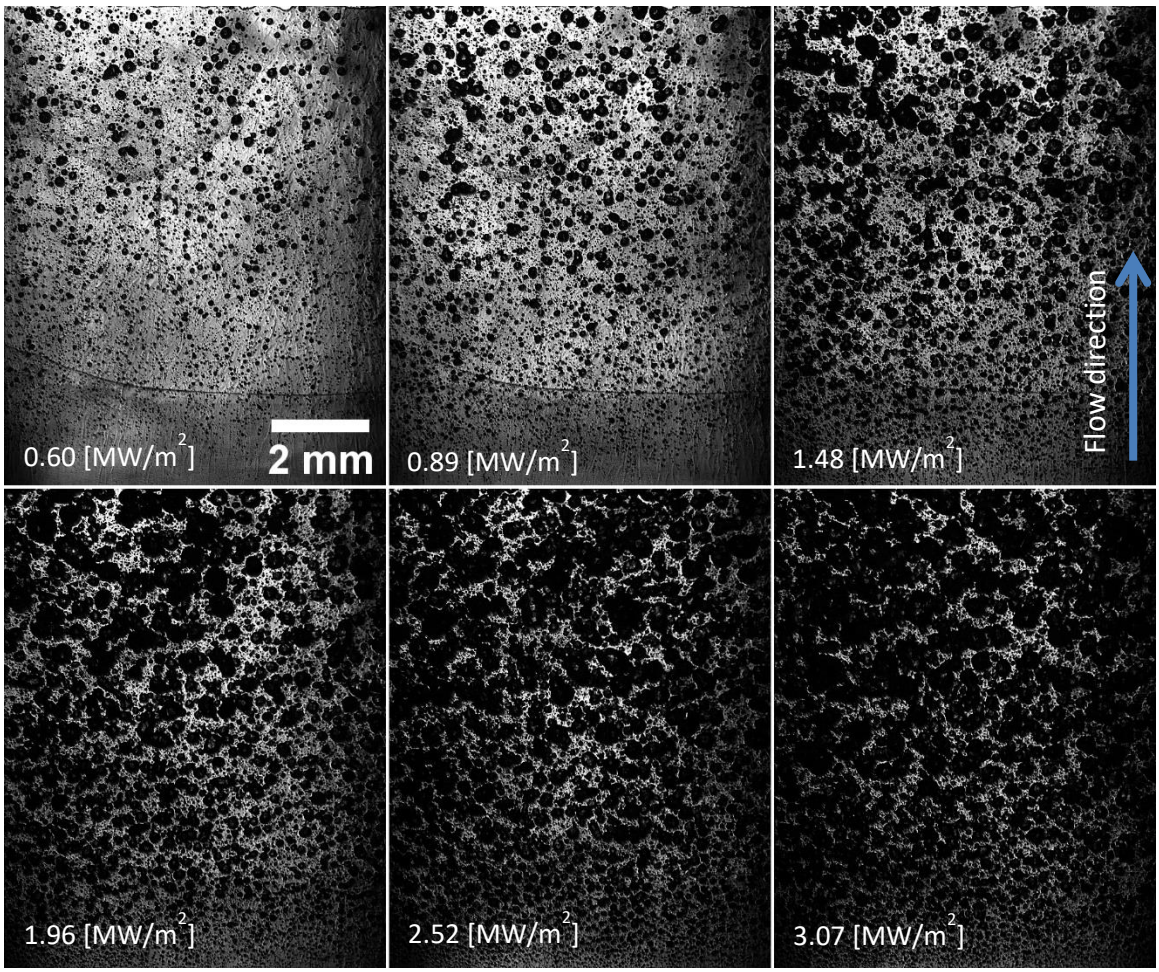

Figure 3-1. Shadowgraphic visualization of flow boiling at 76 bar, 1000 kg/(m^2-s) and 10 ºC of subcooling. The images demonstrate a formation of multiple smaller vapor masses that serve as precursors to a continuous vapor clot that covers the entire boiling surface

More details about the formation and evolution of vapor clots are revealed when phase detection images are examined. Using main and backscattered beams for phase detection (see Figure 2-13) reveals not only the regions of the boiling surface that are dry or covered by microlayers, it also acts similar to shadowgraphic visualization, highlighting projected bubble areas. The distinction between different areas of the boiling surface is demonstrated in Figure 3-2, where dry areas appear as white regions, projected bubble areas appear dark and regions unaffected by vapor clots appear as gray. In Figure 3-3 this visualization technique reveals the development of a vapor clot at different pressures with heat fluxes pushed all the way up to CHF. The last image for each pressure marked as "CHF" shows the distribution of dry areas on the boiling surface right before the formation of an irreversible dry spot. Figure 3-3, shows that the entire boiling surface becomes covered by one continuous vapor clot at high heat fluxes as evidenced by the absence of gray regions

representing uncovered portions of the boiling surface. Similar to observations made in low pressure boiling [28], [93], the passage of a vapor clot or its precursor over the boiling surface does not prevent nucleation, as evidenced by the abundance of dry areas forming under the vapor clot and its precursors. Nevertheless, more research is needed to identify the effect that vapor clotting could have on growth and departure of bubbles.

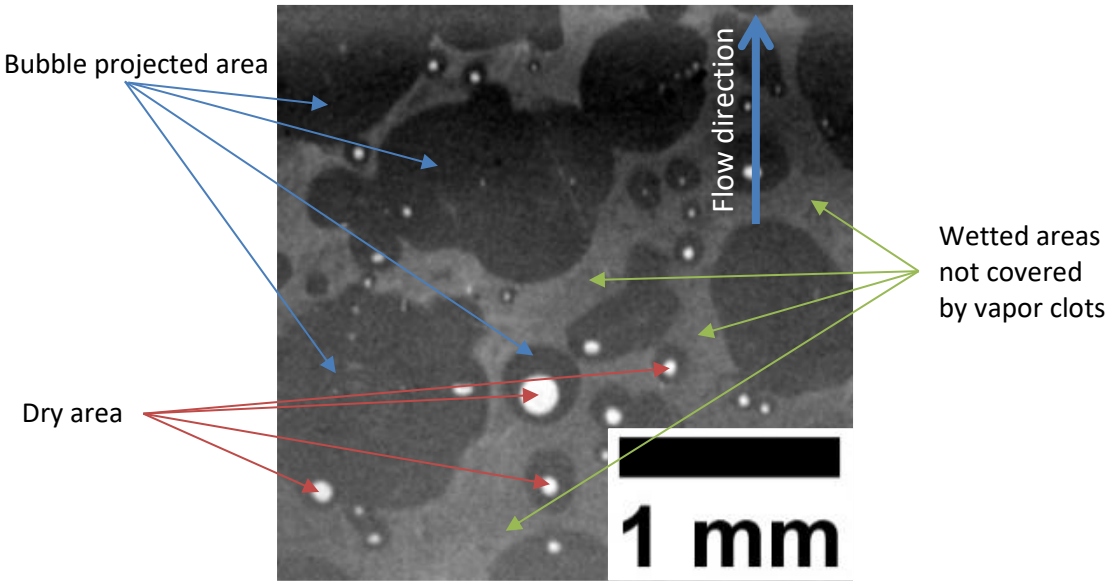

Figure 3-2. Identification of different areas of the boiling surface made possible by the phase detection technique. The image was captured at 10.5 bar, 500 kg/(m^2-s) of mass flux and 10 ºC of subcooling.

While the effect of vapor clotting on bubble departure in high pressure conditions remains uncertain, our data suggests that vapor clots and their precursors may impede the process of bubble sliding. Figure 3-4 demonstrates how a vapor clot precursor consumes a column of sliding bubbles. The column of bubbles can be clearly seen in the first frame (time stamp 0.000). These bubbles are sliding while being attached to the boiling surface as evidenced by bright dry area regions underneath each bubble in a column. Since the vapor clot precursor is positioned further away from the boiling surface than the sliding bubbles, it is exposed to a faster region of the turbulent boundary layer, hence making it move with higher velocity. As the vapor clot precursor catches up with the bubble column it swipes over it, consuming each bubble in the process. The consumption of a bubble can be identified by the disappearance of a dry spot associated with each bubble. This effect should limit the sliding distance for newly departed bubbles, while also increasing the volume of the vapor clot precursor through coalescence. However, the effect it might have on heat transfer is more complicated. While decreasing the sliding distance for bubbles could result in lowering of the heat transfer enhancement associated with sliding (see Sub-Section 1.3.1), the vapor clots could serve as an additional way for boiling to agitate the liquid near the wall, improving the heat transfer. Therefore, the effect of vapor clotting on boiling heat transfer remains uncertain and should be investigated in the future research.

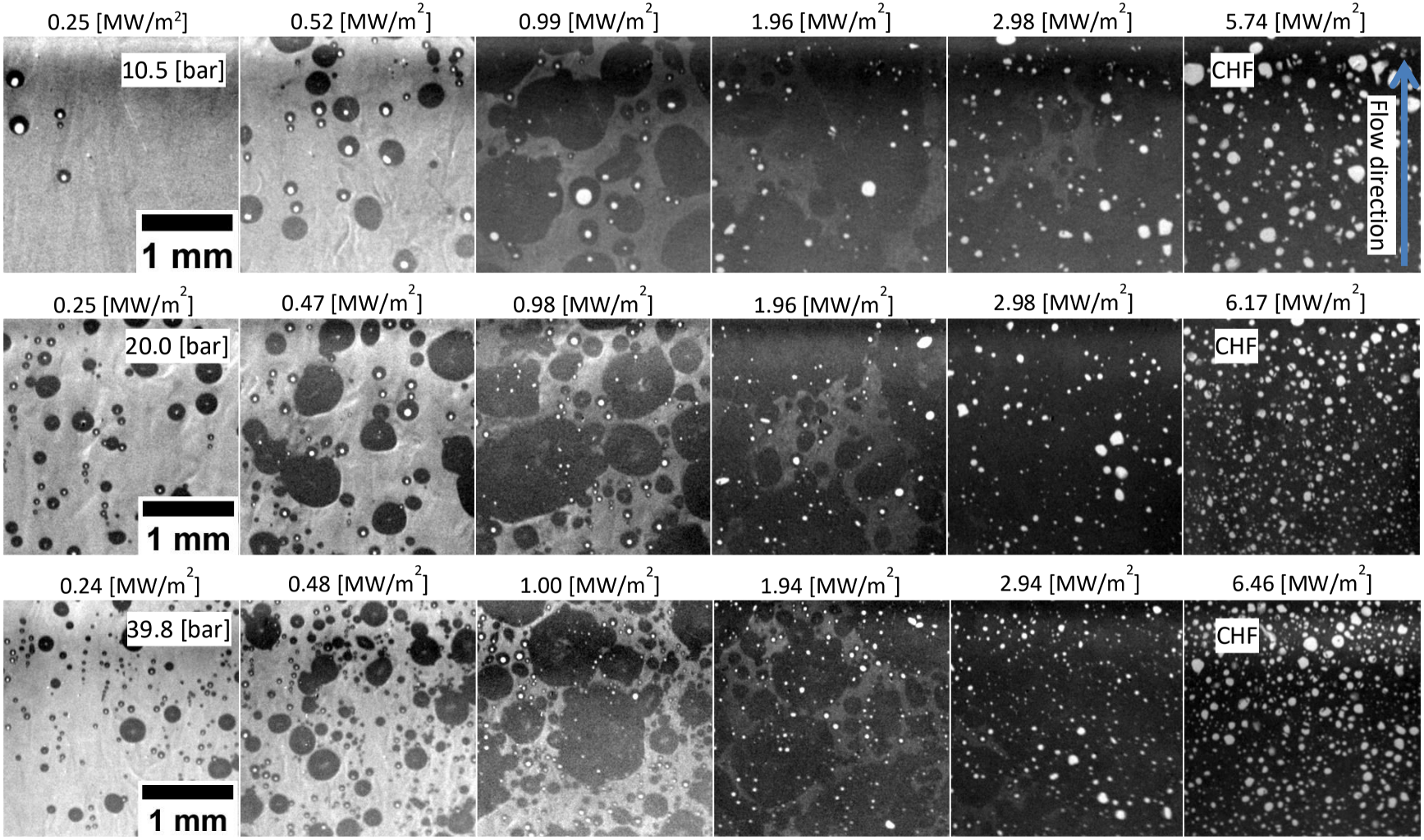

Figure 3-3. Transition from isolated bubble boiling to the regime of vapor clotting for the mass flux of 500 kg/(m^2-s). The boiling surface is almost entirely covered by the vapor clot at 3 MW/m^2, and becomes fully covered as CHF is approached

Figure 3-4. Demonstration of a vapor clot consuming a column of sliding bubbles. Numbers in each frame represent time stamps in ms. The images were captured at 20 bar, 500 kg/(m^2-s) of mass flux and 10 ºC of subcooling

3.2. BUBBLE GROWTH HISTORIES AND THE LIMIT OF INERTIA-CONTROLLED GROWTH PHASE

3.2.1. Theoretical criterion for the limit of inertia-controlled growth phase

Before analyzing the process of bubble departure, it is important to understand which phenomena govern the growth of a bubble at high pressure. Specifically, it should be defined whether the bubble growth is thermally or inertia-controlled. To answer this question, first we analyze a criterion defined in the work of Mikic et al. [94], where a dimensionless time t^+ is said to be much smaller than 1 for inertia-controlled growth and much larger than 1 for thermally controlled growth. Therefore, an approximate boundary between the two regimes could be defined as $t^+ = 1$. The definition of t^+ is given by Equations (3-1) through (3-4)

$$t^+ = \frac{A^2}{B^2} \cdot t \tag{3-1}$$

$$A = \sqrt{\frac{\pi}{7} \cdot \frac{\Delta T \cdot h_{fg} \cdot \rho_g}{T_{sat} \cdot \rho_l}} \tag{3-2}$$

$$B = \sqrt{\frac{12}{\pi} \cdot \alpha_l} \cdot Ja^* \tag{3-3}$$

$$Ja^* = \frac{\Delta T \cdot c_{pl} \cdot \rho_l}{h_{fg} \cdot \rho_g} \tag{3-4}$$

where ΔT is the wall superheat of the liquid that surrounds a growing bubble. ΔT can be approximated as the wall superheat ΔT_w. Starting from the point of bubble nucleation, the time limit indicating the transition between inertia to thermally controlled growth phase is plotted in Figure 3-5 as a function of pressure for several values of the wall superheat. Figure 3-5 shows that even for extremely high wall superheat of 100 ºC, the inertia-controlled growth phase becomes shorter than a microsecond at 10 bar and drops below a nanosecond at 155 bar. This suggests that in high pressure conditions bubble growth is thermally controlled. Therefore, we should expect that the radius of a bubble is proportional to $\sqrt{t}$, where t is the time elapsed since the nucleation of a bubble. In addition to fixing the wall superheats, we can estimate its dependence on pressure by using Jens-Lottes correlation [95] given by Equation (3-5)

$$\Delta T_{w,[°F]} = \frac{60 \cdot \left(\frac{q''_{\left[\frac{Btu}{hr-ft^2}\right]}}{10^6} \right)^{0.25}}{\exp\left(\frac{p_{[psf]}}{900}\right)} \tag{3-5}$$

where imperial units are used and the dimensions of each parameter are shown in square brackets. The heat flux of 0.5 MW/m^2 (0.1585 MBtu/(hr-ft^2)) was used to calculate the wall superheat. This heat flux is close to the ONB heat flux for 1 bar flow boiling with 10 K subcooling. However, since in boiling the wall superheat changes very slowly with heat flux, a particular selection of the heat flux in Equation (3-5) has very small effect on the present analysis. The results obtained with Jens-Lottes correlation are plotted in Figure 3-5, showing that time limit of inertia-controlled growth decreases with pressure at an accelerated rate due to the decrease in wall superheat at higher pressures.

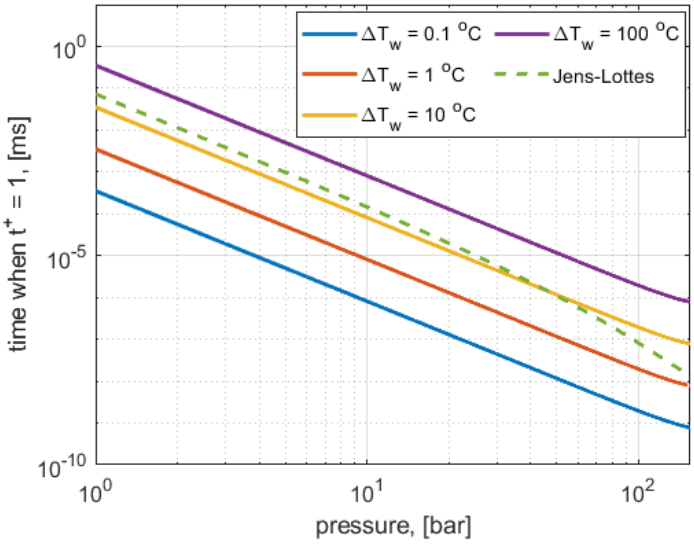

Figure 3-5. Time limit of the inertia-controlled growth for pressures between 1 and 155 bar

3.2.2. Bubble growth histories for low and high pressures

In order to confirm the prediction of Figure 3-5, we can examine experimentally measured bubble growth histories. First, the growth history of an individual bubble in atmospheric pool boiling conditions was captured using the pool boiling apparatus described in Section 2.4. Based on the bottom view of HSV recording, a radius of the bubble as a function of time was measured (Figure 3-6). In Figure 3-6 experimentally measured values are overlaid with two trendlines, indicating two limiting cases: $R \propto t$ for the inertia-controlled growth and $R \propto \sqrt{t}$ for the thermally-controlled growth. Additionally, the limit of the inerta-controlled growth taken directly from the plot in Figure 3-5 is represented as an orange line in Figure 3-6. Clearly the inertia-controlled growth limit presented in Figure 3-5 is a valid criterion for the boundary between two regimes. Figure 3-6 clearly shows that at a time

when $t^+ = 1$ the bubble already deviates from $R \propto t$ trend, while still growing faster than $R \propto \sqrt{t}$ trend. Therefore, a criterion of $t^+ = 1$ serves as a valid boundary between the two growth regimes.

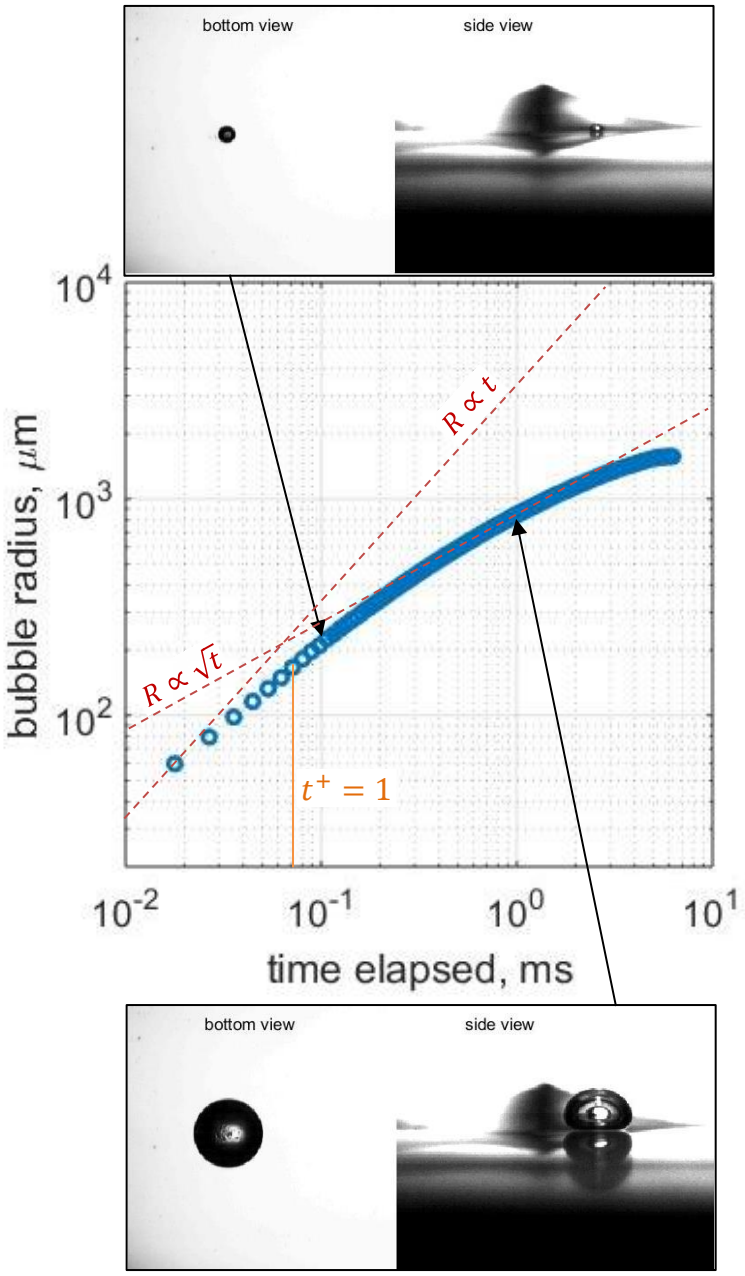

Figure 3-6. Growth history of a bubble in saturated pool boiling of water under atmospheric pressure. The radius is calculated based on the projected bubble area using the images from the bottom view, while ignoring the deformation of the bubble displayed by the side view

In order to fully justify the use of thermally-controlled bubble growth functions, we examine statistically-significant number of bubble growth histories captured at pressures of 20 and 40 bar, 10 ºC of subcooling and mass fluxes of 500, 1000 and 1500 kg/(m^2-s).

For each combination of pressure and mass flux, two different nucleation sites are examined[2]. The bubble tracking algorithm described in Sub-Secction 2.7.1 is applied to each nucleation site and probability density functions (PDFs) of bubble radius as a function of time are reconstructed for each combination of conditions and for each nucleation site. Across all conditions, approximately 15,000 bubbles were tracked, which provides good statistics for judging the mode of bubble growth. The summary of all measurements is presented in Figure 3-7 and Figure 3-8. The solid black line in Figure 3-7 and Figure 3-8 indicates a bubble growth model given by Equation (3-6)

$$R = C_R \cdot B \cdot \sqrt{t} \tag{3-6}$$

where B is given by Equation (3-3) and C_R is a fitting parameter used to match the experimental data. The dashed lines in Figure 3-7 and Figure 3-8 show a $\pm 35\%$ spread in the values of C_R. Such range of C_R captures the statistical spread of the experimental data. The specific values of C_R used in each case are specified in Figure 3-7 and Figure 3-8. Note that with $C_R = 1$, Equation (3-6) will represent Plesset and Zwick relation for the thermally controlled growth phase [94]. It is expected that the radius of a bubble in subcooled flow boiling should be smaller than in the idealized solution of Plesset and Zwick. Therefore, we expect that on average C_R should be less or equal to 1. However, it is more important to ensure that in all cases the radius of a bubble is proportional to the $\sqrt{t}$. This trend is clearly seen in all plots of Figure 3-7 and Figure 3-8, suggesting that thermally controlled growth could serve as a good approximation for high pressure boiling. This mode of bubble growth together with the specified values of the coefficient C_R will be used for further analysis in the subsequent sections.

[2] Only one nucleation site is examined for 20 bar and 1500 kg/(m^2-s) because other nucleation sites in the limited field of view of the HSV camera were not suitable for the bubble tracking algorithm due to the bubble coalescence effects.

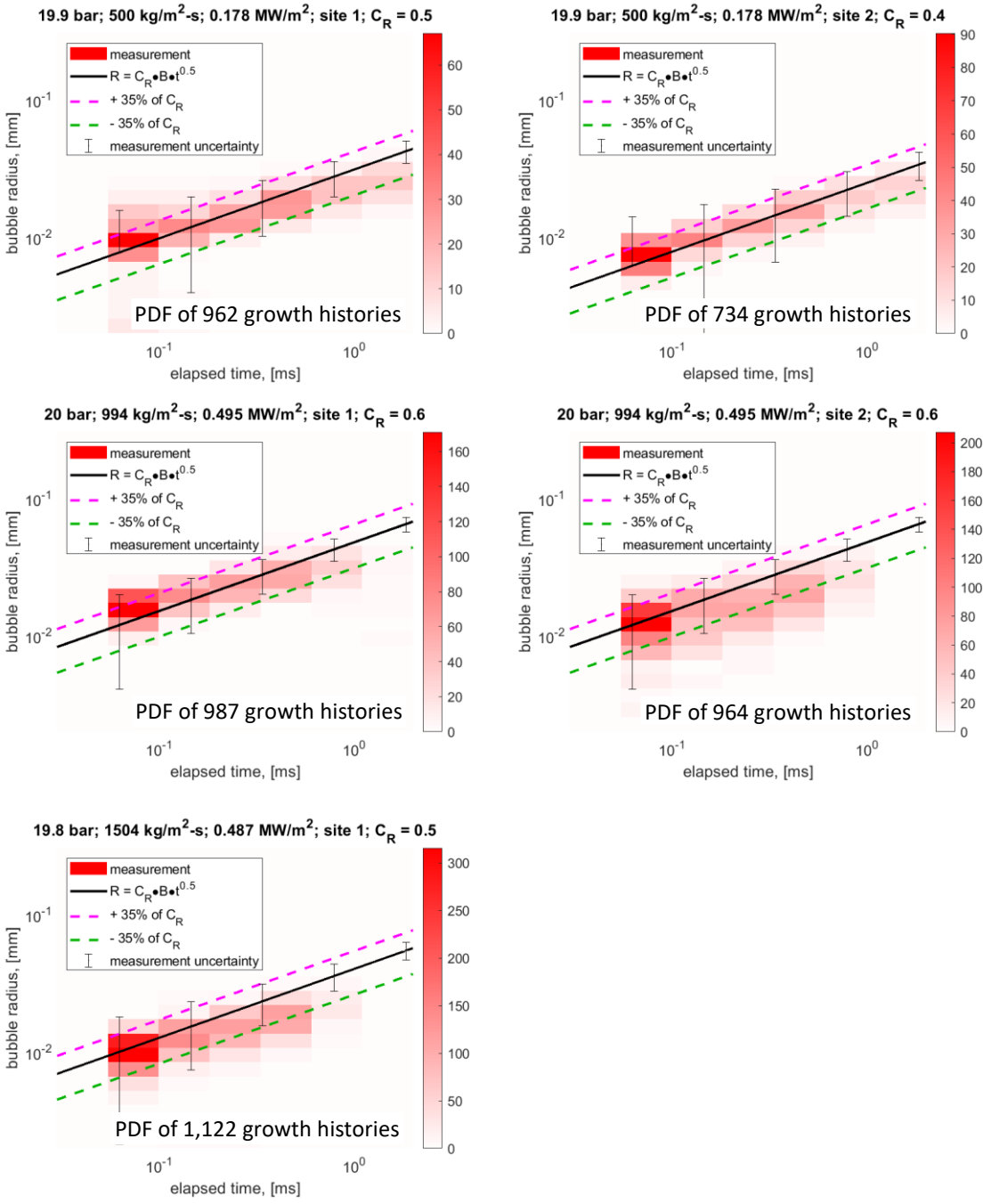

Figure 3-7. Bubble growth histories for the case of 20 bar, 10 ºC of subcooling, 500 (top), 1000 (middle) and 1500 (bottom) kg/(m^2-s) of mass flux. The exact operating conditions for each test are given above each plot

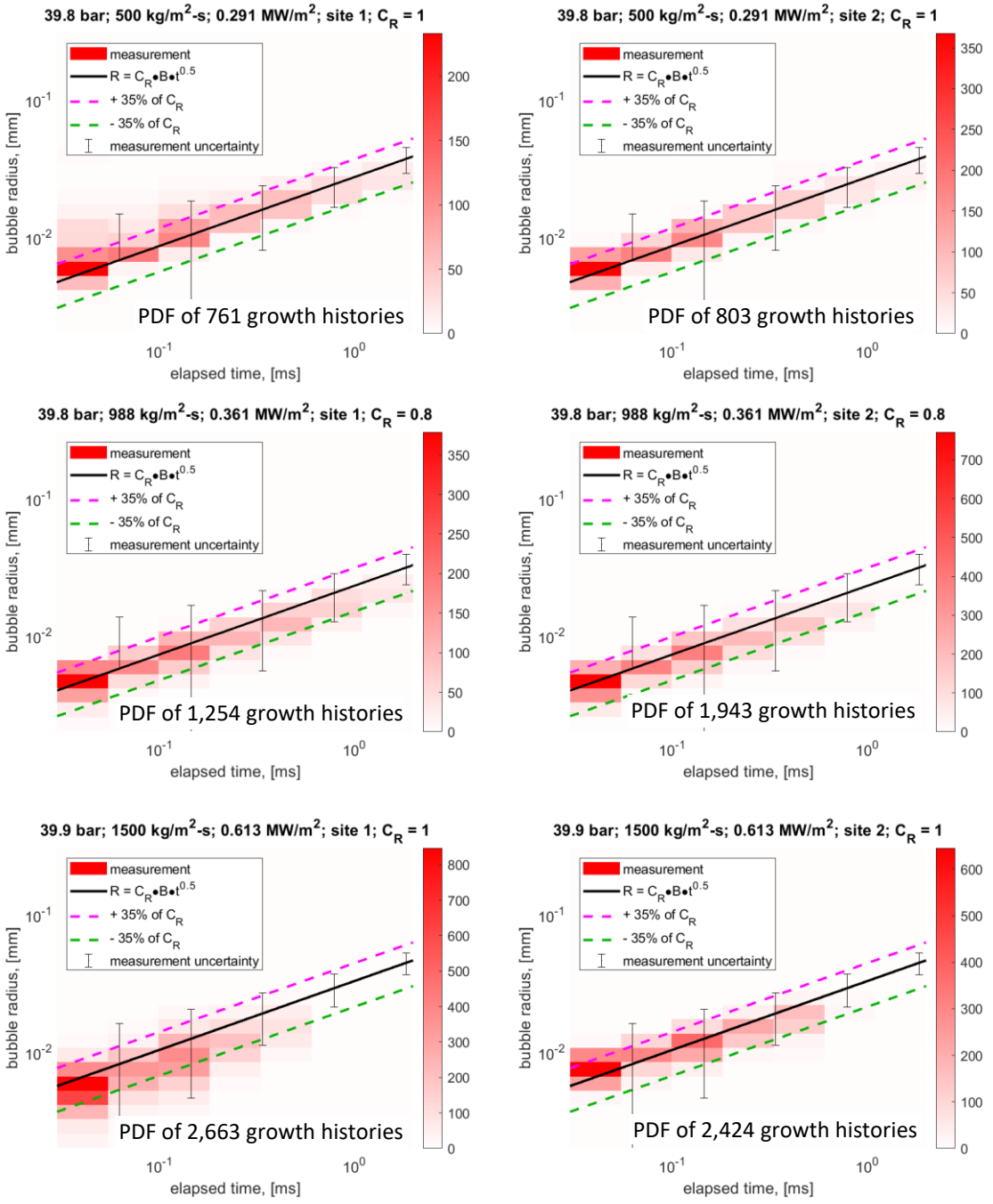

Figure 3-8. Bubble growth histories for the case of 40 bar, 10 ºC of subcooling, 500 (top), 1000 (middle) and 1500 (bottom) kg/(m^2-s) of mass flux. The exact operating conditions for each test are given above each plot

3.3. COMPETITION BETWEEN SLIDING AND LIFT-OFF

Now let us consider a case of flow boiling on a vertically oriented surface. This situation is shown schematically in Figure 3-9. Following the nomenclature presented in Ref. [96], the following forces are shown in Figure 3-9:

- Buoyancy (F_b)
- Drag (F_d)
- Lift (F_l)
- Growth (F_{gr})
- Contact pressure (F_{cp})
- Hydrodynamic (F_h)
- Surface tension (F_{st})

More details about the definition of each force can be found elsewhere ([96], [97]). If a bubble departs by moving in x direction (i.e. along the wall in Figure 3-9), then it is said to depart by sliding. If instead a bubble departs by moving in y direction (i.e. away from the wall in Figure 3-9), then it is said to depart by lift-off. In this Section we will present compelling evidences suggesting that sliding is the only possible mode of bubble departure in high pressure conditions.

According to Figure 3-9 only two forces can prevent a bubble from sliding: growth F_{gr} and surface tension F_{st}. First, consider the surface tension force. The magnitude of the surface tension force in x direction depends on the wetted diameter and the shape of a bubble. An expression to estimate the surface tension force in x direction was proposed by Klausner et al. [97] (Equation (3-7))

$$F_{st} = 1.25 \cdot \pi \cdot D_w \cdot \sigma \cdot \frac{(\theta_\alpha - \theta_\beta)}{\pi^2 - (\theta_\alpha - \theta_\beta)^2} \cdot [\sin(\theta_\alpha) + \sin(\theta_\beta)] \tag{3-7}$$

where D_w is the wetted diameter of a bubble, θ_α and θ_β are advancing and receding contact angles respectively. The first four terms on the RHS of Equation (3-7) quantify the length of the contact line. The longer the contact line, the higher is the surface tension force. The rest of the Equation (3-7) represents the asymmetry in the bubble shape caused by different forces. Such asymmetry is illustrated in Figure 3-9 (left) where the angles of the surface tension force with respect to the x-axis in the upstream and downstream portions of the bubble are drastically different. Such asymmetry creates a net surface tension force in the negative x direction preventing the bubble from sliding. However, we expect that in high pressure boiling the bubbles have much more symmetric and spherical shape, combined with the smaller wetted diameter. In order to characterize the deformation of a bubble we can evaluate the importance of surface tension force compared to buoyancy and viscous forces. Whenever the surface tension is dominant, it will confine a bubble to a spherical shape and remove any asymmetry.

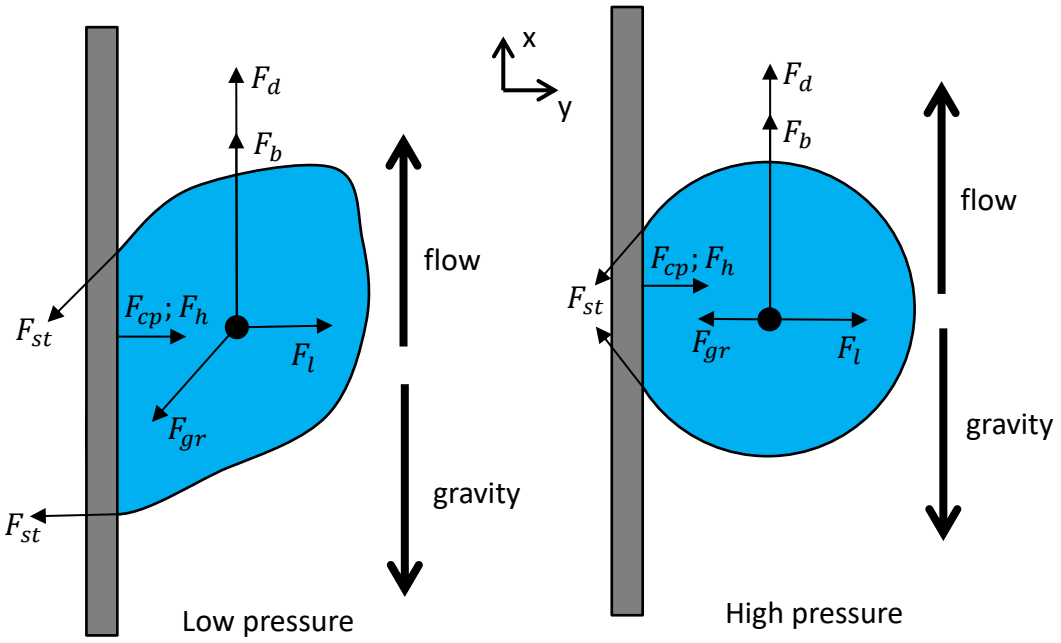

Figure 3-9. Forces acting on a bubble attached to the vertical wall for low pressure (left) and high pressure (right). Flow and gravity have opposite directions

In order to quantify the importance of the surface tension force, we will consider three dimensionless numbers: Bond, Capillary and Weber numbers. The Bond number compares buoyancy and surface tension forces. Bond numbers larger than 1 represent regimes dominated by buoyancy, while bond numbers smaller than 1 represent regimes dominated by surface tension. The expression for the Bond number is given by Equation (3-8)

$$Bo = \frac{(\rho_l - \rho_g) \cdot g \cdot D_b^2}{\sigma} \tag{3-8}$$

where D_b is the diameter of a bubble. An estimate of the bubble diameters at different pressures is given by Cole-Rohsenow correlation, Equation (3-9).

$$D_b = D_{C-R} = 1.5 \cdot 10^{-4} \cdot \sqrt{\frac{\sigma}{g \cdot (\rho_l - \rho_g)}} \cdot \left[\frac{\rho_l \cdot c_{pl} \cdot T_{sat}}{\rho_v \cdot h_{fg}}\right]^{\frac{5}{4}} \tag{3-9}$$

A combination of Equations (3-8) and (3-9) is plotted in Figure 3-10, demonstrating that for all pressures above 1 bar capillary effects are dominant compared to buoyancy.

The Capillary number compares viscous and surface tension forces. Capillary numbers smaller than 1 represent regimes dominated by surface tension. The expression for the Capillary number is given by Equation (3-10)

$$Ca = \frac{\mu_l \cdot u_f(y_{cm})}{\sigma} \tag{3-10}$$

where $u_f(y_{cm})$ is the flow velocity at the distance from the wall y_{cm} equivalent to the center of mass of a bubble. y_{cm} can be approximated as a half of the bubble diameter (see Equation (3-11))

$$y_{cm} = \frac{D_b}{2} = \frac{D_{C-R}}{2} \tag{3-11}$$

The velocity at the center of a bubble can be calculated using law of the wall given by Equation (3-12) [1]

$$u_f^+(y^+) = \begin{cases} y^+; & for\ y^+ \leq 5 \\ 5 \cdot \ln(y^+) - 3.05; & for\ 5 < y^+ \leq 30 \\ 2.5 \cdot \ln(y^+) + 5.5; & for\ y^+ > 30 \end{cases} \tag{3-12}$$

where McAdams correlation [98] was used to calculate the wall shear stress τ_w. Capillary numbers for different mass fluxes and pressures are shown in Figure 3-10 (left). Even at mass fluxes as high as 3600 (i.e. average mass flux of a PWR core [79]) the Capillary number remains much smaller than 1, indicating that surface tension is more dominant than viscous effects for bubble departure in high pressure flow boiling.

The Weber number compares inertia and surface tension forces. Weber numbers smaller than 1 represent regimes dominated by surface tension. The expression for the Weber number is given by Equation (3-14)

$$We = \frac{\rho_l \cdot u_f^2(y_{cm}) \cdot D_b}{\sigma} \tag{3-13}$$

Weber numbers for different mass fluxes and pressures are plotted in Figure 3-10 (right). Figure 3-10 (right) shows that while the Weber number decreases with pressure, for high mass fluxes it can be larger than 1 at all pressures. This result would appear to contradict the hypothesis about the dominance of the surface tension in high pressure flow boiling. However, we believe that at such high mass fluxes the bubble departure diameter will be significantly smaller than the values predicted by Cole-Rohsenow correlation, leading to much smaller values of the Weber number. This assumption will be re-examined in the end of the Chapter, following the demonstration of the effects that the mass flux has on the bubble departure diameter.

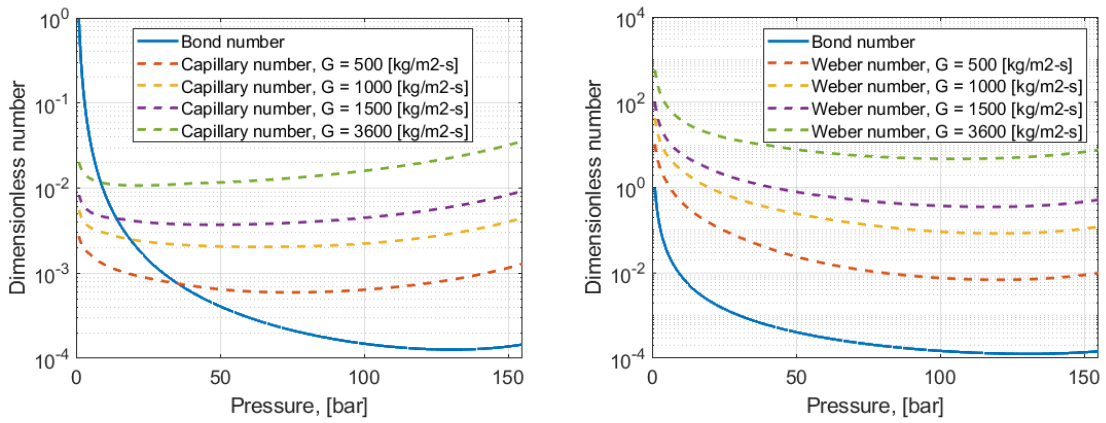

Figure 3-10. Bond and Capillary numbers (left); Bond and Weber numbers (right) for a bubble plotted as a function of pressure and mass flux

Given the results presented in Figure 3-10, we expect the bubbles at high pressures to be almost perfectly spherical, truncated only at the region where they are attached to the wall. Such situation is represented schematically in Figure 3-9 (right). For such a bubble the resulting surface tension force in x direction will be zero. Additionally, the wetted diameter of a bubble should become much smaller at high pressures. This effect is associated with the decrease in contact angle of water with temperature, demonstrated by several studies [99]–[102]. Low contact angle (i.e. high wettability) may hinder the growth of a dry spot underneath the bubble, decreasing the wetted diameter and further diminishing the surface tension force. Therefore, we conclude that the component of the surface tension force in x direction is negligible in high pressure boiling of water on a vertical surface. Notably, the same argument can be made with regards to the growth force. For a symmetrically growing bubble the resulting growth force will be directed towards the wall (Figure 3-9 (right)), making a component of growth force in x direction to be zero. This conclusion has a profound effect on bubble departure. It means that there are no adhesion forces preventing a bubble from sliding immediately after nucleation. Therefore, all bubbles at high pressure should depart by sliding. In the reminder of this Section we present experimental evidences supporting our analysis.

Phase detection images provide a great way to determine bubble departure mode. Figure 3-11 shows the growth and departure of a bubble at 2 bar of pressure visualized by both the side view and the bottom view with phase detection (PD). As the bubble grows and slides near the wall, it remains attached to the surface, forming a footprint consisting of a dry area (solid white regions of the PD image) and a microlayer (areas covered by black and white stripes). The point of lift-off can be defined as the time when the last remnants of the bubble footprint disappear (0.9520 ms in Figure 3-11). Following the footprint disappearance (last 4 frames in Figure 3-11) the bubble rapidly moves away from the boiling surface as demonstrated by the side view. Note that by the time the bubble lifts-off the boiling surface, it had already moved a considerable distance away from the nucleation site, indicating that it had departed by sliding. Figure 3-11 demonstrates that a presence of

a clear bubble footprint in a phase detection image is a sufficient condition for bubble attachment to the boiling surface. Therefore, a bubble that retains a visible footprint while moving away from the nucleation site can be considered as a sliding bubble. However, while the appearance of a bubble footprint is a sufficient condition for bubble sliding, it is not necessary, because a bubble can slide near the wall while trapping a lubrication layer (i.e. a layer of liquid between the wall and a sliding bubble) that is too thick for the phase detection technique to resolve. Therefore, certain bubbles may still slide near the wall while not displaying the footprint on the PD image.

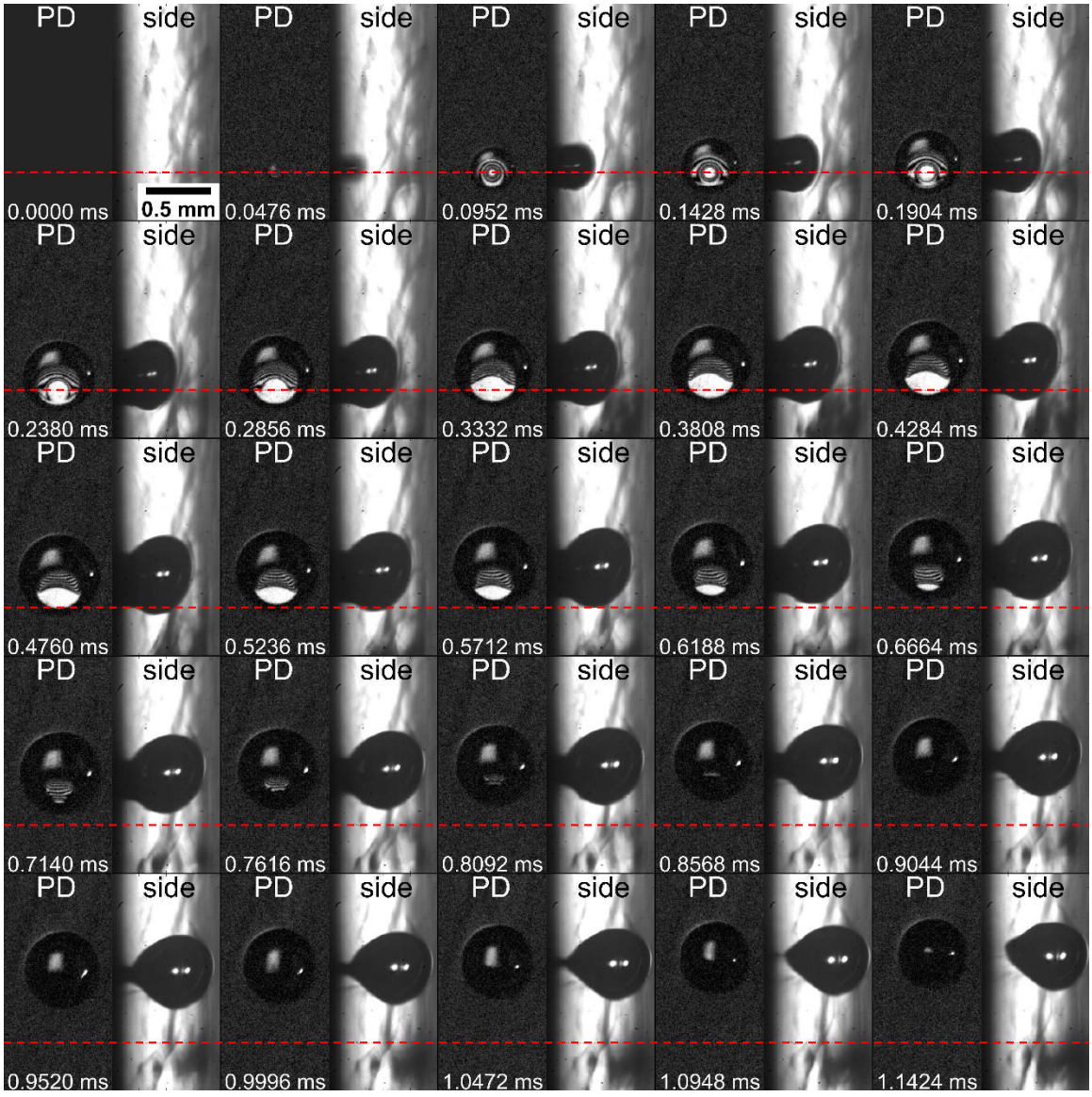

Figure 3-11. A bubble departing by sliding captured at the pressure of 2 bar, mass flux of 759 kg/(m^2-s) and subcooling of 10 ºC

Phase detection images also reveal the prevalence of sliding at higher pressure, namely 10.5 bar (Figure 3-12), 20 bar (Figure 3-13) and 39.8 bar (Figure 3-14). In most cases each

nucleation site creates a bubble column with all bubbles moving at approximately the same velocity. This alone indicates the sliding mode since a bubble that can lift-off the boiling surface will be exposed to the faster region of the turbulent boundary layer and move faster, hence breaking the order of a bubble column. In Figure 3-12, Figure 3-13 (top) and Figure 3-14 (top) the bright spot associated with the bubble footprint is present, providing an additional, more compelling proof of the sliding mechanism than the bubble columns alone. In Figure 3-13 (bottom) and Figure 3-14 (bottom) bubble footprints are not observed, which could be caused by the limited spatial resolution of the optical setup. However, the formation of bubble columns serves as a partial proof of bubble sliding.

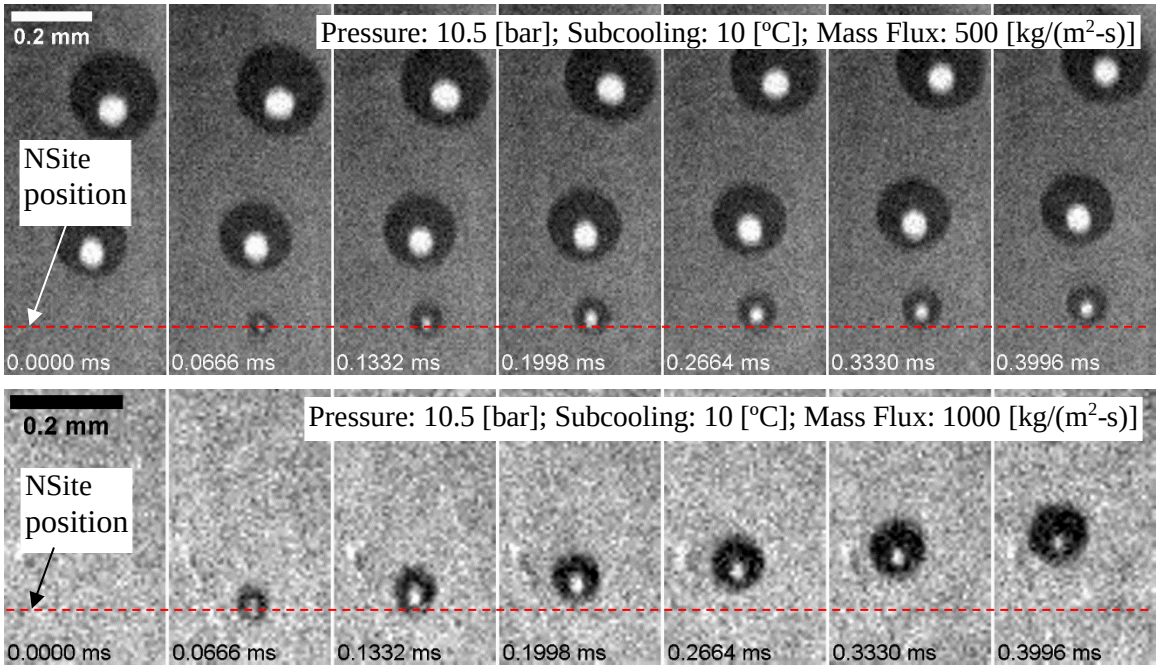

Figure 3-12. Phase detection images of bubbles sliding at 10.5 bar of pressure, 10 ºC of subcooling 500 (top) and 1000 (bottom) kg/(m^2-s) of mass flux

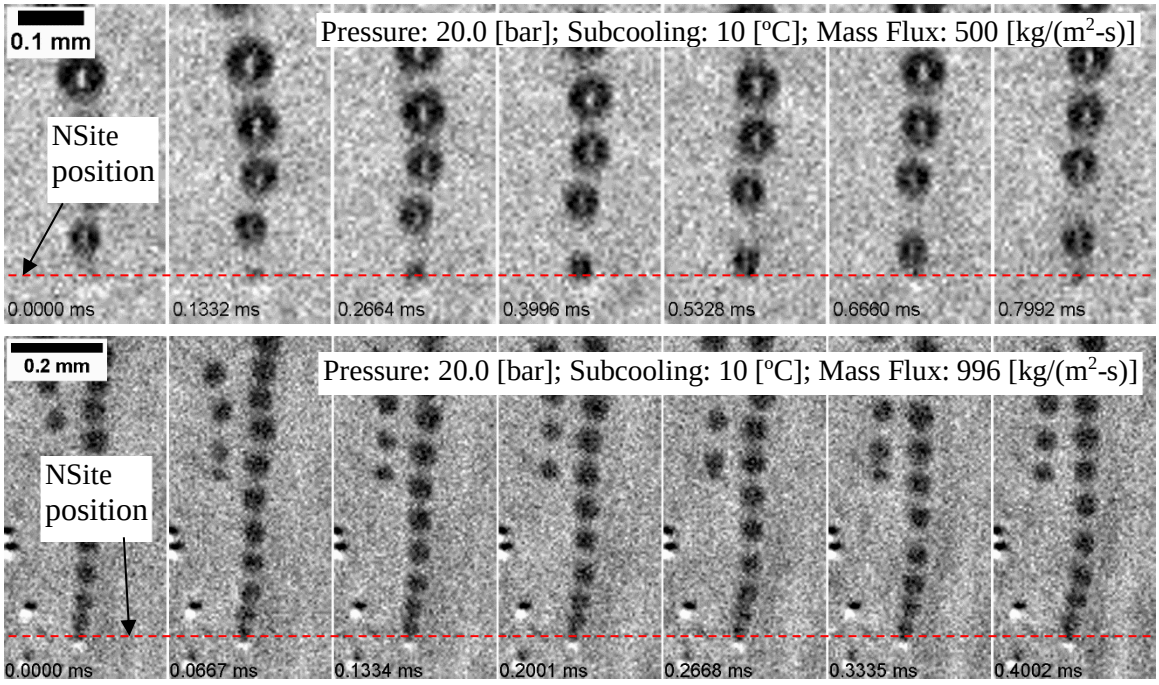

Figure 3-13. Phase detection images of bubbles sliding at 20.0 bar of pressure, 10 ºC of subcooling 500 (top) and 996 (bottom) kg/(m^2-s) of mass flux

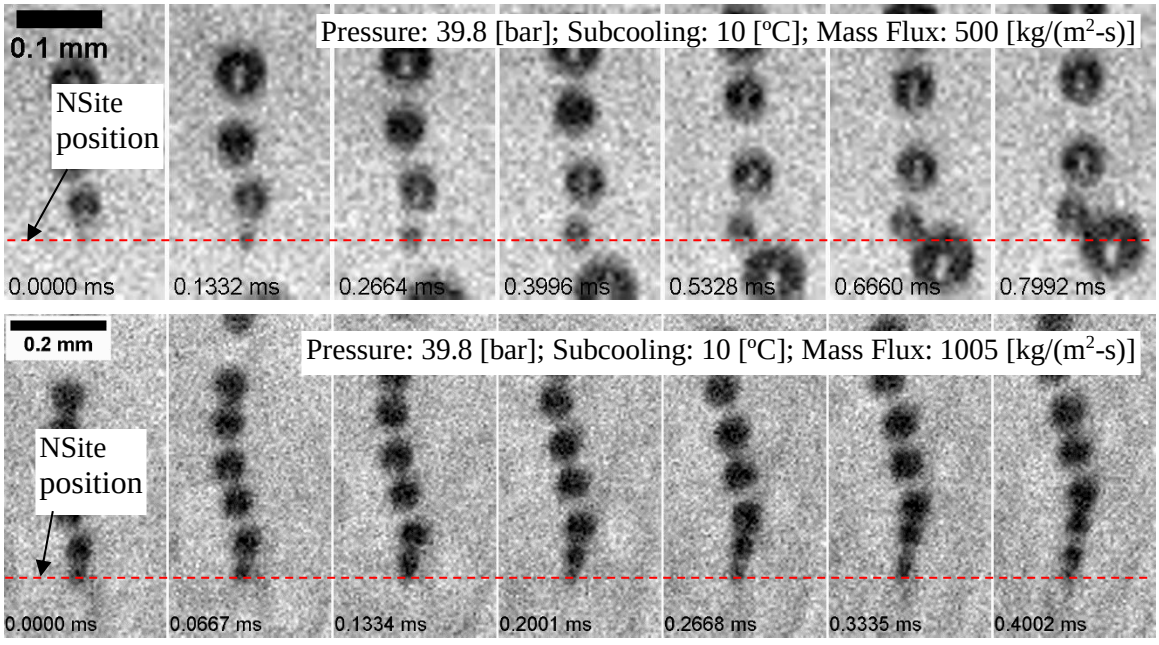

Figure 3-14. Phase detection images of bubbles sliding at 39.8 bar of pressure, 10 ºC of subcooling 500 (top) and 1005 (bottom) kg/(m^2-s) of mass flux

The evidence presented in this section leads to a profound conclusion: there is nothing holding a bubble attached to the nucleation site in high pressure flow boiling on the vertical wall. The components of growth force and surface tension force directed parallel to the boiling wall will become negligible when pressure is increased. On the one side, it makes

the analysis of bubble departure much easier than in the case of low pressure. Not only the bubble shape remains spherical, removing uncertainties associated with bubble deformation, but also several forces (i.e. growth and surface tension) can be neglected, removing the need for heavy empiricism that is normally present when describing these forces within a force balance framework. On the other side, the absence of any adhesion force makes it very challenging to define the point of bubble departure since the departure begins immediately after the nucleation. In the next two sections we will present a simplified force balance model that provides an accurate description of bubble movement during sliding in high pressure flow boiling. The force balance model is followed by the development of a criterion for bubble departure in high pressure boiling and its use to predict bubble departure diameters.

3.4. SIMPLIFIED FORCE BALANCE APPROACH TO DESCRIBE BUBBLE DEPARTURE PROCESS AT HIGH PRESSURE

In this section a simplified force balance approach is used to quantify the movement of a bubble on the boiling surface following nucleation. The initial portion of the derivation is identical to Ref. [12] and will not be duplicated here. Consider a bubble growing on a vertical wall in a non-uniform flow velocity field directed upwards (i.e. against the gravity) (see Figure 3-15). After neglecting the contributions from asymmetric evaporation and the rocket effect (see Ref. [12] for more details), the momentum balance on a bubble can be represented by Equation (3-14)

$$\rho_g \cdot V_b \cdot \frac{d\vec{u}_{cm}}{dt} = \iiint_{V_b} (\rho_g - \rho_l) \cdot \vec{g} \cdot dV + \oint_{CL} \sigma \cdot \vec{t}_\sigma \cdot dL - \iint_{A_{fp}} (p_{g,b} - p_r) \cdot \vec{n} \cdot dA + F_{h,tot} \qquad (3\text{-}14)$$

Where $\vec{u}_{cm}$ is the center of mass velocity of the bubble, CL is the triple contact line at which the bubble is attached to the wall, $p_{g,b}$ is the vapor pressure at the bubble footprint, p_r is the liquid pressure at some reference point and $F_{h,tot}$ is the total hydrodynamic force acting on a bubble. The first term on the RHS of Equation (3-14) represents the buoyancy force, the second term represents the surface tension force and the third term represents the contact pressure force. In this analysis we are interested in the momentum balance in x direction. Since the contact pressure force is directed normal to the boiling surface, it can be neglected. The surface tension force in x direction is also zero (see previous section for detailed discussion). The only contribution to the total hydrodynamic force that is left is the quasi-steady drag induced by the flow. Introducing these simplifications gives us Equation (3-15)

$$\rho_g \cdot V_b \cdot \frac{du_{cm}}{dt} = \iiint_{V_b} (\rho_l - \rho_g) \cdot g \cdot dV \pm \frac{1}{2} \cdot C_D \cdot \pi \cdot \rho_l \cdot R_b^2 \cdot \left(u_f(y_{cm}) - u_{cm}\right)^2 \qquad (3\text{-}15)$$

where R_b is the radius of a bubble, $u_f(y_{cm})$ is the flow velocity at the bubble's center of mass, given by the law of the wall (Equation (3-12)), C_D is the drag coefficient given by Equation (3-16) adapted from [43]

$$C_D = 1.13 \cdot \frac{24}{Re_b} \cdot (1 + 0.104 \cdot Re_b^{0.753}) \tag{3-16}$$

where Re_b is the Reynolds number for a bubble, given by Equation (3-17)

$$Re_b = \frac{\left|u_f(y_{cm}) - u_{cm}\right| \cdot 2 \cdot R_b}{\nu_l} \tag{3-17}$$

where ν_l is the kinematic viscosity of the liquid. The "+" or "-" sign in Equation (3-15) represents the direction of drag force. If the velocity of the bubble is smaller than the velocity of the flow, then the drag force will be co-directional with the buoyancy, resulting in the "+" sign. The opposite situation occurs when the bubble is moving faster than the flow, in which case the drag force will be directed opposite to the buoyancy, slowing the bubble down. In the present analysis we ignored the virtual mass force, assuming that it has very small effect on the final result. The importance of the virtual mass force will be analyzed in the future work. Additionally, we assumed that the bubble is nearly spherical, meaning that the wall distance at which the bubble's center of mass is located is approximately equal to the bubble radius (Equation (3-18)).

$$y_{cm} \cong R_b \tag{3-18}$$

Note that either when the bubble is attached to the wall during growth or when the density of the vapor is low compared to the density of the liquid, the change of the bubble momentum can be neglected, setting the LHS of Equation (3-15) to zero. Neither of these conditions are valid for high pressure. Not only the density of vapor becomes much higher as the pressure increases, but also the bubble is likely to start moving immediately after nucleation as was discussed in the previous Section. Therefore, LHS of Equation (3-15) cannot be neglected in the present analysis. The importance of the inertia force will be demonstrated at the end of the present Section.

Equation (3-15) can be further simplified by integrating the buoyancy force over the volume of the bubble and isolating the acceleration term on the LHS, giving us Equation (3-19).

$$\frac{du_{cm}}{dt} = \frac{(\rho_l - \rho_g)}{\rho_g} \cdot g \pm \frac{1}{2} \cdot C_D \cdot \pi \cdot \frac{\rho_l}{\rho_g} \cdot \frac{R_b^2}{V_b} \cdot \left(u_f(y_{cm}) - u_{cm}\right)^2 \tag{3-19}$$

Under the assumption of a spherical bubble, the bubble volume can be expressed by Equation (3-20).

$$V_b = \frac{4}{3} \cdot \pi \cdot R_b^3 \tag{3-20}$$

Substituting Equation (3-20) into (3-19) gives us Equation (3-21)

$$\frac{du_{cm}}{dt} = \frac{d^2 x_{cm}}{dt^2} = \frac{(\rho_l - \rho_g)}{\rho_g} \cdot g \pm \frac{3}{8} \cdot C_D \cdot \frac{\rho_l}{\rho_g} \cdot \frac{1}{R_b} \cdot \left(u_f(y_{cm}) - u_{cm}\right)^2 \tag{3-21}$$

Equation (3-21) is an ordinary differential equation (ODE), and it can be solved if the bubble radius as a function of time (i.e. $R_b = f(t)$) is known. Solving Equation (3-21) allows us to calculate bubble pathlines, describing the distance that a bubble has traveled from the nucleation site as a function of time. This distance can be readily measured with the bubble tracking algorithm (Sub-Section 2.7.1). Such measurements for pressures of 20 and 40 bar and mass fluxes of 500, 1000 and 1500 kg/(m^2-s) are presented in Figure 3-16 and Figure 3-17 together with solutions of Equation (3-21). Equation (3-21) was solved numerically using a built-in Matlab® function for ODEs. The initial conditions for Equation (3-21) are given in Equation (3-22)

$$\begin{cases} u_{cm}(t = 0) = 0 \\ x_{cm}(t = 0) = 0 \end{cases} \tag{3-22}$$

The relationship between the radius of a bubble and time since the nucleation was already established in Section 3.2 where it was demonstrated that the bubble growth can be approximated as thermally controlled (i.e. $R \propto \sqrt{t}$) with the addition of the coefficient C_R which value was established for each combination of operating conditions and each nucleation site considered. Solutions to Equation (3-21) calculated with the values of C_R specific for each case are shown in Figure 3-16 and Figure 3-17 as solid black lines. Dashed magenta and green lines represent the change in the integral that corresponds to the variation of the bubble radius by 35% (i.e. approximating the spread of the bubble radius measurements). This variation is also plotted as the dashed lines with the same colors in Figure 3-7 and Figure 3-8. Figure 3-16 and Figure 3-17 shows that the solution to Equation (3-21) has a remarkably good agreement with the actual data, demonstrating that indeed there is no adhesion force acting in x direction that could prevent a bubble from sliding. Additionally, accounting for the statistical variation in measured bubble radii also captures the variation in bubble pathlines (dashed lines in Figure 3-16 and Figure 3-17). The worst agreement is achieved for the pressure of 19.9 bar and the mass flux of 500 kg/(m^2-s). We speculate that at such conditions a bubble grow to a sufficiently larger size to stop it from being perfectly spherical and symmetric, which may bring its center of mass closer to the boiling surface or allow for a small contribution from the surface tension force. However, it is important to empathize that the agreement between the data and the model is best when the bubble is still very close to the nucleation site (i.e. small values of elapsed time in Figure 3-16 and Figure 3-17). Good performance in this region is crucially important for the prediction of bubble departure diameter discussed in the next section.

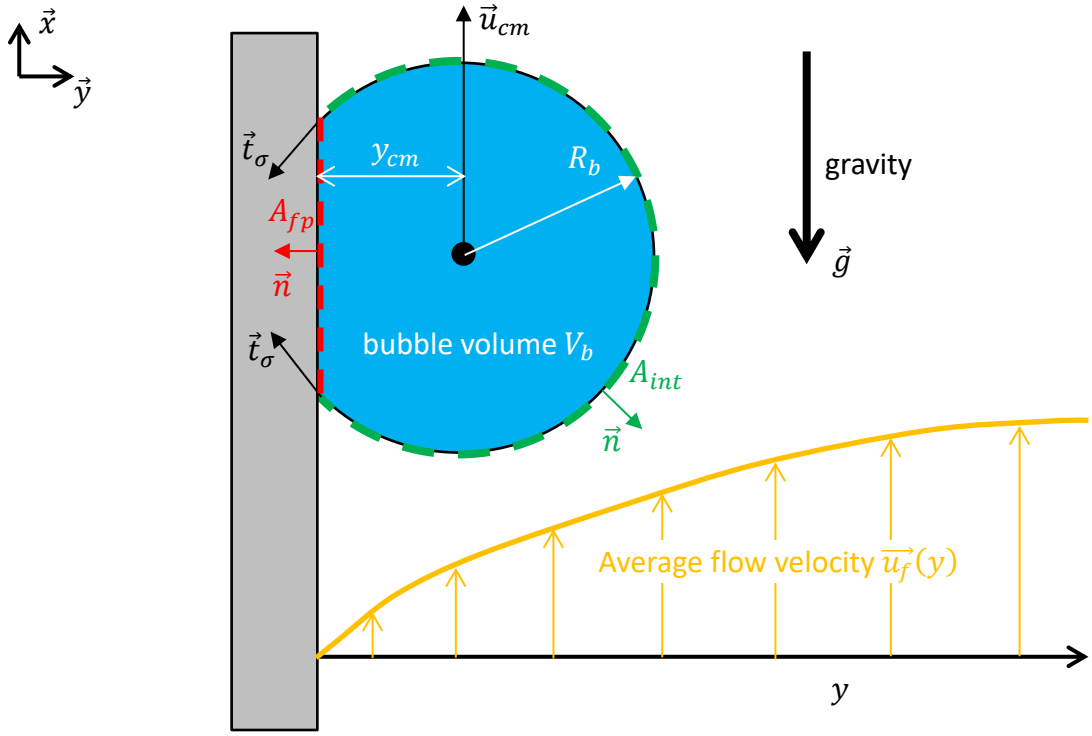

Figure 3-15. Control volume representation of a bubble in high pressure conditions

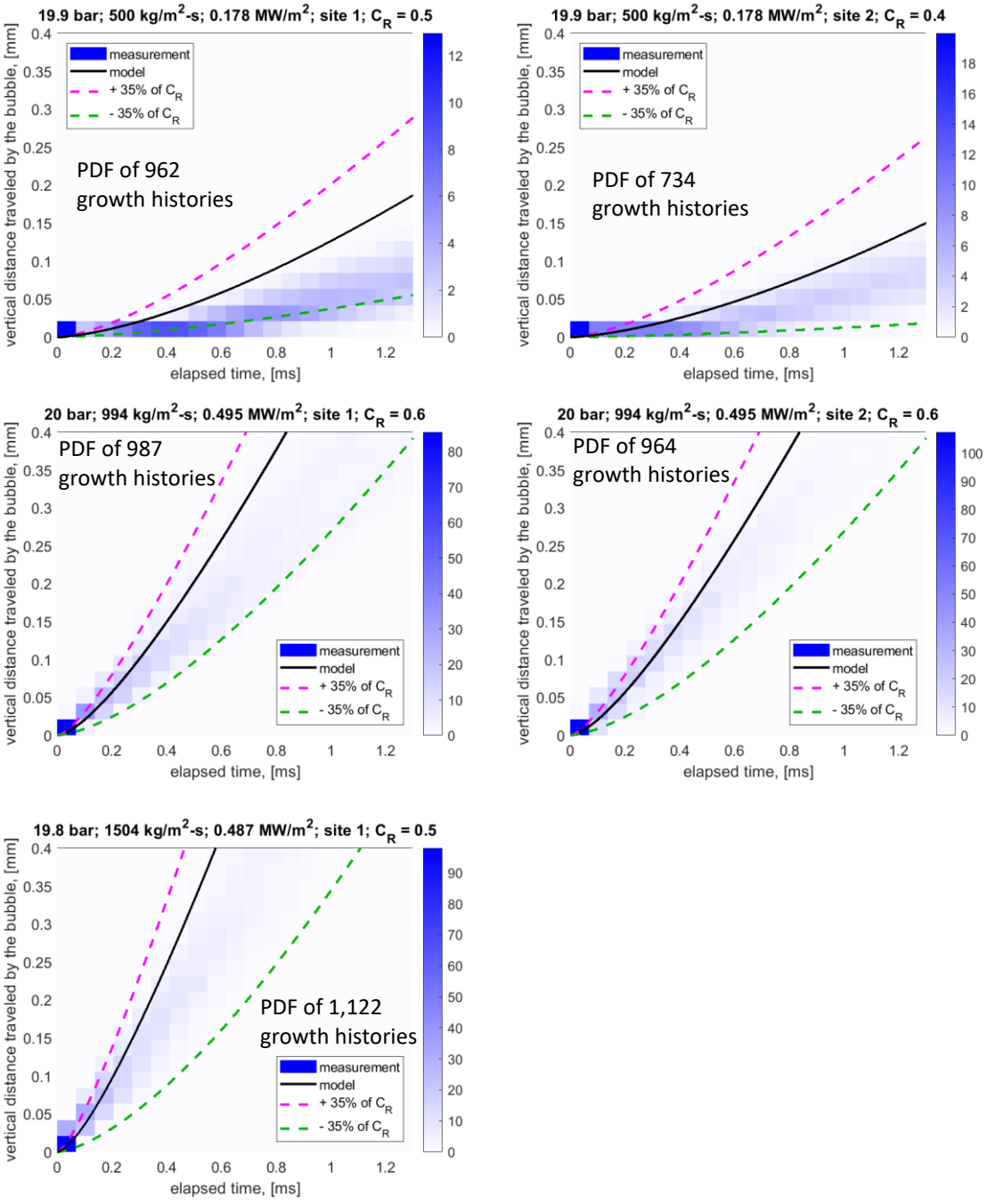

Figure 3-16. PDFs of measured bubble pathlines overlaid with the integral of Equation (3-21) for the pressure of 20 bar. Equation (3-6) was used to prescribe bubble growth histories with the values of the coefficient C_R written in each plot and being identical to Figure 3-7. Dashed lines were calculated using a $\pm$ 35% variation of the coefficient C_R and correspond to the dashed lines of identical colors in Figure 3-7

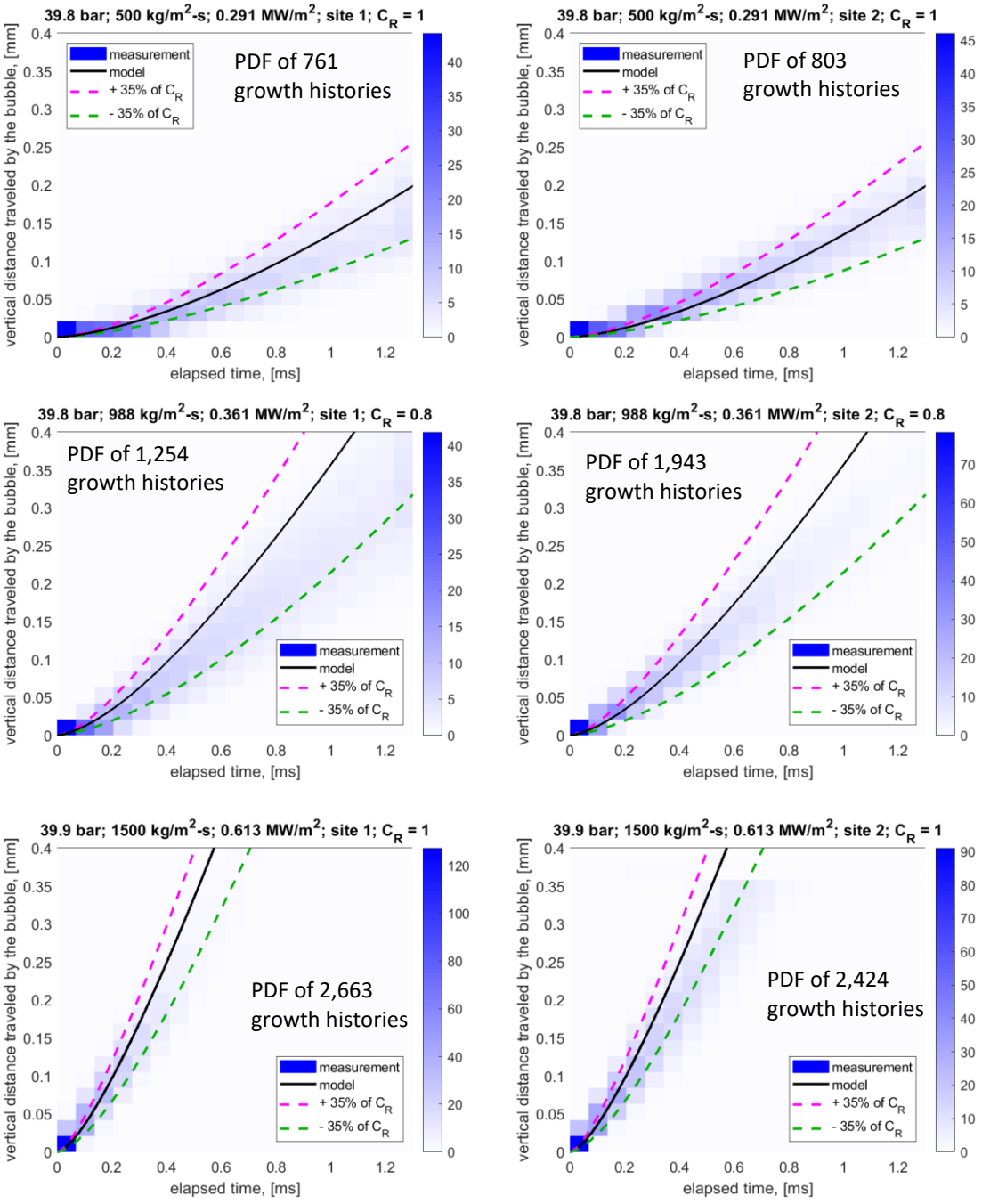

Figure 3-17. PDFs of measured bubble pathlines overlaid with the integral of Equation (3-21) for the pressure of 40 bar. Equation (3-6) was used to prescribe bubble growth histories with the values of the coefficient C_R written in each plot and being identical to Figure 3-8. Dashed lines were calculated using a $\pm$ 35% variation of the of the coefficient C_R and correspond to the dashed lines of identical colors in Figure 3-8

Finally, we can demonstrate the importance of the inertia force by estimating its value in relation to the other two forces. The magnitudes of forces are shown in Figure 3-18 for the

pressure of 20 bar, mass flux of 994 kg/(m^2-s) and the heat flux of 0.495 MW/m^2. Figure 3-18 shows that inertia force is higher than drag and buoyancy forces for the first 0.2 ms after nucleation. It will be shown in the next Section, that for the system parameters shown in Figure 3-18, the departure of a bubble happens within the time period of 0.1 – 0.2 ms, making inertia especially relevant for bubble departure calculations. Note that the drag force becomes negative for times longer than 0.2 ms, indicating that the velocity of a bubble exceeded the local flow velocity due to the additional acceleration induced by buoyancy.

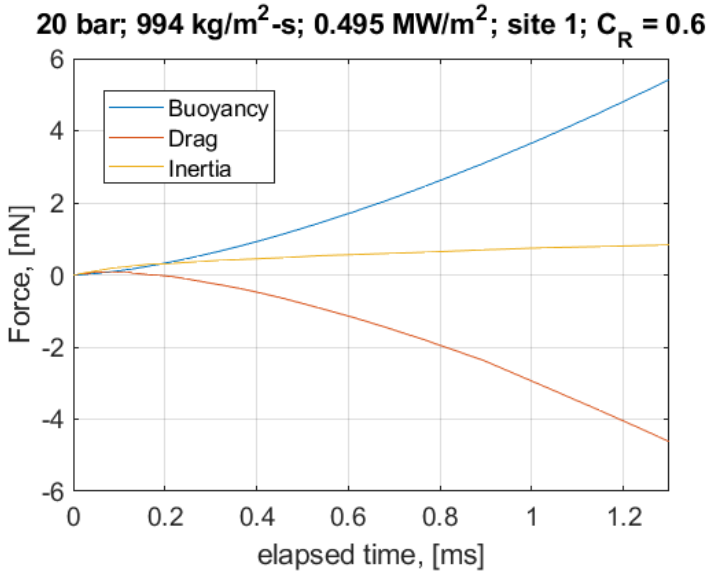

Figure 3-18. Magnitudes of buoyancy, drag and inertia forces calculated for the pressure of 20 bar, mass flux of 994 kg/(m2-s), and heat flux of 0.495 MW/m2. The values of velocities used in the calculation are based on the solution for bubble pathlines (Equation (3-21))

3.5. PROPOSED CRITERION FOR BUBBLE DEPARTURE AT HIGH PRESSURE

In the previous section we have demonstrated that the absence of adhesion forces causes a bubble to depart by sliding immediately after nucleation. This conclusion makes the departure diameter undefined because the bubble keeps growing as it is accelerating by buoyancy and drag. Therefore, it is useful to define a criterion that will indicate bubble departure independently of pressure, mass flux and other system parameters, while also predicting departure diameters that are in a reasonable agreement with the available data. The proposed criterion is illustrated in Figure 3-19, depicting a bubble growth and departure process captured in subcooled flow boiling at 1.12 bar of pressure. The departure criterion is set to be the point when the bubble projected area is no longer covering the nucleation site. Visually this criterion is presented in the HSV images of Figure 3-19, where the bubble is first covering the nucleation site (0.05 and 0.38 ms) and later moves past it (0.71 ms). The moment when the utmost upstream boundary of the bubble's projected area moves past the nucleation site, the bubble is considered to be departed. For a spherical bubble, the same departure criterion can be expressed mathematically by Equation (3-23).

$$x_{cm}(t) = R_b(t) \tag{3-23}$$

Equation (3-23) provides a criterion based on the intersection of two curves: bubble radius and position. Such criterion is also illustrated in Figure 3-19 (right), where the intersection of the two curves is marked by the black dot, indicating the point of departure. This procedure was used to measure the departure diameter of each bubble tracked by the bubble tracking algorithm. The intersection of the two curves was determined using linear interpolation. While the proposed departure criterion might appear arbitrary, it was chosen with the intent to ensure the correct limit for the bubble wait time. Since a new bubble can form at the nucleation site only when it is not affected by other bubbles, the proposed criterion will ensure that the formation of a new bubble is possible immediately after bubble departure (i.e., at the end of the growth phase), ensuring that the wait time will approach zero at the limit when the barrier to bubble nucleation is negligible. Nevertheless, the proposed criterion presumes that a new bubble cannot nucleate while a portion of another bubble is covering the nucleation site. Such assumption is not strictly correct since only the bubble footprint, which is smaller than the bubble itself, can prevent further nucleation. However, since it was not possible to fully quantify the relative size of the bubble footprint in the present study, we presume that the proposed departure criterion provides the best approximation for the point of bubble departure in the absence of reliable bubble footprint size measurements.

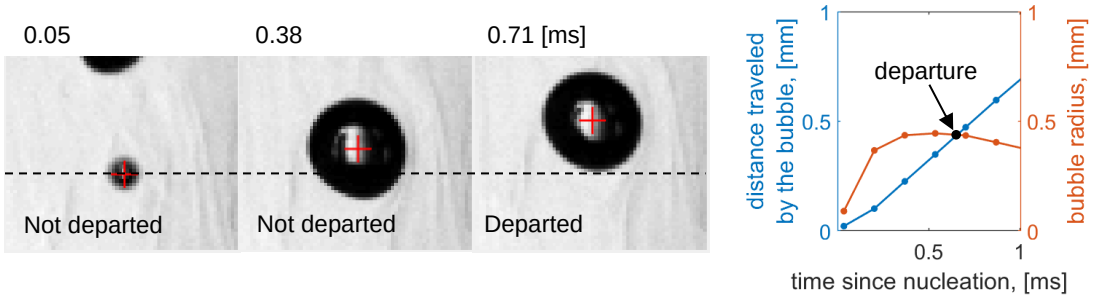

Figure 3-19. Proposed departure criterion illustrated by the bubble departure process captured at the pressure of 1.12 bar, mass flux of 1000 kg/(m^2-s), subcooling of 10 ºC and heat flux of 0.77 MW/m^2

The criterion of Equation (3-23) can also be combined with the solution to Equation (3-21) in order to predict the bubble departure diameter. The process of intersecting the curve that specifies bubble radius with the curve that specifies the distance that the bubble have traveled is shown in Figure 3-20 for two values of the coefficient C_R: 0.5 and 1. This range covers the average values of C_R that were observed experimentally (see Figure 3-7 and Figure 3-8). The comparison between the model and experimental data are shown in Figure 3-21 through Figure 3-23. Each dot in Figure 3-21 through Figure 3-23 represents the average of multiple bubble departure diameters measured for specific operating conditions and for a single nucleation site. The error bars represent the measurement uncertainty only (i.e. the statistical variation of the data is not presented in Figure 3-21 through Figure 3-23).

The difference between each figure is dictated by the averaging process that was applied to the experimental data. Data in Figure 3-21 were produced by calculating the number average of individual bubble departure diameters (Equation (3-24)).

$$D_d[1,0] = \frac{\sum_{i=1}^{N_m} D_{d,i}}{N_m} \tag{3-24}$$

where N_m is the total number of measurements. Data in Figure 3-22 were produced by calculating the Sauter mean diameters (Equation (3-25)), while data in Figure 3-23 was produced by calculating De Brouckere mean diameter (Equation (3-26).

$$D_d[3,2] = \frac{\sum_{i=1}^{N_m} D_{d,i}^3}{\sum_{i=1}^{N_m} D_{d,i}^2} \tag{3-25}$$

$$D_d[4,3] = \frac{\sum_{i=1}^{N_m} D_{d,i}^4}{\sum_{i=1}^{N_m} D_{d,i}^3} \tag{3-26}$$

All three averaging procedures result in very similar values of bubble departure diameters, which are well captured by the model, further supporting the validity of the modeling assumptions.

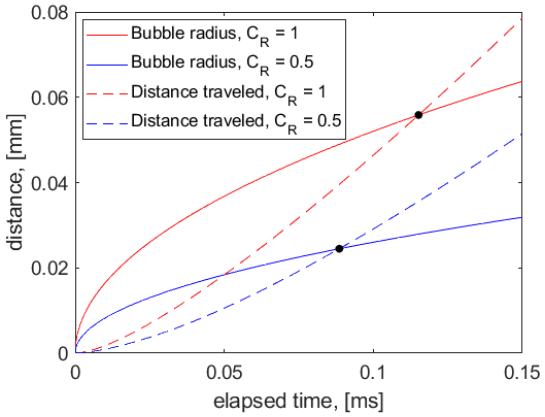

Figure 3-20. Illustration of the bubble departure criterion applied to the solution of Equation (3-21) for the pressure of 10.5 bar, mass flux of 1000 kg/(m^2-s) and two values of C_R: 0.5 and 1.

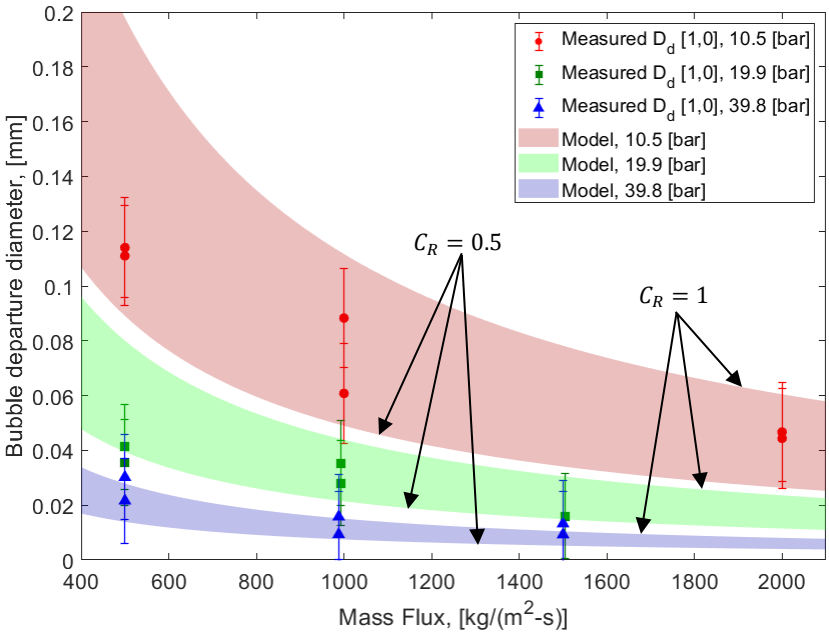

Figure 3-21. Comparison between the departure diameters calculated by solving Equation (3-21) and the number average values of experimental data.

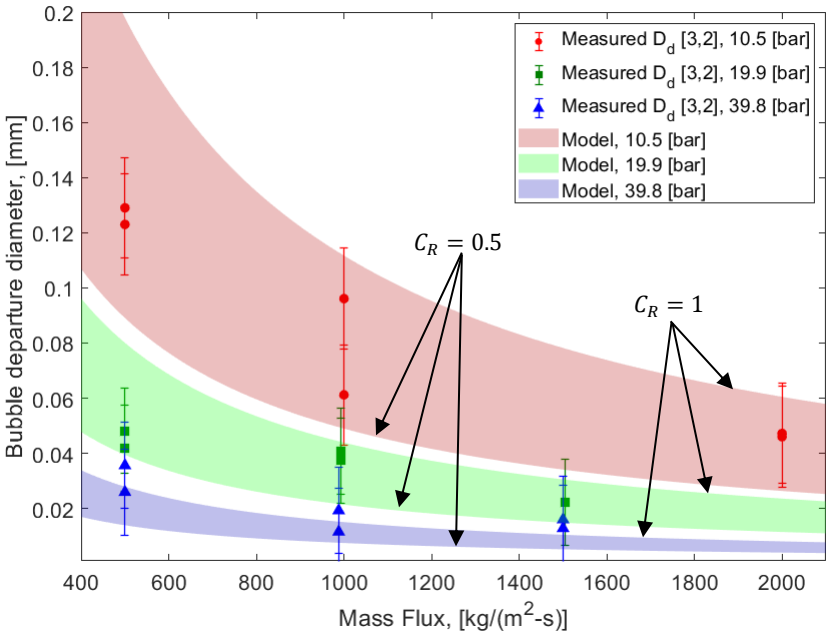

Figure 3-22. Comparison between the departure diameters calculated by solving Equation (3-21) and experimentally measured Sauter mean diameters.

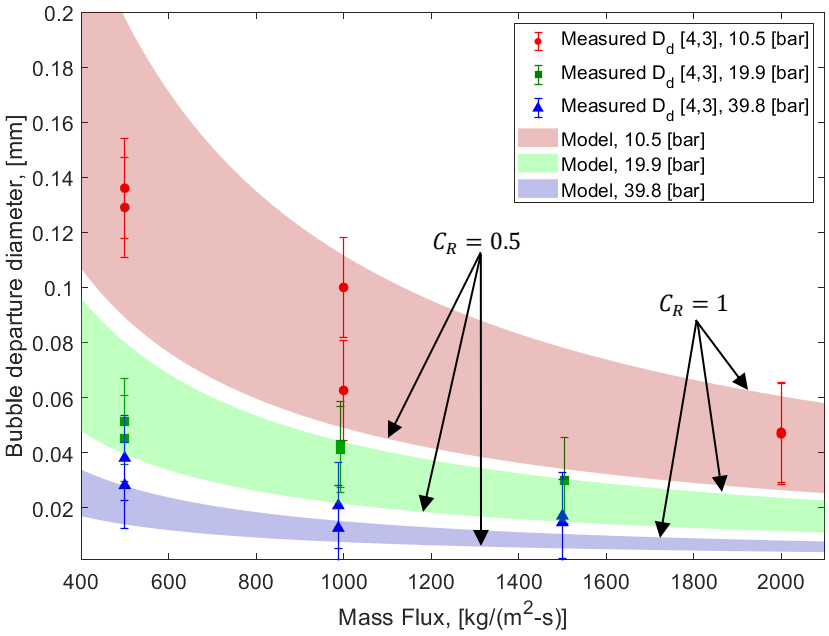

Figure 3-23. Comparison between the departure diameters calculated by solving Equation (3-21) and experimentally measured De Brouckere mean diameters.

Finally, the performance of the model is compared to the data available in the literature for pressures higher than 10 bar. The results are shown in Figure 3-24, where the predicted departure diameters are compared with the data from pool and flow boiling studies. While the pool boiling predictions of the model lie above the majority of Semeria's data [35], as well as the correlation of Cole and Rohsenow, a reasonably good overlap is achieved when compared to the data of Sakashita and Ono [36]. It should be noted that the experiments of Semeria and Sakashita and Ono were performed on a horizontally oriented boiling surface, whereas the model presented here was derived for vertically oriented surface. Additionally, the range of coefficient C_R used in the model was adjusted based on the bubble growth histories measured in flow boiling. Finally, the definition of the bubble departure can be made more accurately in the case of pool boiling on a horizontal surface where the departure mode is always a lift-off. Therefore, we do not expect the model presented here to accurately predict the pool boiling results. Instead we are demonstrating that the values predicted by the model are reasonable when compared to other studies and that they follow the same trend when the pressure is increased. Additionally, the predictions of the model for flow boiling are also shown in Figure 3-24. The model predicts smaller departure diameters for higher mass fluxes, which is reasonable since the presence of flow will introduce additional detachment forces that scale with the flow velocity. In our case, drag is the only detachment force considered. Large drag force will force a bubble to move past its nucleation site faster, satisfying the criterion of Equation (3-23) at smaller bubble diameters. According to Figure 3-24, the departure diameter at PWR conditions (i.e. 155 bar and 3600 kg/(m^2-s)) is approximately 200 nm. Such small diameters cannot be resolved with the optical technique used in the present study. The smallest pixel size achieved in the present study is 5.2 µm. While it is possible to get a sub-micron resolution with optical microscopes, such devices will have to be positioned a few millimeters away from the

boiling surface, leaving no space for thick pressure boundaries required to reach PWR conditions. In fact, while the measurements of bubble departure diameters at the pressure of 76 bar were attempted in the present study, they are not reported here because of the large uncertainties associated with such measurements. At 76 bar of pressure and 1000 kg/(m^2-s) of mass flux the departing bubbles appear as a few pixels that are slightly darker than the background (see Figure 3-25), indicating that the departure diameters of such bubbles could be even smaller than a pixel. Therefore, future studies focusing on bubble departure diameter in high pressure flow boiling will have to either use more advanced optical setup with higher spatial resolution, or make use of the light with shorter wavelengths (i.e. ultraviolet or x-rays).

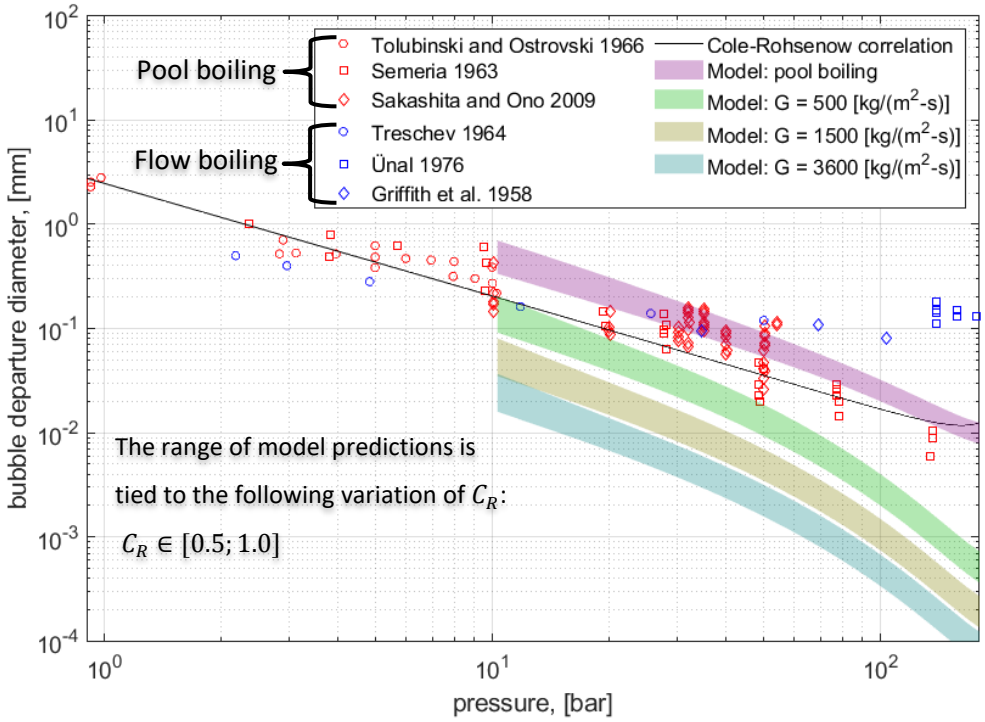

Figure 3-24. Comparison between the model and the data available in the literature

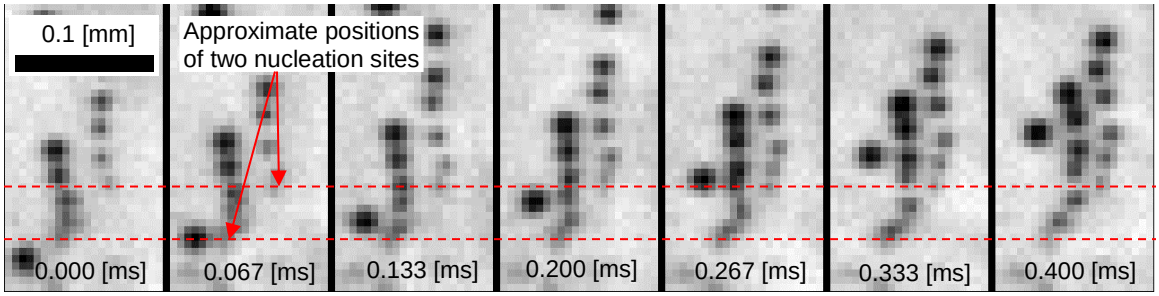

Figure 3-25. Bubble columns appearing from two nucleation sites in flow boiling at the pressure of 76 bar, mass flux of 1000 kg/(m^2-s), 10 ºC of subcooling and 0.22 MW/m^2 of heat flux

Finally, we can use the predicted values of departure diameters shown in Figure 3-24 to re-examine the assumption of bubble sphericity by making better estimations of the Weber number. Such estimations are plotted in Figure 3-26 for three different mass fluxes. Figure 3-26 shows that when the effect of flow on the bubble departure diameter is accounted for, Weber number becomes smaller than 1 for all pressures higher than 10 bar. This supports the assumption made earlier about the spherical shape of the bubble prior to departure.

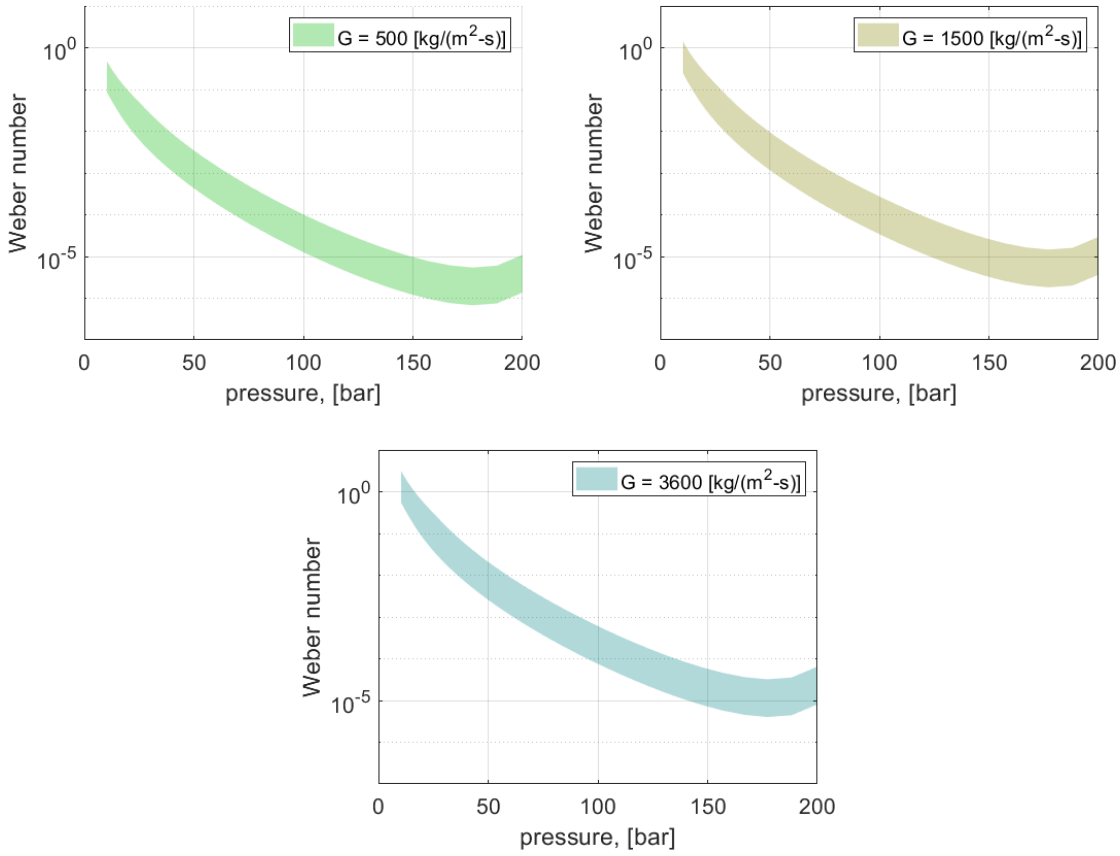

Figure 3-26. Values of the Weber number calculated for different mass fluxes using the departure diameters predicted by the present model

3.6. CONCLUSION TO THE CHAPTER AND FUTURE WORK

In this chapter a broad analysis of bubble departure in higher pressure flow boiling was presented.

- First, the phenomenon of vapor clotting was explored and multiple evidences of its occurrence in high pressure flow boiling were presented. It was demonstrated that vapor clots may affect bubble departure and lift-off processes, warranting further investigation.
- Second, bubble growth at low (atmospheric pool boiling) and high (20 and 40 bar subcooled flow boiling) pressures was analyzed, demonstrating the dominance of thermally controlled growth in high pressure conditions. Additionally, a coefficient C_R was introduced. This coefficient was used to correct the theoretical Plesset and

Zwick solution for thermally controlled growth to better match experimental data. It was established that for pressures of 20 and 40 bar, 10 ºC of subcooling and mass fluxes of 500, 1000 and 1500 kg/(m^2-s) the coefficient C_R ranges between 0.5 and 1. The use of coefficient C_R was likely needed to account for the fact that bubbles grow inside a thermal boundary layer whose temperature is not uniform. Therefore, the exact value of this coefficient should depend on the subcooling, flow rate and the size of the bubble relative to the thickness of the thermal boundary layer. While we did not analyze the dependence of the coefficient C_R on system parameters, we speculate that it could be modeled in the same way as the coefficient χ used in the work of Mazzocco et al. [43], who also applied this coefficient to correct the Plesset and Zwick solution when calculating the growth rate of a bubble in subcooled flow boiling.

- Third, forces acting on a bubble in high pressure flow boiling on a vertical wall were analyzed, leading to the conclusion that there are no adhesion forces present in the direction parallel to the boiling surface. This conclusion indicates that the bubble will depart by sliding immediately after nucleation, making sliding the only possible departure mode in high pressure flow boiling. This conclusion was further corroborated by experimental evidences. The immediacy of the bubble departure will lead to a considerable decrease in bubble growth time in high pressure conditions compared to low pressure. Note that a similar trend of decreasing growth time was previously postulated in the works of Demarly [19] and Kommajosyula [17]. Our experimental results seem to corroborate their assumptions. Furthermore, the ease by which the bubbles can slide near the boiling surface may result in increased importance of the heat transfer enhancement due to sliding bubbles. The importance of sliding bubbles was also emphasized before in the works of Yeoh et al. [14] and Gilman and Baglietto [15].
- Fourth, a simplified force balance model was established, describing the movement of a bubble in the direction parallel to the boiling surface. This force balance model accounted for vapor inertia, buoyancy, and quasi-steady drag, allowing the calculation of the bubble's position as a function of time since nucleation. Calculated values were then compared to experimental data, showing decent agreement, hence supporting the conclusion that no adhesion forces are present in the direction parallel to the boiling surface.
- Fifth, a criterion for bubble departure in high pressure boiling was proposed. This criterion recognizes the absence of adhesion forces and defines the point of bubble departure as the time when the nucleation site is no longer covered by the projected area of the bubble. This criterion was used to measure departure diameters in high pressure flow boiling, as well as to predict the departure diameter based on the simplified force balance model. The measurements and the predictions of the model were in a good agreement. Finally, the performance of the model was also compared to the pool boiling data from other studies, showing slight overestimation of the departure diameter, while following the correct decreasing trend with increasing pressure. Overall, the proposed model showed satisfactory performance for the case of 10 ºC of subcooling and across a range of pressures and mass fluxes.

It is the opinion of the author that the future studies of bubble departure process at high pressure should focus on exploring surface effects, subcooling and vapor clotting.

- Vapor clotting was already discussed in the beginning of this chapter. It is possible that vapor clotting could have a serios effect on the bubble departure process by either preventing the departure completely (i.e. the growing bubble coalesces with the vapor clot before it could depart) or by changing the forces acting on the bubble, hence influencing the departure diameter.
- Subcooling has a strong effect on the bubble size in low pressure boiling. However, in high pressure the bubbles are extremely small and may depart before growing outside of the superheated liquid layer. This could potentially dampen the effect of subcooling on bubble departure diameter. The effect of subcooling is also intertwined with the mass flux, because higher mass fluxes will make the thermal boundary layer thinner. The combined effect of subcooling and mass flux may be used to determine the value of the coefficient C_R that was used in the present study to match the theoretical prediction of bubble growth histories with experimental measurements. Further measurements at a wider range of subcoolings and at different mass fluxes are recommended.
- Surface morphology and wettability may also affect the departure process in a significant way. Higher contact angles may lead to larger, more deformable bubbles that could introduce some adhesion forces preventing the bubble from departure. Additionally, rougher surfaces may have larger TCL length, further bolstering the surface tension force. Therefore, more studies on different boiling surface with the focus on the prototypical nuclear fuel cladding materials should be performed.

4. ROLE OF EVAPORATIVE HEAT TRANSFER IN HIGH PRESSURE FLOW BOILING

In this chapter we examine the evaporative heat transfer in high pressure flow boiling. Microlayer and triple contact line (TCL) are two main phenomena responsible for the heat removal by evaporation. While these phenomena are of major importance in low pressure pool boiling, their effects on high pressure flow boiling are not well understood, motivating the present research. The chapter is divided in 5 sections. Section 4.1 provides a qualitative view on the microlayer formation at different pressures and mass fluxes, highlighting the disappearance of the microlayer at high pressure as well as its deformation under the effect of flow. Section 4.2 develops a quantitative criterion for the transition between microlayer and TCL evaporation regimes, while also providing a measurement of the critical contact line velocity. Section 4.3 analyzes the relative importance of thermal and hydrodynamic dewetting in an attempt to determine which of the two phenomena define the critical contact line velocity. Section 4.4 provides the measurements of the contact line density for pressures at which the microlayer is absent. These measurements are combined with the TCL evaporation model in order to estimate the importance of the triple contact line evaporation in high pressure boiling. Section 4.5 provides a conclusion to the present chapter and proposes future work.

4.1. EFFECT OF PRESSURE AND FLOW ON MICROLAYER FORMATION

Pressure and flow can affect the shape, radial size and the average thickness of the microlayer. Figure 4-1 shows the effect of flow velocity on the microlayer formation. As a reference, the first row in Figure 4-1 shows the microlayer growing in saturated pool boiling conditions under atmospheric pressure, while the rest of the images in Figure 4-1 show the growth of the microlayer in subcooled flow boiling, with pressure close to atmospheric and different mass fluxes. The pool boiling test was performed using the pool boiling setup described in Section 2.4, while recording the main beam only (see Figure 2-13 for more details). The flow boiling test was performed using the low pressure flow boiling setup described in Section 2.3, while recording the main and SG beams (see Figure 2-13 for more details). Due to the difference in phase detection approaches between the pool and flow boiling tests, the outline of the bubble can be seen in flow boiling images, while only dry area and the microlayer are seen in pool boiling images. In each row, the first image marked as 0.0000 ms represents the first frame in which the bubble was detected on the HSV recording. Therefore, it approximates the instance of nucleation with the uncertainty equal to the time interval between two consecutive HSV frames. For pool boiling test such time interval equals 0.1 ms (i.e. the recording was performed at 10,000 fps), while for flow boiling tests such interval equals 0.0476 ms (i.e. the recording was performed at 21,000 fps).

Initially, the microlayer growth in flow boiling appears to be similar to the pool boiling case. During this initial stage, the only difference between the pool and flow boiling cases appears to be in the radial size of the microlayer. Such difference is likely related to the smaller bubble size caused by the combination of subcooling and flow rate. In fact, the bubbles continue to get smaller as the mass flux increases. This effect can be attributed to

the thinner thermal boundary layer in higher velocity flows, which in turn reduces the amount of energy available for bubble growth. While an additional decrease in bubble size can be attributed to the slight increase in pressure between different mass fluxes shown in Figure 4-1, this effect has secondary significance. The latter statement is corroborated by the evidences presented in Figure 4-2, which shows the effect of pressure on the microlayer formation. Figure 4-2 clearly demonstrates that for low mass flux in order to reach the same bubble sizes as in the case of 1.22 bar and 1265 kg/(m^2-s) (last row in Figure 4-1), the pressure must be increased to 2.5 bar (5^{th} row in Figure 4-2). At the later stages of bubble growth, the presence of flow results in a deformation of the microlayer. Such deformation results in a decrease of the microlayer thickness over the upstream half of the microlayer, eventually leading to its dryout. At the same time, the downstream portion of the microlayer continues to grow. Additionally, as the upstream portion of the microlayer starts to deform, it develops a bulge. In other words, the thickness of the microlayer reaches its peak somewhere in between the dry area and the outer edge of the microlayer. The bulge persists until the upstream portion of the microlayer is fully evaporated. Such a bulge can be seen clearly in Figure 4-1, row 3, 0.2856 ms, where the dark interference fringe forms a shape of a cross, indicative of the extremum in the microlayer thickness. The appearance of such bulge is not limited to flow boiling. In fact, several recent studies observed its appearance in pool boiling experiments [28], [66]. While it is not shown in Figure 4-1 and Figure 4-2, our pool boiling data also exhibits the bulge near the end of the bubble growth cycle (i.e. times much larger than 0.3 ms).

The effect of pressure on the microlayer formation can be seen in Figure 4-2. As the pressure increases, the relative area occupied by the microlayer decreases, until the microlayer becomes present only at the very early stages of the bubble growth (last row in Figure 4-2). This trend continues into higher pressures, until the microlayer disappears completely. Figure 4-3 shows that for pressure as low as 4 bar, the microlayer is no longer present and the only footprints left by bubbles are dry areas. The bubble outlines are not present in Figure 4-3 because it was captured using the main beam only (see Figure 2-13 for more details).

In this section we have demonstrated that both flow and pressure affect the formation of the microlayer. Under the effect of flow, microlayer first deforms, and eventually disappeares in the upstream half of the bubble, while continuing to grow in the downstream half. Under the effect of pressure, the entire region of the microlayer is affected, with high pressure leading to the complete disappearance of the microlayer. The next Section provides a quantitative view on these phenomena and identifies the criterion for microlayer existence in pressurized flow boiling of water.

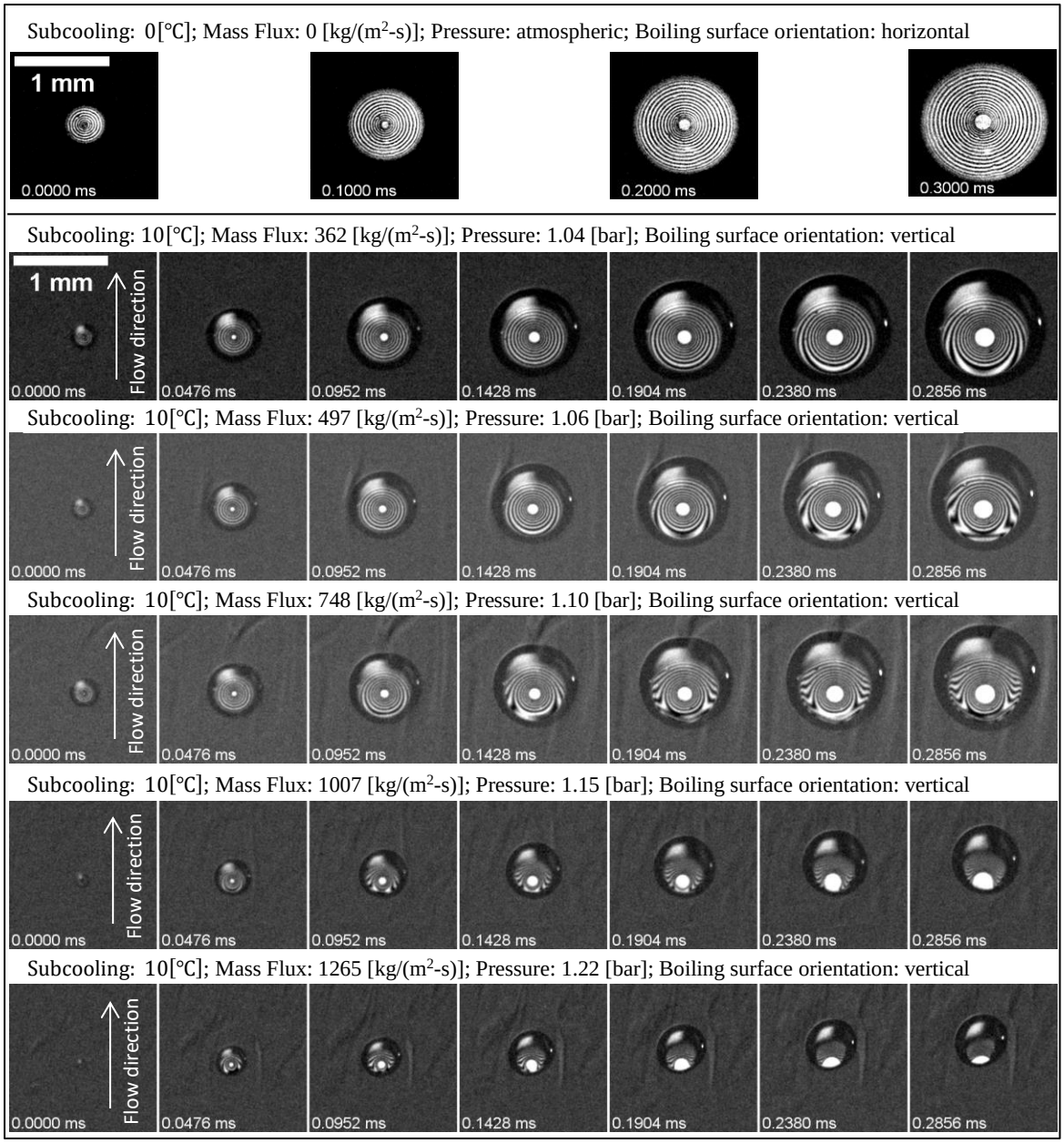

Figure 4-1. Deformation of the microlayer under the influence of flow. The first row of images serves as a reference by displaying the growth of microlayer in saturated pool boiling under atmospheric pressure

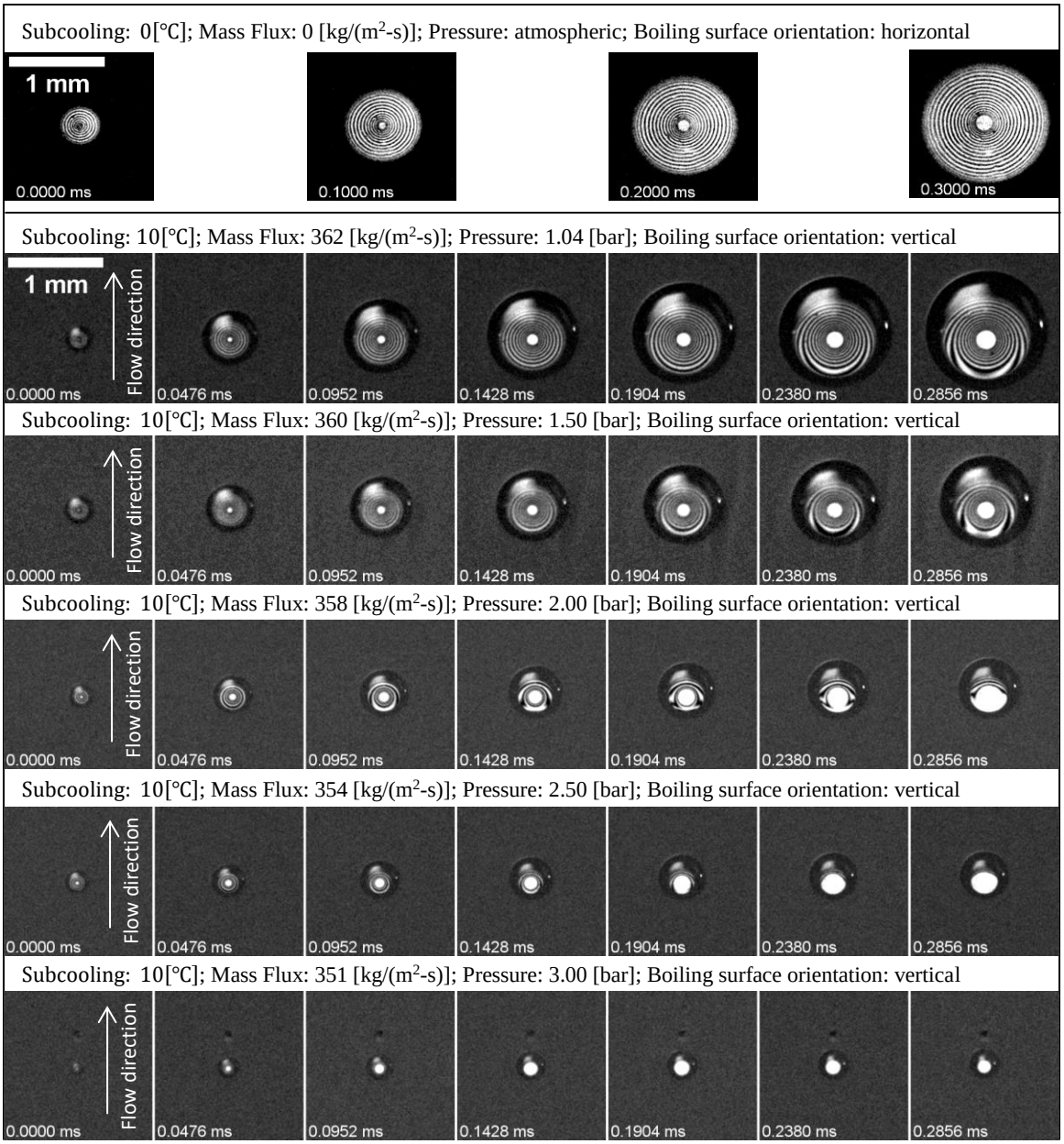

Figure 4-2. Change in microlayer formation under the influence of pressure. The first row of images serves as a reference by displaying the growth of microlayer in saturated pool boiling under atmospheric pressure

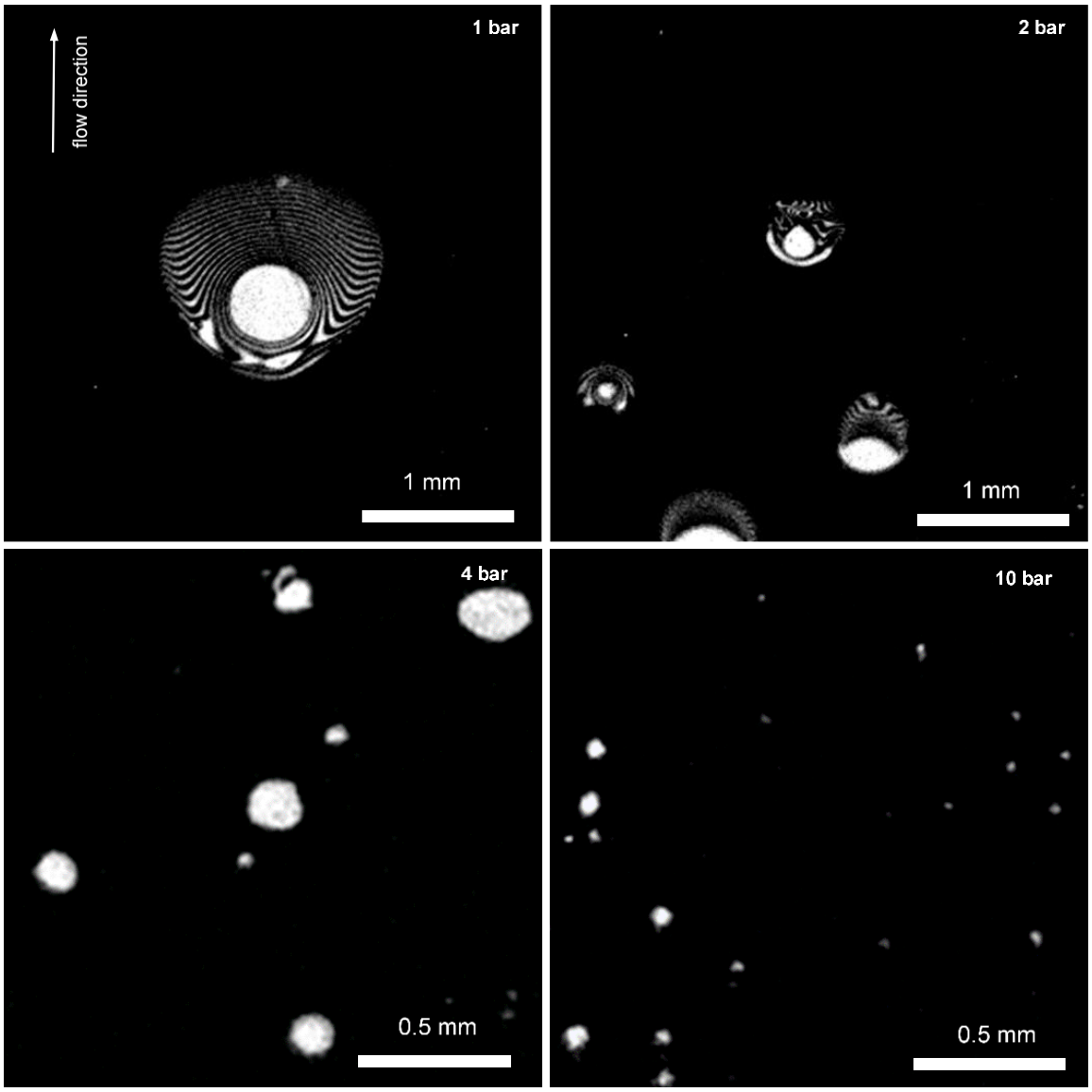

Figure 4-3. Demonstration of the microlayer disappearance in high-pressure flow boiling. These images were taken in subcooled flow boiling conditions at pressures ranging from 1 to 10 bar, with a mass flux of 1000 kg/m^2-s, a subcooling of 10 ˚C, and a heat flux of 1.0 MW/m^2

4.2. CRITERION FOR MICROLAYER DISAPPEARANCE

A criterion for microlayer disappearance can be formulated in terms of the critical apparent contact line velocity. In order to quantify the critical velocity, first the positions of the apparent contact line (ACL) and real contact line (RCL) were measured during the growth cycle of a bubble. Measurement procedures are described in Sub-Section 2.7.3. For each combination of pressure and mass flux, one bubble was randomly chosen and the positions of ACL and RCL for this bubble were identified. Figure 4-4 through Figure 4-7 show the results of the measurements as a function of the time elapsed since the nucleation of the bubble. Whenever ACL and RCL are separated, the microlayer is present, occupying the

distance between ACL and RCL. In contrast, when ACL and RCL coincide, the microlayer is absent. While the actual measurements of contact line velocities are discussed later in the chapter, Figure 4-4 through Figure 4-7 provide a qualitative view of the changes in contact line velocities based on the slopes of the curves. While the slopes of RCL stay approximately constant, the slopes of ACL change considerably throughout the growth of a bubble. While the ACL is moving relatively fast during the initial stage of bubble growth, it slows down considerably as the bubble continues to grow. Such trend is consistent with the prevalence of the thermally controlled bubble growth, which was demonstrated in the previous Chapter. Additionally, the upstream ACL reverses its movement direction shortly after the nucleation. This effect is cause by the presence of flow, which pushes the bubble along the wall, leading to the movement of the ACL. Therefore, the movement of the ACL is driven by both the growth of the bubble and by the flow. The relative importance of the two mechanisms changes with the flow rate and the time elapsed since the nucleation. For small flow rates and short times the movement of the ACL is governed by the bubble growth, while for large flow rates and long times the movement of the ACL is determined by the flow. Notably, the velocity of the RCL does not change much throughout the bubble growth cycle, especially in the upstream portion of the bubble. This results in the competition between ACL and RCL velocities. Initially, when the velocity of ACL is large, RCL cannot catch up to it, resulting in the formation of the microlayer. However, as the ACL slows down, it is possible for RCL to catch up leading to the disappearance of the microlayer. In the upstream portion of the bubble the ACL stops and reverses its direction under the influence of flow, making it easy for RCL to catch up with the ACL. In contrast, ACL continues to move relatively fast within the downstream portion of the bubble, preventing the RCL from converging to the ACL. Such variation in ACL velocity causes the deformation of the microlayer observed in Figure 4-1.

Higher pressure effectively reduces the contribution to ACL velocity from the bubble growth. Assuming that ACL velocity is proportional to the growth rate of the bubble, we can analyze its dependence on the thermophysical properties by using Plesset and Zwick solution for the thermally controlled growth [94]. The resulting expression for the bubble growth rate is given in Equation (4-1)

$$u_{ACL} \propto \frac{dR_b}{dt} = \frac{B}{2 \cdot \sqrt{t}} = \sqrt{\frac{12}{\pi} \cdot \alpha_l} \cdot Ja^* \cdot \frac{1}{\sqrt{t}} = \sqrt{\frac{12}{\pi} \cdot \alpha_l} \cdot \frac{\Delta T \cdot c_{pl} \cdot \rho_l}{h_{fg} \cdot \rho_g} \cdot \frac{1}{\sqrt{t}} \tag{4-1}$$

Equation (4-1) demonstrates that the growth rate of the bubble is proportional to the density ratio. The density ratio has a strong dependence on pressure, leading to smaller values at higher pressures. This results in a considerable decrease in the bubble growth rate at higher pressures, making it easier for the RCL to catch up with the ACL. Interestingly, the presence of flow may offset the decrease in bubble growth rate, allowing for the microlayer to persist for longer. This effect can be observed in Figure 4-6 and Figure 4-7, where for low flow rates the microlayer disappears entirely before the disappearance of the dry spot, while for high flow rates the microlayer persists in the downstream portion of a bubble.

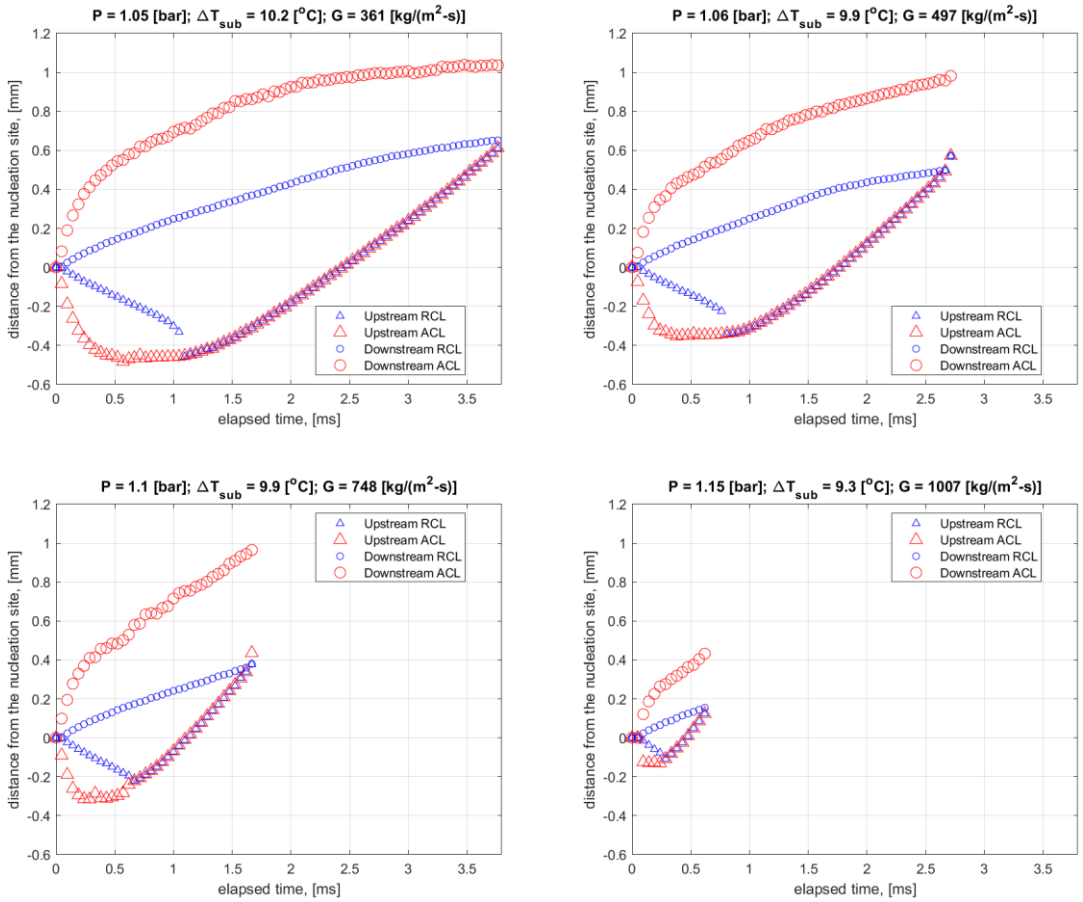

Figure 4-4. Positions of real and apparent contact lines for the pressure of 1 bar and four different mass fluxes. The exact operating conditions of each experiment are shown in each plot. The x-axis shows the time elapsed since the nucleation of the bubble

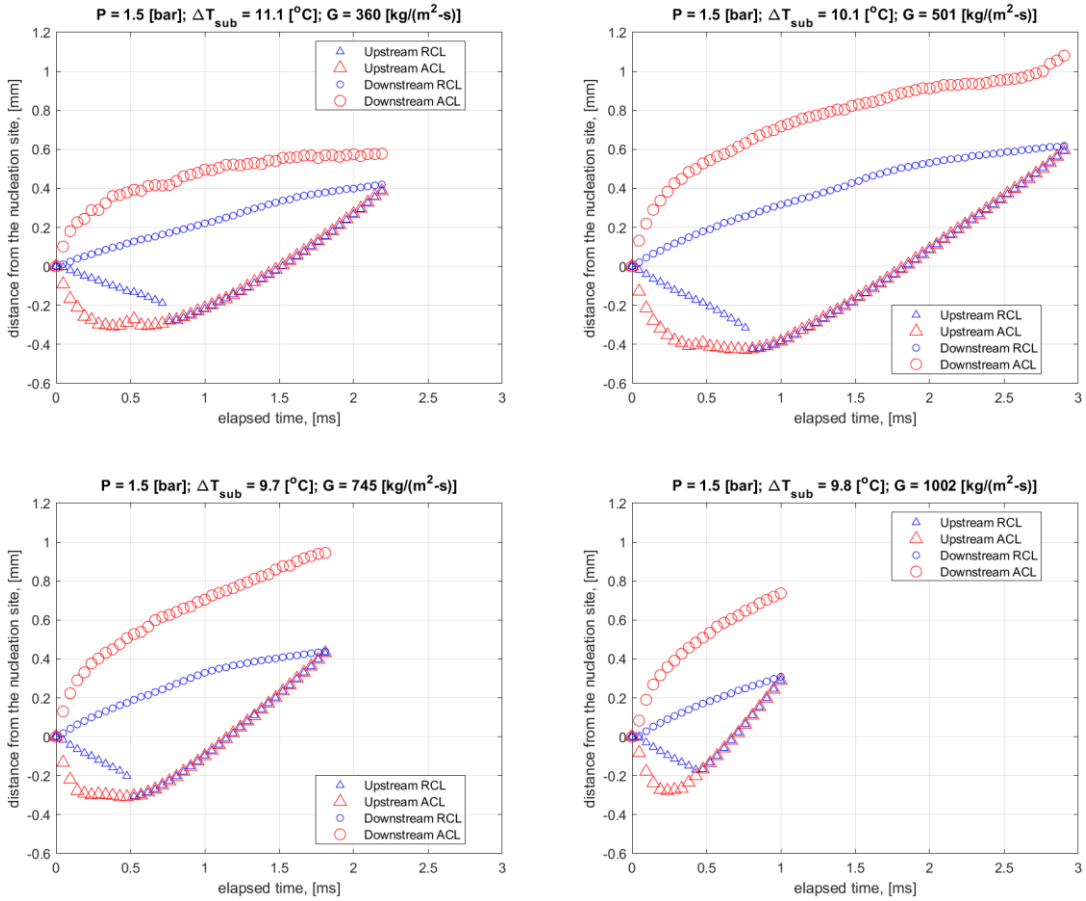

Figure 4-5. Positions of real and apparent contact lines for the pressure of 1.5 bar and four different mass fluxes. The exact operating conditions of each experiment are shown in each plot. The x-axis shows the time elapsed since the nucleation of the bubble

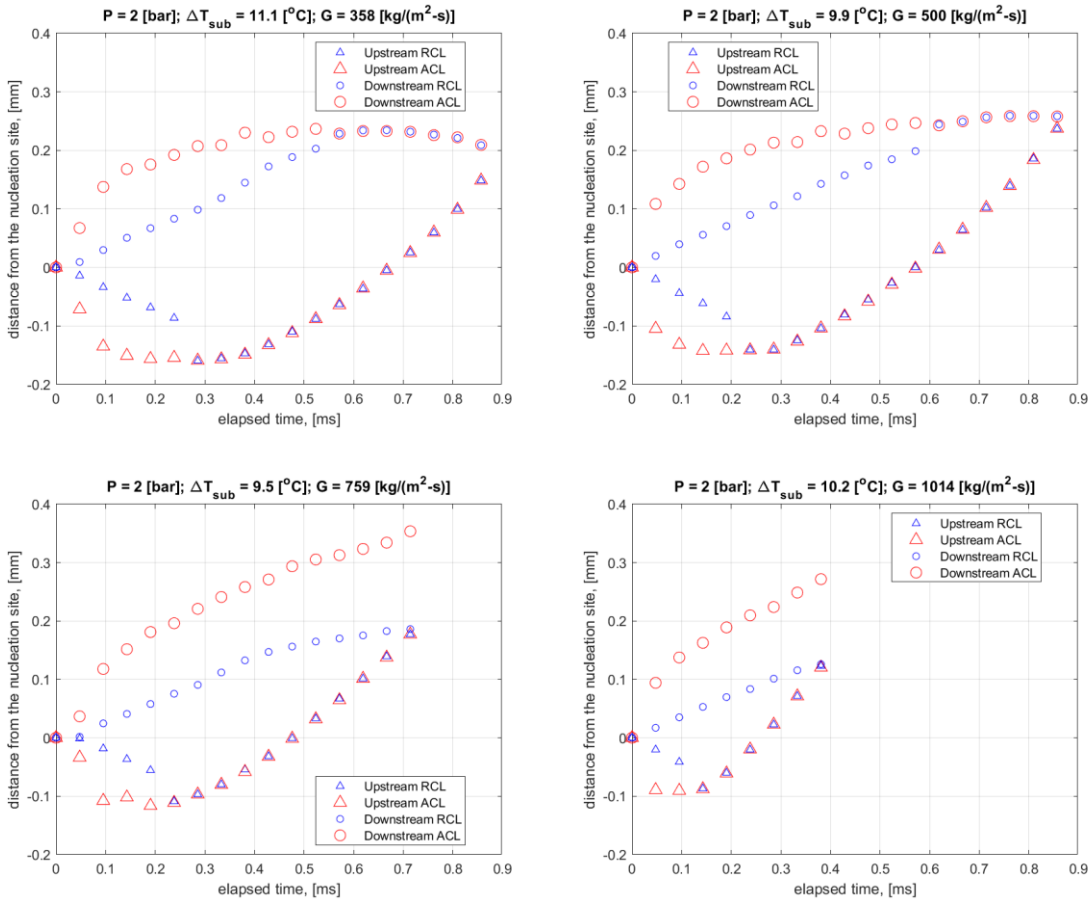

Figure 4-6. Positions of real and apparent contact lines for the pressure of 2 bar and four different mass fluxes. The exact operating conditions of each experiment are shown in each plot. The x-axis shows the time elapsed since the nucleation of the bubble

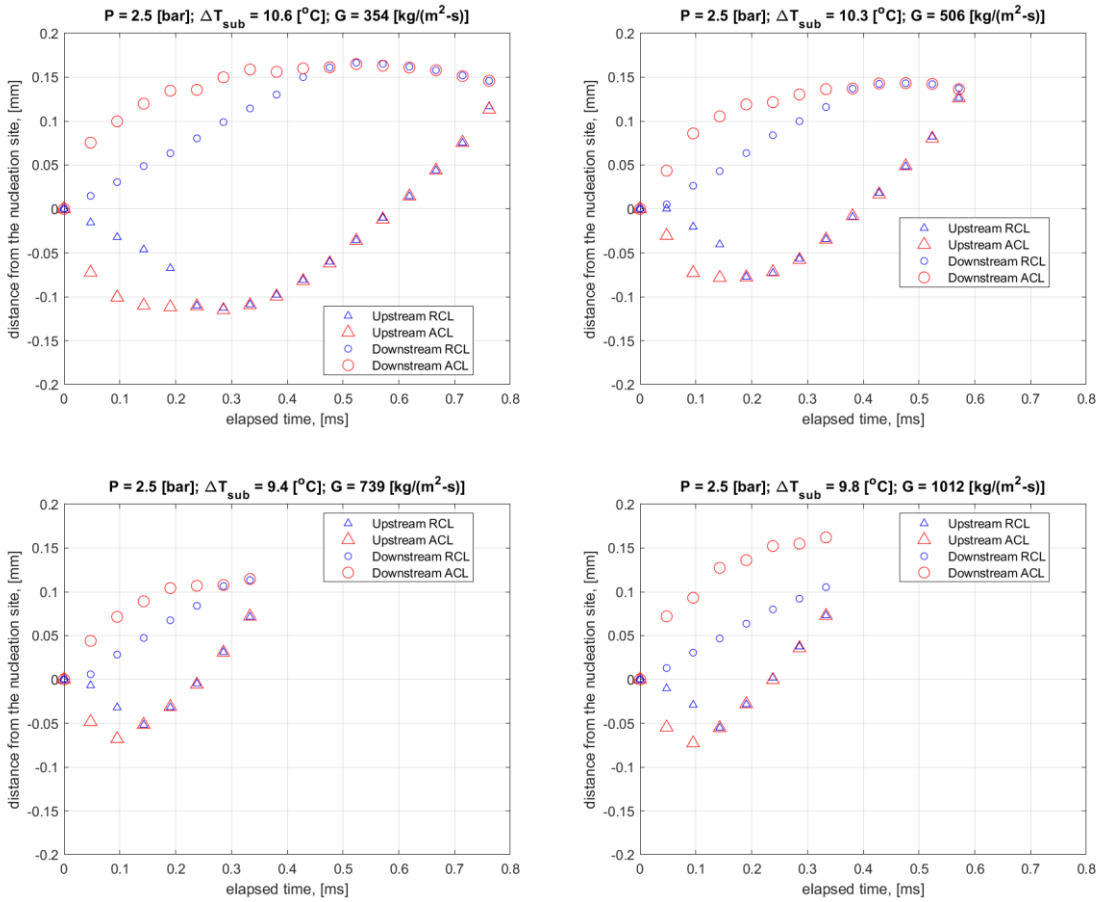

Figure 4-7. Positions of real and apparent contact lines for the pressure of 2.5 bar and four different mass fluxes. The exact operating conditions of each experiment are shown in each plot. The x-axis shows the time elapsed since the nucleation of the bubble

The results shown in Figure 4-4 through Figure 4-7 suggest a criterion for microlayer disappearance. The microlayer will not form if the velocity of the ACL is smaller than the velocity of the RCL for the entire growth cycle of a bubble. If ACL velocity is larger than RCL velocity during the initial stage of bubble growth, then microlayer can form, but it may disappear if RCL is able to catch up with the ACL. Therefore, it is important to know the relative magnitudes of RCL and ACL velocities when developing the criterion for microlayer disappearance. Figure 4-8 aggregates all contact line velocity measurements from different pressures and mass fluxes, representing them in terms of Capillary numbers, given by Equation (4-2)

$$Ca = \frac{\mu_l \cdot u_{CL}}{\sigma} \tag{4-2}$$

where u_{CL} is the velocity of the contact line. For each set of data (i.e. upstream and downstream) lines representing best linear fit are also shown in Figure 4-8. The correlation coefficients [103] calculated using Equation (4-3) are given in the legend of the plot.

$$r = \frac{\sum_1^n \left[\left(Ca_{ACL,i} - \overline{Ca_{ACL}} \right) \cdot \left(Ca_{RCL,i} - \overline{Ca_{RCL}} \right) \right]}{\sqrt{\sum_1^n \left[\left(Ca_{ACL,i} - \overline{Ca_{ACL}} \right)^2 \right] \cdot \sum_1^n \left[\left(Ca_{RCL,i} - \overline{Ca_{RCL}} \right)^2 \right]}} \quad (4\text{-}3)$$

Figure 4-8 shows a fairly weak correlation between ACL and RCL velocities. The correlation is especially weak for the upstream direction. The upstream direction is more representative of the early period of bubble growth because the microlayer does not exist for very long time at the upstream portion of the bubble. Note that negative data (i.e. ACL velocities after the reversal of its movement direction) are ignored in Figure 4-8, which explains the absence of multiple data points lying on top of the $Ca_{RCL} = Ca_{ACL}$ line for the upstream direction. The results shown in Figure 4-8 suggest that for the operating conditions explored here the relationship between RCL and ACL velocities is either weak, or does not exist at all, especially for the early stages of bubble growth. Most importantly, it shows that the RCL velocity stays approximately in the same ballpark, despite the wide range of pressures and mass fluxes that are covered by the data. Therefore, the average of the RCL velocity can be considered as the critical dewetting velocity because no microlayer will form if ACL is moving slower than RCL.

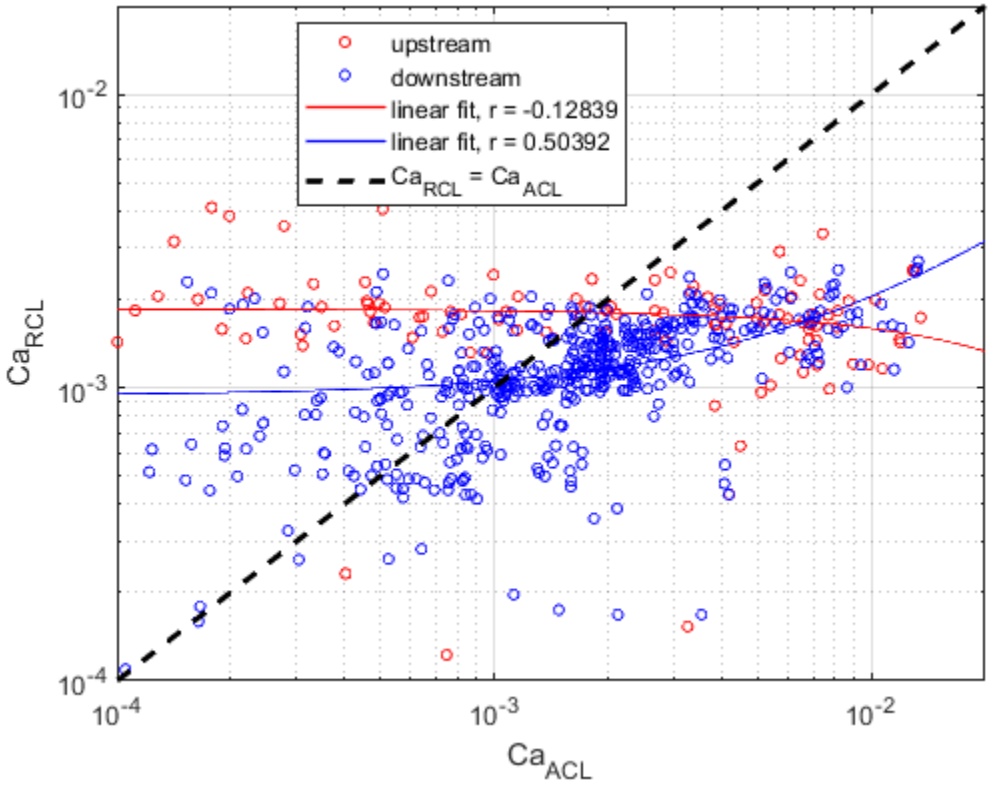

Figure 4-8. Comparison between RCL and ACL capillary numbers

While Figure 4-8 shows the relationship between RCL and ACL velocities for the entire bubble growth cycles, it does not provide a good estimation of the critical dewetting velocity. The critical dewetting velocity should be measured at the earliest stage of bubble

growth, because the earliest stage of bubble growth will determine whether the microlayer will form or not. For this purpose, additional measurements of RCL and ACL velocities were made using the first 2 frames for which a bubble was detected on the HSV image. Such measurements were performed for several bubbles at different pressures and the lowest mass flux (approximately 355 kg/(m^2-s)). The selection of the lowest mass flux allowed us to isolate the effect of pressure on contact line velocities, without considering the microlayer deformation due to flow. Number averages of such measurements are shown in Figure 4-9 with error bars representing a variation of $\pm\sigma_{SD}$, where σ_{SD} is the standard deviation of the measurements. The measurements were performed on both the upstream and downstream portions of the microlayer. Figure 4-9 shows that RCL velocity stays constant for all pressures, while the ACL velocity decreases significantly when pressure is increased. The dashed blue line representing the critical Capillary number was calculated by taking an average of all RCL velocity measurements. The trend of ACL velocity can be predicted by utilizing Plesset and Zwick's relation for thermally controlled growth. The shaded region in Figure 4-9 was calculated using Equation (4-4), which represents the combination of Equations (4-1) and (4-2).

$$Ca_{ACL} = C_R \cdot \frac{\mu_l}{\sigma} \cdot \sqrt{\frac{12}{\pi} \cdot \alpha_l} \cdot \frac{\Delta T \cdot c_{pl} \cdot \rho_l}{h_{fg} \cdot \rho_g} \cdot \frac{1}{\sqrt{t}} \tag{4-4}$$

where similarly to Chapter 3 a fitting coefficient C_R was introduced. In the case of Figure 4-9 C_R was set to 0.6. The spread of the shaded region reflects the uncertainty in the identification of the nucleation event due to the frame rate of the HSV camera. The cause of such uncertainty is shown schematically in Figure 4-10. Depending on the relative synchronization between the bubble nucleation and HSV camera, any situation in between of the two scenarios shown in Figure 4-10 is possible. In the case of scenario 1, a HSV frame was recorded right before the instance of bubble nucleation. Therefore, whenever a bubble is detected in the HSV frame, such bubble will have already been growing for the time equal to the time difference between the two HSV frames. Therefore, the real time at which the velocity is calculated will be $1.5\Delta t$, where Δt is the time between the two HSV frames. Scenario 1 in Figure 4-10 corresponds to the lower boundary of the shaded region in Figure 4-9. In contrast, if the first HSV frame in which the bubble is detected happened to coincide exactly with the nucleation event, then the velocity will be calculated at the time equivalent to $0.5\Delta t$. This corresponds to Scenario 2 in Figure 4-10 and the upper boundary of the shaded region in Figure 4-9.

Whenever the ACL Capillary number falls below the critical Capillary number, the microlayer will disappear. The measurements presented in Figure 4-9 suggest that the maximum pressure at which the microlayer can be found is approximately 3 bar. These results are in good agreement with Figure 4-3, which demonstrates that no microlayer is present for pressures of 4 bar and higher. Note that while the shaded region in Figure 4-9 slightly overpredicts the ACL capillary number, it still provides a good estimation for the microlayer disappearance pressure.

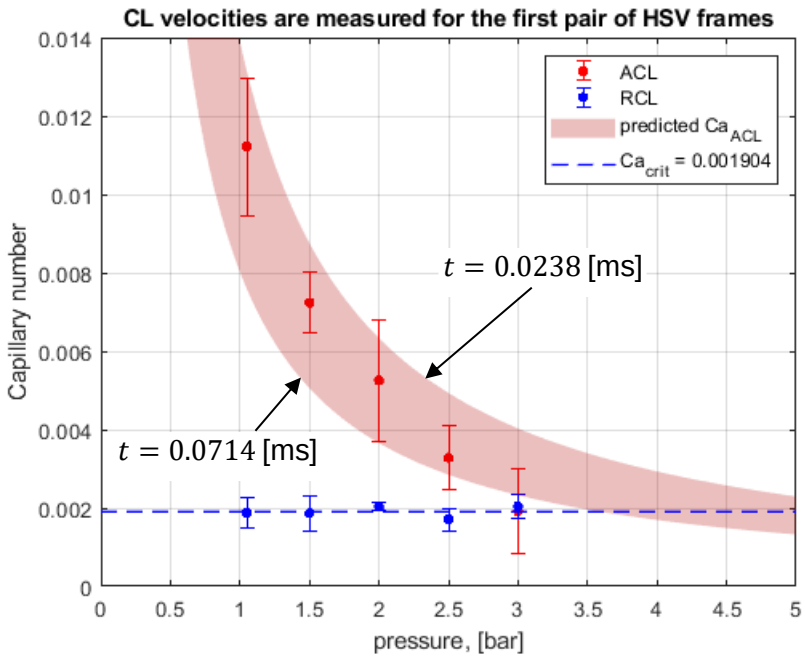

Figure 4-9. Contact line velocities during the initial stage of bubble growth. The error bars represent the standard deviation of measurements

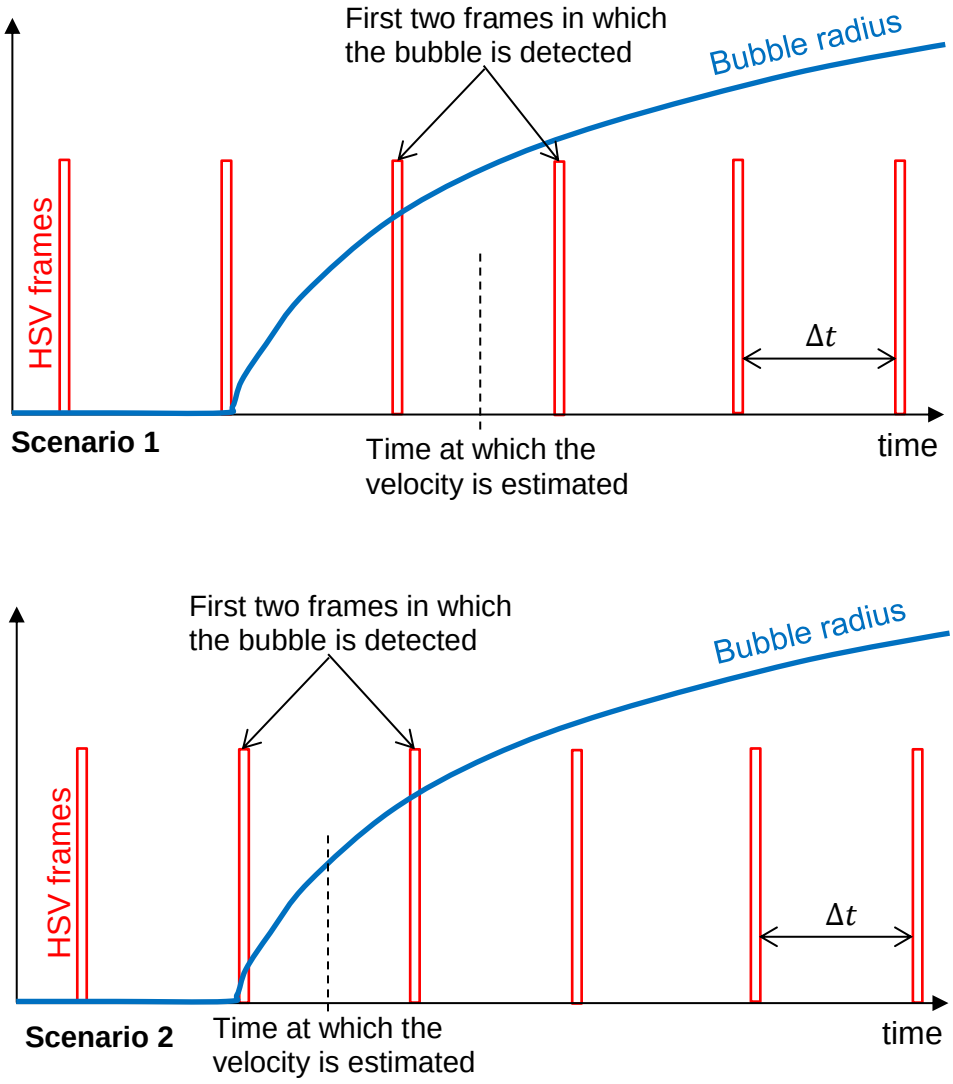

Figure 4-10. Visual representation of two limiting scenarios for the detection of a nucleation event.

We can also compare the value of the critical capillary number measured in the present study to the prediction of Demarly [19]. Demarly used the results of direct numerical simulation (DNS) of Guion [20] to predict the ratio between the dry area and microlayer diameters using Equation (4-5)

$$\frac{D_{dry}}{D_{\mu L}} = 0.1237 \cdot Ca_{ACL}^{-0.373} \cdot \sin(\theta) \tag{4-5}$$

where θ is the contact angle. For a given value of the contact angle θ, the critical Capillary number is found by setting the ratio of dry area and microlayer diameters to one (see Equation (4-6)).

$$\frac{D_{dry}}{D_{\mu L}} = 0.1237 \cdot Ca_{ACL}^{-0.373} \cdot \sin(\theta) = 1 \tag{4-6}$$

The solution to Equation (4-6) is plotted in Figure 4-11 together with the experimentally measured value of the critical Capillary number. Equation (4-6) falls in the same order of magnitude as the measured value, while also providing a good match for the contact angle of 51.5º. While the contact angle on ITO is typically higher (approximately 80º). The results predicted by Equation (4-6) are still close to the experiment, especially considering that Equation (4-6) was based on hydrodynamic dewetting alone (i.e. no evaporation was modeled in the DNS calculation of Guion [20]). Furthermore, it is possible that ITO surface becomes more hydrophilic after prolonged exposure to hot water (i.e. operating conditions of the present experiment). Therefore, we conclude that Equation (4-6) could serve as a decent approximation for the critical Capillary number. Nevertheless, more studies should be made to not only investigate experimentally the dependence of the critical capillary number on the contact angle, but also include the evaporation of the microlayer in the DNS analysis.

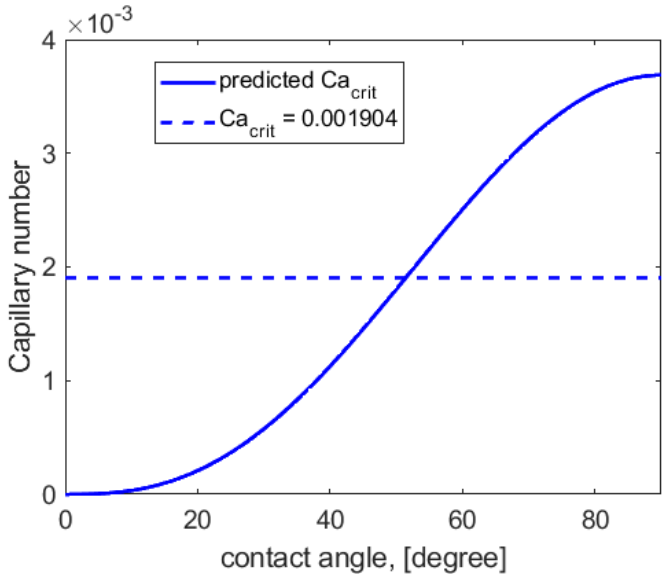

Figure 4-11. Critical Capillary Ca_{crit} number predicted by Equation (4-6) (solid line) together with the experimentally measured $Ca_{crit} = 0.001904$ (dashed line)

Based on the measured value of the critical capillary number it is possible to reconstruct the regime map for microlayer formation. Such regime map is shown in Figure 4-12. Each red line in Figure 4-12 shows the bubble growth velocity at different times t since the nucleation calculated using Equation (4-4). The blue line displays a critical capillary number, which is also shown in Figure 4-9. While the growth of every bubble starts in the inertia-controlled regime, in which the ACL velocity is large enough to form the microlayer, the growth process eventually transitions to the thermally controlled phase, in which the longer a bubble grows, the smaller its ACL velocity will be. As long as the ACL Capillary number stays above the critical Capillary number (above the blue line in Figure

4-12), the microlayer will be growing by covering larger area under the bubble. However, as soon as the ACL capillary number drops below the critical capillary number (below the blue line in Figure 4-12) the microlayer will start to shrink, until the RCL can catch up to ACL, leaving only the dry area under a bubble. Note that for higher pressures the ACL capillary number drops below the critical Capillary number for much earlier stages of bubble growth. This means that even if the microlayer is formed during a very early portion of the bubble growth, it will disappear almost immediately, making it practically undetectable. Such short-lived microlayers will also remove little to no energy, and can be ignored when constructing an HFP framework. Additionally, the regime map shown in Figure 4-12 assumes that the bubble starts to grow from infinitesimally small size, while in reality the growth process will start from a finite size defined by the nucleation cavity. Therefore, it is possible to have a bubble that grows at a rate smaller than the critical Capillary number during its entire life cycle, eventually leading to the complete absence of the microlayer. While the regime map shown in Figure 4-12 is useful in understanding the limits of microlayer growth, it is more important to understand which physical mechanisms determine the particular value of the critical Capillary number that was presented here. The next Section provides additional insights into the mechanism of RCL movement by considering thermal and hydrodynamic dewetting processes.

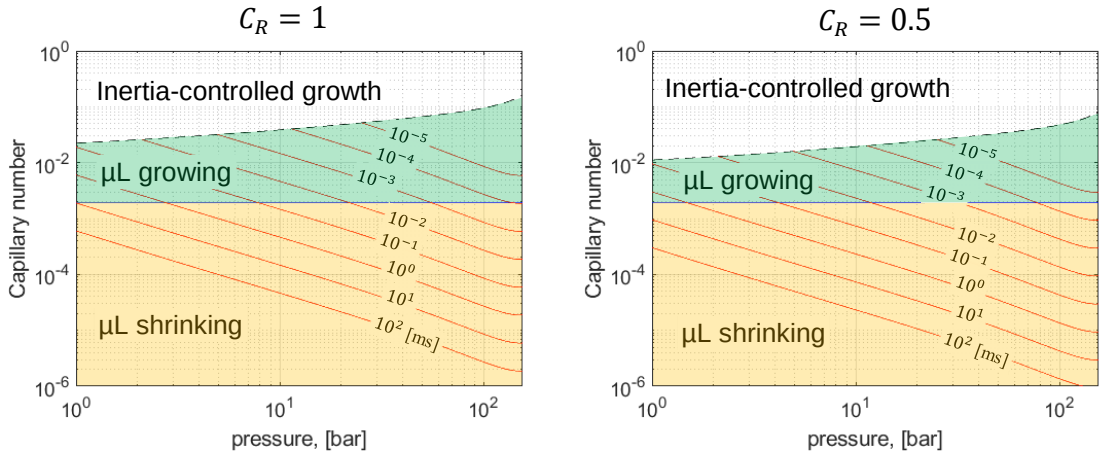

Figure 4-12. Regime map for microlayer formation calculated for $C_R = 1$ (left) and $C_R = 0.5$ (right). The blue line represents the critical capillary number while the red lines show the velocities of the ACL at different times since the nucleation calculated with the use of Equation (4-4). Dashed line represents the approximate boundary of the inertia-controlled growth regime

4.3. RELATIVE IMPORTANCE OF THERMAL AND HYDRODYNAMIC DEWETTING

The specific value of the critical Capillary number can be explained by either thermal or hydrodynamic dewetting, or the combination of both. Thermal dewetting is governed by the evaporation rate of the microlayer, while hydrodynamic dewetting is governed by either

the movement of the RCL under surface tension forces, or depletion of the microlayer by the residual flow present after its formation. In the present section we aim at quantifying thermal dewetting process and comparing its magnitude to the experimentally measured microlayer depletion rate.

For the present analysis, a bubble growing in flow boiling conditions under the pressure of 1.5 bar, subcooling of 9.7 ºC and mass flux of 745 kg/(m^2-s) was selected. For this particular bubble, microlayer thickness was measured according to the procedures presented in Sub-Section 2.7.2. microlayer thickness was measured for each frame starting with the bubble nucleation and finishing with the complete rewetting of the dry area. The measured thickness is shown in Figure 4-13.

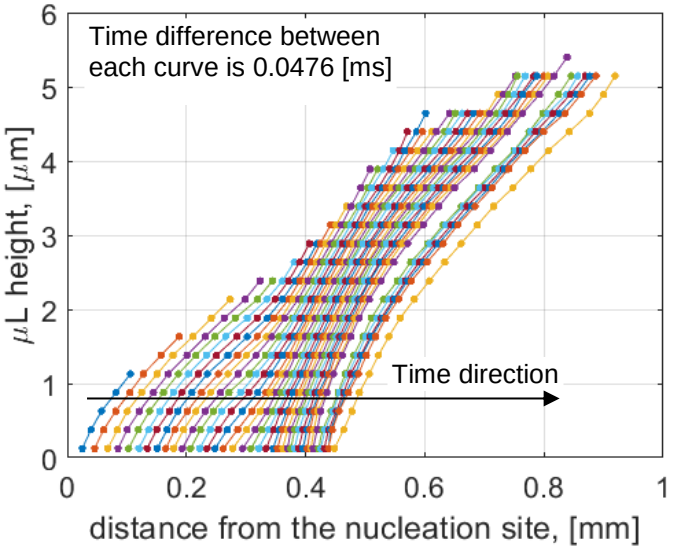

Figure 4-13. Microlayer thickness measured for the downstream portion of the bubble. Measurements are performed for the pressure of 1.5 bar, subcooling of 9.7 ºC and mass flux of 745 kg/(m^2-s)

Microlayer thickness shown in Figure 4-13 can be converted into the microlayer heat flux $q''_{\mu L}$ using Equation (4-11) and heat transfer coefficient (HTC) $h_{\mu L}$ using Equation (4-12)

$$q''_{\mu L}(\delta_{\mu L}) = \frac{T_w - T_{sat}}{\frac{\delta_{\mu L}}{k_l} + R_{ev}} \tag{4-7}$$

$$h_{\mu L}(\delta_{\mu L}) = \frac{1}{\frac{\delta_{\mu L}}{k_l} + R_{ev}} \tag{4-8}$$

where $\delta_{\mu L}$ is the microlayer thickness, T_w is the wall temperature, T_{sat} is the saturation temperature, and R_{ev} is the evaporative thermal resistance. The evaporative thermal

resistance acts as the major unknown when estimating the heat transfer due to the microlayer evaporation. Having no evaporative resistance leads to the highest possible microlayer HTC and represents the simplest case of evaporation dynamics. However, several studies of Giustini et al. [104], [105] suggest that evaporative thermal resistance is far from zero when the evaporation of the microlayer during nucleate boiling is concerned. In their later study [105], a value of evaporative thermal resistance $R_{ev} = 3.846 \left[\frac{m^{2}\cdot^{o}C}{MW}\right]$ is recommended, which corresponds to the accommodation coefficient of 0.03 in the context of the kinetic theory developed by Schrage. Figure 4-14 illustrates the change in microlayer HTC between the case with no evaporative resistance $\left(R_{ev} = 0 \left[\frac{m^{2}\cdot^{o}C}{MW}\right]\right)$ and evaporative resistance recommended in Ref. [105] $\left(R_{ev} = 3.846 \left[\frac{m^{2}\cdot^{o}C}{MW}\right]\right)$. The two cases shown in Figure 4-14 are analyzed in the present study in order to identify the accurate quantification of the microlayer heat transfer.

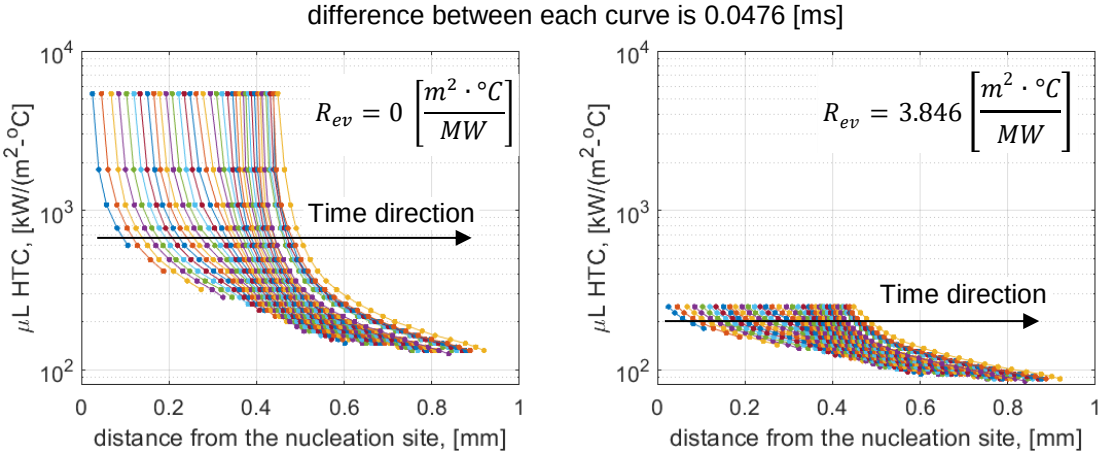

Figure 4-14. Heat transfer coefficient of the microlayer calculated using the microlayer thickness measurements shown in Figure 4-13 and the evaporative thermal resistance of zero (left) and 3.846 (m2-ºC)/MW (right).

The values of microlayer HTC were used as boundary conditions for a 2D axisymmetric transient conduction simulation. The simulation was performed using Partial Differential Equation Toolbox in Matlab. A small section of sapphire and ITO were simulated using the mesh shown in Figure 4-15. The size of the mesh was set to 33.3 μm. This mesh size was sufficiently fine for the prediction of the wall temperature, which serves as a figure of merit in the present analysis. The sensitivity of the solution to the mesh size is shown in Figure 4-16 (top left). The time step was set to 18.1 μs. The sensitivity of the solution to the time step is shown in Figure 4-16 (top right). ITO was modeled as a 2 μm thick layer on top of the sapphire. The actual ITO thickness used in the experiment is approximately 0.7 μm. However, creating a mesh for such a small thickness was difficult and led to the artifacts in the final solution. Therefore, the heat capacity of the ITO was set to 0.01 J/(kg-ºC), making its thermal resistance negligible. The sensitivity to the ITO thickness is shown in Figure 4-16 (bottom). Overall, Figure 4-16 shows that the final solution is nearly independent of the selected values of the mesh size, time step, and ITO thickness.

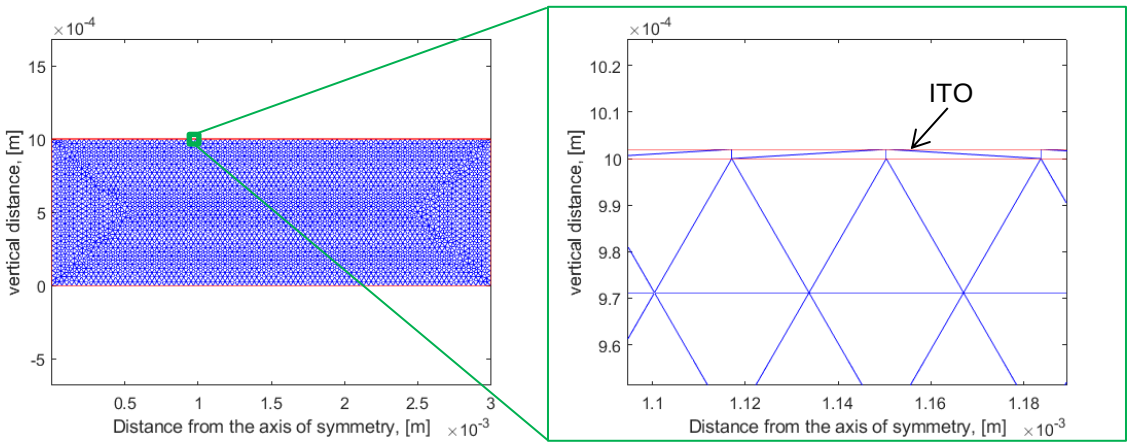

Figure 4-15. Triangular mesh used for the simulation

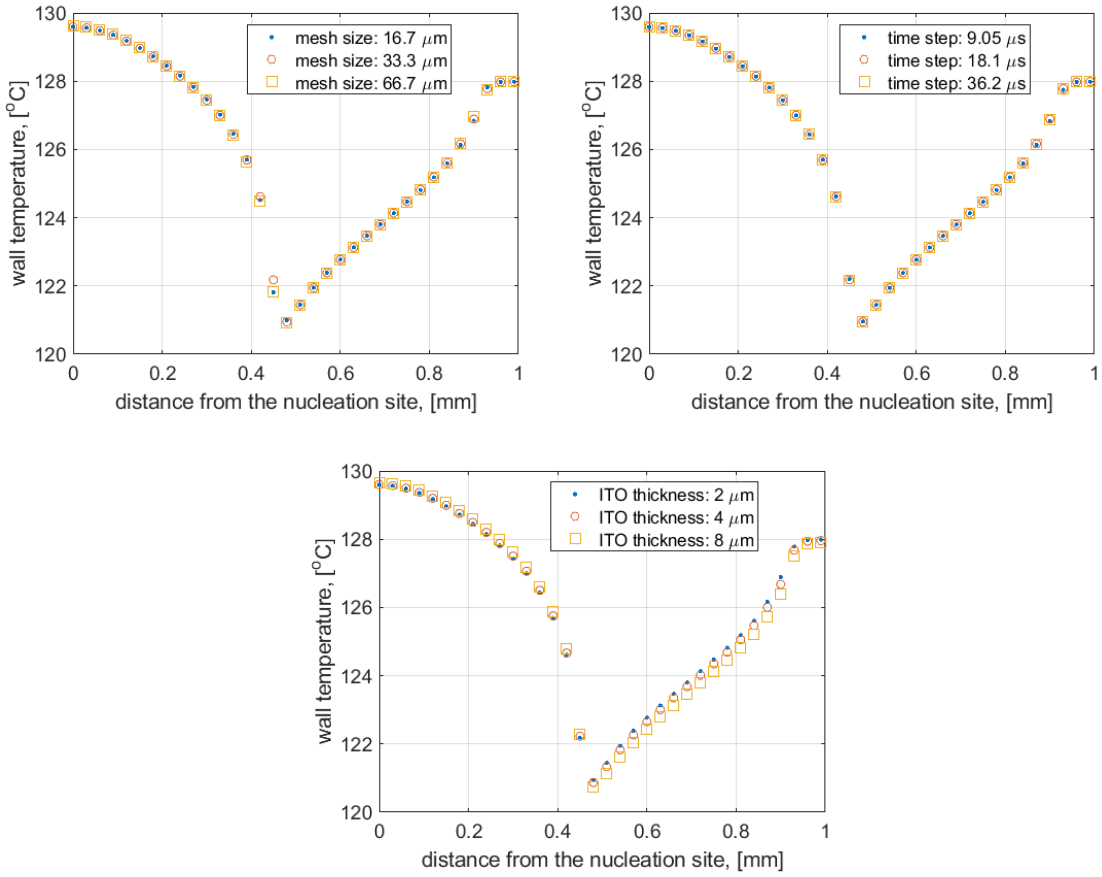

Figure 4-16. Wall temperature predicted by the last time step of the simulation, showing the sensitivity to the mesh size (top left), time step (top right), and ITO thickness (bottom)

Adiabatic boundary conditions were used on all sides of the computational domain with the exception of the top ITO surface. On top of the ITO, time- and space-dependent heat transfer coefficient was applied. The applied HTC was represented by a lookup table based on the HTC values shown in Figure 4-14. The color maps of the lookup tables are shown in Figure 4-17. Areas covered by microlayer are represented as areas with high HTC in Figure 4-17. Region to the left of the microlayer front was assumed to be dry and HTC of zero was applied there. Areas to the right of the microlayer were cooled by the forced flow, hence forced convection HTC was applied there. ITO layer served as a volumetric heat source, mimicking the heat flux applied in the experiment. Temperature of the domain at a start of the simulation was set to the average wall temperature right before the nucleation of the bubble.

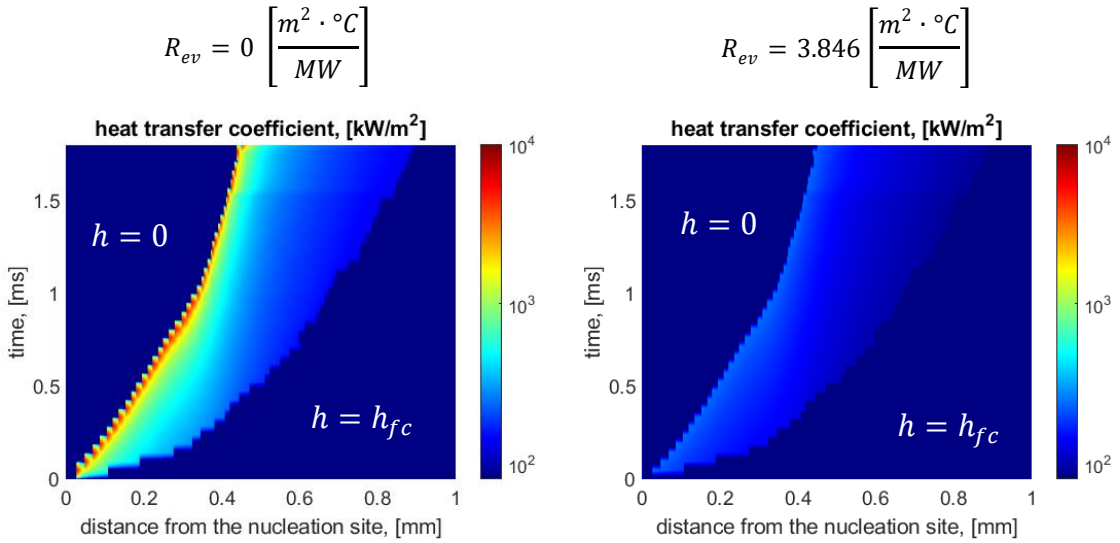

Figure 4-17. Space and time distribution of the top boundary condition

The results of the simulation are compared to the wall temperature measured by the IR camera. The distributions of the wall temperature together with the line temperature profiles taken at the bubble centerline are shown in Figure 4-18. As shown in Figure 4-18, temperature profile under the bubble is not symmetric due to the presence of flow. In contrast, the simulation performed here assumes axial symmetry. Because of this difference, we expect errors occurring near the inner edge of the microlayer and within the dry area. However, due to the extremely high microlayer HTC, the areas occupied by the microlayer should not be seriously affected.

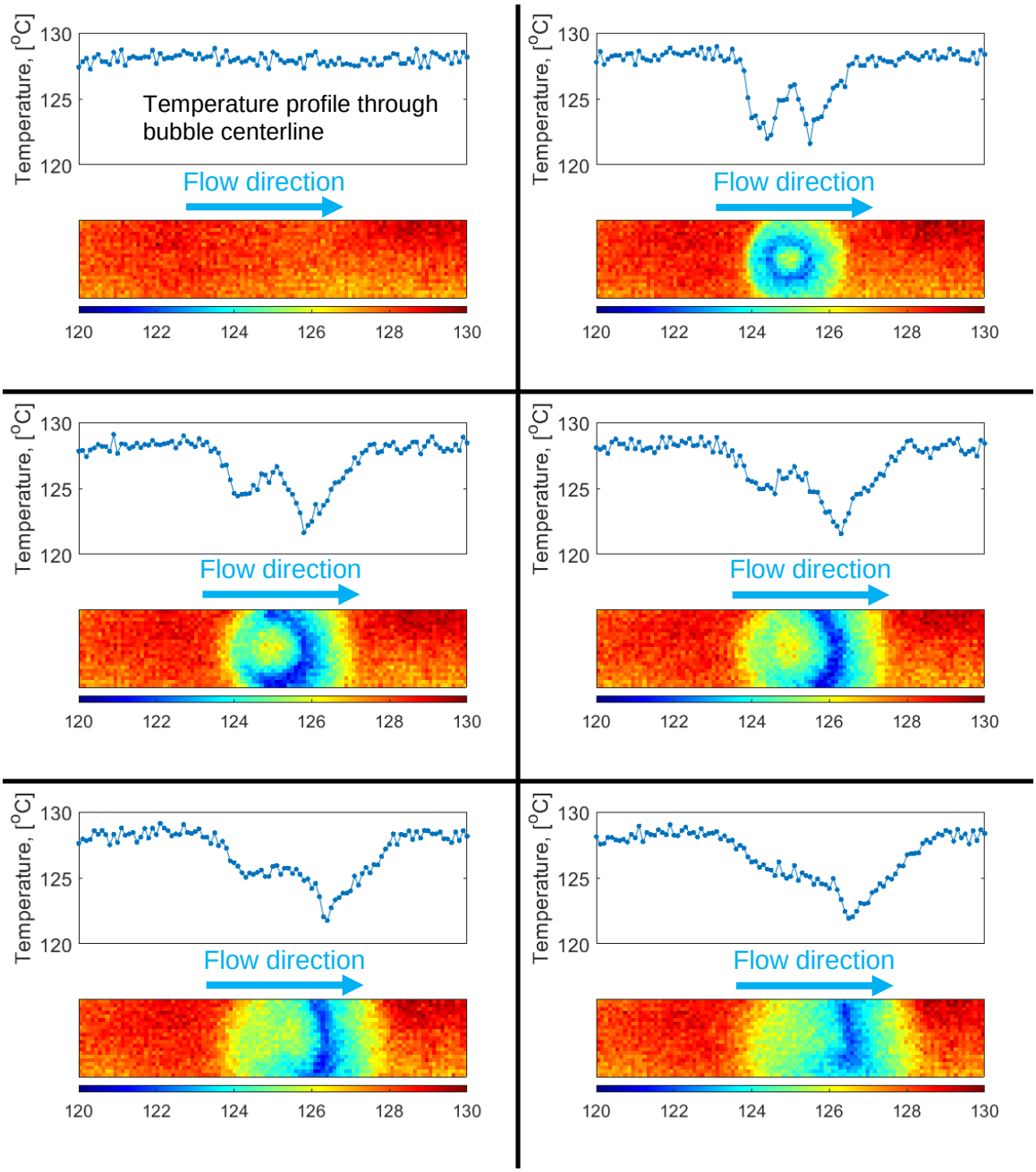

Figure 4-18. Temperature distribution under the growing bubble and its microlayer. In each figure the plot represents a line profile along the bubble centerline, while the color maps represent 2D spatial distribution captured by the IR camera.

The comparison between simulation results and IR camera measurements are shown in Figure 4-19 and Figure 4-20. Figure 4-19 shows the results for $R_{ev} = 3.846$ (m^2-ºC)/MW, and Figure 4-20 shows the results for $R_{ev} = 0$ (m^2-ºC)/MW. Figure 4-20 clearly shows that if evaporative thermal resistance is set to zero, the wall temperature is significantly underpredicted. At the same time, evaporative thermal resistance $R_{ev} = 3.846$ (m^2-ºC)/MW taken from Ref. [105] leads to a good agreement between the simulation and measurements. Note that the evaporative thermal resistance R_{ev} may depend on multiple

parameters, including the working fluid, pressure, and heat flux. While the conditions of the present study are not the same as in Ref. [105], they are close (i.e., water was used as a working fluid in both studies, the pressure difference is only 0.5 bar and the heat fluxes are kept low to prevent excessive nucleation and bubble interaction). Therefore, we conclude that by using evaporative resistance from Ref. [105], we can accurately capture the heat transfer through the microlayer for the operating conditions considered in the present study. However, a reevaluation of the evaporative thermal resistance might be needed when different operating conditions or fluids are explored.

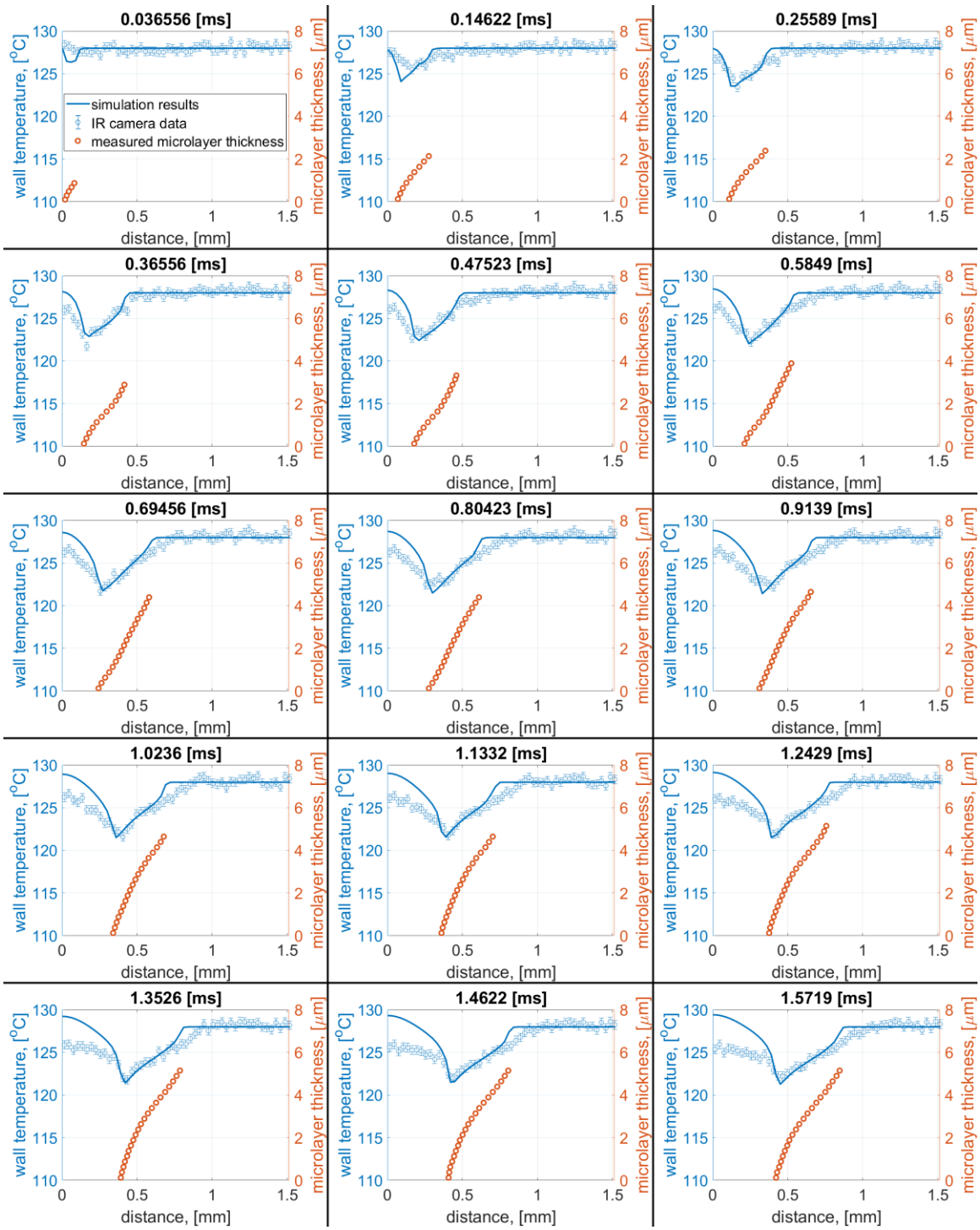

Figure 4-19. Comparison between the simulation and IR measurements for $R_{ev} = 3.846$ (m^2-ºC)/MW

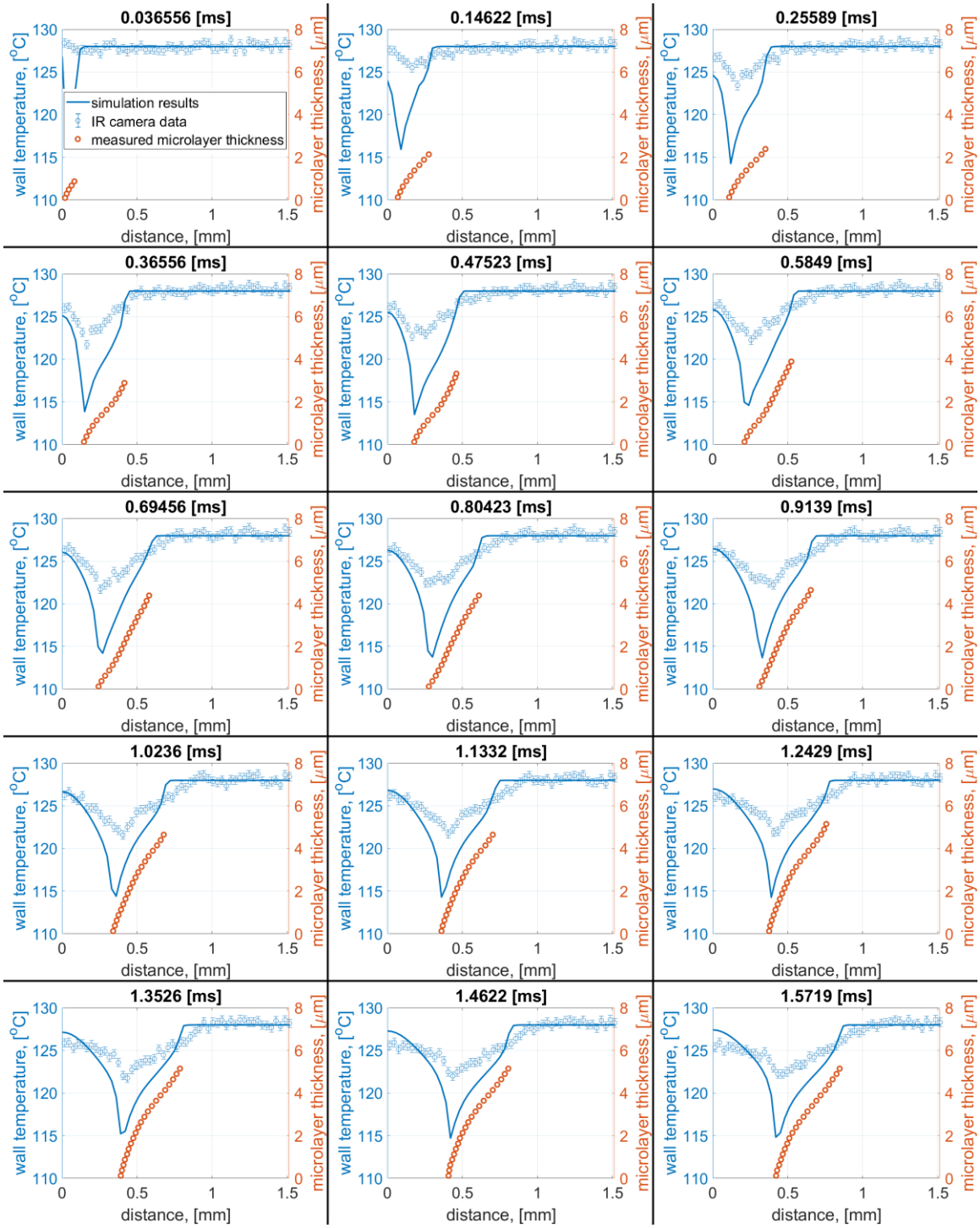

Figure 4-20. Comparison between the simulation and the IR measurements for $R_{ev} = 0$ (m^2-°C)/MW

Figure 4-19 demonstrates that the value of evaporative resistance obtained from Ref. [105] leads to a good match between the simulation results and IR measurements. Next, we

introduce mass transfer due to microlayer evaporation into the analysis to understand if evaporation alone can account for the microlayer depletion. To achieve this goal, the top boundary condition was changed from the time-dependent microlayer thickness measured in the experiment, to the initial microlayer thickness. The simulation is then completed and time and space dependent distribution of wall temperature is recorded. This distribution is then used to calculate the reduction in microlayer thickness due to evaporation at each time step and spatial position according to Equation (4-13)

$$\delta_{\mu L}(x;t) = \delta_{\mu L}\big(x;t_{ini}(x)\big) + \int_{t_{ini}(x)}^{t} \frac{T_{sat} - T_w}{\rho_l \cdot h_{fg} \cdot \left(\frac{\delta_{\mu L}}{k_l} + R_{ev}\right)} \cdot dt \tag{4-9}$$

where x is the spatial coordinate, t is time, and t_{ini} represents the time at which the microlayer first formed at the spatial coordinate x. Note that for each spatial coordinate x the time of the initial microlayer formation $t_{ini}(x)$ is different because while the leading edge of the microlayer is forming due to the movement of the ACL, the trailing portion of the microlayer undergoes depletion. Equation (4-13) can be rewritten in a discretized form to be directly applicable to the simulation. The discretized form is given by Equation (4-10)

$$\delta_{\mu L}(x_i;\, t_j) = \delta_{\mu L}(x_i;\, t_{j-1}) + \\ + \frac{1}{2} \cdot \left[\frac{\big(T_{sat} - T_w(x_i;\, t_{j-1})\big)}{\rho_l \cdot h_{fg} \cdot \left(\frac{\delta_{\mu L}(x_i;\, t_{j-1})}{k_l} + \frac{1}{h_{ev}}\right)} + \frac{\big(T_{sat} - T_w(x_i;\, t_j)\big)}{\rho_l \cdot h_{fg} \cdot \left(\frac{\delta_{\mu L}(x_i;\, t_j)}{k_l} + \frac{1}{h_{ev}}\right)} \right] \cdot (t_j - t_{j-1}) \tag{4-10}$$

where x_i represents the spatial coordinate of the ith cell, and t_j represents the jth time step. As a whole, Equation (4-14) represents a step-by-step numerical integral performed using a trapezoid rule. Once the depletion of the microlayer is completed and the new and adjusted microlayer thickness is known, the simulation is repeated again with this new time- and space-dependent microlayer thickness. The new microlayer thickness will lead to the new, more accurate distribution of the wall temperature, which is then used again to deplete the microlayer thickness. The whole process is repeated until convergence is achieved, providing a measure of microlayer depletion due to evaporation alone.

The initial microlayer thickness was estimated based on the time dependent microlayer thickness shown in Figure 4-13. To the best of author's knowledge, there are two methods that can be used to estimate the initial microlayer thickness. The first method only considers the microlayer thickness measured at the leading edge of the microlayer, as close as possible to the ACL. This approach assumes that the time passed since the formation of the microlayer at its leading edge is small enough to make microlayer depletion negligible. The second method was used in the work of Jung and Kim [106], where the initial microlayer thickness measured with the first method was increased based on the offset between the curves representing time-dependent microlayer thickness (i.e. curves similar to Figure 4-13). In the work of Jung and Kim [106] the microlayer thickness measured

using the second method is called “isothermal initial thickness”. It is author’s opinion that neither of the two methods provide an absolutely accurate measurement of the initial microlayer thickness. The method of Jung and Kim [106] attempts to capture the microlayer thickness as it would be if no evaporation was occuring (e.g. a saturated steam bubble injected into a pool of saturated water through a mcroscale orifice). However, in reality the microlayer grows and depletes at the same time but at different spatial positions. Such behavior will make the outer edge of the microlayer to be thinner because by the time it starts to form, a big portion of the microayer will have already depleted. Therefore, in the present study we adopt the first method of the initial microlayer thicness measurement. The first method will provide the lower limit of the initial microlayer thickness, and, to the best of author’s knowledge, is more accurate for the application to the realistic microlayer dynamics, in which both the formation of the microlayer and its depletion occur simultaneously. The process of obtaining the initial microlayer thickness using the first method is shown in Figure 4-21.

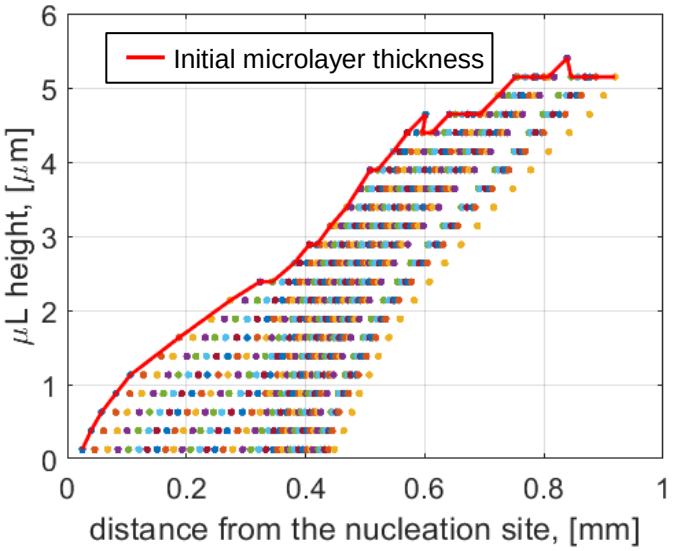

Figure 4-21. Microlayer thickness measured for the downstream portion of the bubble. Measurements are performed for the pressure of 1.5 bar, subcooling of 9.7 ºC and mass flux of 745 kg/(m^2-s). Colored dots represent time-dependent microlayer thickness, while solid red line represents initial microlayer thickness

The final outcome of combining the initial microlayer thickness measurement of Figure 4-21 and the iterative microlayer depletion procedure is shown in Figure 4-22. Solid orange line in Figure 4-22 represents the microlayer thickness calculated with the iterative microlayer depletion procedure, while orange circles represent experimentally measured, time-dependent microlayer thickness. Figure 4-22 shows that the solid orange line always remains above the orange circles, indicating that the microlayer depletion due to evaporation is much slower than what is observed experimentally. Our results suggest that both thermal and hydrodynamic depletion of the microlayer play a role. Additionally, both effects appear to be equally important, since a significant portion of the microlayer is depleted by evaporation, while also leading to a considerable discrepancy between

measured and predicted microlayer profiles. The outcome of the present section has two major implications:

1. The critical Capillary number shown in the regime map of Figure 4-12 may be affected by both the heat transfer and hydrodynamics. Since the critical Capillary number is based on the movement of the RCL, it will be fully governed by the depletion rate of the microlayer. We speculate, that the relative importance of thermal and hydrodynamic dewetting may be connected to the wettability of the boiling surface. ITO heaters used in the present study normally exhibit slightly hydrophilic behavior (i.e. contact angle slightly below 90º). Therefore, for such surfaces the dewetting due to evaporation and surface tension driven RCL recession could be important. In contrast, for superhydrophilic surfaces, the hydrodynamic dewetting could only occur through the presence of the residual flow inside the microlayer. While there are evidences supprting the idea of a strong residual flow [106], it is not clear whether the effect of the residual flow could be dominant over the surface tension driven dewetting. In contrast, there are multiple studies that demostrate the strong dependence of the microlayer characteristics and critical Capillary number on the contact angle [20], [25], [26]. Therefore, future work should be concentrated on examining microlayer formation on surfaces with different wettabilities, since it may affect the dominating mechanism of microlayer depletion. The change in microlayer depletion mechanism may alter the critical Capillary number, changing the regime map of Figure 4-12 and altering the limit of microlayer formation at high pressure.
2. The presence of the hydrodynamic microlayer depletion has implications for the heat flux partitioning. Specifically, not all of the initial microlayer volume may contribute the microlayer evaporation heat flux. Therefore, understanding the relative importance of thermal and hydrodynamic dewetting for realistic water boiling experiments could provide a criterion for the relative magnitudes of thermal and hydrodynamic depletion of the microlayer, hence leading to a more accurate formulation of the evaporation partitioned heat flux.

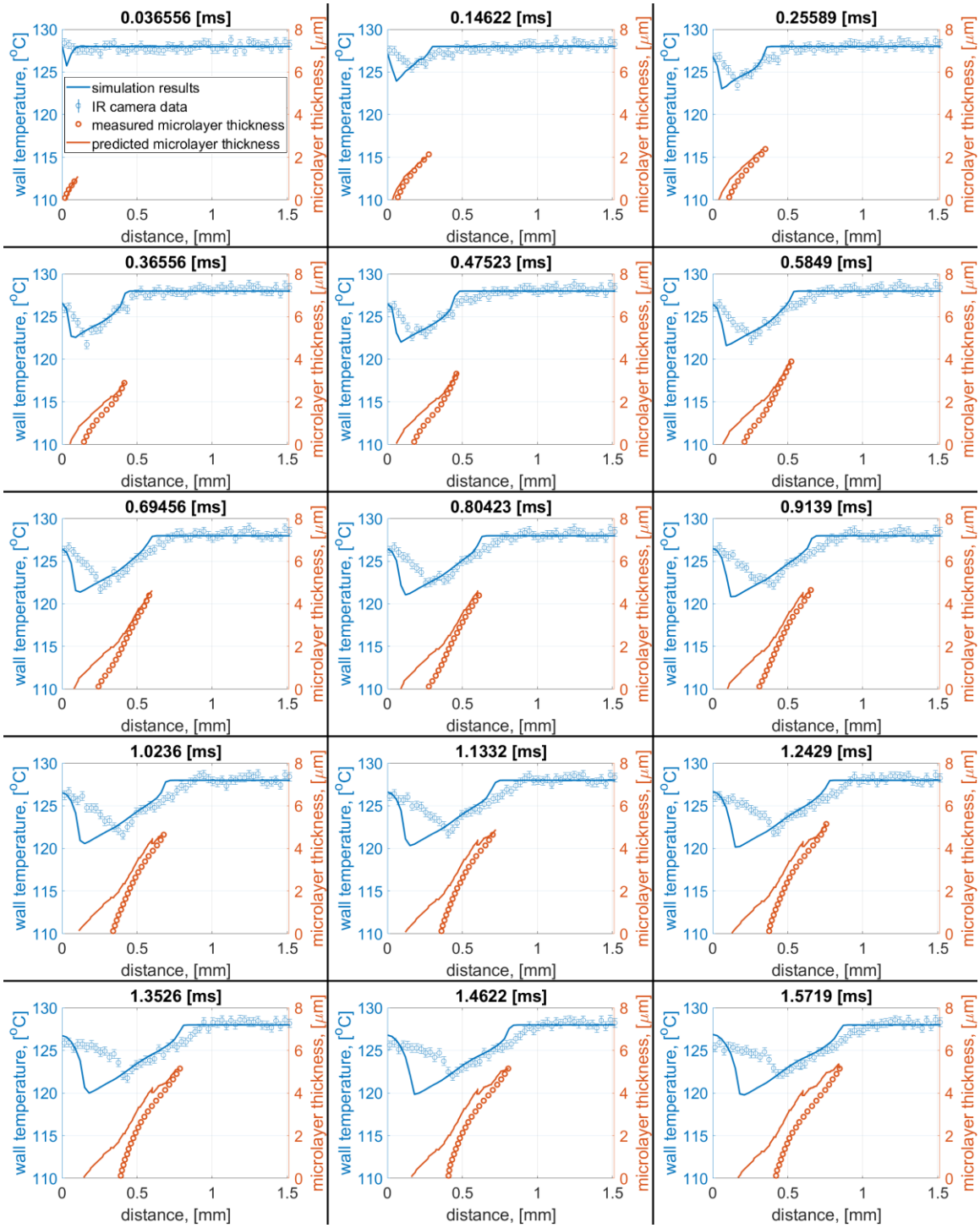

Figure 4-22. Comparison between the measured and simulated time-dependent microlayer thickness. Simulated microlayer profile is based on the initial microlayer thickness and microlayer depletion due to evaporation alone. The analysis was made for $R_{ev} = 3.846$ (m^2-°C)/MW

4.4. RELATIVE IMPORTANCE OF THE TRIPLE CONTACT LINE EVAPORATION

Previous Sections demonstrated that microlayer evaporation becomes insignificant for pressures above 3 bar. Therefore, for the majority of high-pressure applications the only way for the vapor phase to be created is through the evaporation of the superheated liquid layer close to the boiling surface or the evaporation of the triple contact line (TCL). Among the two mechanisms, only TCL evaporation is considered when a true wall HFP model is constructed. In this section we examine the importance of the TCL evaporation relative to the total heat flux at the boiling surface.

The region where the TCL evaporation happens is shown schematically in Figure 4-23. The rest of the bubble footprint that is typically considered to be in the direct contact with vapor is actually covered by a very thin layer of liquid, called the adsorbed layer. The thickness of this layer is determined by the disjoining pressure between the liquid and the substrate. The disjoining pressure decays as the distance from the wall to the power 3 (i.e. $p_D \propto 1/y^3$, where y is the wall distance). This leads to very high disjoining pressures close to the wall, preventing any evaporation of liquid films that have the size in the order of a few nanometers, resulting in the absence of any evaporative heat flux within the adsorbed layer. However, in the vicinity of the triple contact line, the thickness of the liquid film becomes much larger, leading to the decrease in local disjoining pressure at the liquid-vapor interface, allowing for evaporation to happen. While the liquid film near the TCL is larger than the adsorbed layer, it still has the thickness that is on the order of tens of nanometers. Such small thickness makes conductive thermal resistance negligible, leading to high evaporative heat flux. Measuring the evaporation rate at the triple contact line of a bubble is a challenging task because of the small scales involved in this process. Therefore, in the present work we perform analytical calculations of the TCL heat transfer using the model of Stephan and Hammer [107] with certain modifications necessary for its application to water and its decoupling from the conduction in the substrate. The model of Stephan and Hammer will allow us to estimate the power removed by the TCL evaporation per unit length of the TCL. The values predicted by the analysis are then combined with the actual measurements of TCL density in order to calculate the heat flux removed by the TCL evaporation in high pressure boiling.

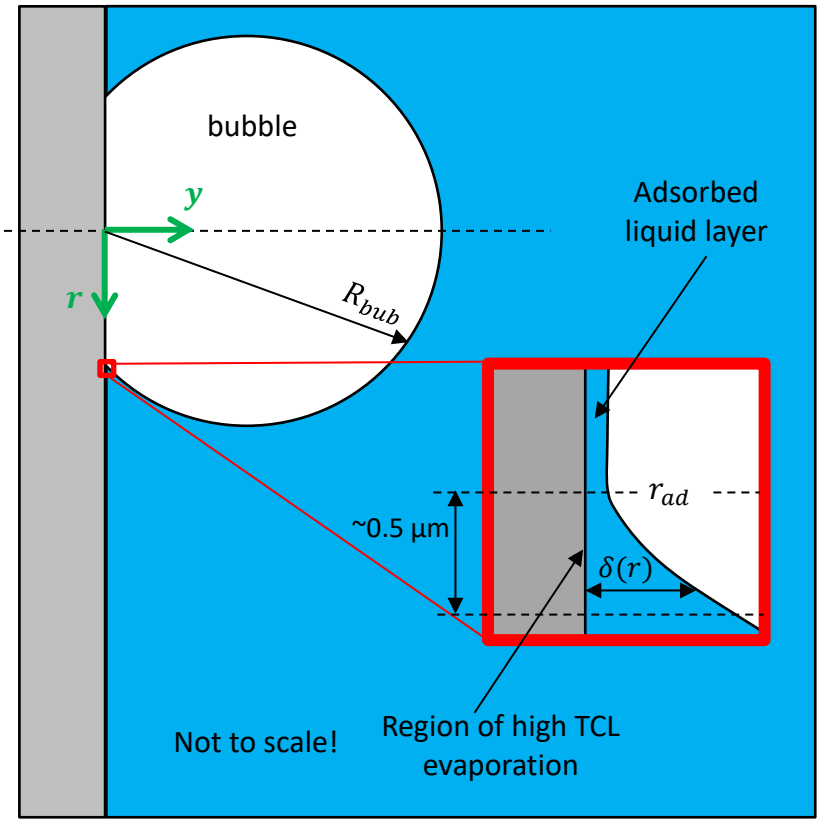

Figure 4-23. Schematic representation of the region dominated by the triple contact line evaporation

Since the derivation of the model is described in detail by Ref. [107], only the final set of equations will be presented here. The heat flux due to the evaporation of the TCL is a strong function of the local liquid film thickness. Its values can be calculated by solving a set of differential Equations (4-11) through (4-13).

$$\frac{d^2\delta}{dr^2} = \left[\frac{1}{\sigma}\cdot\left(p_c - \frac{A_H}{\delta^3}\right) - \frac{1}{r}\cdot\frac{\frac{d\delta}{dr}}{\sqrt{1+\left(\frac{d\delta}{dr}\right)^2}}\right]\cdot\left[1+\left(\frac{d\delta}{dr}\right)^2\right]^{\frac{3}{2}} \tag{4-11}$$

$$\frac{dp_c}{dr} = -\frac{3}{2\pi\cdot r}\cdot\frac{\nu_l\cdot\dot{Q}}{h_{fg}\cdot\delta^3} \tag{4-12}$$

$$\frac{d\dot{Q}}{dr} = 2\pi\cdot r\cdot\frac{T_w - T_{sat}\cdot\left(1+\frac{p_c}{h_{fg}\cdot\rho_l}\right)}{R_i + \frac{\delta}{k_l}} \tag{4-13}$$

where δ is the local thickness of the liquid film, r is the radial distance from the bubble center, σ is the surface tension, p_c is the capillary pressure, A_H is the Hamaker constant, ν_l

is the kinematic viscosity of the liquid, h_{fg} is the latent heat of vaporization and T_w is the wall temperature. $\dot{Q}$ is the total power transferred in the area between the adsorbed layer boundary r_{ad} and the coordinate r. $\dot{Q}$ is calculated using Equation (4-14)

$$\dot{Q} = \int_{r_{ad}}^{r} q''(r) \cdot 2\pi \cdot r \cdot dr \tag{4-14}$$

where $q''(r)$ is the local heat flux at the distance r calculated using Equation (4-15).

$$q''(r) = \frac{T_w - T_{sat} \cdot \left(1 + \frac{p_c}{h_{fg} \cdot \rho_l}\right)}{R_i + \frac{\delta}{k_l}} \tag{4-15}$$

R_i in Equations (4-13) and (4-15) represents the evaporative thermal resistance and is calculated using Equation (4-16)

$$R_i = \frac{T_{sat} \cdot \sqrt{2\pi \cdot R_g \cdot T_{sat}}}{h_{fg}^2 \cdot \rho_g} \cdot \frac{2 - f}{2 \cdot f} \tag{4-16}$$

where R_g is the gas constant and f is the accommodation coefficient. In order to solve Equations (4-11) through (4-13) a set of initial conditions at the boundary of the adsorbed liquid layer (i.e. at $r = r_{ad}$) is needed. The set of initial conditions used in Ref. [107] is given by Equation (4-17)

$$\begin{cases} \delta(r = r_{ad}) = \left(\frac{A_H}{p_{c,ad}}\right)^{\frac{1}{3}} \\ \left.\frac{d\delta}{dr}\right|_{r=r_{ad}} = 0 \\ p_c(r = r_{ad}) = p_{c,ad} \\ \dot{Q}(r = r_{ad}) = f(R_{bub}) \end{cases} \tag{4-17}$$

where $p_{c,ad}$ is the capillary pressure at the adsorbed liquid layer, also known as the disjoining pressure. $p_{c,ad}$ is calculated with Equation (4-18).

$$p_{c,ad} = \left(\frac{T_w}{T_{sat}} - 1\right) \cdot h_{fg} \cdot \rho_l \tag{4-18}$$

The initial value of $\dot{Q}$ is adjusted to match the curvature of bubble when r is large. The curvature of the liquid film K is calculated with Equation (4-19), while the curvature of the bubble K_{bub} is calculated with Equation (4-20), assuming that the bubble can be modeled as a truncated sphere with the radius R_{bub}.

$$K = \frac{\frac{d^2\delta}{dr^2}}{\left[1+\left(\frac{d\delta}{dr}\right)^2\right]^{\frac{3}{2}}} + \frac{1}{r}\cdot\frac{\frac{d\delta}{dr}}{\sqrt{1+\left(\frac{d\delta}{dr}\right)^2}} \tag{4-19}$$

$$K_{bub} = \frac{1}{R_{bub}} \tag{4-20}$$

In the present work the set of initial conditions was modified because it was not possible to achieve a converged solution using Equation (4-17). This problem is likely caused by the setup of the model in the present work compared to Ref. [107]. In Ref. [107] the model for TCL evaporation was coupled with the simulation of conduction in the substrate as well as the surrounding liquid. The purpose of the present analysis is to provide the upper limit for TCL evaporation, hence the analysis is simplified by only considering the region of TCL evaporation and fixing the wall superheat to a constant value. In order to reach a converged solution with the present setup, the initial conditions were modified. The new set of initial conditions are shown in Equation (4-21)

$$\begin{cases} \delta(r = r_{ad}) = \left(\frac{A_H}{p_{c,ad}}\right)^{\frac{1}{3}} \\ \left.\frac{d\delta}{dr}\right|_{r=r_{ad}} = f(T_w;\ R_{bub}) \\ p_c(r = r_{ad}) = p_{c,ad} \\ \dot{Q}(r = r_{ad}) = f(R_{bub}) \end{cases} \tag{4-21}$$

The only difference between Equations (4-17) and (4-21) is in the initial conditions for the first derivative of the film thickness. This initial condition was set to a value that is as small as possible, while still giving a converged solution. Therefore, the solution process used in the present study can be summarized as follows:

1) Set the initial condition for $\left.\frac{d\delta}{dr}\right|_{r=r_{ad}}$ to a value large enough to ensure convergence
2) Iterate on the solution by varying the initial condition for $\dot{Q}(r = r_{ad})$ until the correct curvature is achieved
3) Decrease the value of $\left.\frac{d\delta}{dr}\right|_{r=r_{ad}}$ and repeat step (2).

4) If the solution is converged, continue decreasing the value of $\left.\frac{d\delta}{dr}\right|_{r=r_{ad}}$ until the convergence is no longer achieved.
5) The lowest value of $\left.\frac{d\delta}{dr}\right|_{r=r_{ad}}$ gives the most accurate solution. This statement will be supported by the sensitivity analysis of the solution to the value of $\left.\frac{d\delta}{dr}\right|_{r=r_{ad}}$, which is presented later.

Similar to Ref. [107], the fourth order Runge-Kutta method was used to numerically integrate Equations (4-11) through (4-13). It should be noted that the convergence issue encountered in the present study does not relate to the numerical method used for the integration. In order to confirm this, several other methods were applied to the problem, including built-in Matlab functions for solving differential equations, as well as the implicit Crank-Nicolson scheme. All methods resulted in a similar convergence limit.

Since multiple modifications to the solution process were made in the present work compared to Ref. [107], the first step in the analysis was to ensure that the present methodology can replicate the results presented in Ref. [107]. Using thermophysical properties of R114 [108], [109] and system parameters from Ref. [107] (i.e. wall superheat $\Delta T_w = 3.5$ °C, pressure $p = 2.47$ bar and bubble radius $R_{bub} = 125$ μm) while also setting $\left.\frac{d\delta}{dr}\right|_{r=r_{ad}} = 3 \cdot 10^{-4}$ m/m the numerical integration of Equations (4-11) through (4-13) was performed and the results are compared to the work of Stephan and Hammer [107] in Figure 4-24. The main difference between the results of the present analysis and Ref. [107] appears to be in translation along the x-axis. Such discrepancy is expected, since the introduction of a positive perturbation in $\left.\frac{d\delta}{dr}\right|_{r=r_{ad}}$ will drive the liquid film thickness to increase faster. Nevertheless, both the slope of the liquid film thickness (Figure 4-24 left) and the shape of heat flux distribution (Figure 4-24 right) are very similar. In fact, the most important parameter for the present analysis is the integral of the heat flux curve (Figure 4-24 right) since such integral will represent the linear power of the triple contact line (i.e. q', [W/m]). Since both curves differ by translation only, the final integral will be unchanged.

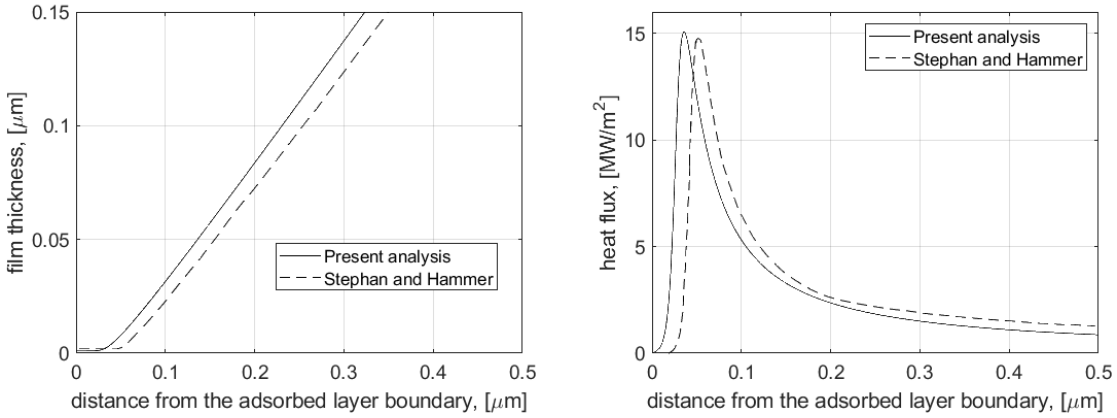

Figure 4-24. Comparison between the present analysis and the work of Stephan and Hammer [107]. Thickness of the liquid film near the TCL is shown on the left, while the heat flux due to the film evaporation is shown on the right. All calculations were performed for R114, wall superheat of $\Delta T_w = 3.5$ ºC, pressure $p = 2.47$ bar, bubble radius $R_{bub} = 125$ µm, accommodation coefficient $f = 1$ and the Hamaker constant $A_H = 2 \cdot 10^{-21}$ J

In addition, the sensitivity to $\left.\frac{d\delta}{dr}\right|_{r=r_{ad}}$ was tested based on the R114 case. The comparison between the results of the analysis for different values of $\left.\frac{d\delta}{dr}\right|_{r=r_{ad}}$ are shown in Figure 4-25. Notably, the strong difference in the slope of the liquid film and the shape of the heat flux curve only appear for the values of $\left.\frac{d\delta}{dr}\right|_{r=r_{ad}}$ that are larger than $3 \cdot 10^{-2}$, suggesting that for small values of $\left.\frac{d\delta}{dr}\right|_{r=r_{ad}}$ the solution is insensitive to this initial condition, leading only to the translation of the resulting curves along the x-axis. Overall, the comparison between the current approach and the results presented in Ref. [107] suggests the validity of the modifications made to the model of Stephan and Hammer, specifically when the linear power of the TCL is the desired output of the analysis.

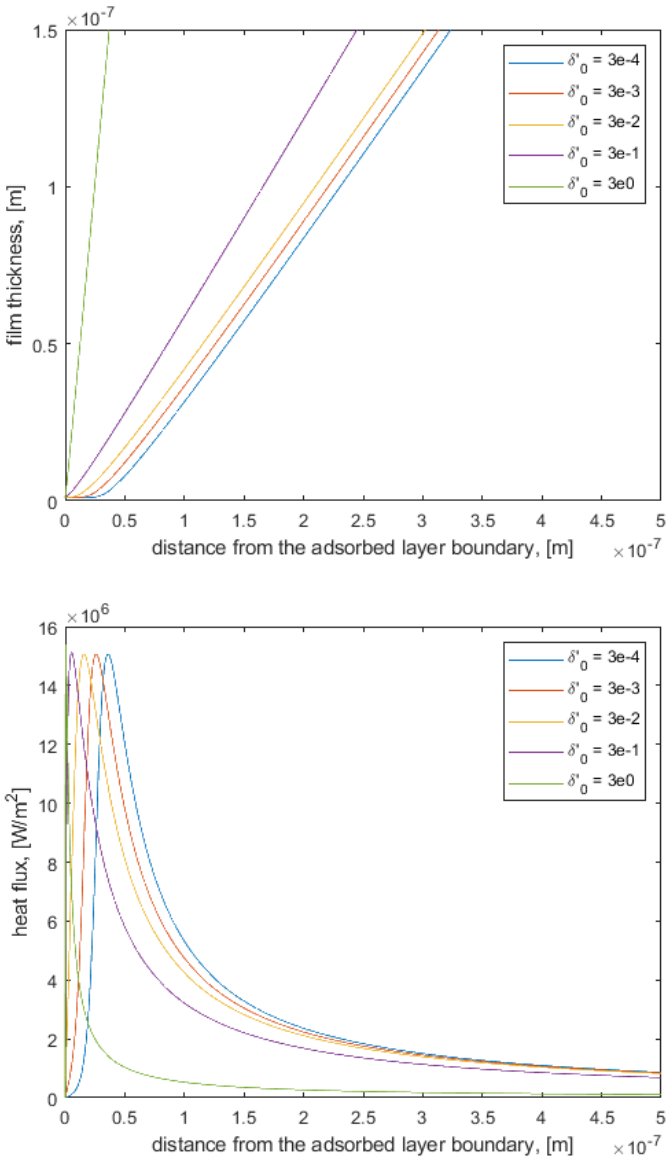

Figure 4-25. Sensitivity of the present analysis to the initial value of $\frac{d\delta}{dr}$

In order to extend the present analysis to water at high pressure, a set of input parameters must be identified. The Hamaker constant for water depends on the material of the boiling surface. Several values of the Hamaker constant for water can be found in Ref. [110]. Overall, the Hamaker constant for water-oxide systems falls between $1 \cdot 10^{-20}$ and $10 \cdot 10^{-20}$ J. In the present work indium-tin oxide (ITO) was used as the boiling surface. Since the exact value of the Hamaker constant for ITO – water system is unknown, the middle of the range for oxides (i.e. $A_H = 5 \cdot 10^{-20}$ J) was used.

For the estimation of TCL heat flux, a test performed at the pressure of 10.5 bar and the mass flux of 500 kg/(m^2-s) was selected. This test was chosen because of the relatively large bubble sizes, reducing the uncertainty in the measurements of the contact line density

and the dry spot radius. Such measurements are shown in Figure 4-26. Figure 4-26 (right) shows that the average dry spot radius remains approximately constant across all heat fluxes. For the calculation of the TCL heat flux we used the representative value of 50 μm. This value is used in place of the adsorbed layer radius r_{ad}. The radius of the bubble compared to the dry spot can be estimated using Figure 4-27, which shows the phase detection image in which both the bubble and its dry spot are distinguished. For the case shown in Figure 4-27 the diameter of the bubble is approximately 2.5 times larger than the diameter of the dry spot. Therefore, we can use the bubble radius $R_{bub} = 125$ μm. Note that Figure 4-27 provides only a rough estimation of the relative sizes between the dry spot and the bubble. In high heat fluxes, bubbles will interact with each other and may coalesce with the vapor clots, making their size and shape to change in a complex way. However, we believe that the approximation shown in Figure 4-27 is sufficient for the present analysis. For the wall superheat a value of 25 ºC was chosen, which is representative of the pressure of 10.5 bar. Since the purpose of the present analysis is to estimate the upper limit for the TCL evaporation, the condensation coefficient f was set to 1, leading to high evaporation heat transfer.

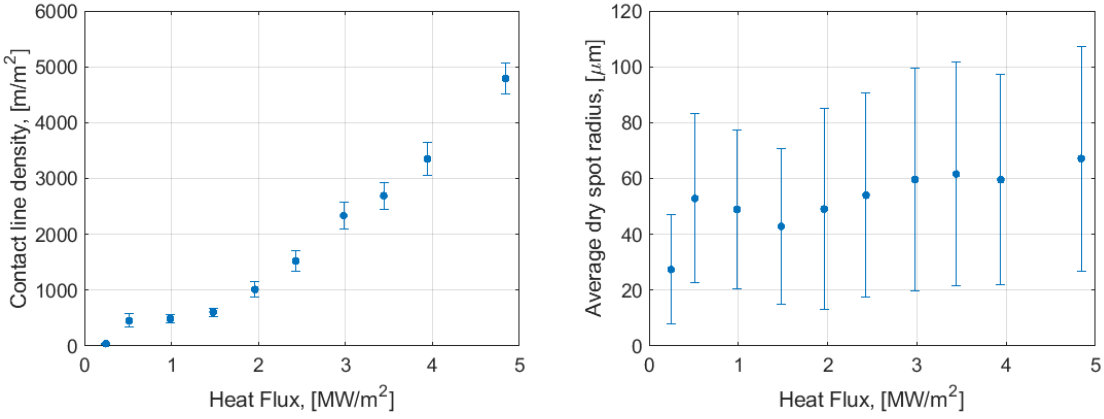

Figure 4-26. Contact line density (left) and average dry spot radius (right) measured for the pressure of 10.5 bar, subcooling of 10 ºC and the mass flux of 500 kg/(m^{2}s). Error bars represent the standard deviation of the measurements

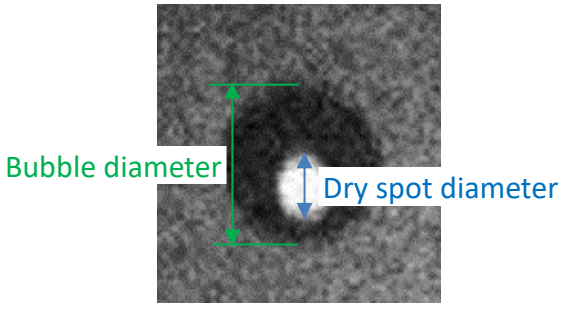

Bubble diameter ≈ 2.5 · Dry spot diameter

Figure 4-27. Estimation of the bubble diameter relative to the dry spot diameter

The results of the solution for water are shown in Figure 4-28. Due to high latent heat of vaporization and wall superheat, the TCL heat flux for water is two orders of magnitude higher than it is for R114. In order to estimate the linear power of the TCL, the heat flux curve (Figure 4-28 right) was integrated between r_{ad} and R_{bub} according to Equation (4-22)

$$q'_{TCL} = \int_{r_{ad}}^{R_{bub}} q''(r) \tag{4-22}$$

leading to the value of $q'_{TCL} = 255.5$ W/m. Using this value and the measurements of the contact line density shown in Figure 4-26 (left), the fraction of the heat flux attributed to the TCL evaporation is calculated using Equation (4-23)

$$\alpha_{TCL} = \frac{q'_{TCL} \cdot CLD}{q''_{tot}} \tag{4-23}$$

where CLD stands for the contact line density and q''_{tot} is the applied heat flux. The final results are shown in Figure 4-29. Figure 4-29 shows that TCL evaporation could reach 20% of the applied heat flux. However, the results of the present analysis represent the upper bound of the TCL evaporation heat flux. First, previous section demonstrated that a high value of evaporative thermal resistance and low accommodation coefficient are typical for water. In the analysis of the TCL heat flux we used a low value of evaporative thermal resistance, which might not be representative of water. Additionally, extremely high heat fluxes shown in Figure 4-28 will inevitably drive the wall temperature down, further lowering TCL heat flux. Therefore, we expect the real TCL heat flux partitioning to be considerably lower. Nevertheless, the estimation of the upper limit to the TCL evaporation heat flux could be useful in understanding its contribution to the overall evaporation heat flux.

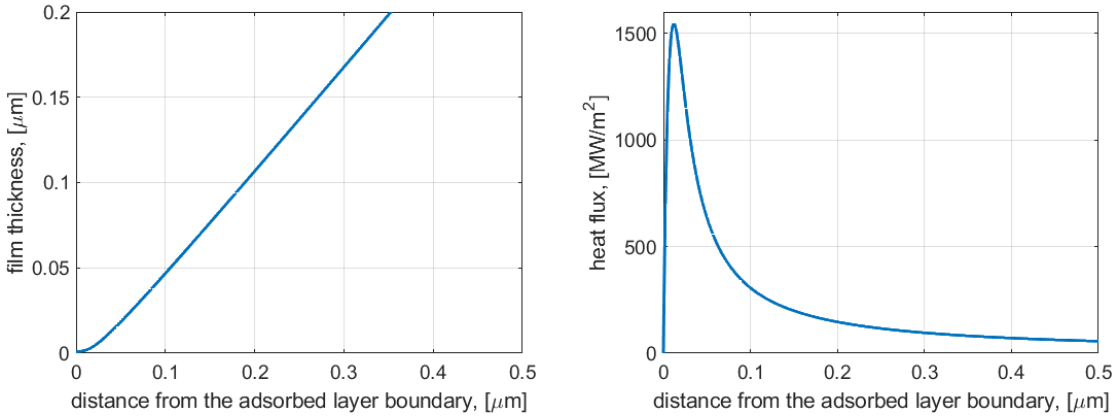

Figure 4-28. Thickness of the liquid film near the TCL (left) and the heat flux due to the film evaporation (right). All calculations were performed for water, wall superheat of

$\Delta T_w = 25$ °C, pressure $p = 10.5$ bar, bubble radius $R_{bub} = 125$ µm, condensation coefficient $f = 1$ and the Hamaker constant $A_H = 5 \cdot 10^{-20}$ J

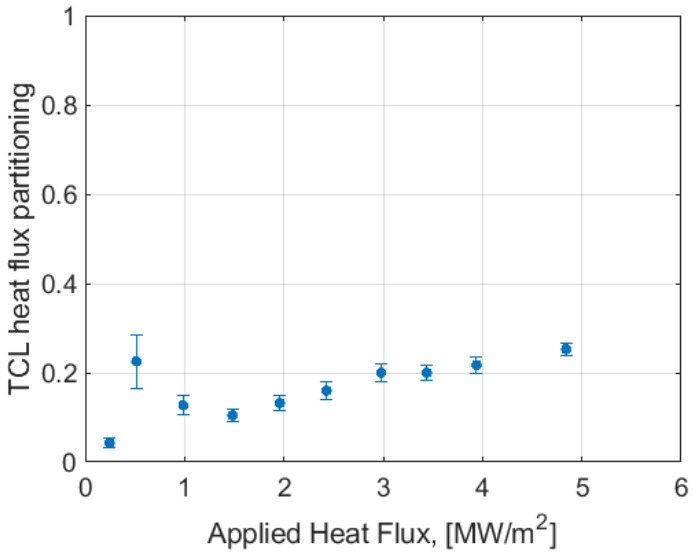

Figure 4-29. Evaluation of the upper bound for the TCL heat flux partitioning for the pressure of 10.5 bar, subcooling of 10 °C and the mass flux of 500 kg/(m^{2}s)

4.5. CONCLUSION TO THE CHAPTER AND FUTURE WORK

In this chapter we analyzed the change in evaporative heat transfer characteristics with respect to pressure. The focus of the present chapter was on microlayer and TCL evaporation. These two mechanisms describe the entire evaporation term within the true wall HFP model. Based on our experiments and analysis, we conclude that for pressures higher than 3 bar, evaporative heat flux becomes exceedingly small. First, the extent of microlayer shrinks considerably with pressure, leading to a complete disappearance of the microlayer at pressures higher than 3 bar. Second, the increase in TCL density with pressure is not sufficient to result in a significant contribution from TCL evaporation. The absolute upper limit of TCL evaporation for the case of 10.5 bar was estimated to be approximately 20%. Therefore, we conclude that in high pressure conditions the majority of the phase change processes happen near the wall. The bubbles grow by evaporating superheated liquid layer near the wall and condense when they depart into the bulk flow.

The future work should be concentrated on testing surfaces with different wettability at near-atmospheric pressures to better understand the mechanism of microlayer disappearance. In the present study we were able to connect the disappearance of the microlayer with the movement velocity of the RCL, which was characterized as the critical Capillary number. In the present study the critical capillary number was constant and unchanged by pressure. Further analysis revealed that RCL movement, which defines the value of the critical Capillary number, is governed by both thermal and hydrodynamic depletion of the microlayer. Since these two mechanisms are affected by multiple system,

fluid, and surface parameters, there is no reason to believe that the value of the critical Capillary number measured in the present study is universal. We believe, that surface wettability could play a major role in changing the critical capillary number, which could change the maximum pressure at which microlayer forms. In fact, the prediction of the critical Capillary number made by using the expression from the work of Demarly [19], which in turn was based on the DNS analysis of Guion [20], displays a strong dependence of the critical Capillary number on the contact angle (see Figure 4-11). Furthermore, the measured value of the critical Capillary number matches the prediction for the contact angle of 51.5º, meaning that the prediction is in the same ballpark as the measurement. Note that DNS analysis of Guion [20] only considered hydrodynamic dewetting. The fact that measured and predicted values of the critical Capillary number are similar further supports the importance of hydrodynamic effects for the microlayer depletions. Therefore, future studies should be focused on studying the mechanisms of microlayer formation and depletion at surfaces with different wettability to better understand the process of hydrodynamic microlayer depletion.

5. HEAT FLUX PARTITIONING IN HIGH PRESSURE BOILING

In this Chapter we analyze key boiling parameters which form the basis of heat flux partitioning models. A novel approach to the measurement of the key boiling parameters is adapted here, allowing us to measure bubble growth and wait times (t_g and t_w), as well as the total area visited by the dry spot A_{bub}[3] for virtually all nucleation events. Additionally, this approach allows us to identify the positions of nucleation sites and connect each nucleation event to a particular site, giving us a unique opportunity to study the variation of boiling parameters between nucleation events and nucleation sites. The observed variability in boiling parameters is crucially important for the development of models that predict such parameters, since it highlights the potential interconnection between the boiling parameters, which may not be captured in the present models. Additionally, we explore the effect of the averaging process on the predictions of the partitioned heat fluxes. Understanding the effect of the averaging process is important when comparing different experimental databases and when a particular database is used for the development of HFP models. The present Chapter starts with a demonstration of a strong variability in bubble departure frequency between the nucleation sites (Section 5.1). In Section 5.2 three averaging methods are developed to provide a mathematical basis for the comparison between their performance. The experimentally measured distributions of the key boiling parameters are presented in Section 5.3, highlighting their variation between the individual nucleation events and nucleation sites. In Section 5.4, estimations of partitioned heat fluxes from forced convection and transient conduction are made based on the measured values of boiling parameters and binary images derived from phase detection measurements (i.e. time- and space-resolved distributions of dry spots). All analysis presented in the present Chapter was done for the pressure of 10.5 bar. Selecting the pressure of 10.5 bar allowed us to minimized the potential uncertainties when using the dry area tracking algorithm (see Sub-Section 2.7.4 for details) because the bubble size remains relatively large.

5.1. IMPORTANCE OF THE SPECTRAL NUCLEATION SITES PROPERTIES

Spectral nucleation site properties were measured according to the procedure presented in Sub-Section 2.7.4. Figure 5-1 shows the spectral nucleation site maps together with the color maps representing the probability to find the dry area at a particular position on the boiling surface. The color maps were calculated by using binary images of dry spot distribution (see Sub-Section 2.7.4. for more details). Each pixel of a frame in a binary image has an intensity $I_B(x, y, f_i)$ which is either 1 or 0. Here x and y represent the spatial coordinates of the pixel, while f_i represents the frame number. The probability to find the dry area at a particular pixel of the boiling surface is calculated using Equation (5-1)

[3] See Sub-Section 2.7.4 for the definition of A_{bub} together with the procedure used to measure this parameter

$$P_{DA}(x,y) = \frac{\sum_{i=1}^{N_f} I_B(x,y,f_i)}{N_f} \quad (5\text{-}1)$$

where N_f is the total number of frames in a video. Figure 5-1 shows that regions with high dry area probabilities are occupied by tight clusters of nucleation sites with high bubble departure frequencies, while the regions with low dry area probabilities are occupied by fewer nucleation sites which also have much lower departure frequencies. Similar to low pressure experiments, the density of nucleation sites and bubble departure frequency increase with increasing heat flux, leading to higher dry area probabilities. In addition, the density of nucleation sites increases significantly at higher pressure. An important observation stemming from Figure 5-1 is that the nucleation sites with high departure frequencies are much fewer in number compared to the nucleation sites with low departure frequencies. The effect is better illustrated by Figure 5-2, which shows probability density functions of finding nucleation sites with a particular bubble departure frequency. As a reference, the bubble departure frequency calculated with the model of Cole [111] is also plotted in Figure 5-2. The Cole-Rohsenow correlation for bubble departure diameter was used as an input for the departure frequency model of Cole. Figure 5-2 shows that a single boiling surface can contain many nucleation sites with bubble departure frequencies spanning several orders of magnitude. Therefore, a single value of the departure frequency cannot properly characterize the breadth of departure frequencies present in the realistic boiling scenario. Additionally, there are orders of magnitude more nucleation sites with low frequencies than there are with high frequencies. These results have serious implications for the modeling of boiling heat transfer. While individually the nucleation sites with low nucleation frequencies might not contribute much to the overall heat removal from the boiling surface, as a whole their contribution cannot be ignored due to a large number of such sites. This finding highlights the importance of capturing the distribution of bubble departure frequencies among the nucleation sites when constructing a mechanistic HFP model, demonstrating that a single average value of the bubble departure frequency cannot be applied to all nucleation sites on the boiling surface. Interestingly, the lower limit of bubble departure frequencies shown in Figure 5-2 is not the actual limit to bubble departure frequency but rather related to the limit in the total recording time for each phase detection video. To reconstruct the distributions shown in Figure 5-2, the video duration of 0.25 seconds was used, making it impossible to measure frequencies lower than 4 Hz. However, Figure 5-2 shows that the distributions could extend further to the frequency range that is lower than 4 Hz. We speculate that multiple nucleation sites with even lower nucleation frequencies may still exist on the boiling surface. Furthermore, the probability of finding sites with lower frequencies may be much higher, making the contribution of low-frequency nucleation sites even more important. We may also consider a high-frequency cutoff related to the frame rate of the HSV camera. Since the HSV recording was taken at 30,000 Hz, we can define the upper frequency limit to be a half of the camera frame rate (i.e. we need at least one frame in which the bubble is present at the boiling surface and another frame in which the bubble is absent to identify separate nucleation events). Therefore, the high frequency limit will be 15,000 Hz. The distributions shown in Figure 5-2 do not exceed the frequencies of a few kilohertz, hence demonstrating

that bubbles do not exceed the high frequency limit of the measurement setup. Note that a large number of measurements is required to achieve the convergence of the distributions shown in Figure 5-2. In fact, over a million nucleation events were analyzed. Such a level of statistical significance can only be achieved with the combination of high-resolution measurements and automated post-processing. Interestingly, the distribution of bubble departure frequencies is similar in nature to the scale-free distributions of the bubble footprint area observed in the work of Zhang et al. [7]. This observation suggests that it is necessary to account for all temporal scales (i.e. all bubble departure frequencies) when considering the heat transfer on the boiling surface. The implications of this finding for HFP modeling frameworks is analyzed in the reminder of the Chapter.

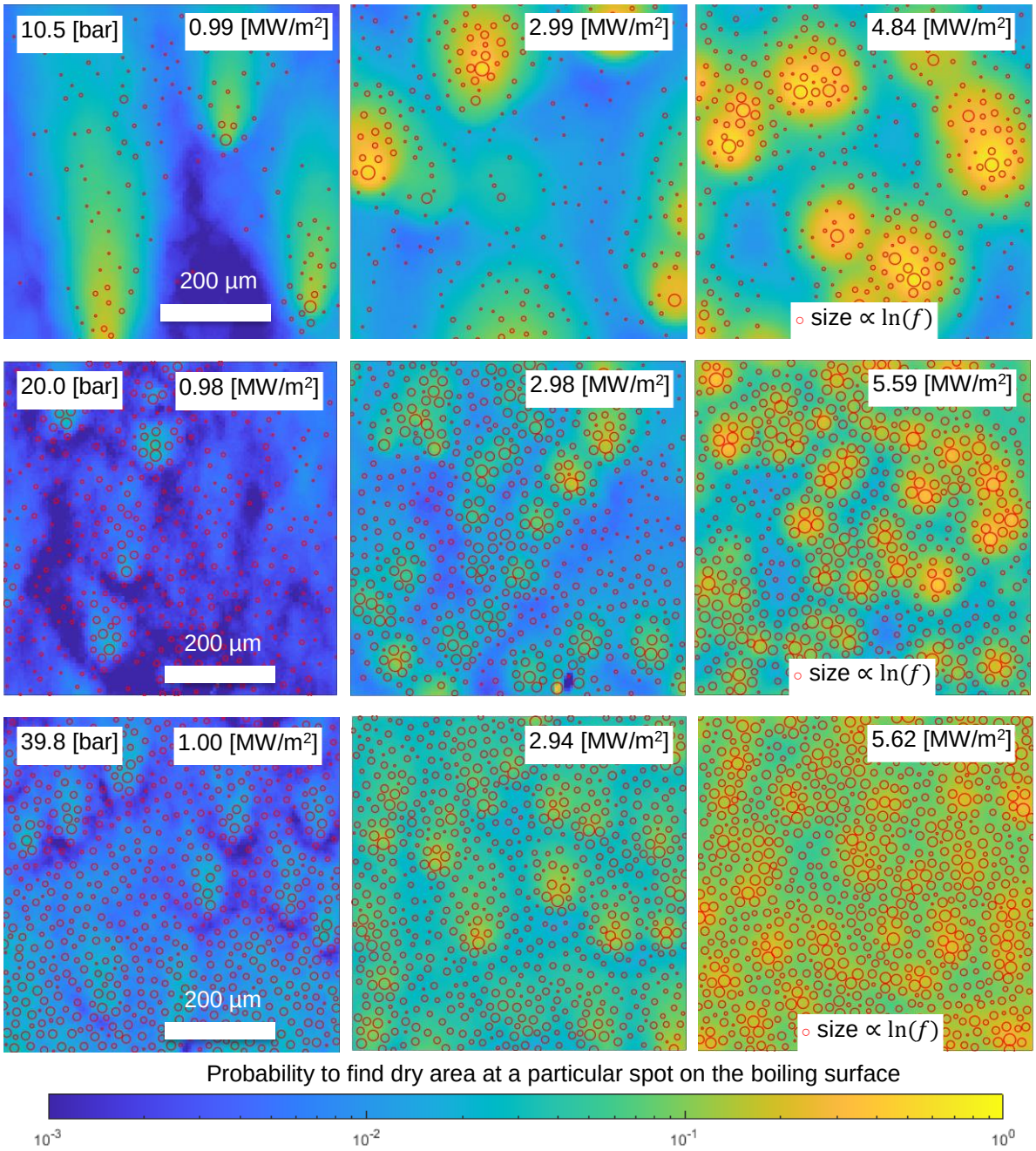

Figure 5-1. Spatial distribution of dry area probability overlaid with the spectral nucleation sites map. Each red circle represents the position of a nucleation site, while the size of each circle is proportional to the natural logarithm of the bubble departure frequency for each site.

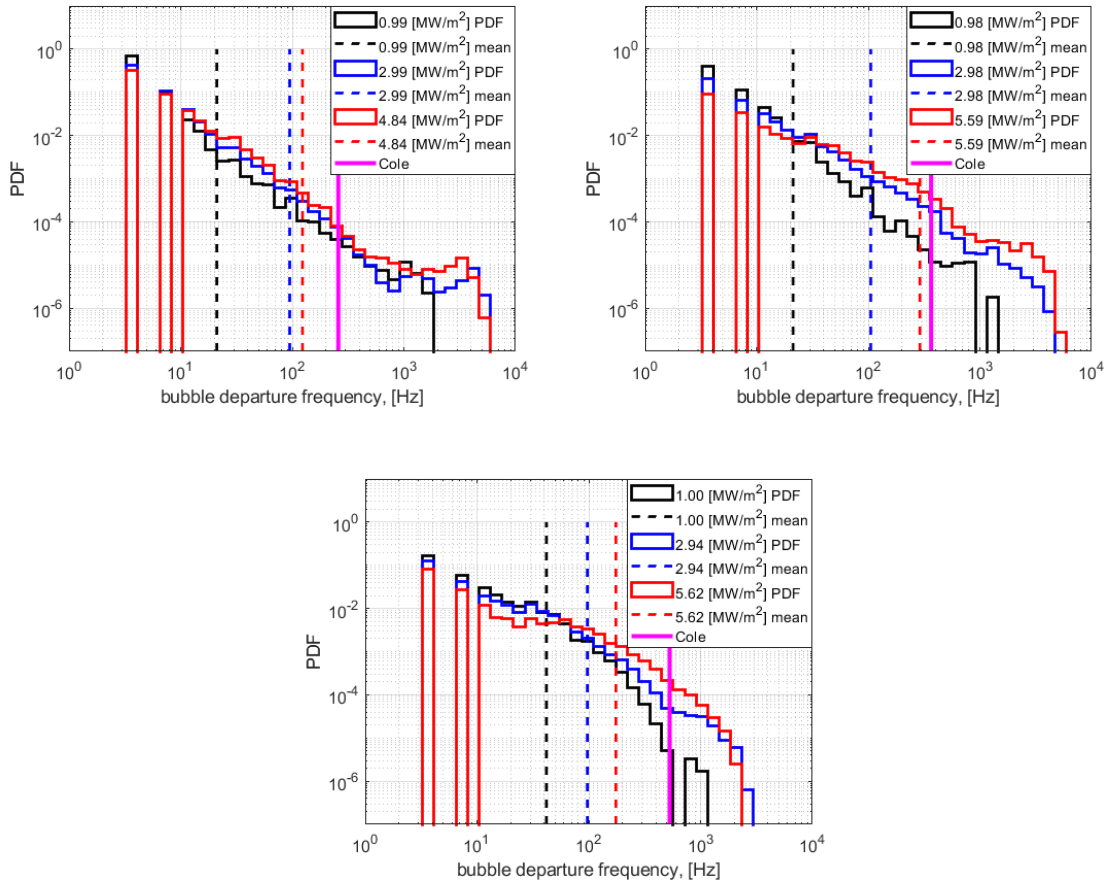

Figure 5-2. Probability density functions (PDFs) of bubble departure frequency. The distributions can be used to calculate the probability of finding a nucleation site within a defined range of bubble departure frequency.

5.2. RELEVANT PARAMETERS FOR HEAT FLUX PARTITIONING – DERIVATION

Figure 5-2 shows a strong variation of bubble departure frequency among the nucleation sites. In the next Section we will demonstrate that all boiling parameters exhibit strong variation not only between the nucleation sites, but also between individual nucleation events. The variation of boiling parameters makes it challenging to convert experimentally measured distributions into average values which are useful for the partitioning calculations. While this problem may seem purely experimental, in reality it affects the majority of models that are used to predict the boiling parameters. Since the only way to confirm the validity of a particular model is to compare it to the experimentally measured values of boiling parameters, many models were calibrated based on the available data and specific averaging procedures used in the experimental database. In the present Chapter we will examine the effect of the averaging method on the heat flux partitioning calculations. In the present Section we will introduce three Tiers of averaging methods, with Tier I being

the simplest, while Tier III being the most accurate. The details of each averaging method are presented next.

5.2.1. Heat flux due to transient conduction

Transient conduction was used in multiple non-evaporative heat enhancement models (see Table 1-3 for more details). After the departure of a bubble, the area that was previously occupied by it will be quenched by colder liquid that is rushing in to occupy the vacated space. Similar effects could be observed for sliding bubbles. In the present analysis we will designate the total area visited by the bubble during its growth and sliding periods as A_{bub}. The simplest approximation of the heat transfer in the wake of sliding and departed bubbles is the transient conduction within a semi-infinite body with a constant wall temperature. In the case of boiling, bulk fluid acts as a semi-infinite body with the wall temperature of the boiling surface T_w serving as the boundary condition. The heat flux due to transient conduction q''_{tc} as a function of time elapsed since the removal of a bubble t is given by Equation (5-2)

$$q''_{tc} = \frac{\varepsilon_l}{\sqrt{\pi}} \cdot \frac{T_w - T_b}{\sqrt{t}} \tag{5-2}$$

where ε_l is the liquid thermal effusivity and T_b is the bulk liquid temperature. Assume that for a bubble nucleated at a site s during the nucleation event e the total area visited during the growth and sliding is given by $A_{bub}(s;e)$. The transient conduction heat transfer rate (in [W]) is given by Equation (5-3)

$$\dot{q}_{tc}(s;e) = \frac{\varepsilon_l}{\sqrt{\pi}} \cdot \frac{T_w - T_b}{\sqrt{t}} \cdot A_{bub}(s;e) \tag{5-3}$$

The energy removed by transient conduction for the site s and event e is given by Equation (5-4).

$$Q_{tc}(s;e) = \int_0^{t_{tc}(s;e)} \dot{q}_{tc}(s;e) \cdot dt = \frac{2\varepsilon_l}{\sqrt{\pi}} \cdot A_{bub}(s;e) \cdot (T_w - T_b) \cdot \sqrt{t_{tc}(s;e)} \tag{5-4}$$

where $t_{tc}(s;e)$ is the time during which transient conduction is dominant, given by Equation (5-5)

$$t_{tc}(s;e) = \min[t_w(s;e); t^*] \tag{5-5}$$

Where $t_w(s;e)$ is the wait time for site s and event e and t^* is the characteristic time after which transient conduction becomes less effective than forced convection, given by Equation (5-6)

$$t^* = \frac{1}{\pi} \cdot \left(\frac{\varepsilon_l}{h_{fc}} \right)^2 \tag{5-6}$$

where h_{fc} is the forced convection heat transfer coefficient. The energy removed by a single nucleation site is given by Equation (5-7), while the energy removed by the entire boiling surface is given by Equation (5-8).

$$Q_{tc}(s) = \frac{2\varepsilon_l}{\sqrt{\pi}} \cdot (T_w - T_b) \cdot \sum_{e=1}^{N_e(s)} \left[A_{bub}(s;e) \cdot \sqrt{t_{tc}(s;e)} \right] \tag{5-7}$$

$$Q_{tc} = \frac{2\varepsilon_l}{\sqrt{\pi}} \cdot (T_w - T_b) \cdot \sum_{s=1}^{N_s} \sum_{e=1}^{N_e(s)} \left[A_{bub}(s;e) \cdot \sqrt{t_{tc}(s;e)} \right] \tag{5-8}$$

where $N_e(s)$ is the number of nucleation events for nucleation site s and N_s is the total number of sites on the boiling surface. Finally, the energy conserving form of the transient conduction heat flux is given by Equation (5-9)

$$q''_{tc} = \frac{2\varepsilon_l}{\sqrt{\pi}} \cdot (T_w - T_b) \cdot \frac{1}{A_{tot} \cdot t_{tot}} \cdot \sum_{s=1}^{N_s} \sum_{e=1}^{N_e(s)} \left[A_{bub}(s;e) \cdot \sqrt{t_{tc}(s;e)} \right] \tag{5-9}$$

where A_{tot} is the total area of the boiling surface and t_{tot} is the total time during which the boiling surface was observed.

Next, we will identify the relevant group of parameters for transient conduction heat flux as well as the proper averaging procedures for such parameters. Starting with Equation (5-7), we can define the power of site s using Equation (5-10)

$$\dot{Q}_{tc}(s) = \frac{Q_{tc}(s)}{t_{tot}} = \frac{2\varepsilon_l}{\sqrt{\pi}} \cdot (T_w - T_b) \cdot \frac{\sum_{e=1}^{N_e(s)} \left[A_{bub}(s;e) \cdot \sqrt{t_{tc}(s;e)} \right]}{\sum_{e=1}^{N_e(s)} [t_b(s;e)]} \tag{5-10}$$

where $t_b(s;e)$ is the bubble departure period for site s and event e. We can replace sums in Equation (5-10) with averages and also introduce the average bubble departure frequency for site s, $\bar{f}(s)$ calculated with Equation (5-11).

$$\bar{f}(s) = \frac{N_e(s)}{t_{tot}} = \frac{N_e(s)}{\sum_{e=1}^{N_e(s)} t_b(s;e)} = \frac{\cancel{N_e(s)}}{\langle t_b(s;e) \rangle_e \cdot \cancel{N_e(s)}} = \frac{1}{\langle t_b(s;e) \rangle_e} \tag{5-11}$$

With these adjustments Equation (5-10) is transformed into Equation (5-12)

$$\dot{Q}_{tc}(s) = \frac{2\varepsilon_l}{\sqrt{\pi}} \cdot (T_w - T_b) \cdot \bar{f}(s) \cdot \langle A_{bub}(s;e) \cdot \sqrt{t_{tc}(s;e)} \rangle_e \tag{5-12}$$

where the operator $\langle\ \rangle_e$ represents averaging performed for all events of a particular nucleation site s. The power of the entire boiling surface is found with Equation (5-13) and the heat flux is given by Equation (5-14).

$$\dot{Q}_{tc} = \frac{2\varepsilon_l}{\sqrt{\pi}} \cdot (T_w - T_b) \cdot N_s \cdot \langle \bar{f}(s) \cdot \langle A_{bub}(s;e) \cdot \sqrt{t_{tc}(s;e)} \rangle_e \rangle_s \tag{5-13}$$

$$q''_{tc,III} = \frac{2\varepsilon_l}{\sqrt{\pi}} \cdot (T_w - T_b) \cdot N''_a \cdot \langle \bar{f}(s) \cdot \langle A_{bub}(s;e) \cdot \sqrt{t_{tc}(s;e)} \rangle_e \rangle_s \tag{5-14}$$

where N_s is the total number of active nucleation sites on the boiling surface and N''_a is the active nucleation site density. Equation (5-14) represents Tier III averaging method since it accounts for the variation in boiling parameters between nucleation sites, individual nucleation events, and complex non-linearities present within transient conduction equations. Note, that in contrast to the microlayer evaporation (Equation (1-15)), the transient conduction heat flux is a complicated function of the temporal parameters, since the departure frequency $\overline{f(s)}$ wait time $t_w(s;e)$, and characteristic conduction time t^* affect overall heat transfer. Therefore, in order to characterize transient conduction heat flux, we will be looking for the distribution of the parameter ξ_{tc} among nucleation sites (see Equation (5-15)).

$$\xi_{tc} = \bar{f}(s) \cdot \langle A_{bub}(s;e) \cdot \sqrt{t_{tc}(s;e)} \rangle_e \tag{5-15}$$

The average of the parameter ξ_{tc} is given by Equation (5-16).

$$\bar{\xi}_{tc} = \langle \bar{f}(s) \cdot \langle A_{bub}(s;e) \cdot \sqrt{t_{tc}(s;e)} \rangle_e \rangle_s \tag{5-16}$$

Next, we provide expressions for Tiers I and II averaging methods. Tier II averaging method recognizes the variability of boiling parameters between nucleation sites, while ignoring the non-linearity of transient conduction equations. Transient conduction heat flux calculated using Tier II averaging method is given by Equation (5-17).

$$q''_{tc,II} = \frac{2\varepsilon_l}{\sqrt{\pi}} \cdot (T_w - T_b) \cdot N''_a \cdot \langle \bar{f}(s) \rangle_s \cdot \langle \langle A_{bub}(s;e) \rangle_e \rangle_s \cdot \sqrt{\langle \langle t_{tc}(s;e) \rangle_e \rangle_s} \quad (5\text{-}17)$$

Finally, a Tier I averaging method is given by Equation (5-18).

$$q''_{tc,I} = \frac{2\varepsilon_l}{\sqrt{\pi}} \cdot (T_w - T_b) \cdot N''_a \cdot \langle \bar{f}(s) \rangle_s \cdot \langle A_{bub}(b) \rangle_b \cdot \sqrt{\langle t_{tc}(b) \rangle_b} \quad (5\text{-}18)$$

where b stands for a bubble nucleated anywhere on the boiling surface. Tier I method only accounts for the variability in boiling parameters between nucleation events. Note that all derivations presented here ignore the possibility of a bubble nucleating at the area that undergoes transient conduction heat transfer. If nucleated, such bubble may end the period of transient conduction prematurely within its region of influence (i.e. before the time t_{tc} has elapsed). The effect of this limitation will be examined later in the Chapter.

5.2.2. Heat flux due to forced convection

In the case of forced convection, the most important parameter to quantify is the effective area occupied by bubbles $A_{bub,eff}$. Then, the forced convection heat flux can be found using Equation (5-19)

$$q''_{fc} = h_{fc} \cdot (T_w - T_b) \cdot \left(1 - \frac{A_{bub,eff}}{A_{tot}}\right) \quad (5\text{-}19)$$

For a site s and nucleation event e the effective area occupied by a bubble is given by Equation (5-20)

$$A_{bub,eff}(s;e) = A_{bub}(s;e) \cdot \frac{t_g(s;e) + t_{tc}(s;e)}{t_b(s;e)} \quad (5\text{-}20)$$

where $t_g(s;e)$ is the growth time for site s and event e. The average effective area for site s is given by Equation (5-21)

$$\overline{A_{bub,eff}}(s) = \langle A_{bub}(s;e) \cdot \frac{t_g(s;e) + t_{tc}(s;e)}{t_b(s;e)} \rangle_e \quad (5\text{-}21)$$

The total effective area covered by bubbles is given by Equation (5-22)

$$A_{bub,eff} = N_s \cdot \langle \langle A_{bub}(s;e) \cdot \frac{t_g(s;e) + t_{tc}(s;e)}{t_b(s;e)} \rangle_e \rangle_s \quad (5\text{-}22)$$

Note that Equation (5-22) could overestimate the effective area covered by bubbles because occasionally a bubble may nucleate within the area that undergoes transient conduction heat transfer, hence resulting in two bubbles occupying the same effective area. Substituting Equation (5-22) into Equation (5-19) we arrive to the final expression for the forced convection heat flux given by Equation (5-23)

$$q''_{fc,III} = h_{fc} \cdot (T_w - T_b) \cdot \left(1 - N''_a \cdot \langle\langle A_{bub}(s;e) \cdot \frac{t_g(s;e) + t_{tc}(s;e)}{t_b(s;e)} \rangle_e \rangle_s \right) \tag{5-23}$$

Finally, the relevant group of parameters for the forced convection heat flux ξ_{fc} is given by Equation (5-24)

$$\xi_{fc} = \langle A_{bub}(s;e) \cdot \frac{t_g(s;e) + t_{tc}(s;e)}{t_b(s;e)} \rangle_e \tag{5-24}$$

Equation (5-23) represents a Tier III averaging method. Tiers I and II are given by Equations (5-25) and (5-26) respectively

$$q''_{fc,I} = h_{fc} \cdot (T_w - T_b) \cdot \left(1 - N''_a \cdot \langle A_{bub}(b) \rangle_b \cdot \langle \bar{f}(s) \rangle_s \cdot \left[\langle t_g(b) \rangle_b + \langle t_{tc}(b) \rangle_b \right] \right) \tag{5-25}$$

$$\begin{aligned} q''_{fc,II} = {} & h_{fc} \cdot (T_w - T_b) \\ & \cdot \left(1 - N''_a \cdot \langle \langle A_{bub}(s;e) \rangle_e \rangle_s \cdot \langle \bar{f}(s) \rangle_s \cdot \left[\langle \langle t_g(s;e) \rangle_e \rangle_s + \langle \langle t_{tc}(s;e) \rangle_e \rangle_s \right] \right) \end{aligned} \tag{5-26}$$

5.2.3. Differences between averaging methods

In the present Section we introduced three methods of averaging that can be used when adapting experimentally measured values of boiling parameters to the calculation of partitioned heat fluxes. The simplest and most common averaging approach consists of gathering the values of boiling parameters from all nucleation events observed in the experiment and calculating the number average of each parameter. In the present Chapter we call this a Tier I averaging method. Tier I averaging is easy to implement, but it ignores the variability of boiling parameters between nucleation sites. Therefore, boiling parameters measured by such process will be incompatible with certain nucleation site density models. For example, the model of Hibiki and Ishii [49] predicts the number of nucleation sites based on the distribution of microscopic cavities on the boiling surface. Therefore, we may presume that the model of Hibiki and Ishii identifies all nucleation sites present on the boiling surface, regardless of their characteristics. In contrast, departure frequency models (e.g. the model of Cole [111]) are not able to capture the complicated frequency distributions displayed in Figure 5-2. Therefore, the values of the bubble departure frequency predicted by models will be skewed towards bubbles with high

departure frequency, while in reality the majority of sites have low departure frequency (see Figure 5-2). When departure frequency and nucleation site density are multiplied together within HFP equations, the overestimated value of the departure frequency will lead to the overestimation of the partitioned heat flux. A more complicated approach requires the measurements of boiling parameters to be done for each nucleation site. Then the variability of the boiling parameters between the sites can be included in the averaging process. In the present Chapter, we call this a Tier II averaging method. The final and most accurate approach consists of creating specific groups of boiling parameters for each partitioned heat flux and averaging them in a way that conserves the rate of energy transfer (see Sub-Section 2.7.4. for more details). We refer to this method as a Tier III method. Tiers II and III averaging methods are difficult to achieve since they require high resolution diagnostics and automated post-processing algorithms to reach sufficient level of statistical significance. In the reminder of this Chapter we will demonstrate the influence of the averaging procedures on the values of boiling parameters and partitioned heat fluxes, while focusing on the partitioned heat fluxes due to forced convection and transient conduction.

5.3. RELEVANT PARAMETERS FOR HEAT FLUX PARTITIONING – MEASUREMENTS

The distributions of the key boiling parameters are shown in Figure 5-3 through Figure 5-9. For the distributions of the total area visited by a bubble A_{bub}, growth time t_g, wait time t_w, transient conduction time t_{tc}, and bubble period t_b the distributions between nucleation sites and nucleation events are presented separately. The maximum bubble footprint area A_{bub} represents the total area of the boiling surface covered by a bubble during its growth and sliding periods. The definition and measurement procedure for A_{bub} are presented in Sub-Section 2.7.4. To create a distribution based on the nucleation events, all nucleation events were considered, regardless of the spatial position where the event occurred. Therefore, the distributions that are based on nucleation events represent the probability for a bubble anywhere on the boiling surface to have a particular value of the boiling parameter. In contrast, the distributions that are based on nucleation sites represent the probability of finding a nucleation site which creates bubbles with a particular value of the boiling parameter. Note that with the exception of the growth time and transient conduction time, the values of boiling parameters span many orders of magnitude, highlighting the highly stochastic nature of boiling. The limited spread of the transient conduction time is explained by Equation (5-5), where the values of the transient conduction time are limited by the characteristic time t^*. Since t^* depends on the forced convection heat transfer coefficient h_{fc}, the spread of the transient conduction time becomes smaller for higher mass fluxes. Among the boiling parameters considered here, wait time and bubble period show the biggest difference between nucleation sites- and nucleation events-based distributions. The difference between the two distribution bases is directly related to the variation in bubble departure frequency between nucleation sites (Figure 5-3). Since multiple sites have very small departure frequencies, these sites will also have, on average, very long wait times. For such sites, the bubble period is dominated by the wait time, hence leading to significant similarities in the shape of the distributions for bubble wait time and bubble period. Due to the significant spread of the distributions shown in Figure 5-3 through Figure 5-9, we expect that three Tiers of averaging, which were presented in the

previous section, should lead to differences when calculating partitioned heat fluxes. Such differences are explored in the next section.

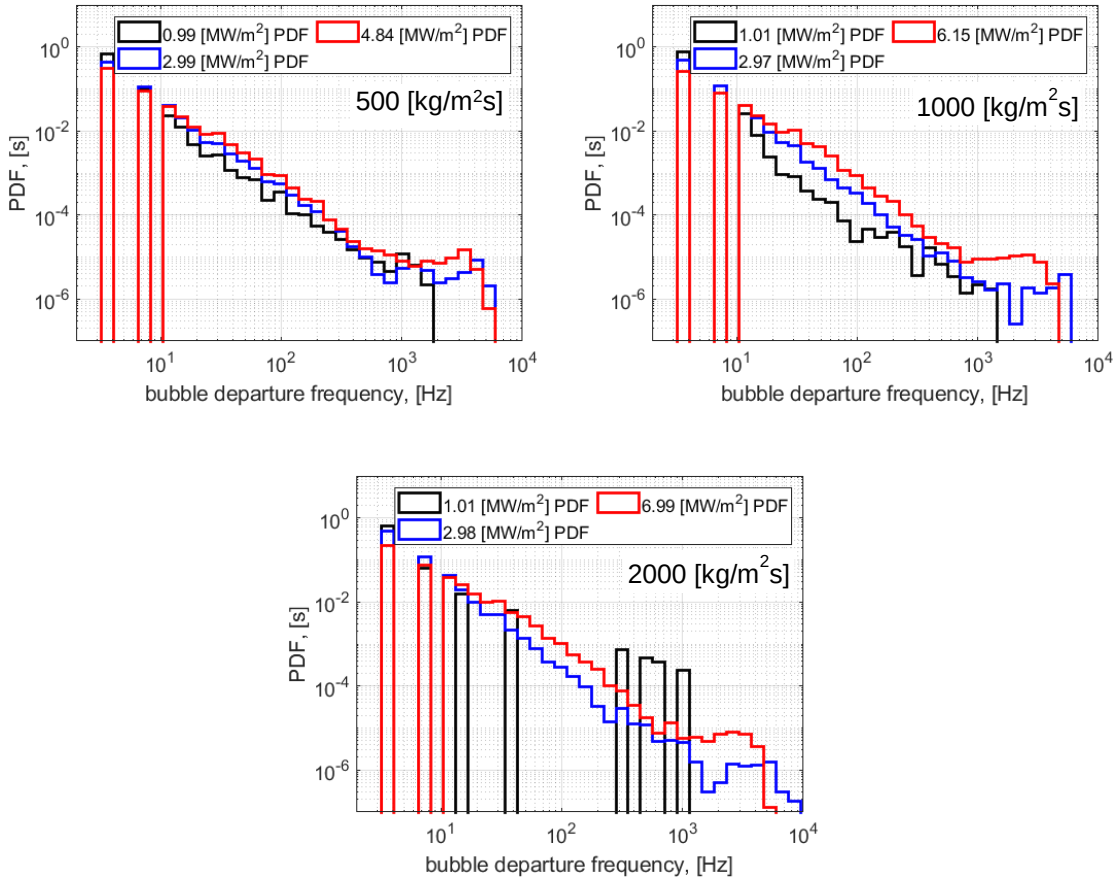

Figure 5-3. Distribution of bubble departure frequency between nucleation sites for the pressure of 10.5 bar and several mass fluxes and heat fluxes. The specific conditions for each distribution are specified in each plot

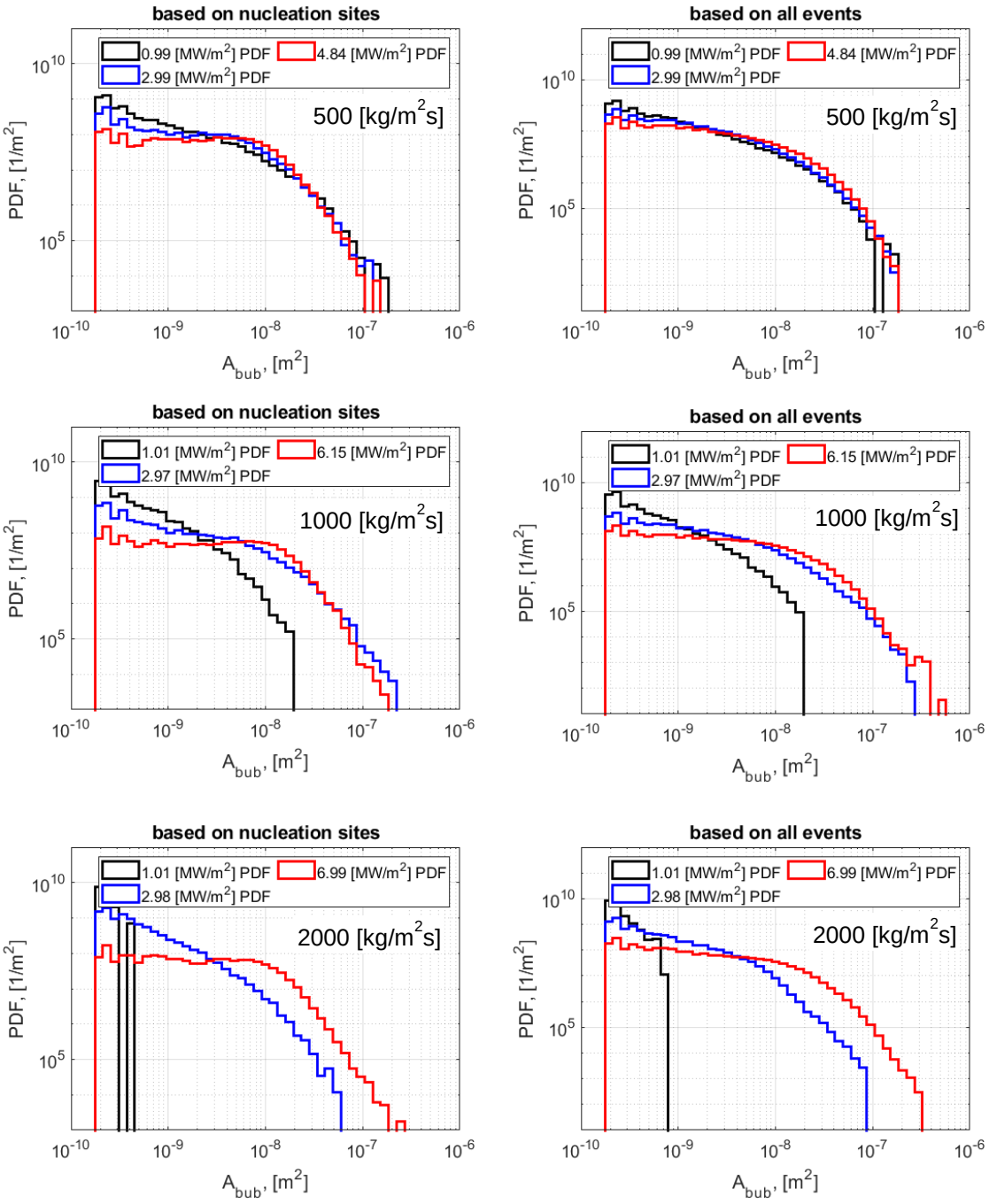

Figure 5-4. Distributions of the total area visited by a bubble A_{bub} between nucleation sites (left) and nucleation events (right) for the pressure of 10.5 bar and several mass fluxes and heat fluxes. The specific conditions for each distribution are specified in each plot

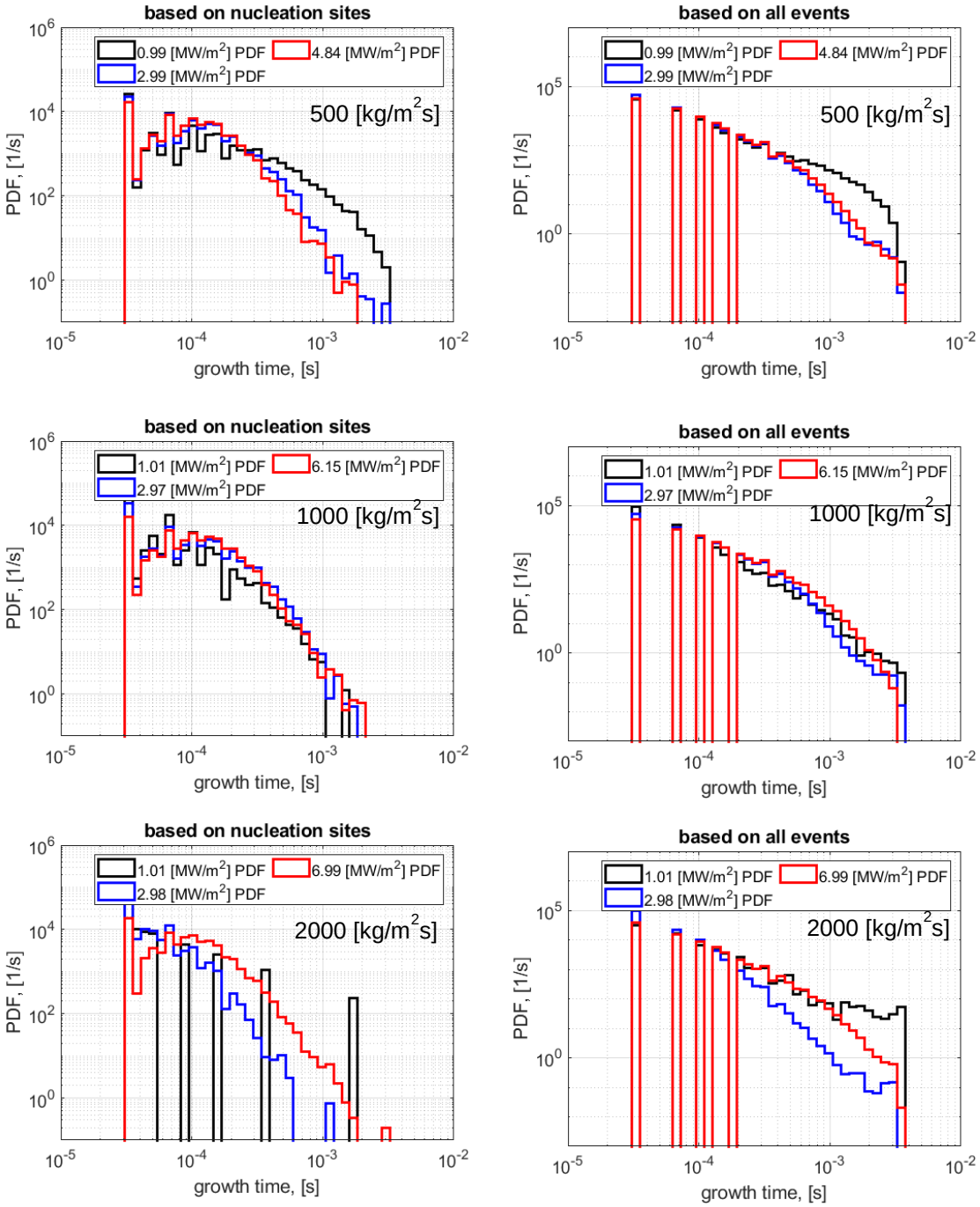

Figure 5-5. Distributions of the bubble growth time between nucleation sites (left) and nucleation events (right) for the pressure of 10.5 bar and several mass fluxes and heat fluxes. The specific conditions for each distribution are specified in each plot

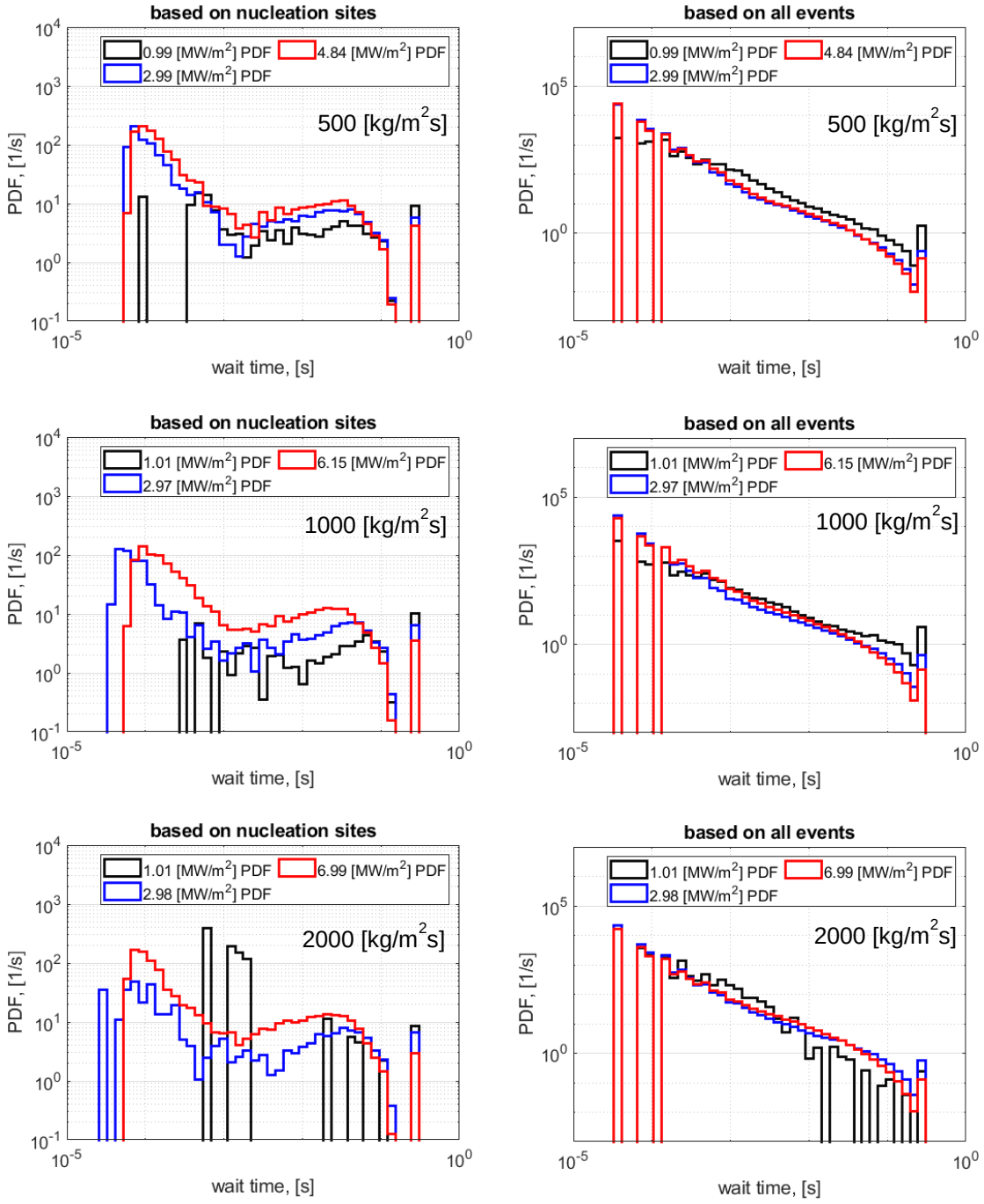

Figure 5-6. Distributions of the bubble wait time between nucleation sites (left) and nucleation events (right) for the pressure of 10.5 bar and several mass fluxes and heat fluxes. The specific conditions for each distribution are specified in each plot

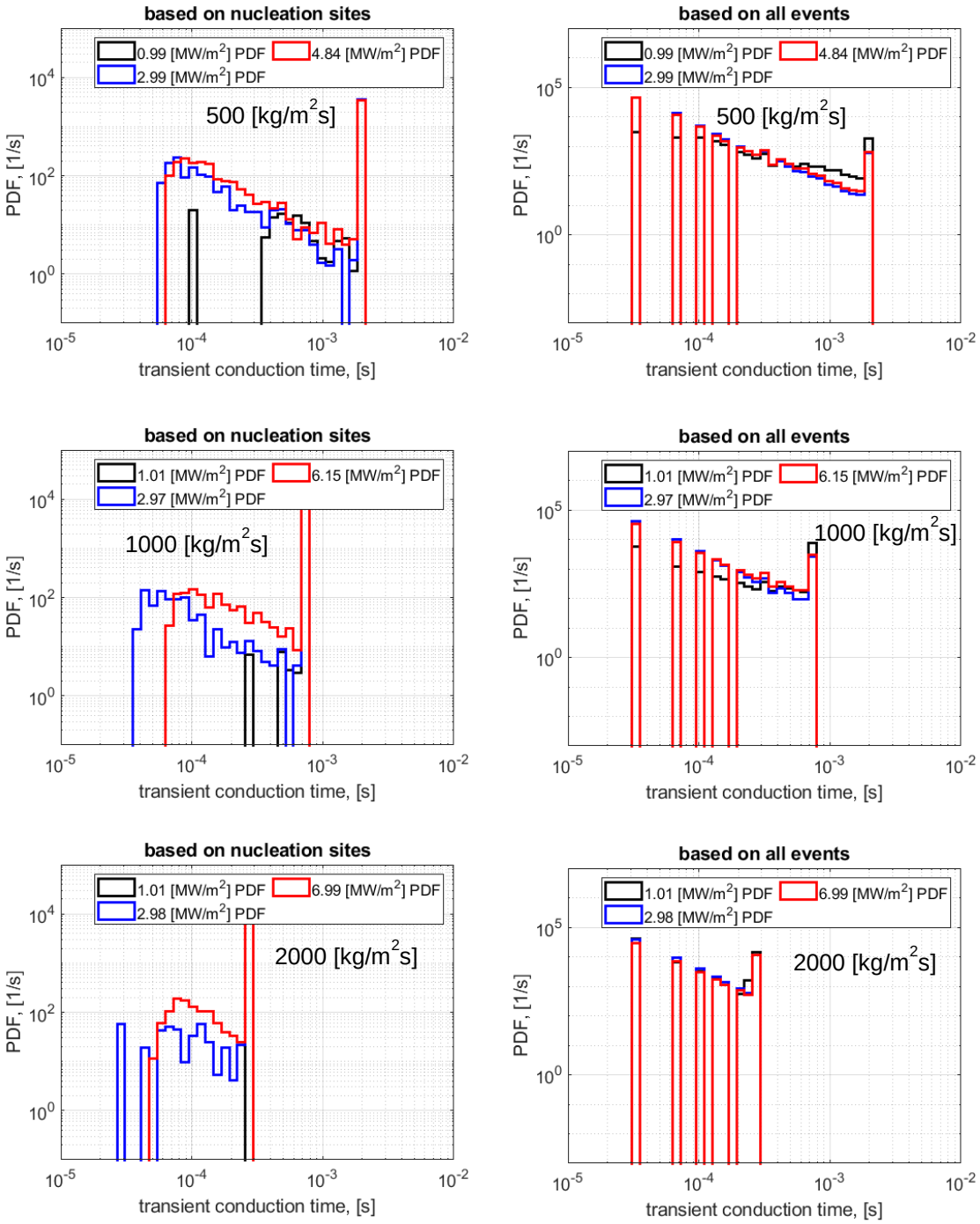

Figure 5-7. Distributions of the transient conduction time between nucleation sites (left) and nucleation events (right) for the pressure of 10.5 bar and several mass fluxes and heat fluxes. The specific conditions for each distribution are specified in each plot

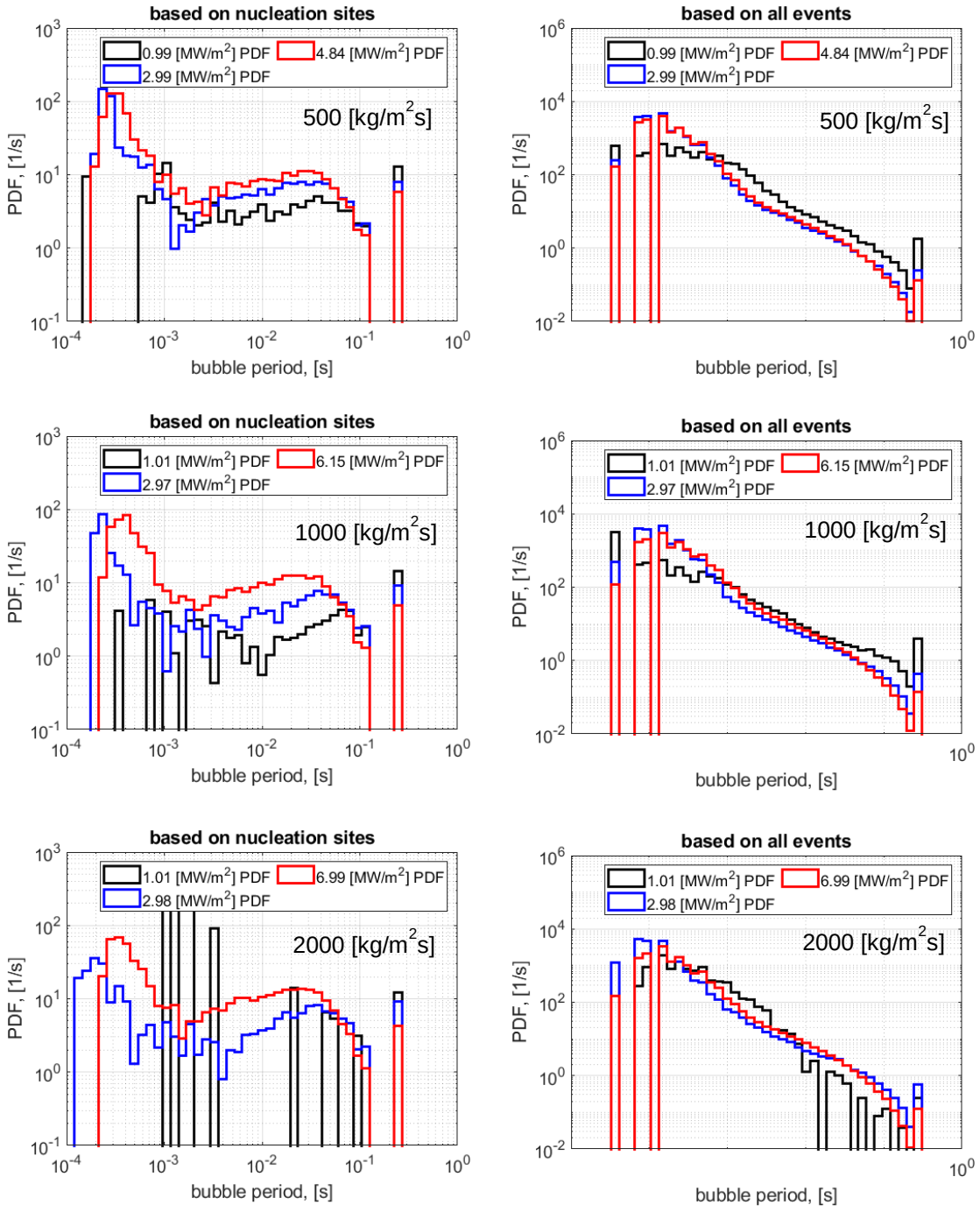

Figure 5-8. Distributions of the bubble period between nucleation sites (left) and nucleation events (right) for the pressure of 10.5 bar and several mass fluxes and heat fluxes. The specific conditions for each distribution are specified in each plot

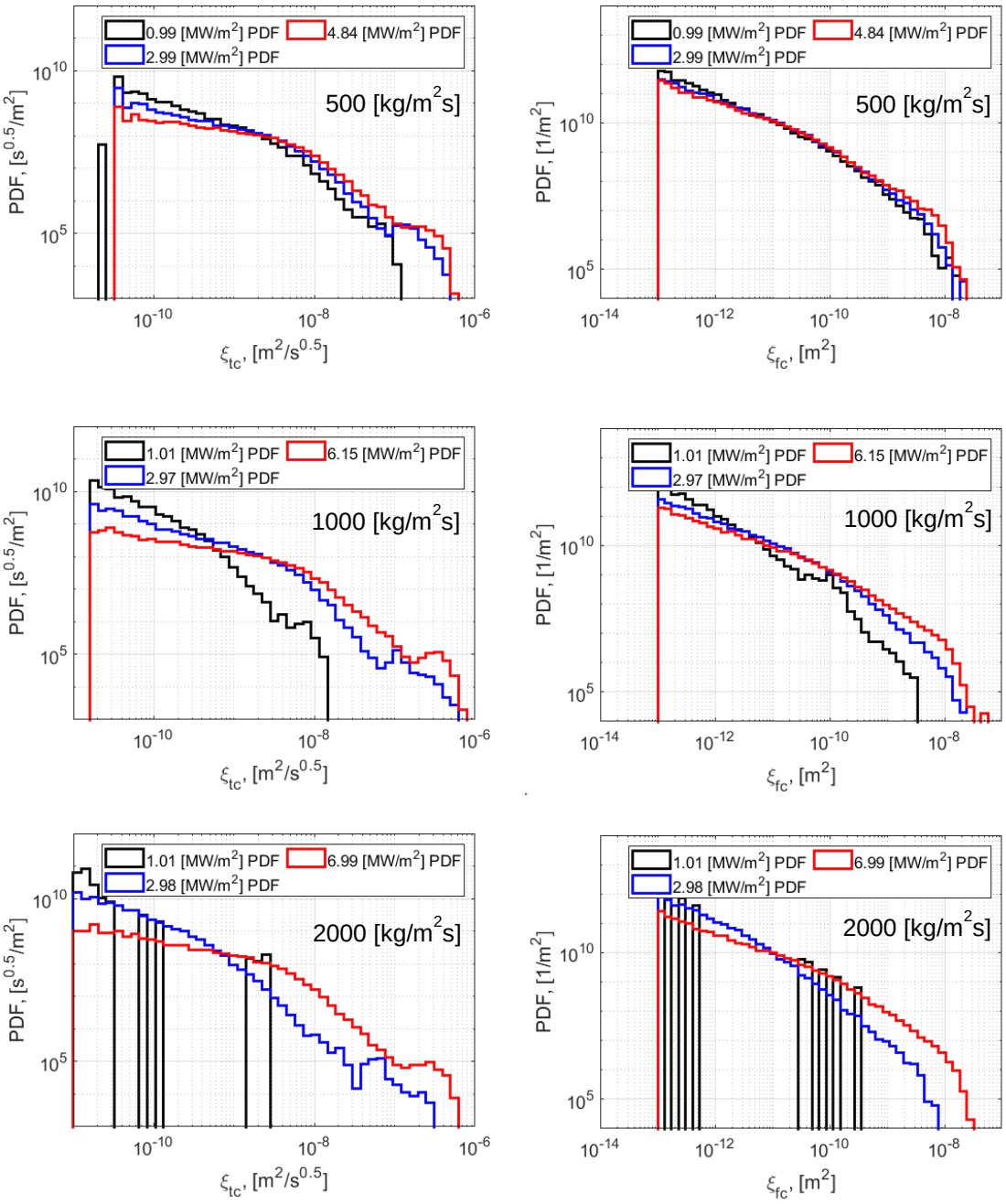

Figure 5-9. Distributions of the transient conduction group (left) and forced convection group (right) for the pressure of 10.5 bar and several mass fluxes and heat fluxes. The specific conditions for each distribution are specified in each plot

5.4. HEAT FLUX PARTITIONING CALCULATIONS

Once the distributions of the key boiling parameters are known, it is possible to calculate partitioned heat fluxes due to the transient conduction and forced convection. The calculations of the partitioned heat fluxes for three Tiers of averaging methods are given

in Figure 5-10. The average values of various boiling parameters that were used in the calculation are given in Figure 5-11 through Figure 5-17. The wall superheat and heat flux were taken from the measured boiling curves (see Figure 5-18). In order to determine which averaging method is the most accurate we used an additional technique to calculate partitioned heat fluxes, using binary images that represent time- and space-resolved distributions of dry spots on the boiling surface (see Figure 2-23 for the details about the binarization of the phase detection images). Each pixel and frame of the binary image was analyzed, and a value of the heat flux was assigned to each pixel based on the distribution of the dry spots. If a pixel located at coordinates x and y was dry during the frame f_i and became wet during the frame f_{i+1}, then transient conduction heat flux was assigned to this pixel starting at frame f_{i+1} and ending either when this pixel became dry again, or when the time elapsed since the rewetting of this pixel exceeded characteristic transient conduction time (t^*, Equation (5-6)). The transient conduction heat flux was calculated according to Equation (5-27)

$$q''_{tc} = \frac{\varepsilon_l}{\sqrt{\pi}} \cdot \frac{T_w - T_b}{\sqrt{t_{wet}}} \tag{5-27}$$

where t_{wet} is the time elapsed since the rewetting of the pixel. Forced convection heat transfer coefficient was assigned to all pixels that are neither dry nor undergoing transient conduction heat transfer. The forced convection heat transfer coefficient was inferred from the single-phase portions of the boiling curves (Figure 5-18). The process of measuring transient conduction heat flux is demonstrated in Figure 5-19, which shows several bubbles slide over the boiling surface, resulting in streaks of high heat flux being created in the wake of bubble footprints. Note that both the measurement procedure shown in Figure 5-19 and the dry area tracking algorithm shown in Figure 2-23 take sliding bubble into account. In the case of the dry are tracking algorithm, the total area visited by a bubble A_{bub} is comprised of the area visited by the bubble footprint during its growth and sliding periods. The calculation method that is based on binary images provides the highest accuracy because it considers overlaps between effective bubble areas and will react to bubbles nucleating within regions that are already influenced by other bubbles through the transient conduction heat transfer mode. The difference in partitioned heat fluxes calculated with the boiling parameters and binary images serves as a figure of merit when the accuracy of averaging methods is evaluated.

Figure 5-10 shows that a Tier III averaging method is the most accurate, since it is closest to the partitioned heat fluxes inferred from binary images. Surprisingly, Tier II averaging method leads to the worst performance, especially for low mass flux. For lower mass fluxes the characteristic time t^* is large, making wait time more relevant for transient conduction calculations. However, since the majority of nucleation sites have low departure frequency and long wait time, Tier II averaging method shifts the wait time towards larger values, resulting in overprediction of the transient conduction heat flux. Such shift can be observed in Figure 5-14 and Figure 5-15. In contrast, for higher mass fluxes the characteristic time t^* is small, leading to the majority of transient conduction heat flux to be terminated before the nucleation of a new bubble (i.e. $t_w > t^*$). We can conclude, that while Tier III

averaging method leads to superior accuracy, it is not too far from the simplest Tier I method (at least for transient conduction and forced convection heat fluxes and operating conditions explored in the present study). Notably, poor performance of the Tier II method suggests that the variability of boiling parameters between nucleation sites cannot be addressed for each parameter separately without recognizing their connection within partitioned heat flux equations.

The most important conclusion of the present Chapter stems from the magnitudes of partitioned heat fluxes shown in Figure 5-10. For high wall superheats and high heat fluxes transient conduction and forced convection components account only for 30% – 40% of the total applied heat flux. In the previous Chapter we have demonstrated that the only evaporative term that is present in high pressure boiling is due to the triple contact line evaporation. It was also shown that this term cannot be larger than 20%. This leaves more than 40% of the total heat flux unaccounted for with the present understanding of partitioned heat flux mechanisms. It could be argued, that transient conduction mechanism affects larger areas than what is covered by bubble footprint. However, we believe that this is not the case and the majority of transient conduction heat transfer enhancement is limited to the bubble footprint area. Our conjecture is corroborated by Figure 5-20, which shows the departure process of a single bubble captured at 1 bar of pressure, allowing the visualization of the enhanced heat transfer in a wake of a sliding bubble to be made with infrared thermometry. Figure 5-20 shows that the majority of the enhanced heat transfer is concentrated in the area that was previously occupied by the bubble footprint and not by the projected area of the bubble. Therefore, by extending this low-pressure observation to high pressure cases, we assume that the majority of the transient conduction heat flux is still concentrated at the bubble footprint area. Additionally, there is not much room for expanding the surface area affected by the transient conduction. Figure 5-21 shows the fraction of the boiling surface area that is either occupied by bubble footprints or affected by transient conduction. The area fraction shown in Figure 5-21 was measured directly using binary images and, therefore, it is unaffected by the selection of the averaging method. Figure 5-21 demonstrates that the area occupied by bubble footprints and transient conduction already reaches 70% for the case of 500 kg/(m^2-s). Therefore, we should not expect the transient conduction component to be stronger by more than 30% compared to the measurements shown in Figure 5-10, still making it insufficient to account for the entirety of the applied heat flux. Furthermore, by increasing the area occupied by transient conduction, we will decrease the area occupied by forced convection, making the overall improvement in heat flux partitioning predictions even smaller. The findings of the present Chapter suggest that we are missing a possible heat transfer enhancement mechanism that could be responsible for more than 40% of the total heat removal when considering high heat fluxes close to CHF. While it is not known at the moment which mechanisms is responsible for the missing heat flux in our calculations, we speculate, that it may be related to the forced convection or transient conduction heat transfer coefficients or both.

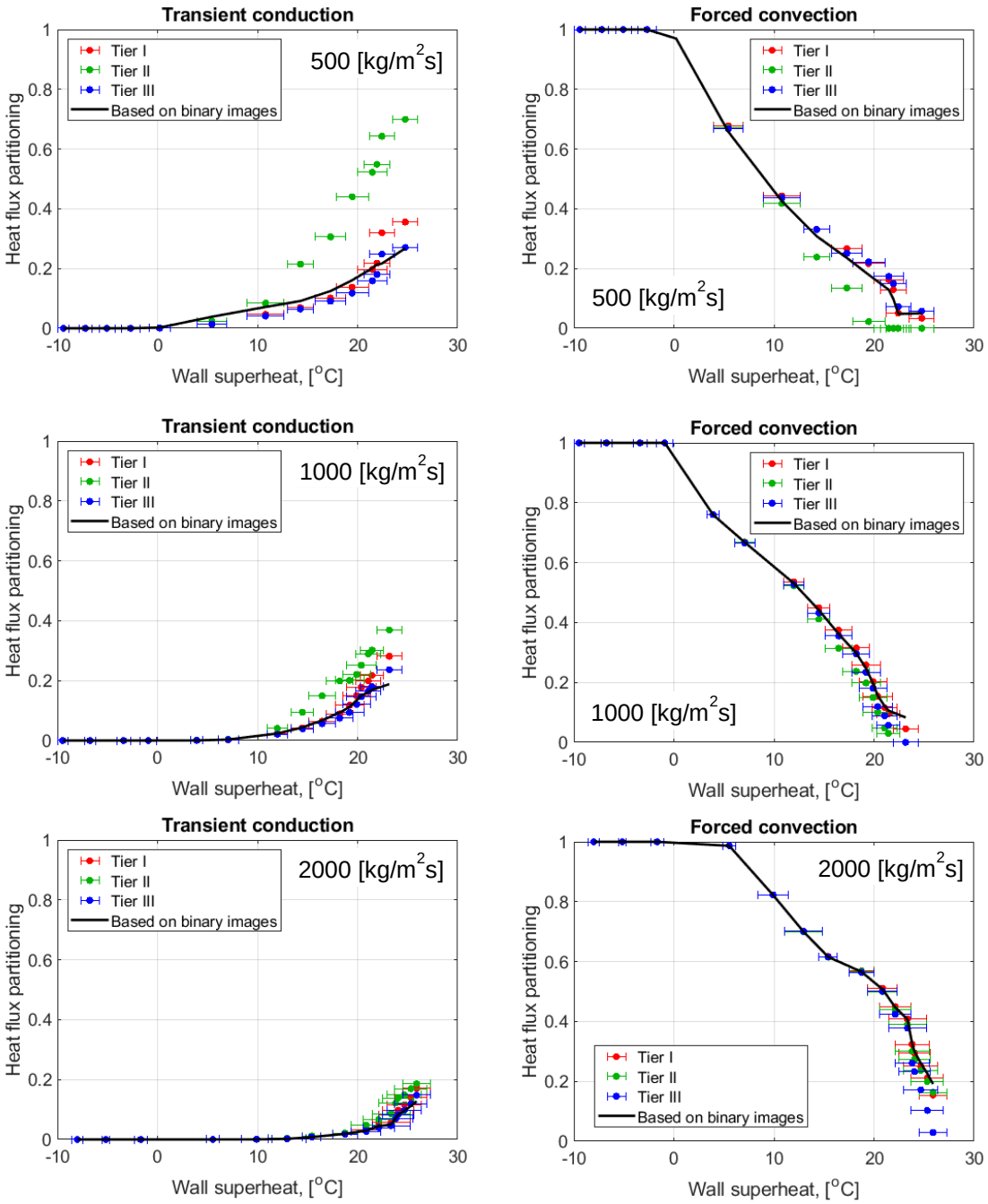

Figure 5-10. Comparison between different approaches to the calculation of partitioned heat fluxes. Filled circles represent the calculations which are based on the three different averaging methods. Solid lines represent the calculations which are based on space- and time-resolved binary images acquired with the phase detection technique. Each frame of the binary image represents instantaneous distribution of dry spots on the boiling surface (see Figure 2-23 for the description of the procedure used to binarize phase detection images)

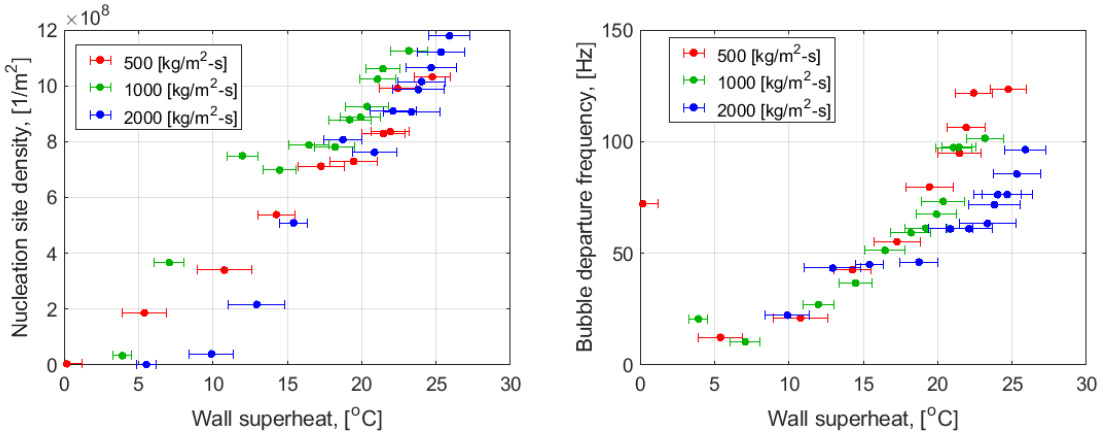

Figure 5-11. Nucleation site density (left) and average bubble departure frequency (right) for the pressure of 10.5 bar and mass fluxes of 500, 1000 and 2000 kg/(m^2-s)

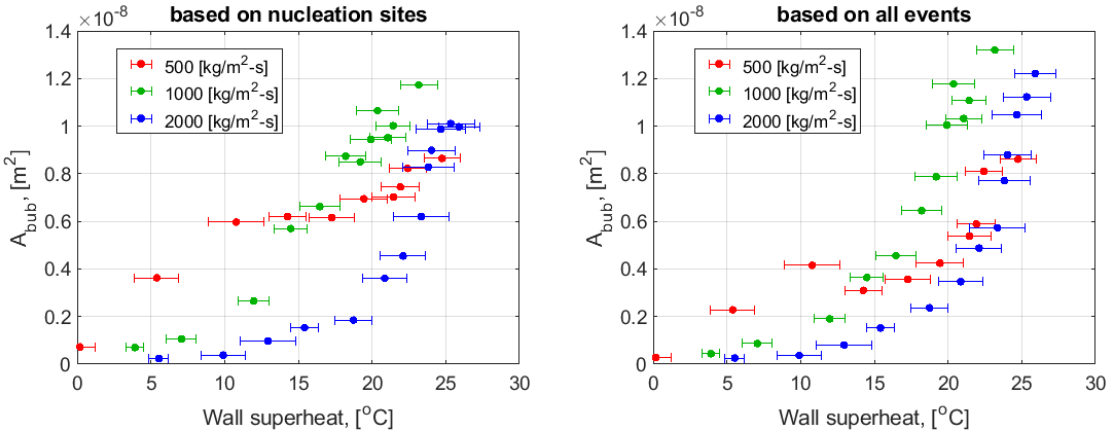

Figure 5-12. Mean values of the total area visited by a bubble A_{bub} for the pressure of 10.5 bar and mass fluxes of 500, 1000 and 2000 kg/(m^2-s). The averaging was done using distributions which are based on the nucleation sites (left) and nucleation events (right).

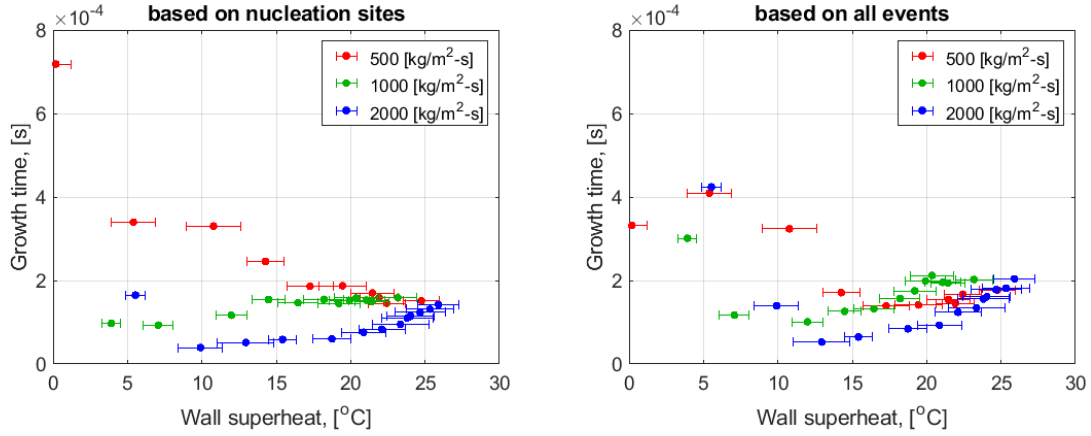

Figure 5-13. Mean values of the bubble growth time for the pressure of 10.5 bar and mass fluxes of 500, 1000 and 2000 kg/(m^2-s). The averaging was done using distributions which are based on the nucleation sites (left) and nucleation events (right).

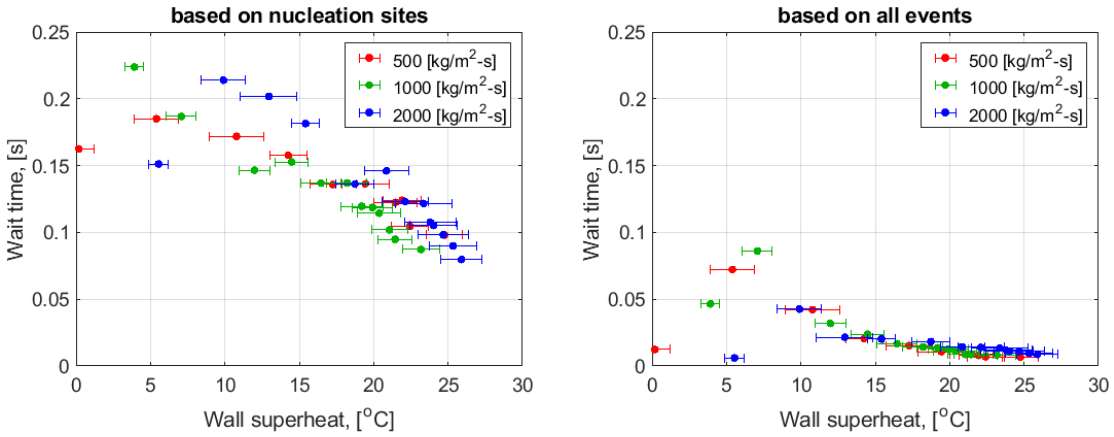

Figure 5-14. Mean values of the bubble wait time for the pressure of 10.5 bar and mass fluxes of 500, 1000 and 2000 kg/(m^2-s). The averaging was done using distributions which are based on the nucleation sites (left) and nucleation events (right).

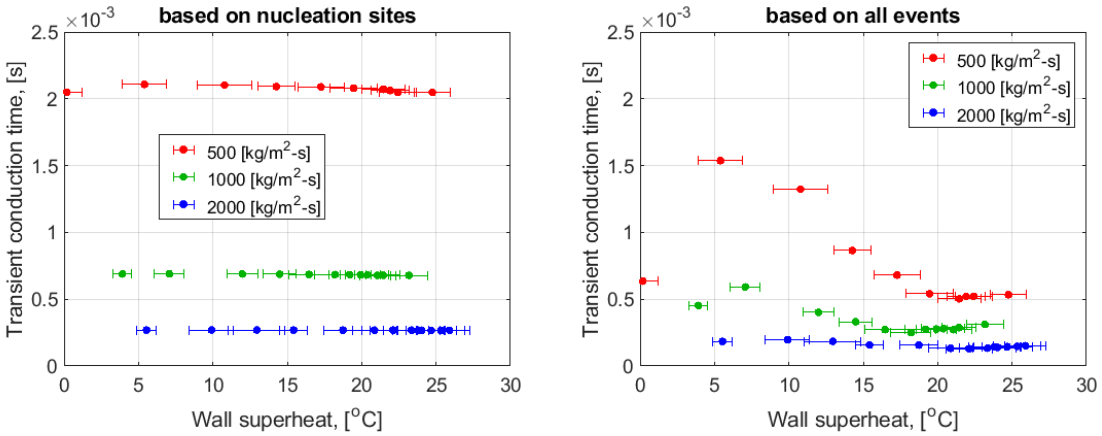

Figure 5-15. Mean values of the transient conduction time for the pressure of 10.5 bar and mass fluxes of 500, 1000 and 2000 kg/(m^2-s). The averaging was done using distributions which are based on the nucleation sites (left) and nucleation events (right).

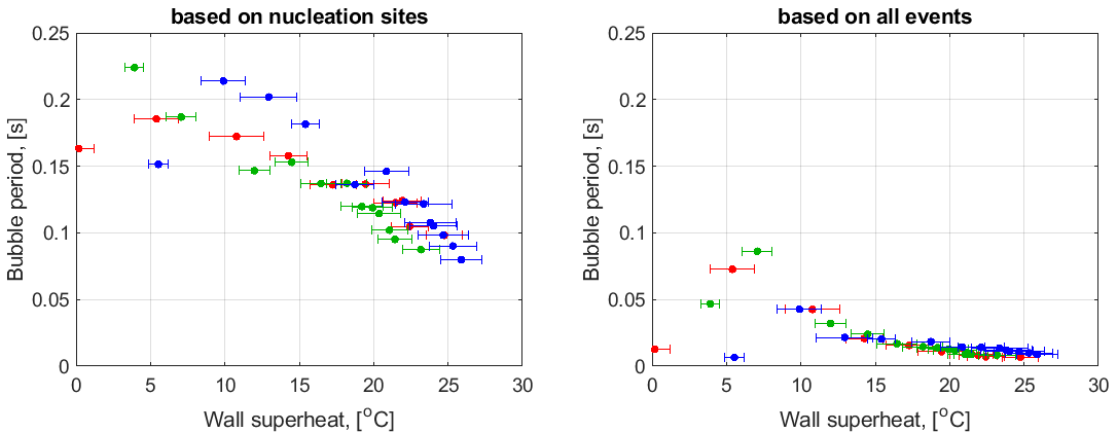

Figure 5-16. Mean values of the bubble period for the pressure of 10.5 bar and mass fluxes of 500, 1000 and 2000 kg/(m^2-s). The averaging was done using distributions which are based on the nucleation sites (left) and nucleation events (right).

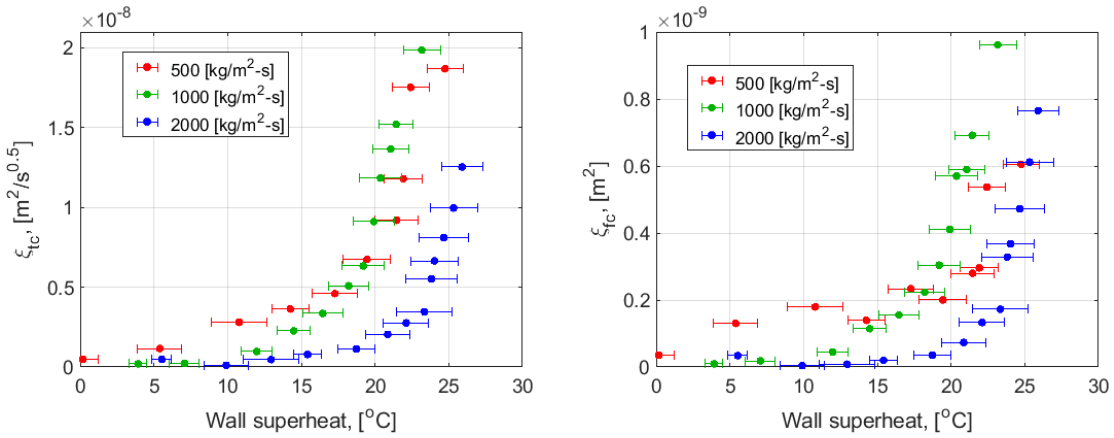

Figure 5-17. Transient conduction (left) and forced convection (right) boiling parameter groups measured for the pressure of 10.5 bar and mass fluxes of 500, 1000 and 2000 kg/(m^2-s).

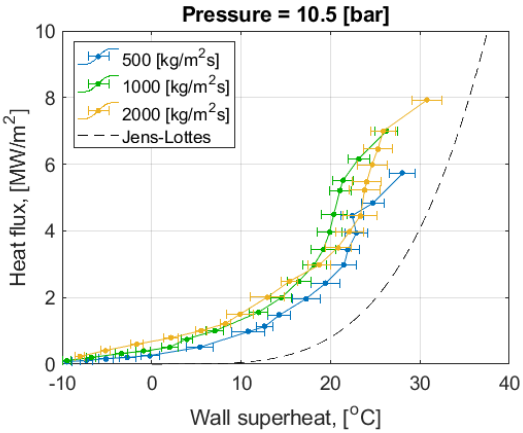

Figure 5-18. Boiling curves for the pressure of 10.5 bar and mass fluxes of 500, 1000, and 2000 kg/(m^2-s). The error bars represent the standard deviation of the measurements.

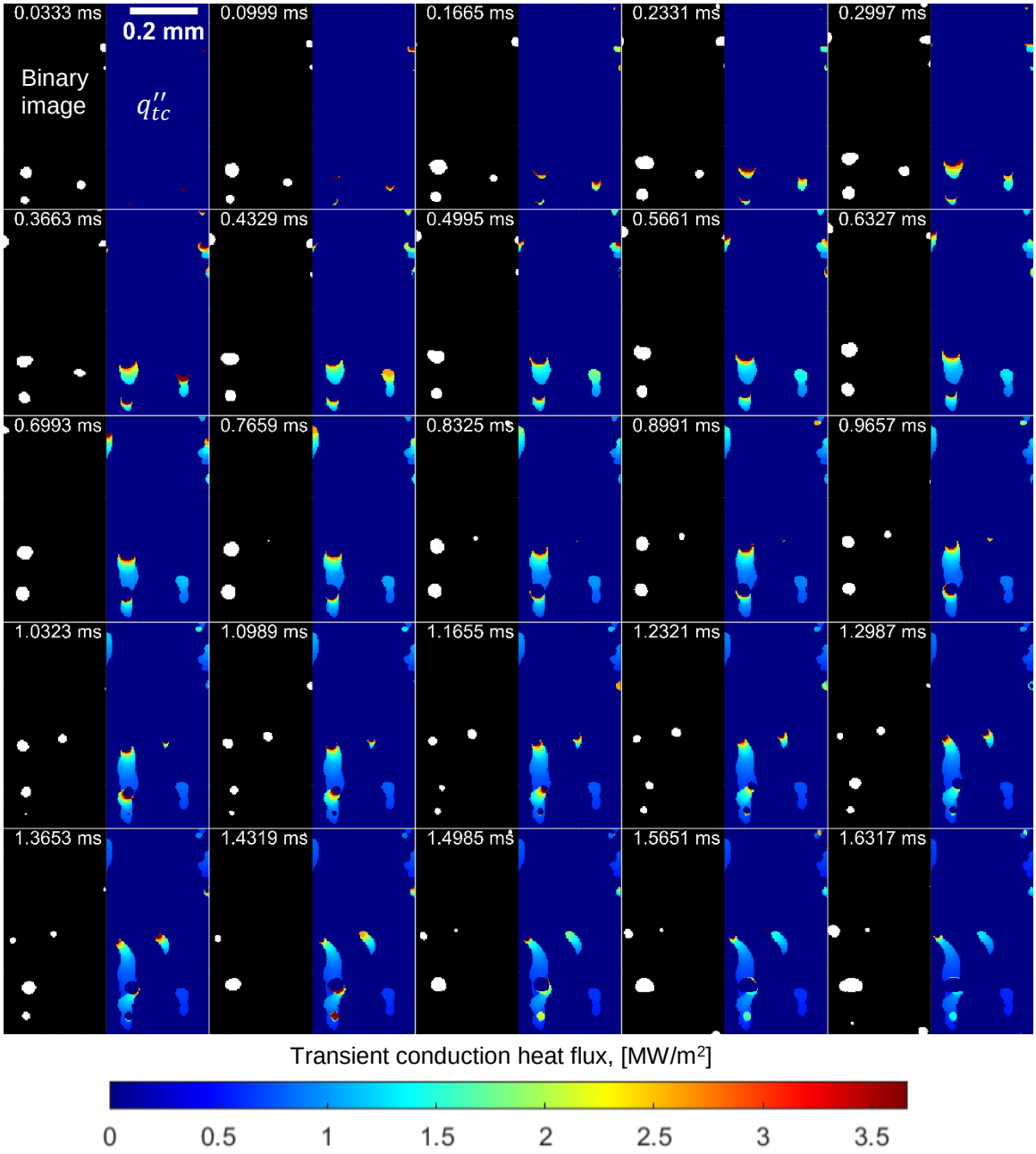

Figure 5-19. Demonstration of the procedure used to calculate transient conduction heat flux based on the binary images. In each frame, a binary image is shown on the left, and inferred transient conduction heat flux is shown on the right. Each frame of the binary image represents instantaneous distribution of dry spots on the boiling surface (see Figure 2-23 for the description of the procedure used to binarize phase detection images)

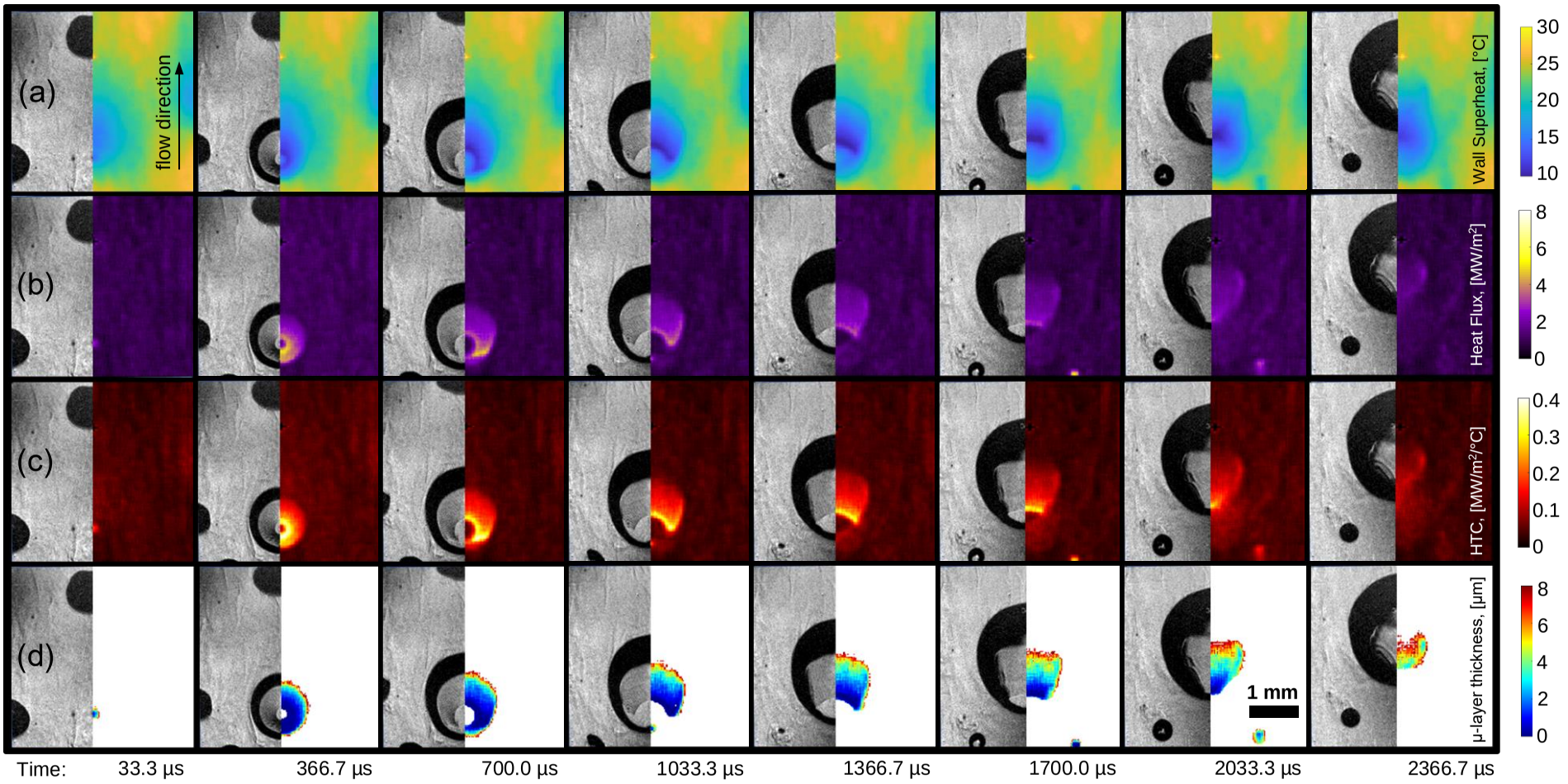

Figure 5-20. HSV images obtained with the main and BS beams (see Figure 2-13), shown together with the corresponding distribution of wall superheat [°C] (a), heat flux [MW/m^2] (b), heat transfer coefficient [MW/m^2/°C] (c), and microlayer thickness inferred from infrared thermometry [μm] (d). These images were taken in subcooled flow boiling conditions at ambient pressure, with a mass flux of 1000 kg/m^2/s, a subcooling of 10 ˚C, and a heat flux of 1.0 MW/m^2. The pixel size of the HSV images is 21.2 μm.

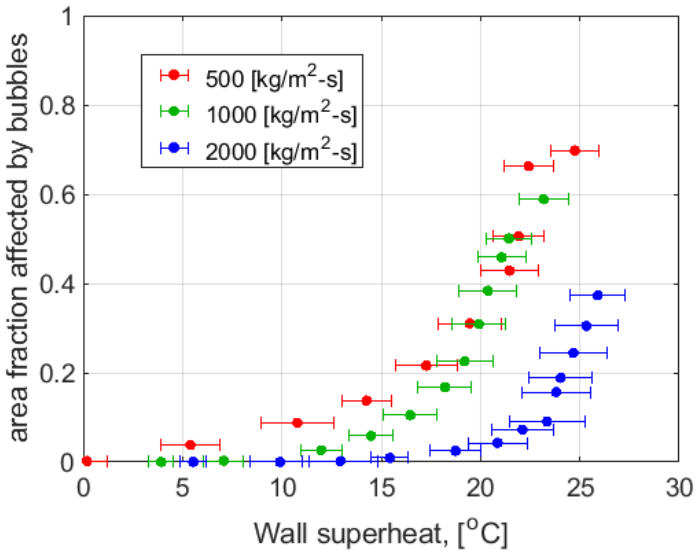

Figure 5-21. Fraction of the boiling surface area that is affected by bubbles for the pressure of 10.5 bar

5.5. CONCLUSION TO THE CHAPTER AND FUTURE WORK

In this Chapter we demonstrated the variation of boiling parameters between nucleation sites and nucleation events. The biggest variation is observed for temporal parameters, including bubble departure frequency, bubble wait time, and bubble period, with the exception of the bubble growth time, for which the variation is small. The total area visited by a bubble A_{bub} also varies by several orders of magnitude, with the variation between nucleation sites and nucleation events being very similar. The variation of boiling parameters may have implications for the heat flux partitioning calculations, since the models for various boiling parameters (i.e. bubble departure frequency, nucleation site density, etc.) were developed independently, oftentimes ignoring the connections between the boiling parameters and their statistical distributions. Note that the connection between the nucleation site density N'', temporal parameters (i.e., growth time t_g and departure frequency f), and the bubble size was emphasized before in the work of Gilman and Baglietto [15]. Our work further highlights such connection, while also demonstrating that all boiling parameters vary in a complex way. The complexities of the boiling parameter distributions may change the results of the partitioning calculations depending on the averaging method used to combine these distributions within the heat flux partitioning equations. The effect of the averaging method is explored in the present Chapter by analyzing three tiers of averaging methods.

- Tier I method ignores the variation of boiling parameters between nucleation sites and the non-linearities of heat flux partitioning equations. It only considers the variation between individual nucleation events.
- Tier II method ignores the non-linearities of heat flux partitioning equations, while considering the variations of boiling parameters between nucleation events and sites.

- Tier III considers all aspects of boiling parameter distributions and heat flux partitioning equations, leading to the most accurate way of averaging the boiling parameters.

Practically, Tier I method is the easiest to implement, while Tier III method is the most accurate. Interestingly, our results suggest that the difference between Tier I and Tier III is not large, at least for transient conduction and forced convection heat fluxes and the range of operating conditions explored here. The worst performance was observed for Tier II averaging method, suggesting that whenever the variation between nucleation sites and events is considered, the non-linearities of the heat flux partitioning equations must be considered as well.

The major finding of the present Chapter stems from the magnitude of heat flux partitioning calculated by various methods. The highly accurate method for calculating transient conduction and forced convection heat fluxes was implemented by analyzing time- and space-resolved dry spot distributions, revealing a significant underestimation of the partitioned heat fluxes based on the currently known mechanisms. Our measurements suggest that between 40% and 60% of the total heat flux at the boiling surface is unaccounted for by the three main heat flux partitioning mechanisms (i.e. forced convection, transient conduction and evaporation). We speculate, that other mechanisms result in the enhancement of the heat transfer at the boiling surface. Based on the low pressure experiments performed in our laboratory in which the partitioned heat flux can be measured directly using infrared thermometry, we speculate that the unknown mechanism affects the forced convection heat transfer coefficients. Future work should be concentrated on gathering more high-resolution data at low and high pressures to further study the effects of boiling parameters variation on the calculation of the partitioned heat fluxes. The low-pressure data will reveal if the amount of unaccounted heat flux observed in the present study is universally present at all pressures, or if it is a unique aspect of high pressure boiling. Additionally, by expanding current databases and amassing more knowledge about the heat transfer enhancement in flow boiling, it would be possible to either shed the light onto the new heat transfer mechanism, or reassess and improve currently available heat flux partitioning frameworks.

6. DEPARTURE FROM NUCLEATE BOILING

The final chapter of the Thesis takes a brief look at the departure from nucleate boiling (DNB) and critical heat flux (CHF). The values of CHF are presented in Section 6.1 and their trends with respect to pressure and mass flux are discussed. Section 6.2 examines the distributions of dry spots before and at the moment of DNB.

6.1. CRITICAL HEAT FLUX

In each experimental run, the heat flux was increased in several steps until the boiling crisis was reached. The measured values of CHF for different pressures and mass fluxes are shown in Figure 6-1. The measured values of CHF exhibit the expected trends, with higher mass fluxes leading to higher values of CHF. Under the change in pressure, CHF values experience a similar trend to the dimensional analysis of Kutateladze [98], Equation (6-1)

$$q''_{CHF,K} = 0.16 \cdot h_{fg} \cdot \rho_v \cdot \left(\frac{\sigma \cdot (\rho_l - \rho_v) \cdot g}{\rho_v^2} \right)^{\frac{1}{4}} \tag{6-1}$$

where h_{fg} is the latent heat of vaporization, ρ_v is the density of steam, ρ_l is the density of water, σ is the surface tension and g is the gravitational acceleration. This suggests that the effects of pressure are directly tied to the set of thermophysical properties given in Equation (6-1). However, since many key boiling parameters (e.g. bubble departure frequency, nucleation site density, and others) are tied to the same set of thermophysical properties, the change in these properties could also have a strong effect on the boiling process as a whole. Therefore, it is crucially important to also explore the dependence of the key boiling parameters on pressure in order to understand the physical mechanisms leading to DNB.

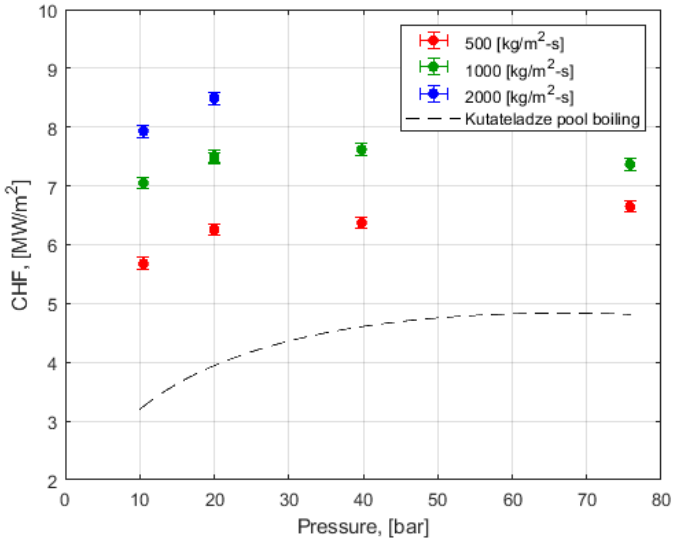

Figure 6-1. Critical heat fluxes measured at different pressures and mass fluxes

6.2. DRY AREA DISTRIBUTIONS

The process of DNB at pressures between 10.5 and 75.8 bar and the mass flux of 500 kg/(m^2-s) is visualized in Figure 6-2. Figure 6-2 demonstrates how individual dry spots created by bubbles eventually grow and merge to form one large dry spot. Similar behavior was observed by other researchers in low pressure experiments [8], [51], [52], suggesting that at least qualitatively the mechanism of DNB does not differ significantly between low and high pressures. There are also no apparent differences in either the time or the length scales of irreversible dry spots shown in Figure 6-2. In the majority of our tests, the power was cut down when the dry spot reached approximately 1 – 2 mm in diameter. This was done to prevent damage to the heater. However, in a few tests, the dry spot was allowed to grow undefinitely. In those cases, the dry spot rapidly covered the entire field of view of the camera, eventually shattering the sapphire substrates due to the thermal shock caused by the temperature excursion in the area of a dry spot. Nevertheless, the values of CHF measured in the destructive tests were similar to the values measured in non-destructive tests. These destructive cases confirm that the CHF values measured by cutting the power at an early stage of dry spot formation are indeed representative of the runaway dryout induced by the boiling crisis. One major difference between pressures that can be observed in Figure 6-2 is the absence of small dry spots associated with individual bubbles for the pressure of 75.8 bar. This is likely caused by the decrease in the size of individual dry spots, making them undetectable with the current optical setup (i.e. with the pixel size between 5 and 6 μm). Such a conclusion is corroborated by Figure 6-3, which shows phase detection images of individual bubbles at low heat fluxes close to the onset of nucleate boiling (ONB). Due to the low heat fluxes, both the outlines of the bubbles and the dry areas are present in Figure 6-3. Note that the size of the dry areas gets smaller with increasing pressure, making them undetectable at the pressure of 39.8 bar. These results suggest that at 75.8 bar the dry areas become even smaller. Note that with increasing heat flux, the dry areas become larger, allowing us to detect them at the pressure of 39.8 bar and high heat

fluxes (see Figure 6-2). However, we speculate that at 75.8 bar the dry spots are so small, that they become difficult to detect even at high heat fluxes.

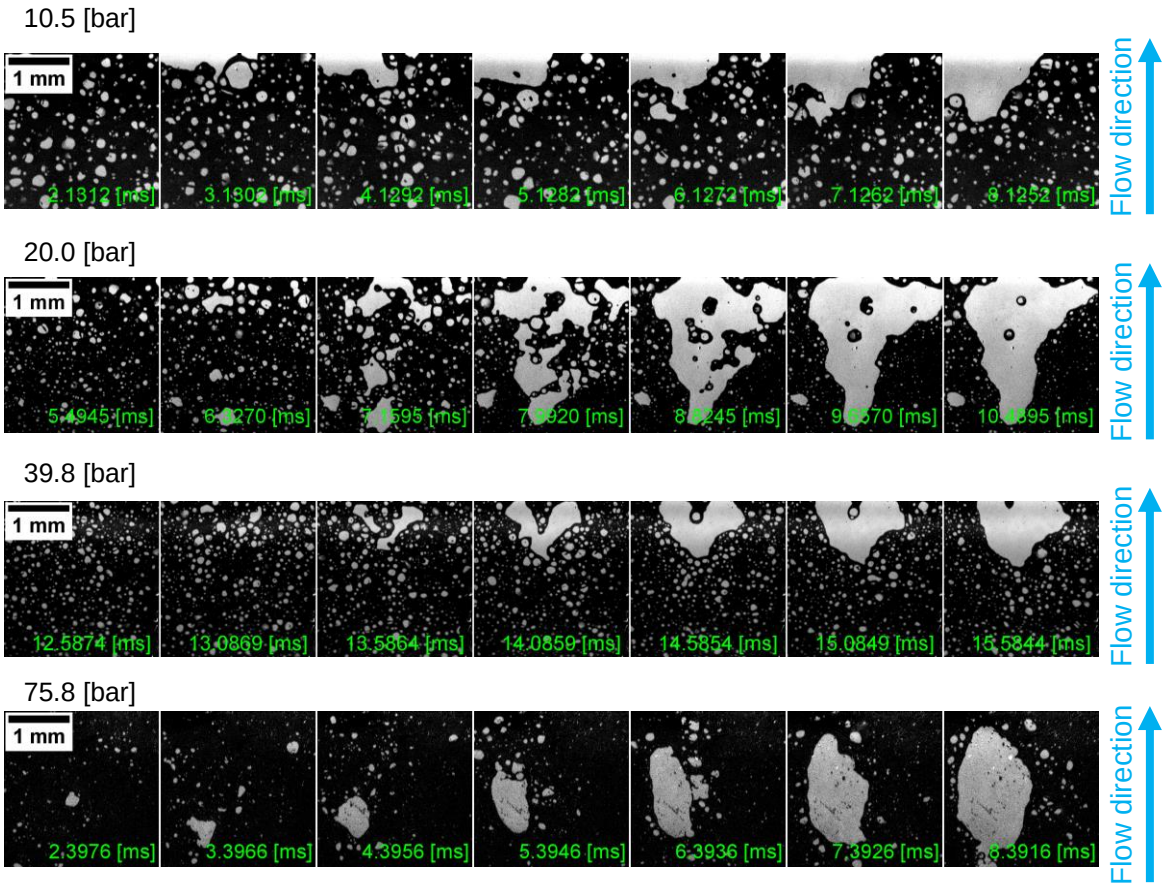

Figure 6-2. Visualization of the irreversible dry spot formation leading to the DNB for pressures between 10.5 and 75.8 bar and the mass flux of 500 kg/(m2-s). The bright regions in each image represent the dry areas, while the dark regions are in contact with the liquid.

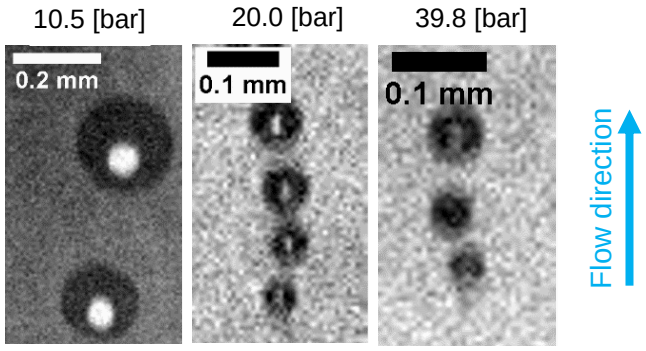

Figure 6-3. Change in dry area size under individual bubbles for pressures between 10.5 and 39.8 bar, mass flux of 500 kg/(m2s), and several heat fluxes close to the onset of

nucleate boiling. The dry areas associated with each bubble appear as bright regions in each picture. The images demonstrate how the dry areas associated with individual bubbles get smaller with increasing pressure, becoming almost undetectable when the pressure reaches 39.8 bar.

The distributions of dry area sizes are shown in Figure 6-4. Similar to the work of Zhang et al. [7], these distributions tend to follow power laws (with negative exponents smaller than three, which makes them "scale-free") when the heat flux approaches CHF. Whenever the system is at or above the CHF limit, it forms large dry patches, leading to supercritical distributions (101% - 102% CHF in Figure 6-4). In all cases the exponent of the critical distribution was approximately 2. For low heat fluxes (i.e. 1.94 – 1.97 MW/m^2 in Figure 6-4) the distribution of bubble footprint size follows an exponentially damped distribution given by Equation (6-2)

$$P(R) = \frac{\pi \cdot R}{2 \cdot \langle R \rangle^2} \cdot \exp\left(-\frac{\pi \cdot R^2}{4 \cdot \langle R \rangle^2}\right) \tag{6-2}$$

where R is the footprint radius and $\langle R \rangle$ is the average footprint radius. The conversion between the radius and the footprint area was made under the assumption of the circular bubble footprint shape (i.e. $A = \pi R^2$). Interestingly, the exponentially damped portion of the distribution appears to dominate the region of low bubble footprint area even for heat fluxes which are close to CHF. We believe that this effect could be caused by the limited interaction between bubble footprints when the footprint size is too small. To further support this statement, we calculated the probability of bubble footprint interaction using the complete spatial randomness method and its modifications suggested in Ref. [15]. The expression for the probability of bubble footprint interaction is given by Equation (6-3)

$$P_{interaction}(R) = 1 - \exp\left(-f \cdot t_g \cdot N_a'' \cdot \pi \cdot R^2\right) \tag{6-3}$$

where bubble departure frequency f, growth time t_g, and nucleation site density N_a'' were measured using the dry area tracking algorithm (see Sub-Section 2.7.4). The resulting interaction probability is plotted in Figure 6-5 for the pressures of 10.5, 20 and 39.8 bar. Due to the small footprint size, it was not possible to make reliable measurements for f, t_g, and N_a'' for the pressure of 75.8 bar. Dashed lines in Figure 6-5 represent a tentative boundary between exponentially damped and critical distributions in Figure 6-4. Figure 6-5 suggests that indeed the boundary between exponentially damped and critical distributions appear to coincide with the bubble footprint size for which the probability of interaction is above 50%.

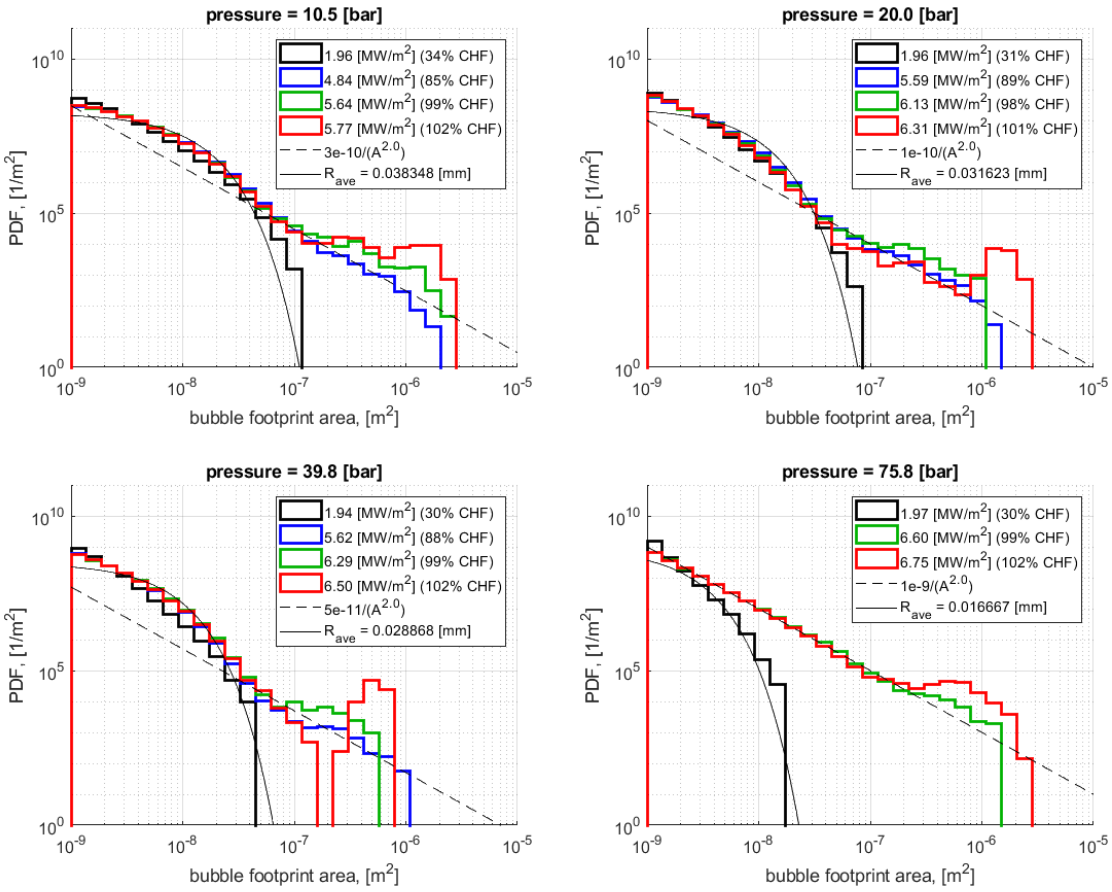

Figure 6-4. Probability density functions for bubble footprint areas captured at pressures between 10.5 and 75.8 bar, mass flux of 500 kg/(m^2-s), and subcooling of 10 ºC

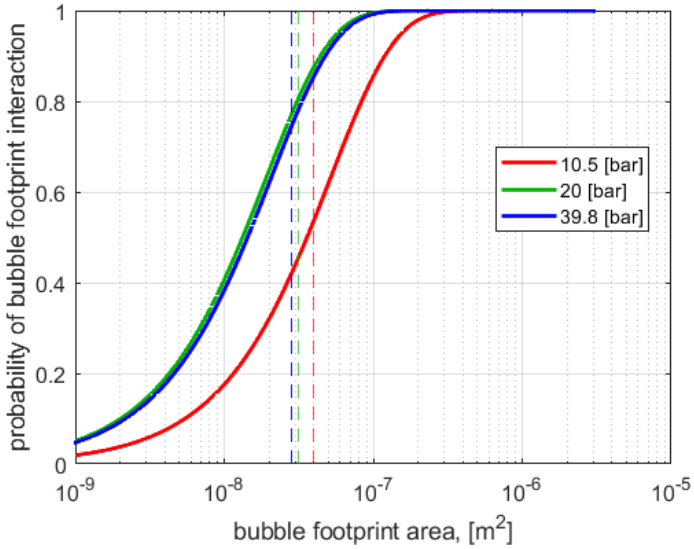

Figure 6-5. Probability of bubble footprint interaction. Dashed lines represent a tentative boundary between exponentially damped and critical distributions in Figure 6-4

6.3. CONCLUSION TO THE CHAPTER AND FUTURE WORK

In the present Chapter we briefly examined experimental results concerning the departure from nucleate boiling. The values of critical heat flux exhibit the same general trend with respect to pressure as the dimensional analysis of Kutateladze. The formation of irreversible dry spot at DNB is qualitatively similar with the low-pressure cases. The distribution of dry spots area becomes critical close to the point of CHF, similar to the observations presented in Ref. [7]. Interestingly, the critical distribution does not extend to the smallest bubble footprint areas, instead transitioning to the exponentially damped distribution. We speculate that such behavior can be explained by limited interaction between bubble footprints for very small footprint areas. However, further analyses would be required before we can draw clear conclusions.

7. CONCLUSION AND FUTURE WORK

7.1. CONCLUSIONS

In this Thesis we presented an extensive scientific analysis of high pressure boiling of water. We created a unique experimental apparatus, making it possible to visualize the behavior of bubbles in high pressure flow boiling conditions with high-resolution imaging techniques. We developed a new phase detection approach, making it possible not only to simplify the measurement setup, but also resolve dry areas and microlayers with high level of detail. The combination of the new experimental apparatus and phase detection technique allowed us to examine various aspects of high pressure boiling, with the emphasis on physical mechanisms that determine modeling strategies for boiling heat transfer. The highest pressure reached in the present study was 76 bar. The highest mass flux was 2000 kg/(m^2s). All test, with the exception of a few saturated pool boiling experiments, were performed at 10 ºC of subcooling.

First, we addressed the process of bubble departure by analyzing bubble growth histories and bubble pathlines measured at different pressures and mass fluxes. The analysis of bubble departure was performed for low heat fluxes and was limited to the regime of isolated bubbles. The process of bubble departure at higher heat flux warrants a separate investigation with the focus on the effect of vapor clotting on departure and lift-off processes. We observed vapor clotting appear in all tests as soon as the bubbles began to merge. While we did not quantify the size of vapor clots, qualitatively we observe that higher heat fluxes lead to larger vapor clots. Based on qualitative observations, we concluded that vapor clotting may affect the process of bubble departure and lift-off.

Regarding the process of bubble departure at low heat flux, the key finding are as follows:

- Bubble growth in high pressure boiling is dominated by the thermally controlled growth phase. The change in bubble radius with time elapsed since its nucleation was well predicted with the theoretical Plesset and Zwick solution for thermally controlled growth (i.e., proportional to the square root of time) with the addition of a fitting coefficient C_R that varied between 0.5 and 1 depending on the operating conditions. The use of coefficient C_R was likely needed to account for the fact that bubbles grow inside a thermal boundary layer whose temperature is not uniform. Therefore, the exact value of this coefficient should depend on the subcooling, flow rate and the size of the bubble relative to the thickness of the thermal boundary layer. While we did not analyze the dependence of the coefficient C_R on system parameters, we speculate that it could be modeled in the same way as the coefficient χ used in the work of Mazzocco et al. [43], who also applied this coefficient to correct the Plesset and Zwick solution when calculating the growth rate of a bubble in subcooled flow boiling.
- Analysis of forces acting on a bubble led us to the conclusion that in the case of high-pressure flow boiling on a vertical wall nothing prevents a bubble from sliding immediately after its nucleation. The only forces relevant when analyzing bubble departure by sliding at high pressures are drag, buoyancy and inertia. We also demonstrated that inertial force is not negligible, and could have a larger magnitude

than buoyancy during the initial stage of the bubble growth. The immediacy of the bubble departure will lead to a considerable decrease in bubble growth time in high pressure conditions compared to low pressure. Note that a similar trend of decreasing growth time was previously postulated in the works of Demarly [19] and Kommajosyula [17]. Our experimental results seem to corroborate their assumptions. Furthermore, the ease by which the bubbles can slide near the boiling surface may result in increased importance of the heat transfer enhancement due to sliding bubbles. The importance of sliding bubbles was also emphasized before in the works of Yeoh et al. [14] and Gilman and Baglietto [15].

- In contrast to the low pressure boiling, a large magnitude of the inertial force in high-pressure conditions makes it possible to apply a force balance approach to characterize the bubble departure process. Therefore, a simplified force balance was constructed and used to solve for bubble pathlines (i.e., bubble position vs. time). Bubble pathlines predicted with the force balance were in a good agreement with the experimentally measured bubble pathlines.
- Since we found that bubbles depart as soon as they nucleate, defining the departure diameter became difficult. Therefore, a criterion for bubble departure in high pressure boiling was proposed. This criterion recognizes the absence of adhesion forces and defines the point of bubble departure as the time when the nucleation site is no longer covered by the projected area of the bubble. This criterion was used to measure departure diameters in high pressure flow boiling, as well as to predict the departure diameter based on the simplified force balance model. The measurements and the predictions of the model were in a good agreement.
- Finally, the predictions for the bubble departure diameter were also compared to the pool boiling data from other studies, showing slight overestimation of the departure diameter, while following the correct decreasing trend with increasing pressure. Overall, the proposed model for bubble departure diameter showed satisfactory performance for the case of 10 ºC of subcooling and across a range of pressures and mass fluxes.

Second, we studied aspects of evaporative heat transfer in low- and high-pressure conditions with the focus on the microlayer and triple contact line (TCL) evaporation. The purpose of this analysis was to characterize the magnitude of the evaporative heat flux and the disappearance of the microlayer in high-pressure flow boiling. We studied velocities of the apparent contact line, ACL (i.e. the contact line formed by the edge of the bubble footprint), and real contact line, RCL (i.e. the contact line formed by the edge of the dry spot), at different pressures and mass fluxes. Contact line velocities in the upstream and downstream portions of a bubble were studied separately to quantify the flow-induced deformation of the microlayer. For a selected test case, the profile of the microlayer was measured by analyzing interference fringes. The measured microlayer profile was used within a 2D transient conduction simulation to attempt the quantification of the heat and mass transfer in the microlayer region, allowing for the determination of the mechanisms that govern RCL movement. With regard to the microlayer evaporation, the following conclusions were reached:

- We observed a complete disappearance of the microlayer for pressures higher than 3 bar. The disappearance was connected to the decrease in the initial ACL velocity

(i.e. the ACL velocity in the very beginning of the bubble growth) with pressure. Initial RCL velocity remained unchanged across several pressures. Whenever ACL velocity dropped below the RCL velocity, microlayer was no longer forming. Therefore, a constant RCL velocity observed in the present study can be thought of as a measure of the critical dewetting velocity. Based on the measured value of the RCL velocity and the analytical solution for the thermally controlled growth of a bubble, we developed a regime map, showing in which pressures and stages of the bubble growth will the microlayer exist.

- Presence of flow results in a deformation of the microlayer, leading to its disappearance in the upstream portion of the bubble footprint, while enhancing microlayer growth in the downstream portion. The deformation of the microlayer was also tied to the ACL velocity, with the upstream portion of the bubble having smaller ACL velocity because of the flow- and buoyancy-induced bubble movement.
- Transient conduction simulation showed that the heat transfer through the microlayer could be well predicted using the evaporative thermal resistance $R_{ev} = 3.846 \left[\frac{m^{2}\cdot^{o}C}{MW}\right]$, which was also identified as a likely R_{ev} value in Ref. [105], while corresponding to the accommodation coefficient of 0.03 in the context of the kinetic theory developed by Schrage. In contrast, the experimentally measured depletion of the microlayer cannot be accounted for by evaporation alone, suggesting that both thermal and hydrodynamic depletion play a role in determining the critical Capillary number. Since these two mechanisms are affected by multiple system, fluid, and surface parameters, there is no reason to believe that the value of the critical Capillary number measured in the present study is universal. We believe, that surface wettability could play a major role in changing the critical Capillary number, which could change the maximum pressure at which microlayer forms. In fact, the prediction of the critical Capillary number made by using the expression from the work of Demarly [19], which in turn was based on the DNS analysis of Guion [20], displays a strong dependence of the critical Capillary number on the contact angle (see Figure 4-11). Furthermore, the measured value of the critical Capillary number matches the prediction for the contact angle of 51.5º, meaning that the prediction is in the same ballpark as the measurement. Note that DNS analysis of Guion [20] only considered hydrodynamic dewetting. The fact that measured and predicted values of the critical Capillary number are similar further supports the importance of hydrodynamic effects for the microlayer depletions.

Triple contact line evaporation was studied using the model of Stephan and Hammer [107], together with the experimentally measured values of the contact line density. The results reveal that TCL evaporation cannot account for more than 20% of the total heat flux at the boiling surface. The estimated 20% is an upper bound of the TCL evaporation partitioning and in reality, we expect TCL evaporation to be even weaker.

Third, we investigated statistical variation of boiling parameters (i.e. bubble departure frequency f, wait and growth time (t_w and t_g), and the total area visited by a bubble A_{bub}). An algorithm was created and applied to phase detection recordings to measure these boiling parameters for virtually all nucleation events, while also tying each nucleation

event to a particular nucleation site. The dataset acquired with the new algorithm highlighted the variation of the boiling parameters between nucleation sites and nucleation events, making it important to consider the effect of the averaging method that could be used to convert the distributions of the boiling parameters into average values that are relevant for the heat flux partitioning calculations. Three averaging methods were proposed, named Tier I, II, and III.

- Tier I method ignores the variation of boiling parameters between nucleation sites and the non-linearities of heat flux partitioning equations. It only considers the variation between individual nucleation events.
- Tier II method ignores the non-linearities of heat flux partitioning equations, while considering the variations of boiling parameters between nucleation events and sites.
- Tier III considers all aspects of boiling parameter distributions and heat flux partitioning equations, leading to the most accurate way of averaging the boiling parameters.

Practically, Tier I method is the easiest to implement, while Tier III method is the most accurate. All three averaging methods were then applied to the measured values of boiling parameters to calculate partitioned heat fluxed due to transient conduction and forced convection. The major findings of this analysis are as follows:

- All boiling parameters vary considerably between nucleation sites and individual nucleation events. The biggest variation is observed for temporal parameters, including bubble departure frequency, bubble wait time, and bubble period, with the exception of the bubble growth time, for which the variation is small. The total area visited by a bubble A_{bub} also varies by several orders of magnitude, with the variation between nucleation sites and nucleation events being very similar. Interestingly, the distribution of the bubble departure frequency f between nucleation sites exhibits a power-law similar to the distribution of the bubble footprint area observed in the work of Zhang et al. [7]. In such a power law, the majority of nucleation sites have very small departure frequency, while very few sites exhibit high departure frequency. The appearance of the power-law distribution suggests that all nucleation sites present on the boiling surface are relevant for the heat removal process, despite the low departure frequencies they might have. Note that the connection between the nucleation site density N'', temporal parameters (i.e., growth time t_g and departure frequency f), and the bubble size was emphasized before in the work of Gilman and Baglietto [15]. Our work further highlights such connection, while also demonstrating that all boiling parameters vary in a complex way.
- Among the proposed averaging methods, Tier III is the most accurate. Interestingly, our results suggest that the difference between Tier I and Tier III is not large, at least for transient conduction and forced convection heat fluxes and the range of operating conditions explored here. The worst performance was observed for Tier II averaging method, suggesting that whenever the variation between nucleation sites and events is considered, the non-linearities of the heat flux partitioning equations must be considered as well.
- Calculated partitioned heat fluxes due to transient conduction and forced convection are fairly small, accounting for only 30% to 40% of the total heat flux

transferred at the boiling surface. Even if the upper bound of the TCL evaporation heat flux (i.e. 20%) is added to the heat flux partitioning analysis, around 40% of the total heat flux still remains unaccounted for. We speculate, that other mechanisms result in the enhancement of the heat transfer at the boiling surface. Based on the preliminary low-pressure experiments performed in our laboratory in which the partitioned heat flux can be measured directly using infrared thermometry, we speculate that the unknown mechanism mainly affects the forced convection heat transfer coefficients.

Fourth, a brief analysis of the dry area distributions and irreversible dry spots leading to DNB was performed. The formation of irreversible dry spot at DNB is qualitatively similar to the low-pressure cases. The distribution of dry spots area becomes critical close to the point of CHF, similar to the observations presented in Ref. [7]. Interestingly, the critical distribution does not extend to the smallest bubble footprint areas, instead transitioning to the exponentially damped distribution. We speculate that such behavior can be explained by limited interaction between bubble footprints for very small footprint areas.

Overall, our findings reveal multiple important aspects of high pressure boiling that are in contradiction with the present mechanistic modeling frameworks. Although we proposed a criterion for bubble departure and were able to predict bubble departure diameters from other studies, the whole concept of the bubble departure diameter does not provide a good physical description of the bubble dynamics in high pressure flow boiling. For low heat fluxes bubbles depart immediately after nucleation, turning bubble departure into a continuous process. In contrast, the classical interpretation of bubble departure is discrete, with a clear delineation between time periods when the bubble is attached to the wall and the point of bubble departure. While in reality the departure of a bubble is always continuous (i.e., the bubble cannot suddenly disappear from the boiling surface upon its departure), normally it is possible to clearly identify the onset of bubble departure, making the discrete approximation somewhat reliable. In our analysis we demonstrated that the discrete approximation breaks down completely in high pressure flow boiling. Furthermore, when the heat flux is increased the process of bubble departure will be further altered by the interaction with vapor clots, potentially making the coalescence with the vapor clot a dominant departure mode.

The inability of transient conduction, evaporation and forced convection heat transfer modes to capture heat flux partitioning at high heat fluxes close to CHF also hints at the potentially new heat transfer mechanism that is not captured within the current partitioning frameworks. The identification of this mechanism could remove the need for near-wall partitioning methods (i.e. the methods that consider the evaporation of the entire bubble volume) and may lead to the development of a predictive true wall partitioning model.

7.2. GENERAL DIRECTION FOR THE FUTURE WORK

While many possible directions for the future work are presented in the end of each Chapter, they should mainly be focused on identifying the missing heat transfer mechanism that could allow true wall partitioning frameworks to predict boiling heat transfer in high

pressure conditions. Therefore, a general future research direction proposed here is divided into two stages:

1. The techniques developed in the present Thesis are new and were only applied to the set of operating conditions explored here. Therefore, we should continue to scrutinize the validity and errors of these techniques, compare them to the alternative methods (e.g. infrared thermometry in low pressure boiling) and explore a wider range of operating conditions.
2. If methods presented here prove robust and the same conclusions about the limitations of the current modeling frameworks are reached across a wide range of pressures, mass fluxes, and subcoolings, then a reassessment of the current modeling frameworks should be made, focusing on the identification of the mechanisms responsible for the missing heat flux partitioning and a better definition of the bubble departure diameter in the presence of vapor clots.

REFERENCES

[1] A. F. Mills and V. Ganesan, *Heat transfer*. Pearson Education, 1999.

[2] G. Liang and I. Mudawar, "Review of pool boiling enhancement by surface modification," *International Journal of Heat and Mass Transfer*, vol. 128. 2019, doi: 10.1016/j.ijheatmasstransfer.2018.09.026.

[3] W. R. Gambill and J. H. Lienhard, "An Upper Bound for the Critical Boiling Heat Flux," *J. Heat Transfer*, vol. 111, pp. 815–818, 1989, Accessed: Dec. 19, 2018. [Online]. Available: http://heattransfer.asmedigitalcollection.asme.org/.

[4] Y. Mitsutake and M. Monde, "Ultra high critical heat flux during forced flow boiling heat transfer with an impinging jet," *J. Heat Transfer*, vol. 125, no. 6, pp. 1038–1045, Dec. 2003, doi: 10.1115/1.1621899.

[5] Casl, "Consortium for Advanced Simulation of Light Water Reactors CASL Phase II Summary Report," 2020.

[6] E. Baglietto, E. Demarly, and R. Kommajosyula, "Boiling crisis as the stability limit to wall heat partitioning," *Appl. Phys. Lett.*, vol. 114, no. 10, p. 103701, Mar. 2019, doi: 10.1063/1.5080724.

[7] L. Zhang, J. Hyun Seong, and M. Bucci, "Percolative Scale-Free Behavior in the Boiling Crisis," *Phys. Rev. Lett.*, vol. 122, 2019, doi: 10.1103/PhysRevLett.122.134501.

[8] A. Richenderfer *et al.*, "Investigation of subcooled flow boiling and CHF using high-resolution diagnostics," *Exp. Therm. Fluid Sci.*, vol. 99, no. January, pp. 35–58, 2018, doi: 10.1016/j.expthermflusci.2018.07.017.

[9] R. W. Bowring, "Physical model, based on bubble detachment, and calculation of steam voidage in the sub-cooled region of a heated channel," Halden, Norway, 1962.

[10] N. Kurul and M. Podowski, "Multidimentional effects in forced convection subcooled boiling," in *Proceedings of the Ninth International Heat Transfer Conference*, 1990, pp. 21–26.

[11] B. B. Mikic and W. M. Rohsenow, "A new correlation of pool-boiling data including the effect of heating surface characteristics," *J. Heat Transfer*, vol. 91, no. 2, pp. 245–250, May 1969, doi: 10.1115/1.3580136.

[12] M. BUCCI, "A THEORETICAL AND EXPERIMENTAL STUDY OF VAPOR BUBBLE DYNAMICS IN SEPARATE EFFECT POOL BOILING CONDITIONS," Sep. 2020.

[13] R. L. Judd and K. S. Hwang, "A comprehensive model for nucleate pool boiling heat transfer including microlayer evaporation," *J. Heat Transfer*, vol. 98, no. 4, pp. 623–629, Nov. 1976, doi: 10.1115/1.3450610.

[14] G. H. Yeoh, S. C. P. Cheung, J. Y. Tu, and M. K. M. Ho, "Fundamental consideration of wall heat partition of vertical subcooled boiling flows," *Int. J. Heat Mass Transf.*, vol. 51, no. 15–16, pp. 3840–3853, 2008, doi: 10.1016/j.ijheatmasstransfer.2007.11.047.

[15] L. Gilman and E. Baglietto, "A self-consistent, physics-based boiling heat transfer modeling framework for use in computational fluid dynamics," *Int. J. Multiph. Flow*, vol. 95, pp. 35–53, Oct. 2017, doi: 10.1016/j.ijmultiphaseflow.2017.04.018.

[16] C. Gerardi, J. Buongiorno, L. W. Hu, and T. McKrell, "Study of bubble growth in water pool boiling through synchronized, infrared thermometry and high-speed

video," *Int. J. Heat Mass Transf.*, vol. 53, no. 19–20, pp. 4185–4192, 2010, doi: 10.1016/j.ijheatmasstransfer.2010.05.041.
[17] R. Kommajosyula, "Development and assessment of a physics-based model for subcooled flow boiling with application to CFD," 2020.
[18] L. Gilman, "Development of a General Purpose Subgrid Wall Boiling Model from Improved Physical Understanding for Use in Computational Fluid Dynamics," 2014.
[19] E. Demarly, "A new approach to predicting Departure from Nucleate Boiling (DNB) from direct representation of boiling heat transfer physics," *Massachusetts Inst. Technol.*, 2020.
[20] A. N. Guion, "Modeling and Simulation of Liquid Microlayer Formation and Evaporation in Nucleate Boiling using Computational Fluid Dynamics," no. 2009, p. 252, 2017, [Online]. Available: https://dspace.mit.edu/handle/1721.1/112380.
[21] M. A. Amidu, S. Jung, and H. Kim, "Direct experimental measurement for partitioning of wall heat flux during subcooled flow boiling: Effect of bubble areas of influence factor," *Int. J. Heat Mass Transf.*, vol. 127, pp. 515–533, Dec. 2018, doi: 10.1016/J.IJHEATMASSTRANSFER.2018.07.079.
[22] V. H. Del Valle and D. B. R. Kenning, "Subcooled flow boiling at high heat flux," *Int. J. Heat Mass Transf.*, vol. 28, no. 10, pp. 1907–1920, 1985, doi: 10.1016/0017-9310(85)90213-3.
[23] V. P. Carey, *Liquid-Vapor Phase-Change Phenomena*, 2nd ed. New York: Taylor & Francis Group, 2008.
[24] K. Schweikert, A. Sielaff, and P. Stephan, "On the transition between contact line evaporation and microlayer evaporation during the dewetting of a superheated wall," *Int. J. Therm. Sci.*, vol. 145, no. July, p. 106025, 2019, doi: 10.1016/j.ijthermalsci.2019.106025.
[25] L. M. Hocking, "Meniscus draw-up and draining," 2001.
[26] A. Guion, S. Afkhami, S. Zaleski, and J. Buongiorno, "Simulations of microlayer formation in nucleate boiling," *Int. J. Heat Mass Transf.*, vol. 127, pp. 1271–1284, Dec. 2018, doi: 10.1016/J.IJHEATMASSTRANSFER.2018.06.041.
[27] Z. Chen, A. Haginiwa, and Y. Utaka, "Detailed structure of microlayer in nucleate pool boiling for water measured by laser interferometric method," *Int. J. Heat Mass Transf.*, vol. 108, pp. 1285–1291, May 2017, doi: 10.1016/J.IJHEATMASSTRANSFER.2017.01.003.
[28] Z. Chen, X. Hu, K. Hu, Y. Utaka, and S. Mori, "Measurement of the microlayer characteristics in the whole range of nucleate boiling for water by laser interferometry," *Int. J. Heat Mass Transf.*, vol. 146, p. 118856, Jan. 2020, doi: 10.1016/j.ijheatmasstransfer.2019.118856.
[29] J.-M. Le Corre, S.-C. Yao, and C. H. Amon, "Two-phase flow regimes and mechanisms of critical heat flux under subcooled flow boiling conditions," *Nucl. Eng. Des.*, vol. 240, no. 2, pp. 245–251, Feb. 2010, doi: 10.1016/J.NUCENGDES.2008.12.008.
[30] Y. Haramura and Y. Katto, "A new hydrodynamic model of critical heat flux, applicable widely to both pool and forced convection boiling on submerged bodies in saturated liquids," *Int. J. Heat Mass Transf.*, vol. 26, no. 3, pp. 389–399, 1983, doi: 10.1016/0017-9310(83)90043-1.

[31] A. Serizawa, “Theoretical prediction of maximum heat flux in power transients,” *Int. J. Heat Mass Transf.*, 1983, doi: 10.1016/S0017-9310(83)80116-1.
[32] K. O. Pasamehmetoglu, R. A. Nelson, and F. S. Gunnerson, “Critical Heat Flux Modeling in Pool Boiling for Steady-State and Power Transients,” *J. Heat Transfer*, vol. 112, no. 4, p. 1048, Nov. 1990, doi: 10.1115/1.2910477.
[33] K. O. Pasamehmetoglu, R. A. Nelson, and F. S. Gunnerson, “Critical Heat Flux modeling in Forced Convection Boiling During Power Transients,” *J. Heat Transfer*, vol. 112, pp. 1058–1062, 1990.
[34] V. I. Tolubinsky and J. N. Ostrovsky, “On the mechanism of boiling heat transfer (vapour bubbles growth rate in the process of boiling of liquids, solutions, and binary mixtures),” *Int. J. Heat Mass Transf.*, vol. 9, no. 12, pp. 1463–1470, Dec. 1966, doi: 10.1016/0017-9310(66)90142-6.
[35] R. Séméria, “High-speed cinematography and pool boiling under high pressure,” *La Houille Blanche*, vol. 6, pp. 679–686, 1963.
[36] H. Sakashita and A. Ono, “Boiling behaviors and critical heat flux on a horizontal plate in saturated pool boiling of water at high pressures,” *Int. J. Heat Mass Transf.*, vol. 52, no. 3–4, pp. 744–750, Jan. 2009, doi: 10.1016/j.ijheatmasstransfer.2008.06.040.
[37] G. G. Treschev, “Number of steam generation sites in wall boiling,” in *Convective heat transfer in two-phase and single-phase flows*, 1964, pp. 118–129.
[38] H. C. Ünal, “Maximum bubble diameter, maximum bubble-growth time and bubble-growth rate during the subcooled nucleate flow boiling of water up to 17.7 MN/m2,” *Int. J. Heat Mass Transf.*, vol. 19, pp. 643–649, 1976, doi: 10.1016/0017-9310(76)90047-8.
[39] P. Griffith, J. A. Clark, and W. M. Rohsenow, “Void Volumes in Subcooled Boiling,” *U.S. Natl. Heat Transf. Conf.*, 1958.
[40] G. Kocamustafaogullari, “Pressure dependence of bubble departure diameter for water,” *Int. Commun. Heat Mass Transf.*, vol. 10, pp. 501–509, 1983.
[41] J. Klausner, L. Z. Zeng, J. F. Klausner, and R. Meit, “A unified model for the prediction of bubble detachment diameters in boiling systems-I. Pool boiling ARPA-E Advanced Research in Dry-cooling (ARID) Program View project A unified model for the prediction of bubble detachment diameters in boiling systems-l,” *Artic. Int. J. Heat Mass Transf.*, vol. 36, no. 5, pp. 2261–2270, 1993, doi: 10.1016/S0017-9310(05)80111-5.
[42] R. Sugrue and J. Buongiorno, “A modified force-balance model for prediction of bubble departure diameter in subcooled flow boiling,” *Nucl. Eng. Des.*, vol. 305, pp. 717–722, 2016, doi: 10.1016/j.nucengdes.2016.04.017.
[43] T. Mazzocco, W. Ambrosini, R. Kommajosyula, and E. Baglietto, “A reassessed model for mechanistic prediction of bubble departure and lift off diameters,” *Int. J. Heat Mass Transf.*, vol. 117, pp. 119–124, Feb. 2018, doi: 10.1016/J.IJHEATMASSTRANSFER.2017.09.105.
[44] M. Bucci, J. Buongiorno, and M. Bucci, “The not-so-subtle flaws of the force balance approach to predict the departure of bubbles in boiling heat transfer,” *Phys. Fluids*, vol. 33, no. 1, p. 017110, Jan. 2021, doi: 10.1063/5.0036956.
[45] G. Duhar and C. Colin, “Dynamics of bubble growth and detachment in a viscous shear flow,” *Phys. Fluids*, vol. 18, no. 7, p. 077101, Jul. 2006, doi:

10.1063/1.2213638.
[46] M. Lebon, J. Sebilleau, and C. Colin, “Dynamics of growth and detachment of an isolated bubble on an inclined surface,” *Phys. Rev. Fluids*, vol. 7, no. 3, pp. 1–16, 2018, doi: 10.1103/PhysRevFluids.3.073602.
[47] P. Di Marco, N. Giannini, and G. Saccone, “EXPERIMENTAL MEASUREMENT OF THE ELECTRIC FORCES ACTING ON A GROWING GAS BUBBLE IN QUASI-STATIC CONDITIONS,” *Interfacial Phenom. Heat Transf.*, vol. 3, no. 4, pp. 319–339, 2015, doi: 10.1615/interfacphenomheattransfer.2016014801.
[48] H. Sakashita, “Bubble Growth Rates and Nucleation Site Densities in Saturated Pool Boiling of Water at High Pressures,” *J. Nucl. Sci. Technol.*, vol. 48, no. 5, pp. 734–743, 2011, doi: 10.1080/18811248.2011.9711756.
[49] T. Hibiki and M. Ishii, “Active nucleation site density in boiling systems,” *Int. J. Heat Mass Transf.*, vol. 46, no. 14, pp. 2587–2601, 2003, doi: 10.1016/S0017-9310(03)00031-0.
[50] G. Liang and I. Mudawar, “Pool boiling critical heat flux (CHF) – Part 1: Review of mechanisms, models, and correlations,” *International Journal of Heat and Mass Transfer*, vol. 117. Elsevier Ltd, pp. 1352–1367, Feb. 01, 2018, doi: 10.1016/j.ijheatmasstransfer.2017.09.134.
[51] T. G. Theofanous, T. N. Dinh, J. P. Tu, and A. T. Dinh, “The boiling crisis phenomenon part II: Dryout dynamics and burnout,” *Exp. Therm. Fluid Sci.*, vol. 26, no. 6–7, pp. 793–810, 2002, doi: 10.1016/S0894-1777(02)00193-0.
[52] D. E. Kim, J. Song, and H. Kim, “Simultaneous observation of dynamics and thermal evolution of irreversible dry spot at critical heat flux in pool boiling,” *Int. J. Heat Mass Transf.*, vol. 99, pp. 409–423, 2016, doi: 10.1016/j.ijheatmasstransfer.2016.04.009.
[53] A. A. Maznev and O. B. Wright, “Upholding the diffraction limit in the focusing of light and sound,” *Wave Motion*, vol. 68, pp. 182–189, Jan. 2017, doi: 10.1016/j.wavemoti.2016.09.012.
[54] T. Yabuki and O. Nakabeppu, “Microlayer formation characteristics in pool isolated bubble boiling of water,” *Heat Mass Transf.*, vol. 53, no. 5, pp. 1745–1750, May 2017, doi: 10.1007/s00231-016-1936-9.
[55] M. G. Cooper and A. J. P. Lloyd, “The microlayer in nucleate pool boiling,” *Int. J. Heat Mass Transf.*, vol. 12, no. 8, pp. 895–913, Aug. 1969, doi: 10.1016/0017-9310(69)90154-9.
[56] F. D. Moore and R. B. Mesler, “The measurement of rapid surface temperature fluctuations during nucleate boiling of water,” *AIChE J.*, vol. 7, no. 4, pp. 620–624, Dec. 1961, doi: 10.1002/aic.690070418.
[57] Y. Utaka, Y. Kashiwabara, and M. Ozaki, “Microlayer structure in nucleate boiling of water and ethanol at atmospheric pressure,” *Int. J. Heat Mass Transf.*, vol. 57, no. 1, pp. 222–230, Jan. 2013, doi: 10.1016/J.IJHEATMASSTRANSFER.2012.10.031.
[58] M. Mehrvand and S. A. Putnam, “Transient and local two-phase heat transport at macro-scales to nano-scales,” *Commun. Phys.*, vol. 1, no. 1, pp. 1–13, Dec. 2018, doi: 10.1038/s42005-018-0018-3.
[59] H. Kim and J. Buongiorno, “Detection of liquid-vapor-solid triple contact line in two-phase heat transfer phenomena using high-speed infrared thermometry,” *Int. J. Multiph. Flow*, vol. 37, no. 2, pp. 166–172, Mar. 2011, doi:

10.1016/j.ijmultiphaseflow.2010.09.010.
[60] A. J. Richenderfer, “Development of MIST-IR: Multi-Spectral Infrared Thermography,” Massachusetts Institute of Technology, 2015. Accessed: Jun. 05, 2020. [Online]. Available: http://iibraries.mit.edu/ask.
[61] E. A. Chinnov, F. V. Ron’shin, and O. A. Kabov, “Two-phase flow patterns in short horizontal rectangular microchannels,” *Int. J. Multiph. Flow*, vol. 80, pp. 57–68, Apr. 2016, doi: 10.1016/j.ijmultiphaseflow.2015.11.006.
[62] F. Ronshin and E. Chinnov, “Experimental characterization of two-phase flow patterns in a slit microchannel,” *Exp. Therm. Fluid Sci.*, vol. 103, pp. 262–273, May 2019, doi: 10.1016/j.expthermflusci.2019.01.022.
[63] A. Zou, A. Chanana, A. Agrawal, P. C. Wayner, and S. C. Maroo, “Steady State Vapor Bubble in Pool Boiling,” *Sci. Rep.*, vol. 6, no. 1, p. 20240, Apr. 2016, doi: 10.1038/srep20240.
[64] L. D. Koffman and M. S. Plesset, “Experimental Observations of the Microlayer in Vapor Bubble Growth on a Heated Solid,” *J. Heat Transfer*, vol. 105, pp. 625–632, 1983, Accessed: Mar. 21, 2019. [Online]. Available: https://heattransfer.asmedigitalcollection.asme.org.
[65] H. H. Jawurek, H. G. Macgregor, and J. S. Bodenheimer, “Microlayer Topology And Bubble Growth In Nucleate Boiling,” in *Proc. SPIE 0674, 17th Intl Congress on High Speed Photography and Photonics*, Sep. 1987, vol. 0674, p. 202, doi: 10.1117/12.975554.
[66] Z. Chen, A. Haginiwa, and Y. Utaka, “Detailed structure of microlayer in nucleate pool boiling for water measured by laser interferometric method,” *Int. J. Heat Mass Transf.*, vol. 108, 2017, doi: 10.1016/j.ijheatmasstransfer.2017.01.003.
[67] C. M. Voutsinos and R. L. Judd, “Laser interferometrc investigation of the microlayer evaporation phenomenon,” *J. Heat Transfer*, 1975, Accessed: Apr. 08, 2019. [Online]. Available: https://heattransfer.asmedigitalcollection.asme.org.
[68] I.-C. Chu, H. C. NO, and C.-H. Song, “Visualization of boiling structure and critical heat flux phenomenon for a narrow heating surface in a horizontal pool of saturated water,” *Int. J. Heat Mass Transf.*, vol. 62, pp. 142–152, Jul. 2013, doi: 10.1016/J.IJHEATMASSTRANSFER.2013.02.067.
[69] S. Jung and H. Kim, “An experimental method to simultaneously measure the dynamics and heat transfer associated with a single bubble during nucleate boiling on a horizontal surface,” *Int. J. Heat Mass Transf.*, vol. 73, pp. 365–375, Jun. 2014, doi: 10.1016/J.IJHEATMASSTRANSFER.2014.02.014.
[70] H. J. Chung and H. C. No, “Simultaneous visualization of dry spots and bubbles for pool boiling of R-113 on a horizontal heater,” *Int. J. Heat Mass Transf.*, vol. 46, no. 12, pp. 2239–2251, Jun. 2003, doi: 10.1016/S0017-9310(02)00524-0.
[71] J. C. Dainty, A. E. Ennos, M. Francon, J. W. Goodman, T. S. McKechnie, and G. Parry, *Laser Speckle and Related Phenomena*. Springer-Verlag, 1975.
[72] H. J. Van Ouwerkerk, “Burnout in pool boiling the stability of boiling mechanisms,” *Int. J. Heat Mass Transf.*, vol. 15, no. 1, pp. 25–34, Jan. 1972, doi: 10.1016/0017-9310(72)90163-9.
[73] A. Surtaev, V. Serdyukov, J. Zhou, A. Pavlenko, and V. Tumanov, “An experimental study of vapor bubbles dynamics at water and ethanol pool boiling at low and high heat fluxes,” *Int. J. Heat Mass Transf.*, vol. 126, pp. 297–311, Nov.

2018, doi: 10.1016/j.ijheatmasstransfer.2018.06.001.
[74] R. L. Judd, “Comparison of Experimental Microlayer Thickness Results,” *Trans. Can. Soc. Mech. Eng.*, vol. 1, no. 3, pp. 168–170, Sep. 1972, doi: 10.1139/tcsme-1972-0027.
[75] H. H. Jawurek, “Simultaneous determination of microlayer geometry and bubble growth in nucleate boiling,” *Int. J. Heat Mass Transf.*, vol. 12, no. 8, pp. 843–848, Aug. 1969, doi: 10.1016/0017-9310(69)90151-3.
[76] S. Nishio, T. Gotoh, and N. Nagai, “Observation of boiling structures in high heat-flux boiling,” *Int. J. Heat Mass Transf.*, vol. 41, no. 21, pp. 3191–3201, Jun. 1998, doi: 10.1016/S0017-9310(98)00062-3.
[77] K. Torikai, K. Suzuki, and M. Yamaguchi, “Study on Contact Area of Pool Boiling Bubbles on a Heating Surface : Observation of Bubbles in Transition Boiling,” *JSME Int. journal. Ser. 2, Fluids Eng. heat Transf. power, Combust. Thermophys. Prop.*, vol. 34, no. 2, pp. 195–201, May 1991, doi: 10.1299/jsmeb1988.34.2_195.
[78] S. Nishio and H. Tanaka, “Visualization of boiling structures in high heat-flux pool-boiling,” *Int. J. Heat Mass Transf.*, vol. 47, no. 21, pp. 4559–4568, Oct. 2004, doi: 10.1016/j.ijheatmasstransfer.2003.07.033.
[79] “AP1000 Design Control Document. Tier 2.”
[80] ASME, “Section II,” in *Boiler and Pressure Vessel Code*, ASME.
[81] Ferro Ceramic Grinding, “http://www.ferroceramic.com/sapphire_table.htm.” .
[82] American Society of Mechanical Engineers, *ASME B16.5-2017 Pipe flanges and flanged fittings : NPS 1/2 through NPS 24 metric/inch standard*. .
[83] ASME, *Unified inch screw threads (UN and UNR thread form).* American Society of Mechanical Engineers, 2003.
[84] G.-Y. Su, M. Bucci, T. Mckrell, and J. Buongiorno, “Transient boiling of water under exponentially escalating heat inputs. Part I: Pool boiling,” *Int. J. Heat Mass Transf.*, vol. 96, pp. 667–684, 2016, doi: 10.1016/j.ijheatmasstransfer.2016.01.032.
[85] “(No Title).” https://formlabs-media.formlabs.com/datasheets/High_Temp_Technical.pdf (accessed May 18, 2021).
[86] A. Kossolapov, B. Phillips, and M. Bucci, “Can LED lights replace lasers for detailed investigations of boiling phenomena?,” *Int. J. Multiph. Flow*, vol. 135, p. 103522, Feb. 2021, doi: 10.1016/j.ijmultiphaseflow.2020.103522.
[87] M. Born and E. Wolf, *Principles of Optics: Electromagnetic Theory of Propogation, Interference and Diffraction of Light*, 6th ed. Cambridge: Cambridge University Press, 1999.
[88] “Color Spaces, clarkvision.com.” https://clarkvision.com/articles/color-spaces/ (accessed May 07, 2020).
[89] M. Bucci, A. Richenderfer, G.-Y. Su, T. Mckrell, and J. Buongiorno, “A mechanistic IR calibration technique for boiling heat transfer investigations,” *Int. J. Multiph. Flow*, vol. 83, pp. 115–127, 2016, doi: 10.1016/j.ijmultiphaseflow.2016.03.007.
[90] F. Chavagnat, R. Nop, N. Dorville, B. Phillips, and M. Bucci, “Single-phase heat transfer regimes in forced flow conditions under exponential heat inputs,” *Int. J. Heat Mass Transf.*, vol. 174, p. 121294, Aug. 2021, doi: 10.1016/j.ijheatmasstransfer.2021.121294.
[91] G. P. Celata, M. Cumo, A. Mariani, M. Simoncini, and G. Zummo, “Rationalization

of existing mechanistic models for the prediction of water subcooled flow boiling critical heat flux," *Int. J. Heat Mass Transf.*, vol. 37, no. SUPPL. 1, pp. 347–360, Mar. 1994, doi: 10.1016/0017-9310(94)90035-3.

[92] Y. Katto, "A prediction model of subcooled water flow boiling CHF for pressure in the range 0.1–20 MPa," *Int. J. Heat Mass Transf.*, vol. 35, no. 5, pp. 1115–1123, May 1992, doi: 10.1016/0017-9310(92)90172-O.

[93] A. Kossolapov *et al.*, "The boiling crisis of water under exponentially escalating heat inputs in subcooled flow boiling at atmospheric pressure," *Int. J. Heat Mass Transf.*, vol. 160, p. 120137, Oct. 2020, doi: 10.1016/j.ijheatmasstransfer.2020.120137.

[94] B. B. Mikic, W. M. Rohsenow, and P. Griffith, "On Bubble Growth Rates," Accessed: Jul. 11, 2018. [Online]. Available: https://ac.els-cdn.com/0017931070900402/1-s2.0-0017931070900402-main.pdf?_tid=983f5e7d-5bcb-42c1-bae1-f81b46cea285&acdnat=1531335311_1fef9273a8a88d248a6d2cb2c25f9f22.

[95] W. H. Jens and P. A. Lottes, "Analysis of heat transfer, burnout, pressure drop and density data for high-pressure water," Chicago, May 1951.

[96] T. Mazzocco, W. Ambrosini, R. Kommajosyula, and E. Baglietto, "A reassessed model for mechanistic prediction of bubble departure and lift off diameters," *Int. J. Heat Mass Transf.*, vol. 117, pp. 119–124, Feb. 2018, doi: 10.1016/j.ijheatmasstransfer.2017.09.105.

[97] J. F. Klausner, R. Mei, D. M. Bernhard, and L. Z. Zeng, "Vapor bubble departure in forced convection boiling," *Int. J. Heat Mass Transf.*, vol. 36, no. 3, pp. 651–662, 1993, doi: 10.1016/0017-9310(93)80041-R.

[98] N. E. Todreas and M. S. Kazimi, *Nuclear Systems Volume I: Thermal-Hydraulics Fundamentals*. CRC Press, 2011.

[99] J. Song, M. Ma, and L. Fan, "Understanding the temperature dependence of contact angle of water on a smooth hydrophobic surface at pressurized conditions: An experimental study," *Langmuir*, p. acs.langmuir.0c01671, Jul. 2020, doi: 10.1021/acs.langmuir.0c01671.

[100] J. W. Song, D. L. Zeng, and L. W. Fan, "Temperature dependence of contact angles of water on a stainless steel surface at elevated temperatures and pressures: In situ characterization and thermodynamic analysis," *J. Colloid Interface Sci.*, vol. 561, pp. 870–880, Mar. 2020, doi: 10.1016/j.jcis.2019.11.070.

[101] Y. Hirose, T. Hayashi, T. Hazuku, and T. Takamasa, "Experimental study on contact angle of water droplet in high-temperature condition," in *International Conference on Nuclear Engineering, Proceedings, ICONE*, Sep. 2006, vol. 2006, pp. 709–716, doi: 10.1115/ICONE14-89614.

[102] J. D. Bernardin, I. Mudawar, C. B. Walsh, and E. I. Franses, "Contact angle temperature dependence for water droplets on practical aluminum surfaces," *Int. J. Heat Mass Transf.*, vol. 40, no. 5, pp. 1017–1033, 1997, doi: 10.1016/0017-9310(96)00184-6.

[103] D. W. Scott, *Statistics*. Wiley, 2020.

[104] G. Giustini, S. Jung, H. Kim, and S. P. Walker, "Evaporative thermal resistance and its influence on microscopic bubble growth," *Int. J. Heat Mass Transf.*, vol. 101, pp. 733–741, Oct. 2016, doi: 10.1016/J.IJHEATMASSTRANSFER.2016.05.081.

[105] G. Giustini, S. Jung, H. Kim, K. H. Ardron, and S. P. Walker, “Microlayer evaporation during steam bubble growth,” *Int. J. Therm. Sci.*, vol. 137, pp. 45–54, Mar. 2019, doi: 10.1016/J.IJTHERMALSCI.2018.11.012.
[106] S. Jung and H. Kim, “Hydrodynamic formation of a microlayer underneath a boiling bubble,” *Int. J. Heat Mass Transf.*, vol. 120, 2018, doi: 10.1016/j.ijheatmasstransfer.2017.12.098.
[107] P. Stephan and J. Hammer, “A new model for nucleate boiling heat transfer,” *Wärme - und Stoffübertragung*, vol. 30, no. 2, pp. 119–125, Nov. 1994, doi: 10.1007/BF00715018.
[108] K. Sivanandan and A. Mani, “Estimation of viscosity and thermal conductivity of R142b and R152a,” *Int. J. Energy Res.*, vol. 18, no. 6, pp. 595–603, 1994, doi: 10.1002/er.4440180604.
[109] H. Nabizadeh and F. Mayinger, “Viscosity of refrigerants R12, R113, and R114 and mixtures of R12 + R114 at high pressure,” *Int. J. Thermophys.*, vol. 10, no. 3, pp. 701–712, 1989, doi: 10.1007/BF00507990.
[110] M. N. Rahaman, *Ceramic processing and sintering*. New York: M. Dekker, 2003.
[111] R. Cole, “A photographic study of pool boiling in the region of the critical heat flux,” *AIChE J.*, vol. 6, no. 4, pp. 533–538, 1960, doi: 10.1002/aic.690060405.

8. APPENDICES

A. DETAILS OF FINITE ELEMENT ANALYSIS OF THE TEST SECTION

The FEA of stresses in the sapphire was made using the built-in FE solver in Solidworks. The results are shown in Figure 8-1. The properties of sapphire are listed in Table 8-1. In the analysis, a uniform pressure of 2600 psig, (the highest PRV setpoint in the system) was applied to one side of the window, when the other side was rigidly supported at the periphery, modeling the area of contact between the window and the flange. The peak stress in the sapphire is only 33% of its tensile strength. Stresses in most of the body are even lower.

Table 8-1. Structural properties of Sapphire [81]

Property	Value	Units
Elastic Modulus	36,259	ksi
Poisson's Ratio	0.29	-
Mass density	0.143	Lb/in^3
Tensile Strength	36,259	psi
Compressive Strength	290	ksi

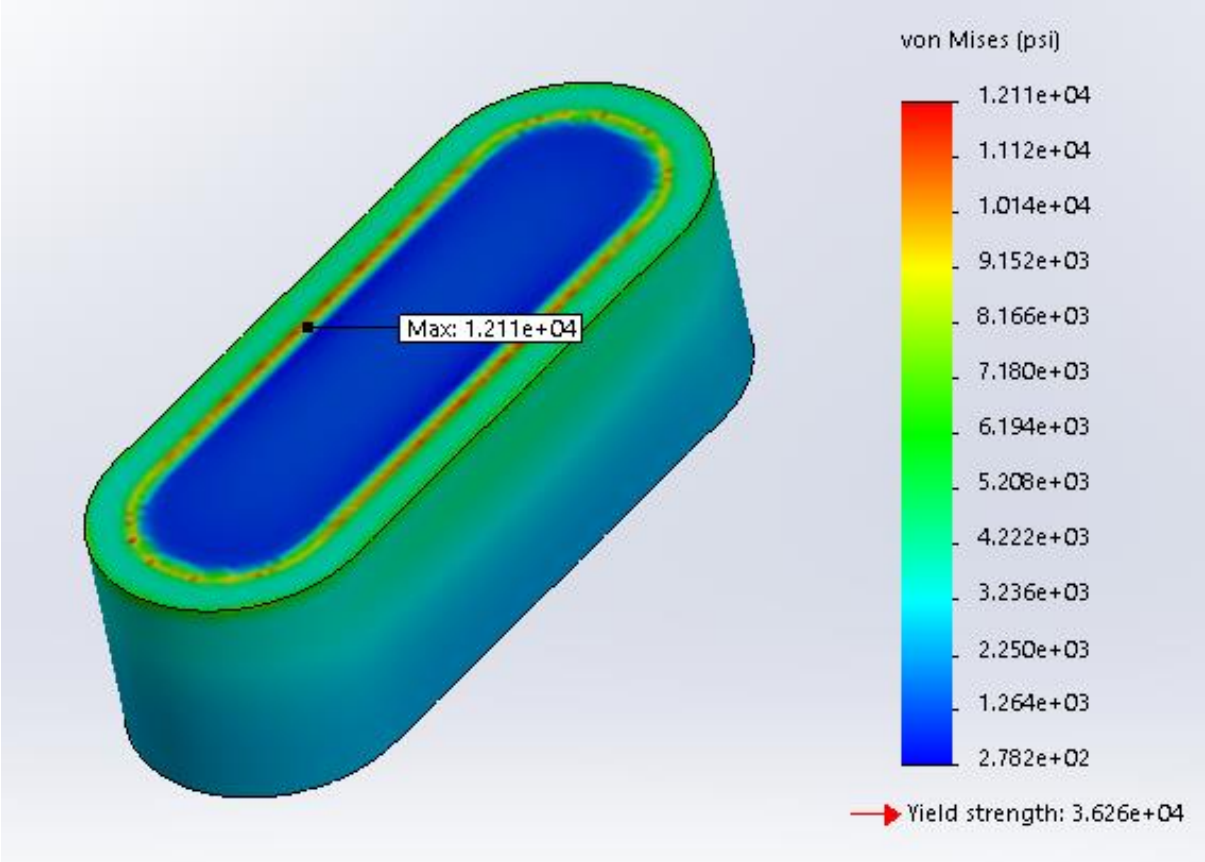

Figure 8-1. FEA of the sapphire window

The FE analysis of Inconel parts was performed by applying pressure of 2600 psig (the highest PRV setpoint in the system) to all surfaces that are exposed to high pressure during the normal operation, including the sealing faces. Additional forces were applied to each threaded hole where a flange is attached to the part that is analyzed. For the analysis of sapphire flange, the force that the window exerts on the flange was used instead of pressure. The properties of Inconel 600 that were used in the analysis are shown in **Error! Reference source not found.**.

Table 8-2 Mechanical properties of Inconel 600

Property	Value	Units
Elastic Modulus (@650 ^{o}F)	28,350 [80]	ksi
Poisson's Ratio	0.31 [80]	-
Mass density	0.300 [80]	Lb/in^3
Tensile Strength (@ room temperature)	94,990 (take from material certificate)	psi
Yield Strength (@ room temperature)	39,140 (take from material certificate)	psi

Two types of fixtures were used in the analysis: roller and radial. The roller fixture constrains the surface and prevents it from moving in a single cartesian direction. This fixture type was used on the areas where bolt heads are pushed against the analyzed part. The radial fixture constrains a cylindrical surface and prevents it from moving radially. This fixture was used on all unthreaded bolt holes.

The test section body was fixed in a different way. A special groove was machined at the bottom of the test section body which fits snugly with the protrusion on the upper flow channel section. Such assembly results in a tight contact between metal faces of the test section body and the upper flow channel section. This contact area was constrained in our analysis.

Figures Figure 8-2 through Figure 8-4 show the result of FEA performed on each Inconel part. According to the ASME Boiler and Pressure Vessel Code Section II, the maximum allowable stress in parts made of Inconel 600 at 650 ^{o}F is 23.3 ksi [80]. The points of peak stress are highlighted and numerical values of peak stress are displayed. In all cases the peak stress is below 23.3 ksi.

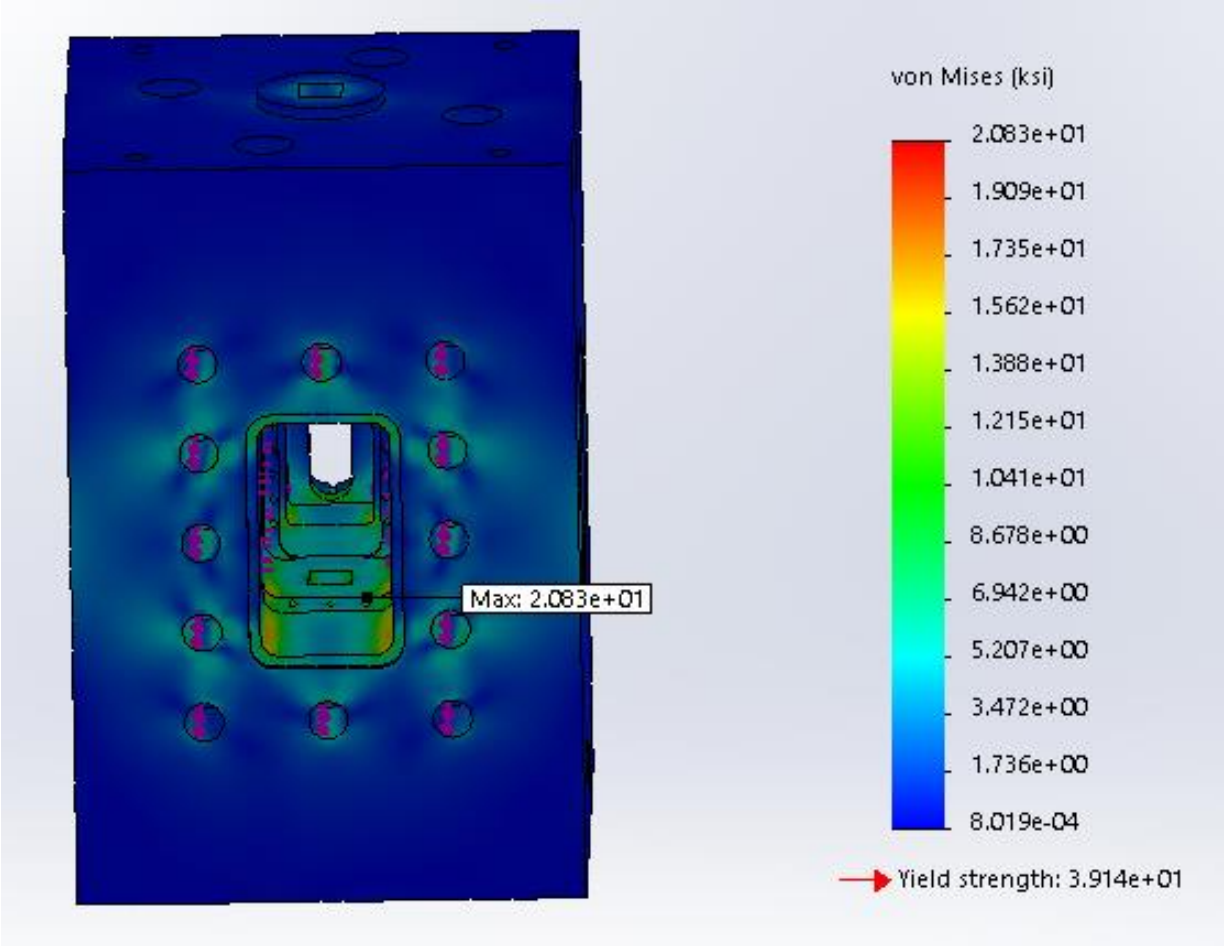

Figure 8-2. FEA of the test section body

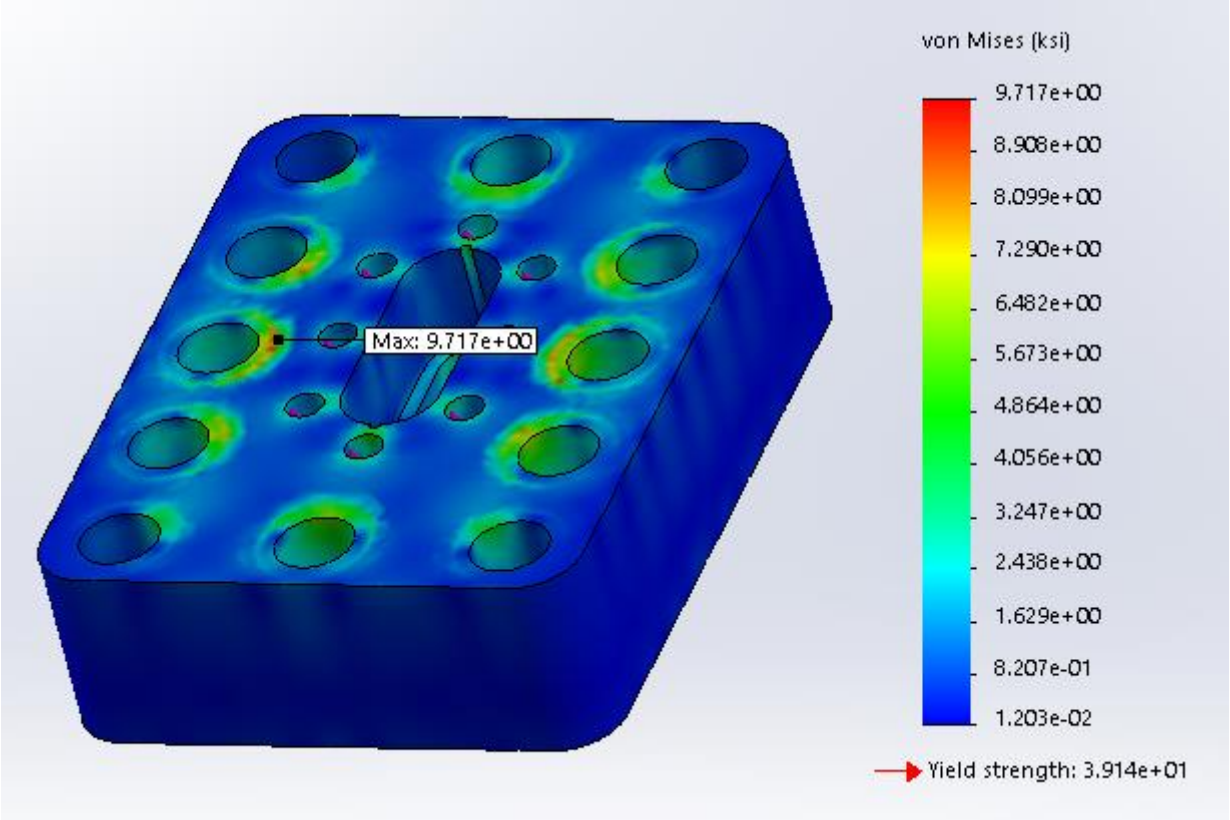

Figure 8-3. FEA of the main front flange

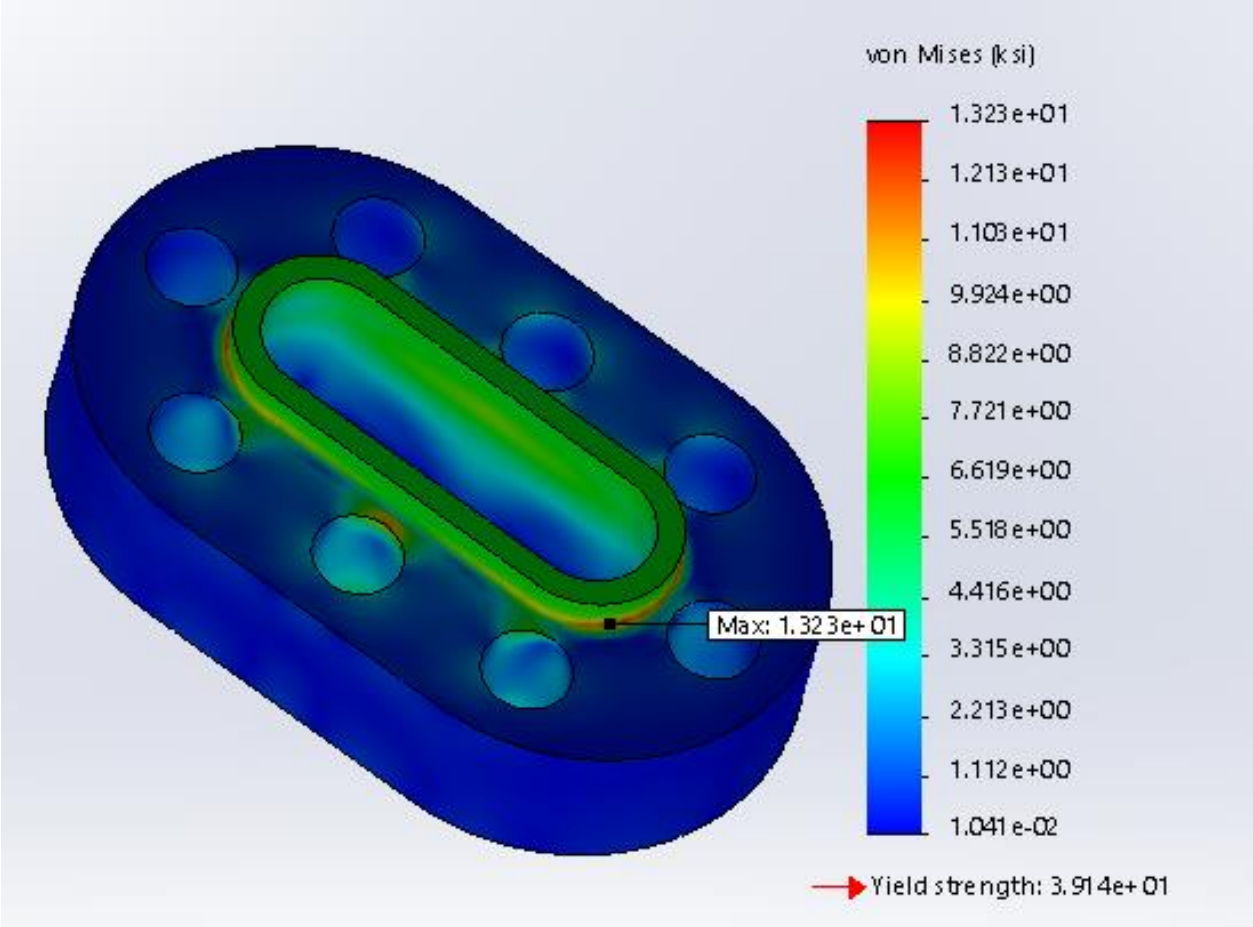

Figure 8-4. FEA of the sapphire flange

The upper and lower flow channel sections were fixed in the same way as the test section body. Figures 7 and 8 show the result of FEA performed on each Stainless Steel part. According to the ASME Boiler and Pressure Vessel Code Section II, the maximum allowable stress in parts made of 316 Stainless steel at 650 ^{o}F is 13.7 ksi. The points of peak stress are highlighted and numerical values of peak stress are displayed. In all cases the peak stress is below 13.7 ksi.

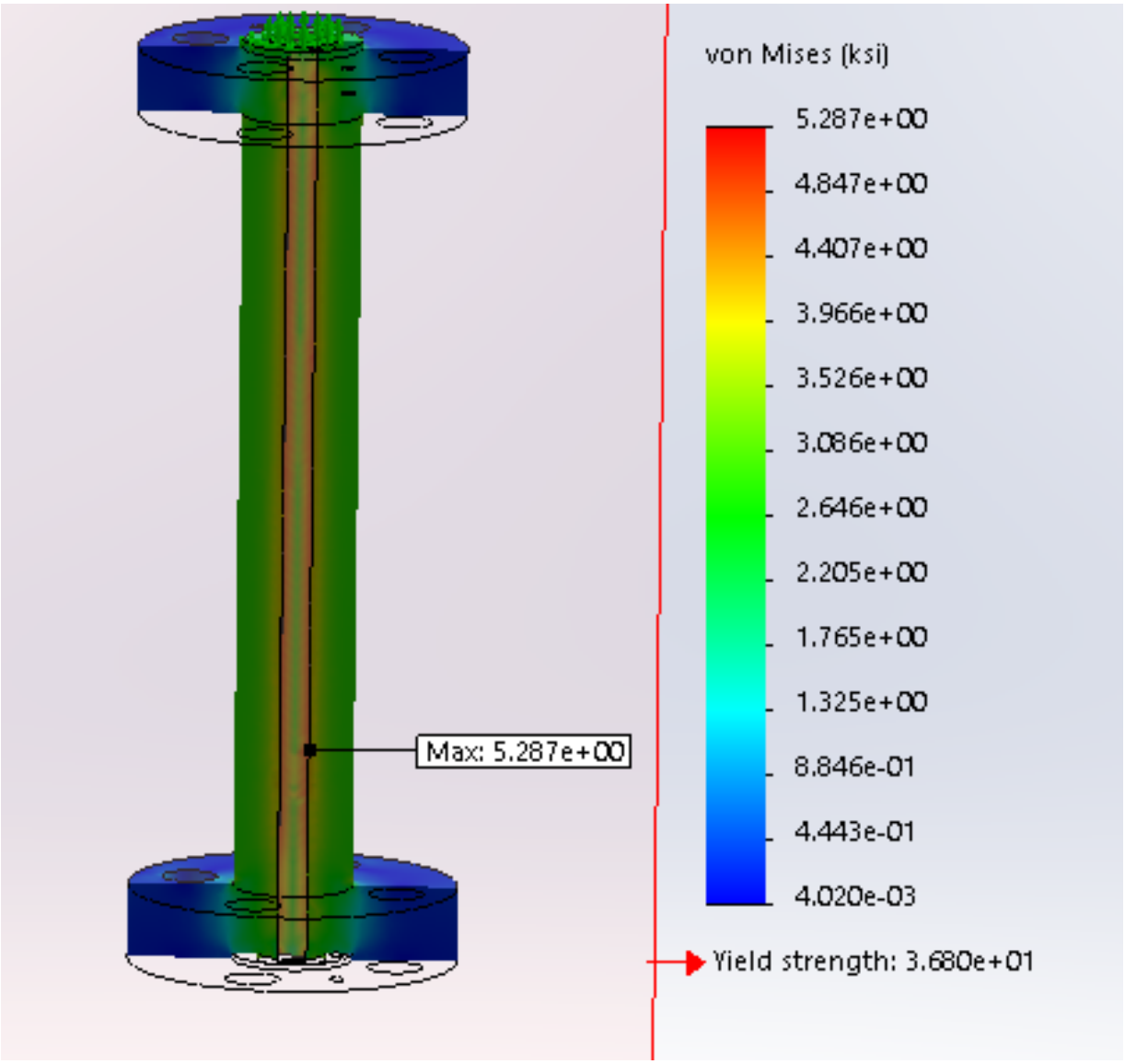

Figure 8-5. FEA of the upper flow channel section

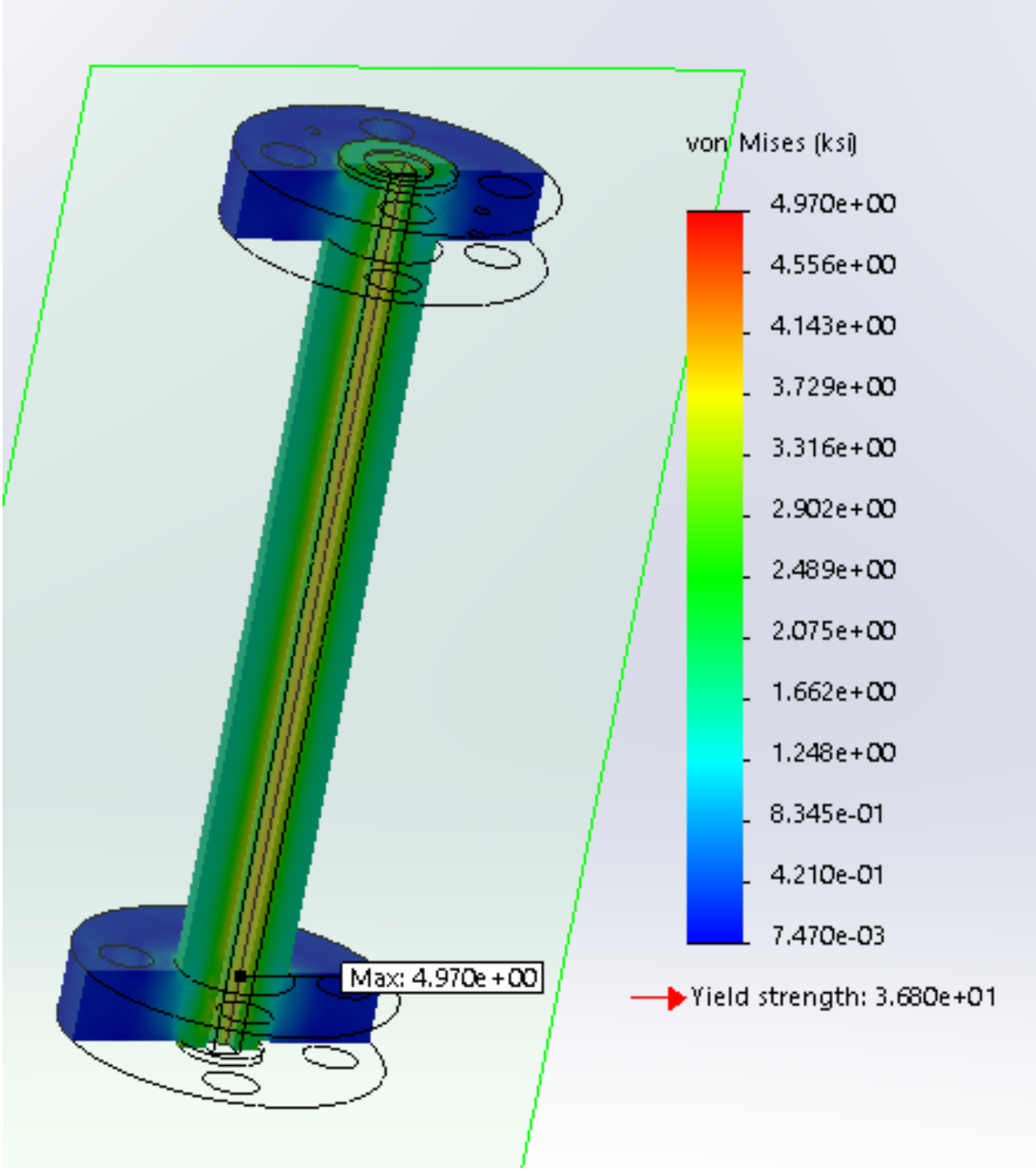

Figure 8-6. FEA of the lower flow channel section